ROYAUME DU MAROC
Université Mohammed V جامعة محمد الخامس
- RABAT - – الرباط –
Faculté des sciences
كلية العلوم

CENTRE D'ETUDES DOCTORALES - SCIENCES ET TECHNOLOGIES

N° d'ordre …………………

THESE

En vue de l'obtention du : ***DOCTORAT***

Structure de Recherche : Equipe de Science de la Matière et du Rayonnement.
Discipline : Physique.
Spécialité : Physique des hautes énergies.

Soutenue le 20/02/2021 par :

HASSANE HAMDAOUI

Observation of light-by-light scattering in heavy-ion collisions with the ATLAS detector at the LHC.

JURY

Prof. Yassine Hassouni	*Faculté des Sciences de Rabat*	*Président*
Prof. Mostapha Mansour	*Faculté des Sciences Ain Chock, Casablanca*	*Rapporteur*
Prof. Rajaa Cherkaoui El Moursli	*Faculté des Sciences de Rabat*	*Rapporteur*
Prof. Rachid Ahl Laamara	*Faculté des Sciences de Rabat*	*Rapporteur*
Prof. Laurent Olivier Schoeffel	*Irfu du CEA de Saclay.*	*Rapporteur*
Prof. Abedllillah Moussa	*Faculté des Sciences d'Oujda*	*Examinateur*
Prof. Yahya Tayalati	*Faculté des Sciences de Rabat*	*Directeur*

Année Universitaire : 2020/2021

🖂 Faculté des Sciences, avenue Ibn Battouta, BP. 1014 RP, Rabat –Maroc
☎ 00212 (05) 37 77 18 76 🖷 00212(05) 37 77 42 61; http://www.fsr.ac.ma/

Acknowledgement

First and foremost, I would like to express my gratitude to my supervisor ***Professor Yahya Tayalati*** *for his guidance, attention, invaluable help, and for finding me very interesting and important projects to work on during the course of this thesis.*

I would also like to thank all the jury members ***Prof. Rajaa Cherkaoui El Moursli****,* ***Prof. Mostafa Mansour, Prof. Rachid Ahl Laamara, Prof. Abedlillah Moussa,*** *and* ***Prof. Laurent Olivier Schoeffel*** *for accepting to review my thesis and providing feedback to improve it. My special thanks also go to the* ***Prof. Yassine Hassouni*** *president of the jury members for accepting to attend the defense of my thesis.*

I also wish to thank the members of the ESMaR team for the friendly work environment and support of all my work. I would like to thank CERN and my collaborators in the ATLAS experiment for successful operation of the LHC and data taking with our detector. This work was performed within the scope of the Heavy Ion Working Group of the ATLAS experiment and the TRT group. I'am grateful to several ATLAS students and senior colleagues for the very inspiring and friendly atmosphere in the group.

I would also like to thank FatimaZahra El Yedmani for reading my write-up and helping me improve it.

I am especially grateful to my family and friends for their support throughout my PhD studies. I thank you all.

This work was supported in part by a grant from the Swedish Research Council for allowing me to travel to CERN. Also many grants from CERN, ICTP, INFN to attend schools and conferences.

Abstract

Observation of light-by-light scattering in heavy-ion collisions with the ATLAS detector at the LHC

Hassane Hamdaoui

Observation of light-by-light scattering in heavy-ion collisions with the ATLAS detector at the LHC is carried out with data collected by ATLAS detector in 2015 and 2018 corresponding to a total luminosity of 2.2 nb^{-1}. The number of event observed is given and the fiducial and differential cross section are calculated. The measured diphoton invariant mass distribution is used to search for axion-like particles and set new exclusion limits on their production assuming 100% decay to photons.

The technical part of this thesis is dedicated to the tuning of argon emulation in the simulation of Transition Radiation Tracker (TRT) which was carried out by testing multiple parameters to decide the best one to be used for emulation argon from xenon without carrying out a full simulation which is time, CPU and disk space consuming.

Résumé

Observation de la diffusion lumière par lumière dans les collisions d'ions lourds avec le détecteur ATLAS du LHC

Hassane Hamdaoui

L'observation de la diffusion lumière par lumière dans les collisions d'ions lourds avec le détecteur ATLAS du LHC est réalisée avec les données collectées par le détecteur ATLAS en 2015 et 2018 correspondants à une luminosité totale de 2,2 nb^{-1}. Le nombre d'événements observés est donné et les sections efficaces fiduciaire et différentielle sont calculées. La distribution de masse invariante des deux photons mesurés est utilisée pour rechercher des particules de type axion et fixer de nouvelles limites d'exclusion sur leur production en supposant une désintégration de 100% en photons.

La partie technique de cette thèse est consacrée à l'optimisation de l'émulation d'argon dans la simulation du Trajectographe à Rayonnement de Transition (TRT) qui a été réalisée en testant plusieurs paramètres pour décider le meilleur à utiliser pour l'émulation d'argon à partir du xénon sans réaliser une simulation complète qui consomme beaucoup de temps, CPU et espace disque.

Contents

List of Figures

List of Tables

Introduction

The nature of light was always a major topic driving scientist and philosophers since the ancient Greek times up to the present day. Through history many distinguished physicist have contributed to our current understanding of light. Maxwell can be thought of as the person who completed the classical description of light with his famous equations. While from the quantum description sides an important number of physicist along the 20th century have contributed to this endeavor. One important breakthrough is the light-by light-scattering which was postulated in the early days of the Quantum Electrodynamics (QED) in 1936 by Heisenberg and Euler. This effect was part of the demonstration that the classical Maxwell equations is not enough to describe the light and its interactions. Which make the way to one of building blocks of the current Standard Model of particles physics which is the leading model to describe the matter and its interactions.

The QED was an important step toward building the current SM of particle physics. Which constitute the more up to date and well tested understanding of the our universe building blocks and their interactions. There are, however, phenomena that Standard Model provides no explanation for such as the existence of dark matter proven from cosmological observation which make the SM providing explanation for nearly 5% of our universe many other shortcoming of the SM are linked to its inability to explain the matter antimatter imbalance in the universe and the hierarchy problem.... These facts proves that despite its success the SM is not a complete theory.

Since its first collision in 2009 The Large Hadrons Collider at CERN keep physicist busy exploring the huge amount of data delivered to different experiment. The LHC was built with two main purposes the first is to test the SM prediction to the highest precision possible and the second is to search for beyond SM physics.

Photon at the ATLAS experiment holds a very important place and they are used to probe many aspect of the SM and beyond. In fact, the Higgs boson di-photon final state, $H \to \gamma\gamma$, is an obvious example. Though the predicted branching ratio for such a decay is around 0.23% for $m_H = 125$GeV, compared to the much larger branching ratios for decays to $bb(58\%)$ or $\tau^+\tau^-(6.3\%)^1$, the larger signal-to-background ratio (the production cross sections of the main SM backgrounds at $\sqrt{s} = 14$TeV are respectively a few μb for $b\bar{b}$ and about five orders of magnitude smaller for $\gamma\gamma$) and the excellent $\gamma\gamma$ invariant mass resolution that can be obtained with modern electromagnetic calorimeters made the di-photon channel one of the best candidates for the Higgs boson discovery at the LHC in 2012 [1].

In this thesis we cover the work that was carried out within the ATLAS collaboration. One concerns tuning argon emulation in the Transition Radiation Tracker(TRT). The second goes under the scoop of ultra peripheral heavy ions collisions and is dedicated to light-by-light scattering measurement using 2015 and 2018 data taken with the ATLAS detector.

Tuning the argon emulation in the TRT was carried out within the TRT group of the ATLAS collaboration. It consists of testing the emulation technique as a replacement of full simulation of the TRT when a gas configuration occurs in particular when switching from Xenon to Argon. The study was mainly focused on the particle identification (PID) capabilities of the TRT since its the one affected by the change of the gas mixture from xenon to Argon. The study is carried out by comparing multiple observable from emulation and full simulation.

Concerning the light-by-light scattering measurement we performed analysis of Pb+Pb data collected with the ATLAS detector in 2015 and 2018 respectively at center-of-mass energy of $\sqrt{s_{NN}} = 5.02$ TeV. After dedicated performances studies and background estimation the measurement provides the number light-by-light event observed, fiducial cross section measurement and differential cross section measurement. The measured diphoton invariant mass distribution of the combined data set is used to set limits on the ALP production via the process $\gamma\gamma \to a \to \gamma\gamma$.

This write-up is divided in six distinguished chapters. Chapter 1 is dedicated to an overview of the current model describing ours current understanding of particles and their interactions. The same chapter also provides an short overview of theories beyond standard model which try to outcome the shortcoming of the standard model. Chapter 2 focus on light-by-light scattering background theory and the physics motivation related to this particular process in particular in beyond standard model measurement. Chapter 3 is assigned to the description of the LHC experimental facilities and the ATLAS detector. It gives an overview of the operation and details about the sub-detectors. The same chapter also provides a description of the physics object reconstruction used in the analysis mainly photons and electrons. The argon emulation studies in TRT is presented in chapter 4. The light-by-light scattering analysis is presented in chapter 5 with dedicated section for event selection, detector performance, background estimation, systematic uncertainties and results. The last chapter 6 we present a short state of the art the results concerning the search for axion like particle.

Chapter 1

The Standard Model (SM) of Particle Physics and beyond

Contents

Introduction

This chapter gives an overview of the up to date theoretical model of particles physics and how the Standard Model is the leading model in explaining the interaction between building blocks of matter. Section 1.1 presents some historical fact and major ideas that led to the Standard Model. Section 1.2 will give an overview of the particle content of the Standard Model as well as the interactions between them while section 1.3 is dedicated to possible extensions of the SM.

1.1 History

The Standard Model of particles physics is a sequence of brilliant ideas built in so many years. The first one was the quark model which was proposed by Gell-Mann and Zweig independently [2, 3] in 1964. The second one was the idea of gauge (or local) symmetry in 1950s and 1960s and the third one was the idea of spontaneously broken symmetry.
The initial step towards the Standard Model was Sheldon Glashow's discovery in 1961 of a way to combine the electromagnetic and weak interactions. In 1967

Steven Weinberg and Abdus Salam incorporated the Higgs mechanism into Sheldon Glashow's electroweak theory, giving it its modern form. Abraham Pais and Sam Treiman created the name "Standard Model" in 1975.

1.2 SM Fundamental Particles and Forces Carriers

1.2.1 The Particles

The standard model account 12 fundamental particles each one associated with its antiparticle with the same mass and spin, but a different electrical charge. Table 1.1 shows the 12 particles and their properties. They can be divided into two families: Quarks, carrying a fractional electric charge of 3/2 for up, charm and top and -1/3 for down, strange and bottom.
Leptons, full electric charge: zero for neutrinos and -1 for charged leptons .
Quarks and leptons also differ from a quantum number: color, associated only to the quarks and bosons that drive the strong interaction, the gluons. It can take three values (red, green or blue) and constrains quarks to form bound states, only neutral states of color can be observed [4].

Generation	Type	Flavor	Symbol	Mass [GeV]	Charge	Discovery
First Generation	Lepton	Electron	e^-	0.511×10^{-3}	-1	1897 [5]
		Neutrino	ν_e	$< 2 \times 10^{-9}$	0	1956 [6]
	Quark	up	u	$2.2^{+0.5}_{-0.4} \times 10^{-3}$	2/3	1968 [7]
		down	d	$4.7^{+0.5}_{-0.3} \times 10^{-3}$	$-1/3$	1968 [7]
Second Generation	Lepton	Muon	μ^-	0.106	-1	1936 [8]
		Neutrino	ν_μ	$< 0.19 \times 10^{-3}$	0	1962 [9]
	Quark	charm	c	$1.275^{+0.025}_{-0.035}$	2/3	1974 [10]
		strange	s	$0.104^{+0.026}_{-0.034}$	$-1/3$	1968 [7]
Third Generation	Lepton	Tau	τ^-	1.78	-1	1975 [11]
		Neutrino	ν_τ	$< 18.2 \times 10^{-3}$	0	2000 [12]
	Quark	top	t	171 ± 2	2/3	1995 [13]
		bottom	b	$4.20^{+0.17}_{-0.07}$	$-1/3$	1977 [14]

Table 1.1: Standard model fermions.

1.2.2 The Interactions

The Standard Model also contains other particles that do not constitute the material but bear the fundamental interactions. Table 1.2 shows the bosons particles that are the mediator of the strong, electromagnetic and the weak interaction. The Standard Model is a quantum field theory, it follows a formalism regrouping the quantum and relativistic worlds, both necessary for the description of the infinitely small. Their union within relativistic quantum mechanics leads to the equations of Dirac and Klein Gordon, but can only describe systems containing a single particle, and cause problems of causality [15]. Field theory allows associating with each particle a field $\psi(\vec{x}, t) = \psi(x_\mu)$, where $\vec{x}$ and t are respectively the position vector and the time, and x_μ is the four-vector space-time. Moreover, the Standard Model is based on the concept of gauge invariance and symmetry, the relation between the two being shown by Noether's theorem [16]. The Lagrangian density describing the elementary particles and their interactions should be invariant under the local gauge symmetry transformation. Such an invariance causes the appearance of new fields describing gauge bosons.The Standard Model is based on a symmetry group given by

$$SU(3)_C \otimes SU(2)_L \otimes U(1)_Y, \tag{1.1}$$

where $SU(3)_C$ corresponds to the symmetry group related to the strong interaction and the product $SU(2)_L \otimes U(1)_Y$ corresponds to the electroweak interaction, both presented in the next paragraphs.

Interaction	Gauge boson	Mass [GeV]	Charge
strong	8 gluons (g)	0	colour (r,g,b)
electromagnetic	photon (γ)	0	electrical
weak	Z	~ 91.2	weak isospin
	W	~ 80.4	

Table 1.2: Standard model bosons.

1.2.3 Electromagnetic interaction: quantum electrodynamics

This is the most well-known interaction as it has been studied since the end of the 19th century, in particular by Maxwell [17]. It exists between two charged particles, whatever their type (quarks, leptons, bosons), it is of infinite range and its intensity depends only on the charge and the distance r between particles. A free elemental charged fermion of mass m, represented by the field $\psi(x)$, is described by the Lagrangian $\mathcal{L}$ of the equation :

$$\mathcal{L} = \bar{\psi}(x)(i\gamma^\mu \partial_\mu - m)\psi(x), \tag{1.2}$$

where γ^μ represent the Dirac matrix. This Lagrangian is invariant under a global $U(1)$ symmetry given by :

$$\psi(x) \xrightarrow{U(1)} \psi^{'}(x) = exp(-i\theta)\psi(x), \tag{1.3}$$

where θ is an arbitrary real constant.
However when θ depends on x , the transformation became local (gauge), then the field and its derivative becomes :

$$\psi(x) \xrightarrow{U(1)} \psi^{'}(x) = exp(-i\theta(x))\psi(x), \tag{1.4}$$

$$\partial_\mu\psi(x) \xrightarrow{U(1)} \partial_\mu\psi^{'}(x) = exp(-i\theta(x))[\partial_\mu - i\partial_\mu\theta(x)]\psi(x), \tag{1.5}$$

$$\mathcal{L}^{'} = \bar{\psi}(x)[(i\gamma^\mu\partial_\mu - m + \gamma^\mu(\partial_\mu\theta(x))]\psi(x), \tag{1.6}$$

the new Lagrangian $\mathcal{L}^{'}$ is not a gauge invariant anymore. we need to introduce a new derivation definition; the covariant derivative. D_μ

$$D_\mu\psi(x) \rightarrow [D_\mu\psi(x)]^{'} = exp(-i\theta(x))D_\mu\psi(x), \tag{1.7}$$

where

$$D_\mu = \partial_\mu + ieA_\mu, \tag{1.8}$$

where A_μ is the gauge field and e is the electric charge. The invariance of the Lagrangian under the $U(1)$ symmetry.

$$A_\mu \rightarrow A^{'}_\mu = A_\mu + \frac{1}{e}\partial_\mu\theta(x), \tag{1.9}$$

Finally, the field A_μ is allowed to propagate by the introduction of a kinetic term given by :

$$\mathcal{L}_{propagation} = -\frac{1}{4}F_{\mu\nu}F^{\mu\nu} \quad \text{where} \quad F_{\mu\nu} = \partial_\mu A_\mu - \partial^\mu A^\mu, \tag{1.10}$$

Consequently, the interaction vertex between two electrically charged fermions is governed by the Lagrangian of the equation

$$\begin{aligned}\mathcal{L} &= \bar{\psi}(x)(i\gamma^\mu D_\mu - m)\psi(x) - \frac{1}{4}F_{\mu\nu}F^{\mu\nu} \\ &= \underbrace{\bar{\psi}(x)(i\gamma^\mu \partial_\mu - m)\psi(x)}_{\text{free Lagrangian}} - \underbrace{\bar{\psi}eA_\mu\psi}_{\text{Interaction}} - \underbrace{\frac{1}{4}F_{\mu\nu}F^{\mu\nu}}_{\text{propagation of } A_\mu} \quad ,\end{aligned} \tag{1.11}$$

The expression 1.11 shows that the interactions between the elementary charged fermions are carried by a boson of gauge A_μ corresponding to the photon. Moreover, a mass term is impossible in this theory because it would break the $U(1)$ gauge symmetry again. This paragraph shows that a symmetry observed in nature makes it possible to constrain the expression of the Lagrangian, and in particular to introduce the field responsible for the propagation of the interaction: the photon.

1.2.4 Electroweak unification

The weak interaction is particularly responsible for β-type nuclear reactions, unlike the electromagnetic interaction, acts only on particles of left chirality. In the 1960s Glashow, Salam and Weinberg [18, 19] described in a similar formalism electromagnetic and weak interactions , leading to a single interaction: the electroweak interaction. The electroweak interaction, governed by the local symmetry group $SU(2)_L \otimes U(1)_Y$ imply the presence of four gauge fields, $W^{1,2,3}$ and B. The first are from $SU(2)_L$ symmetry where the index L indicates that this part of the interaction only acts on the left chirality components particles and the last denoted B is produced because of the $U(1)_Y$ symmetry and acts identically on each of the two chirality components of the particles. where the index Y indicates the hyper-charge. The Lagrangian density describing this interaction is given by:

$$\begin{aligned}\mathcal{L} = i\bar{\psi}_L(x)\gamma^\mu &\left[\partial_\mu + i\frac{g}{2}Y_L B_\mu + i\frac{g'}{2}\begin{pmatrix} W^3 & W^1 - iW^2 \\ W^1 + iW^2 & -W^3 \end{pmatrix}\right]\psi_L(x) \\ &+ i\bar{\psi}_R(x)\gamma^\mu \underbrace{\left[\partial_\mu + i\frac{g}{2}Y_R B_\mu\right]}_{D^{'}_\mu}\psi_R(x) \quad , \\ &- \frac{1}{4}B_{\mu\nu}B^{\mu\nu} - \frac{1}{4}W_{\mu\nu}W_i^{\mu\nu}\end{aligned} \tag{1.12}$$

where g and g' are the coupling constant associated to U(1) and SU(2) respectively. $B_{\mu\nu}$ and $W_{\mu\nu}$ are defined as fellow :

$$\begin{aligned} B_{\mu\nu} &= \partial_\mu B_\nu - \partial_\nu B_\mu \\ W^i_{\mu\nu} &= \partial_\mu W^i_\nu - \partial_\nu W^i_\mu - g'\varepsilon_{ijk} W^j_\mu W^k_\nu, \end{aligned} \tag{1.13}$$

where ε_{ijk} is the structure constant of the SU(2) group. the equation show that the bosons W^i only interact with the left-handed chiral components and the B field interact with all the components. Finally, the $W^\pm$ bosons are a combination of W^1 and W^2 while the Z and γ bosons are a mixture of W^3 and B, the mixing angle is denoted θ_W.

$$\begin{pmatrix} W^3_\mu \\ B_\mu \end{pmatrix} = \begin{pmatrix} cos\theta_W & sin\theta_W \\ -sin\theta_W & cos\theta_W \end{pmatrix} \begin{pmatrix} Z_\mu \\ A_\mu \end{pmatrix}, \tag{1.14}$$

the $W^\pm$ and Z are so far massless!

1.2.5 The strong interaction: quantum chromodynamics

Strong interaction exists only between particles carrying a color charge. One of its main features is the confinement of quarks. Indeed, they carry a load of color, and can not be observed alone: the observable states are only color neutral. Experimentally, two[1] linked states are observed :

- **Mesons**, with a quark and an anti-quark (like the loaded pions $\pi^\pm$, bound states a quark u and an anti-quark d),
- **Baryons**, made up of three quarks (like protons).

The theoretical situation is more complex in the case of QCD than for QED. Indeed, for the latter, rotation operators can switch with different fields, we talk about abelian theory. This is not the case in the context of QCD for which the symmetry group used is $SU(3)_C$. For a quark of flavor f and of color a, described by a field q^a_f, we can write the Lagrangian free (the sum on the states of color a is implied in the sequel

$$\mathcal{L} = \bar{q}_f(i\gamma\partial_\mu - m_f)q_f, \tag{1.15}$$

The same invariance conditions invoked under the QED induce the appearance of eight new gauge fields (corresponding to the number of symmetry generators SU (3), the matrices of Gell-Mann), corresponding to the gluons, and denoted G^i_μ (for the color state i). The final Lagrangian is then given by

$$\begin{aligned} \mathcal{L}_{QCD} = &-\frac{1}{4}(\partial_\mu G^a_\nu - \partial_\nu G^a_\mu)(\partial_\mu G^a_\nu - \partial_\nu G^a_\mu) + \sum_{min}^{max} \bar{q}_f(i\gamma\partial_\mu - m_f)q_f \\ &+ g_s G^a_\mu \sum_f \bar{q}^\alpha_f \gamma_\mu (\frac{\lambda^a}{2})_{\alpha\beta} q^\beta_f \qquad , \\ &+ \frac{g_s}{2} f^a_{bc}(\partial_\mu G^a_\nu - \partial_\nu G^a_\mu) G^b_\mu G^c_\nu - \frac{g_s^2}{4} f^{abc} f_{ade} G^\mu_b G^\nu_c G^d_\mu G^e_\nu \end{aligned} \tag{1.16}$$

---

[1] new bound states containing 4 and 5 quarks were recently observed in the LHCb experiment

The first line defines the propagators of the different fields (gluons and quarks). The second describes the interaction between quarks and gluons, using Gell-Mann λ^a matrices and the strong coupling constant g_s. Finally, the last line shows the effect of the non abelian character of algebra of $SU(3)$, and represents the vertexes with three or four gluons, f^{abc} being the structure constant of algebra.

1.2.6 Spontaneous symmetry breaking and the need for the higgs boson

The main difficulty of the theory at this stage is that all gauge bosons are massless unlike the results of the experiment which show that the bosons vectors of the weak interaction have a mass, unlike the photon, of zero mass. In 1964, the British physicist Peter Higgs and the two Belgian theorists Robert Brout and François Englert offer a possible solution to this problem: symmetry $SU(2)_L \otimes U(1)_Y$ must be broken, while maintaining a conserved $U(1)_{EM}$ symmetry [20–22]. The mechanism of this break, called Brout-Englert-Higgs mechanism requires the introduction of a new doublet of complex scalar fields:

$$\Phi_H = \begin{pmatrix} \Phi^+ \\ \Phi^0 \end{pmatrix}, \tag{1.17}$$

where

$$\begin{aligned} \Phi^+ &= \frac{\phi_1 + i\phi_2}{\sqrt{2}} \\ \Phi^0 &= \frac{\phi_3 + i\phi_4}{\sqrt{2}}, \end{aligned} \tag{1.18}$$

where ϕ_i are real fields. The lagrangian describing this doublet is given by :

$$\mathcal{L}_{Scalaire} = (D_\mu \Phi_H)^\dagger (D^\mu \Phi_H) + V(\Phi_H), \tag{1.19}$$

where V is the Higgs potential described as :

$$V(\Phi_H) = -\mu^2 \Phi_H^\dagger \Phi_H + \lambda (\Phi_H^\dagger \Phi_H)^2, \tag{1.20}$$

The configurations where μ^2 is positive leads to a trivial solution $\Phi_H = 0$ for whom the electroweak bosons are still massless. The V potential for the non trivial case $\mu^2 < 0$ is represented in figure 1.1. Where $R(\Phi)$ and $Im(\Phi)$ represent respectively the real and imaginary parts of the ϕ_H field.The field has the shape of a Mexican hat. The $\Phi_H = 0$ corresponds to a local maximum. The minimum value is reached for an infinite number of combinations. This minimum is named as the expected value in the vacuum. $v = \sqrt{\frac{-\mu^2}{\lambda}} = 246\ GeV$.

The potential and the Lagrangian are so kept invariant under the gauge symmetry, but the field value in the vacuum break it by taking a particular value as

$$\Phi_H^0 = \sqrt{\frac{1}{2}} \begin{pmatrix} 0 \\ v \end{pmatrix}, \tag{1.21}$$

this is what we call spontaneous symmetry breaking. The field fluctuation around its minimum modify the expression of Φ in two different ways :

- A phase variation of the form $exp(i\eta_j)$ where the fields η_j are the massless Goldstone bosons.

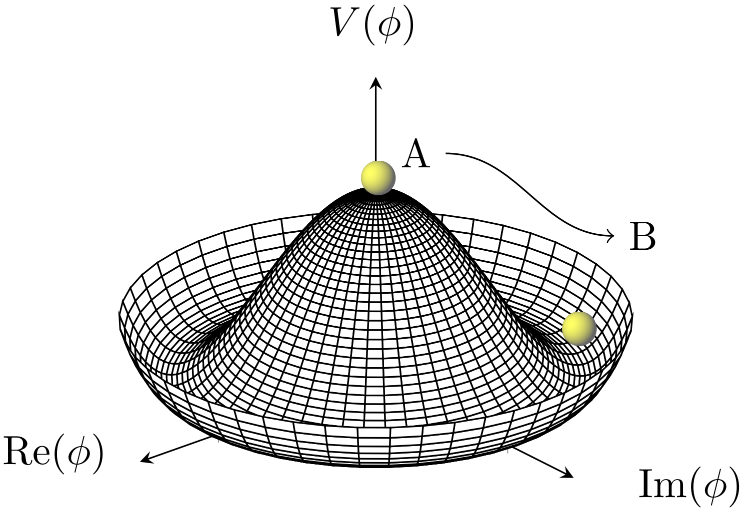

Figure 1.1: The Higgs potential as a function of the complex scalar field.

- A radial fluctuation $v \to v + H$ where H is the field corresponding to the so called *Higgs* boson.

Φ_H is written as :

$$\Phi_H = \frac{e^{\eta_a(x)\tau^a}}{\sqrt{2}} \begin{pmatrix} 0 \\ v+H \end{pmatrix}, \tag{1.22}$$

where $\tau^a (a = 1, 2, 3)$ are the generators of the SU(2) group. The degrees of freedom represented by the Goldstone bosons are absorbed as longitudinal modes of gauge bosons $W^{\pm}$ and Z and the scalar field correspond to the Higgs boson. The introduction of the expression 1.20 in the Lagrangian of equation 1.17 then makes it possible to appear identifiable terms to masses for the $W^{\pm}$ and Z bosons and maintain a massless photon.

$$\begin{aligned} m_W &= \frac{1}{2} v g' \\ m_Z &= \frac{v}{2}\sqrt{g^2 + g'^2}, \\ m_\gamma &= 0 \end{aligned} \tag{1.23}$$

The existence of the Higgs boson also allows the acquisition of a mass for fermions. For this, we consider an interaction between the Higgs field and the fermions, called interaction of Yukawa. They then acquire a mass proportional to v and the coupling between the fermion and the boson of Higgs, called Yukawa coupling.

A first step towards the experimental validation of this mechanism was announced on July 4, 2012 by the discovery of a particle with characteristics similar to the Higgs boson. That day, the ATLAS and CMS experiments present [1, 23] the discovery of a scalar boson of about 125 GeV and can be the boson of Higgs after nearly 60 years of research by all of the experiments of particle physics and in particular in the context of LEP and Tevatron. The discovery was followed by many studies of the properties of this new particle and especially its spin, mass and branching ratios. They show evidence of its scalar character [24, 25] and couplings compatible with the Standard Model [26]. The mass of Higgs boson, determined by the ATLAS experiment in the $H \to \gamma\gamma$ decay channels and $H \to ZZ*$ is currently measured at: $m_H = 125.5 \pm 0.2$ (stat) ${}^{+0.5}_{-0.6}$ (syst) GeV [27].

1.2.7 Success and gaps : The Higgs discovery is not the end of the story

The Standard Model has shown great robustness and a predictive character very often confirmed by experience. For example, the existence of the W and Z bosons was postulated before their experimental discovery in 1983 [28, 29] as well as for the Higgs boson. In addition, the cross sections of various processes, such as the production of top-antitop pairs or gauge bosons are measured experimentally and are compatible with the expectations of the Standard Model as shown in Figure 1.2.

However, there are several indications that the Standard Model may only be an effective theory at low energy. The first theoretical limitation concerns gravitation. This interaction is the only one of the four fundamental interactions not included in the Standard Model. It remains negligible when the energy scale considered is of the order of the electroweak scale ($\approx$ 100GeV). However, at the Planck scale ($\Lambda_p \approx 10^{19}$GeV) , it must be taken into account: the Standard Model is therefore not a valid theory at this energy scale. The difference between the two energy scales (Planck scale and electroweak scale) constitutes one of the difficulties of the Standard Model, called the hierarchy problem. Within the SM, neutrinos are treated as massless, but observation of neutrino oscillation demands that neutrinos in fact do have a non-vanishing mass. The bare mass of the Higgs boson, denoted m_0 is not the mass at which it can be detected, denoted m. The latter is the result of taking into account radiative corrections. For example, a loop of fermions can lead to a given correction, at the first order by the equation 1.24 [30].

$$m^2 = m_0^2 - \frac{\lambda_f^2}{8\pi^2}\Lambda_c^2 + \dots, \tag{1.24}$$

Where λ_f is the Yukawa coupling of the fermion f and Λ_c the energy scale up to which Standard Model is assumed to be valid. Quadratic and higher order terms appear naturally leading to a large expected mass of the Higgs boson. However, experimental constraints and the recent discovery of the Higgs boson show that this mass must be small: the quadratic divergences must be compensated by m_0. In reality the adjustment of the variables m_0 and λ must be realized until the 32^{eme} decimal! This is the problem of naturalness. The particle with the highest Yukawa coupling is the top quark, for which its value is of the order of 1: it turns out to be the fermion leading to the most significant radiative corrections.

Other examples, such as the unexplained number of families (generations) of fermions, the non-prediction of dark matter (whose presence is for example confirmed by observations relating to the rotation of galaxies [31]), the ad-hoc addition to The Higgs mechanism can also constitute weaknesses in the Standard Model.

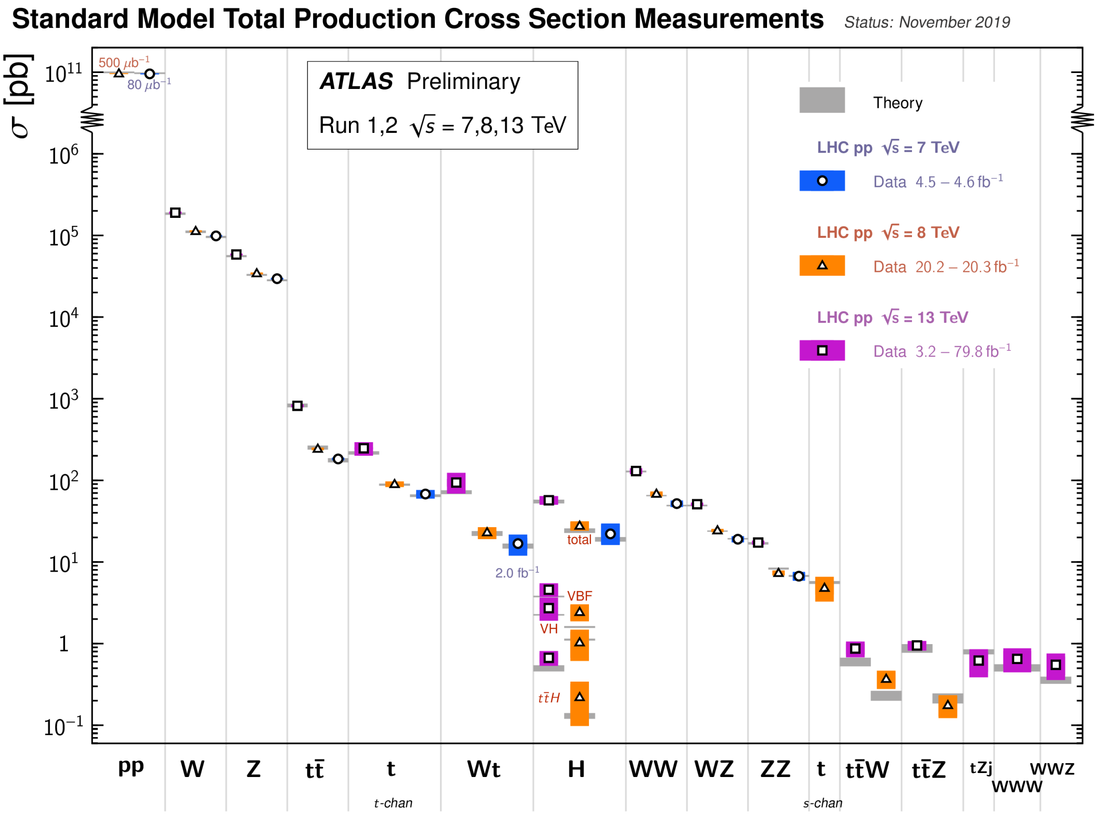

Figure 1.2: Summary of several Standard Model total production cross section measurements, corrected for branching fractions, compared to the corresponding theoretical expectations [32].

1.3 Beyond the Standard Model

Given all the reasons cited in the previous section several extensions of the SM are introduced to solve its shortcoming in answering these open questions. In most of the cases these extension predict the existence of new particles and or mediator not yet observed in experiment.

Supersymmetry is one of the most interesting alternatives to the Standard Model and is the most tested theory in experiments like ATLAS. Section 1.3.1 presents its founding ideas and the state of current research in the context of reference models. Other theories based on the existence of additional dimensions are introduced in the Section 1.3.2

1.3.1 Super symmetry

The supersymmetric models rely on the existence of operators associating with any fermion of the Standard Model a boson and vice versa, which makes it possible to solve the problem of naturalness. Indeed, in second order, the correction linked to a fermion loop (Figure 1.3 (a) is given by:

$$m^2 = m_0^2 - \frac{\lambda_f^2}{8\pi^2}\Lambda_c^2 - \frac{3m_f^2}{8}\ln\left(\frac{\Lambda_c}{m_f}\right)\ldots, \tag{1.25}$$

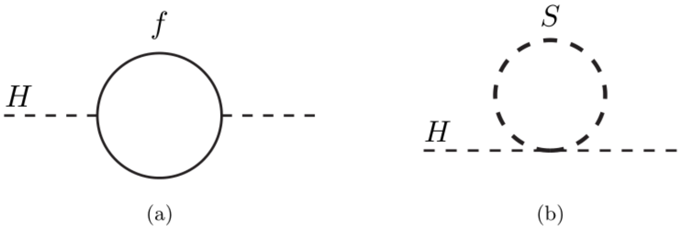

Figure 1.3: Radiative corrections to the mass of the Higgs boson by taking loops into account fermionics (a) and scalar (b).

and the contribution of a scalar loop (Figure 1.3 (b)) is given by the equation:

$$m^2 = m_0^2 + \frac{\lambda_s^2}{16\pi^2}\Lambda_c^2 - \frac{m_s^2}{8}\ln\left(\frac{\Lambda_c}{m_s}\right)\ldots, \tag{1.26}$$

In these equations λ_f is the Yukawa coupling of the fermion f of mass m_f. Similarly, the coupling between the scalar s of mass m_s and the Higgs boson is denoted λ_s

Therefore, it appears that the quadratic divergences can be eliminated if, to each fermion of the Standard Model, there are associated two scalar superpartners presenting the same couplings as the latter $(\lambda_s = \lambda_f)$. And being of the same mass. Only logarithmic divergences remain, and remain small if the mass differences between the particles of the Standard Model and their superpartners are small (typically of the order of TeV). If the supersymmetry is exact, the superpartners must have identical masses, but this hypothesis is contradicted by experimental observations: the supersymmetry is broken. The break should be gentle, avoiding the introduction of new terms diverging quadratically. Its mechanism is currently unknown.

Standard Model fermions and their scalar superpartners are included in a set, called a chiral supermultiplet. The latter contains the spinor of the fermion and the two real partner scalar fields. These fields mix and lead to a complex scalar field, corresponding to a superpartner, called sfermion. In the same way, vector bosons can be found within so-called vector supermultiplets, with their fermionic superpartner, called jaugino. For example, the gluon of spin 1 is associated with the gluino of spin $\frac{1}{2}$. In each of these supermultiplets, the numbers of fermionic and bosonic degrees of freedom are identical $(n_B = n_F = 2)$

The experimental constraints required the introduction of a new quantum number, multiplicative, called parity R. Indeed, the MSSM (Minimum Supersymmetric Standard Model) could lead to a proton lifetime much lower than the current experimental constraint ($> 10^{32}$ years [4]), through violation of the baryonic B and leptonic L numbers. The conservation of the parity R, defined in equation 1.27 (in which s is the spin of the particle) during physical processes makes it possible to suppress such effects.

$$R = (-1)^{3(B-L)+2s}, \tag{1.27}$$

R then takes the value of +1 for the particles of the Standard Model, and of -1 for the supersymmetric particles. The conservation of the parity R leads to several major phenomenological consequences with regard to the supersymmetric models. First of all, the single production of supersymmetric particles is impossible (the parity in the initial state being +1, it must be the same in the final state) and the two-body decay of a particle supersymmetric must include a particle of parity $R = -1$ and a particle of the Standard Model. As a result, the lightest supersymmetric particle (called LSP for Lightest Supersymmetric Particle) is stable, and naturally provides a good candidate for describing dark matter.

Despite the fact that this theory cover a part of unanswered questions in the Standard Model, some of its incarnations may be in contradiction with experimental observations. For example the MSSM can allow a violation of the CP symmetry more important than the experimental constraints [33]. Also, supersymmetric extensions, such as the hybrid models $N = 1/N = 2$ (where N is the number of generators of supersymmetry) or the models with continuous symmetry R (continuous generalization of parity R) offer a solution to these difficulties.

As mentioned earlier, supersymmetry is the subject of a large number of researches using colliders, as it can lead to a multitude of final states: large multiplicity of physical objects (electrons, muons, photons, jets), or very often to a significant missing transverse energy .A summary plot of the research carried out in the ATLAS experiment are presented in Figure 1.4. The latter classifies the experimental constraints according to the type of particle sought. For example, the search for superpartners of third generation quarks (stop and sbottom) leads to experimental constraints which exclude their existence for masses located between 300 and 600 GeV for most of the final states considered. Simplified models make it possible to carry out an inclusive search and to vary all of their parameters. In this context, the masses of gluinos are constrained to be greater than 1 TeV.

1.3.2 Extra dimensions theories

Introduced by Kaluza [35] and Klein [36] in 1921 and 1926 respectively, the notion of additional dimension was more recently complicit by Randall and Sundrum [37] in 1999. In these models, the difference between the electroweak scale and the Planck scale (and therefore gravitation) can be explained by the existence of additional dimensions in which gravitation and its mediating bosons, gravitons , would spread. In this case, the application of the gravitational Gauss theorem would lead to an expression of the gravitational interaction force of the form :

$$F = G_g \frac{m_a m_b}{r_{AB}^{2+d}}, \tag{1.28}$$

where r_{AB} is the distance between the points A and B of respective masses m_A and m_B and G_g is the equivalent of the constant of universal gravitation in the case of $4 + d$ space-time dimensions.

These additional dimensions of space must however be rolled up on themselves (or compacted) in order to preserve the observables predicted by Newton's laws and in particular the orbits of the planets. Thus, equation 1.28 can be written:

$$F = G_g \frac{m_a m_b}{r_{AB}^2 R^d}, \tag{1.29}$$

where R is the compacting radius of the additional dimension. Thus, by identifying equation 1.28 with the classical expression of the gravitational interaction in four dimensions, we draw that:

$$G_N = \frac{G_g}{R^d}, \tag{1.30}$$

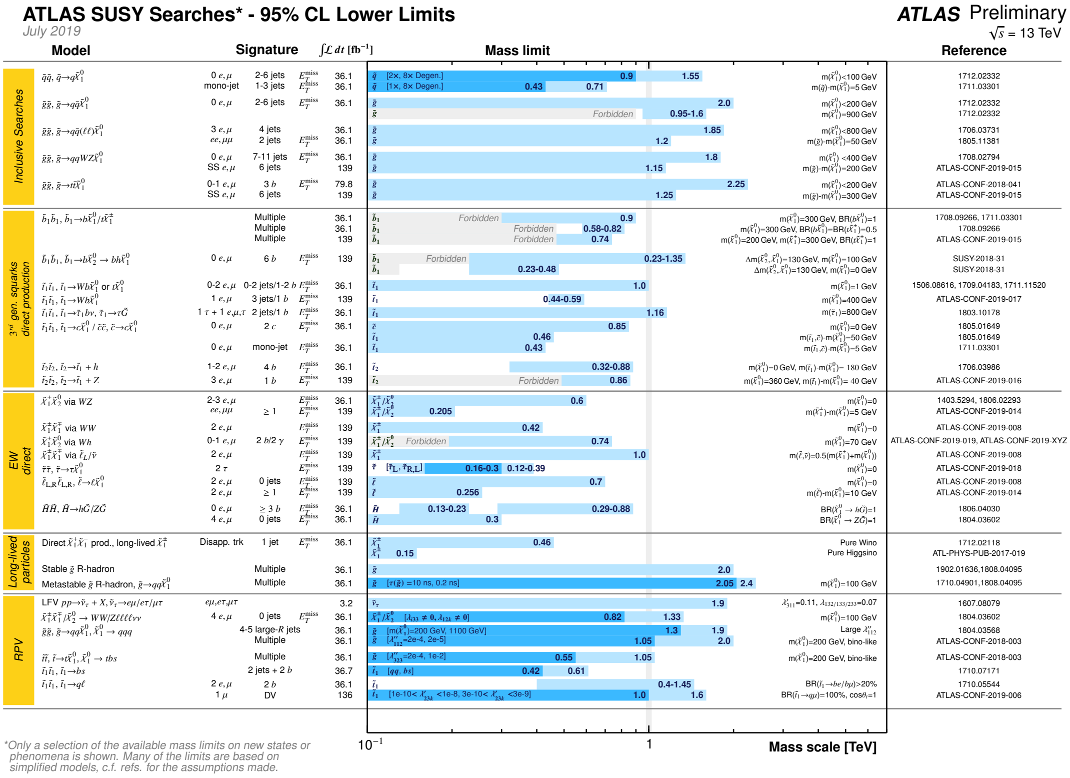

Figure 1.4: Mass reach of the ATLAS searches for Supersymmetry. A representative selection of the available search results is shown. Results are quoted for the nominal cross section in both a region of near-maximal mass reach and a demonstrative alternative scenario, in order to display the range in model space of search sensitivity. Some limits depend on additional assumptions on the mass of the intermediate states, as described in the references provided in the plot. In some cases these additional dependencies are indicated by darker bands showing different model parameters [34].

where G_N is the universal gravitational constant. Consequently, the gravitational interaction would not be weaker than the electroweak interaction in essence, but because it would propagate in more than four dimensions of space-time, solving the problem of hierarchy.

These dimensions can come in different types of geometry. From the above considerations, the hierarchy between gravitation and the electroweak scale can be explained by additional dimensions of large radius of compactification R, or extra dimensions. These two cases make it possible to reduce the value of the constant G_N and correspond to the so-called ADD theories (Arkani, Dimopoulos. Dvali) [38–40]. Other theories, however, consider a single additional dimension of small size. A priori, in a plane geometry, this configuration does not lead to the resolution of the hierarchy problem. In the model introduced in 1999 by Randall and Sundrum [37], the compactification of the unique additional spatial dimension is carried out according to an orbifold of symmetry S^1/Z_2 (Figure 1.5). In these models there are two branes (four-dimensional hyper planes) located at fixed points on the orbifold and identified in the additional dimension by the coordinate $y : y = 0$ (called Planck's brane) and $y = \pi R$ (brane of the Standard Model) where R is the radius of the circle defined by the symmetry S^1 The metric used is then defined by:

$$ds^2 = e^{-k|y|} dx^\mu dx^\nu \eta_{\mu\nu} + dy^2, \tag{1.31}$$

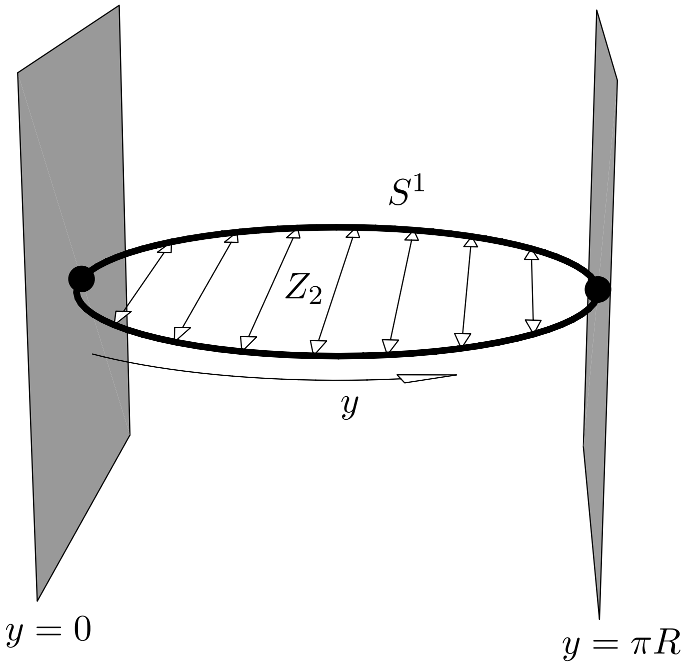

Figure 1.5: Diagram of the compactification used for the dimension of additional space within the framework of the Randall-Sundrum models (orbifold S^1/Z_2), as well as the two branes [41].

where k represents the curvature of the space-time introduced by this choice, $\eta_{\mu\nu}$ the classic Minkowski metric, and $e^{-k|y|}$ is the factor of curvature.

Thus, on the Planck brane ($y = 0$), the Planck scale is of the order of 10^{19} GeV. On the Standard Model brane, this scale is weighted by the curvature factor $e^{-k\ piR}$. Typically, a reasonable value of the product kR is 11 [42], that is, a Planck scale of the order of TeV on the bran of the Standard Model, solving the hierarchy problem.

In the original model [37] , the Standard Model particles were forced to remain in the Standard Model brane, while the gravitons could propagate in the five dimensions of space-time. However, this model leads to large contributions (in comparison to experimental constraints) of flavor violation processes by neutral current (FCNC) [43] To overcome these difficulties, one solution is to leave the particles of the Standard Model free: they can be (with the exception of the Higgs boson) between the two branes, making it possible to explain, among other things, the mass hierarchies between the different particles [43]. Such models also lead to the appearance of new excitations of the particles of the Standard Model, called excitations of Kaluza Klein, mode 0 corresponding to the state of the particle in the four dimensions of space time, therefore, that of Standard model.

Conclusion

The world of the infinitely small is currently described by the Standard Model of particle physics, some of it founding ideas were presented during this chapter, in particular the importance of the concept of symmetry. The Standard Model of particle physics is surely one of the most successful models in physics. So far, it withstands all tests and has been experimentally verified with tremendous precision.

But, it still has limits and gaps, which are related to its inability to explain a variety of experimental observation, such as gravity, dark matter, neutrino masses... Two major ranges of theories have been presented in this chapter and some other extension will be presented in the next chapter.

Within this thesis , the probe is the photon. Occupying a special place in the Standard Model and in all LHC searches because of its properties, it can also be coupled to the particles of New Physics, so that any deviation from the predictions of the Standard Model would lead to the highlights of New Physics.

Chapter 2

Light-by-light Scattering

Contents

Introduction

Understanding light properties has been and still driving scientist and especially physicist to achieve all what we know about it from theoretical and experimental sides. The most advanced to date theory describing it is QED. Studying the light involves comprehension of its interaction with other particles and with itself. We talk about light-by-light (LbyL) scattering. This chapter present in section 2.1 a short review of the history of light and in section 2.2 the theoretical background of LbyL scattering . Section 2.3 concerns the experimental attempt done to measure the light-by-light scattering process, while section 2.4 is dedicated to the measurement of this process at the LHC and section 2.5 summarizes possible BSM measurement that can be done using the LbyL scattering.

2.1 History of light

2.1.1 Antiquity

It was in the 3rd century BCE (Beffor Common Era) that the Greeks really became interested in questions related to light and vision. The science of optics will see the light of day with Euclid's Treatise on Optics. However, before the Hellenistic era proper, we find among the Presocratics, Plato and Aristotle attempts to theorize light phenomena. Until Aristotle, the nature of light conforms to the poetic representation of Homer. It appears as a particular type of fire whose specificity is, for Heraclitus and Empedocles, to be continuous. Among atomists, it is conceived as a mass of moving corpuscles. Plato takes up this description in Timaeus where light is a fire made up of streaks of tetrahedrons imperceptible to the eyes and moving at high speed. For Empedocles, Democritus or Plato, light emerges from incandescent sources but also from the eyes. Contrary to this conception of material light which propagates with a finite speed, light in Aristotle is instantaneous. It is no longer a question here of sets of corpuscles projected by light sources. It is defined as the expression of a modification of the environment which shelters the emitting source and the observing subject. Aristotle has a dynamic vision of light. In the Hellenistic era and at the beginning of the Alexandrian era, the two main reference texts on light and vision are: Euclid's Treatise on Optics and Claude Ptolemy's Optics. For these authors, light cannot have its own independent existence. It is linked to the viewer's vision and is defined geometrically as rectilinear rays emitted by the eye. This representation is a continuation of Plato's thesis and will last for almost all of medieval times. The biggest breakthrough in ancient times was made by al-Haytham an Islamic mathematician around 1000. He argued that sight is due only to light entering the eye from an outside source and there is no beam from the eye itself. He gave a number of arguments to support this claim, the most persuasive being the camera obscura, or pinhole camera. Here light passes through a pinhole shining on a screen where an inverted image is observed.

2.1.2 The Renaissance and the modern era

At the end of the 16th century, the development of optics in practical fields was in full swing with the identification of the properties of lenses and by extension the discovery of the telescope. Questions about the nature of light reappear and scholars wonder whether light is a body or the manifestation of the movement of a body. It is Descartes who revived the subject around the nature of light and questioned the role of the medium it crosses. The laws of Snell-Descartes mark in 1625 a considerable advance in the development of optics. Descartes, unlike Galileo, considered that the propagation of light is instantaneous. It was not until the work of Rømer in 1676 that a first approach to the speed of light emerged. In 1676, Christian Huygens, in his Treatise on Light, shows that the laws of Snell-Descartes can only be validated if we consider light as a wave that propagates in a rectilinear manner. He opposes Newton's theory, which prefers the corpuscular design and determines the nature of light as a set of moving grains. Building on these successes of the time, Isaac Newton won the victory of this scientific battle by publishing Opticks in 1704. Using the prism, Newton manages to decompose the light and reveals the spectrum of white light. The seven colors which he thus highlights are, according to him, related to the size of the grains of light which constitute them. His corpuscular theory overshadows the wave design of Huygens which was abandoned until the beginning of the 19th century.

2.1.3 The 19th and 20th centuries

From the 1800s, the physicists Thomas Young and Augustin Fresnel carried on and experimented Huygens' wave theory. The development of spectroscopy makes it possible to extend research on the relationship between radiation and matter over a wider field than that of the visible. We conclude, therefore, by a series of experiments on the thermal effects of bodies and on the chemical actions of silver salts, that invisible waves exist: infrared and ultraviolet. In 1864, James Clerk Maxwell established through his equations - Maxwell's equations - the relationship between electric field and magnetic field. The speed of the waves he then measured was surprisingly close to that of light ... Maxwell's conclusion was therefore that light is an electromagnetic wave which belongs to the electromagnetic spectrum and is only a part of it, the visible part. It travels at a finite speed of around 300,000 km/s.

2.2 Theoretical background

At first glance, the idea of the interaction of a photon with another photon is surprising. Indeed, Maxwell's equations do not predict that one photon will interact directly with another. When two beams of light cross, they do not interact. They may possibly interfere locally (an effect linked to the superposition of their electromagnetic fields), but they continue on their way without being modified. From the classical electrodynamics point of view the superposition principle hold true, therefore direct interaction of electromagnetic fields is forbidden within this framework. The superposition principle is described with the following equation:

$$\mathcal{L}_0 = -\frac{1}{4\mu_0} F^{\mu\nu} F_{\mu\nu} = \frac{1}{2}\epsilon_0 \left(\mathbf{E}^2 - c^2\mathbf{B}^2\right) = \frac{1}{2}\left(\epsilon_0\mathbf{E}^2 - \frac{1}{\mu_0}\mathbf{B}^2\right), \tag{2.1}$$

$$F^{\mu\nu} = \begin{pmatrix} 0 & -\frac{1}{c}E_1 & -\frac{1}{c}E_2 & -\frac{1}{c}E_3 \\ \frac{1}{c}E_1 & 0 & -B_3 & B_2 \\ \frac{1}{c}E_2 & B_3 & 0 & -B_1 \\ \frac{1}{c}E_3 & -B_2 & B_1 & 0 \end{pmatrix}, \tag{2.2}$$

where $F^{\mu\nu}$ is the electromagnetic field strength tensor give by eq. 2.2 and the velocity of light (squared) is given by $c^2 = 1/\left(\epsilon_0\mu_0\right)$ with ϵ_0, μ_0 being the dielectric permeability and the magnetic permittivity of the vacuum, respectively. A characteristic feature of the Maxwell theory is that the Lagrange density of the electromagnetic field is quadratic in the electric (**E**) and magnetic (**B**) fields. Electromagnetic theories which model direct interaction processes of electromagnetic fields have to be described by Lagrange densities that contains higher powers of the electromagnetic fields.

In the 1940s, following the development of quantum physics, researchers rewrote the theory of electromagnetism in its quantified form, quantum electrodynamics (QED). But as early as 1934, Heisenberg and Euler had proposed a theory which announced the future QED. The two researchers then suggested that, through non-linear effects, two photons could interact.

How does QED describe this process? Two electrons interact through the exchange of one or more photons: this is the translation into quantum language of electromagnetic interaction. In the same way, two photons can interact via the exchange of an electron (and more generally of any particle carrying an electric charge) as shown in Figure 2.1. The key point is that the electrons carry an electrical charge which must be retained

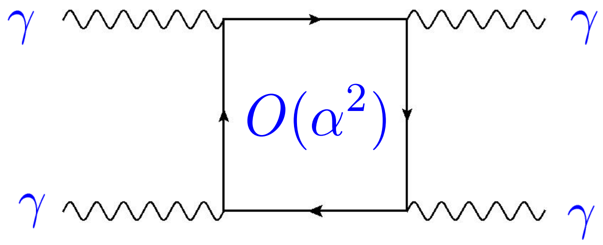

Figure 2.1: Generic QED diagram for the light-by-light scattering process.

during the process. Consequently, the first photon will have to send back the electron received from the second photon, which produces a return of electrons. In QED, we talk about a box-shaped (or looped) exchange that includes electrons and their antiparticles (positrons). In this purely quantum effect, the exchanged particles only appear for a very short period of time, corresponding to the duration of the interaction: we speak of virtual particles.

In 1935 Euler and Kockel [44, 45] determined the leading perturbative correction (for small field strengths and photon frequencies well below the electron-positron pair production threshold) to the Lagrange density $\mathcal{L}_0$ of the Maxwell field. They found :

$$\begin{aligned}\mathcal{L} &= \mathcal{L}_0 + \frac{\alpha^2}{360}\frac{\epsilon_0^2 c^3 \lambdabar_e^4}{\hbar}\left[4\left(F^{\mu\nu}F_{\mu\nu}\right)^2 + 7\left(F^{\mu\nu}F^{\star}_{\mu\nu}\right)^2\right] \\ &= \mathcal{L}_0 + \frac{2\alpha^2}{45}\frac{\epsilon_0^2 \lambdabar_e^4}{\hbar c}\left[\left(\mathbf{E}^2 - c^2\mathbf{B}^2\right)^2 + 7c^2(\mathbf{EB})^2\right] \quad , \\ &= \mathcal{L}_0 + \frac{2\alpha^2}{45}\frac{\lambdabar_e^4}{\hbar c}\left[4\mathcal{L}_0^2 + \frac{7}{\mu_0^2}(\mathbf{EB})^2\right]\end{aligned} \tag{2.3}$$

Where α is the fine structure constant, $\lambdabar_e = \hbar/\left(m_e c\right)$ is the (reduced) Compton wavelength of the electron with mass m_e and $F^{\star}_{\mu\nu} = \epsilon_{\mu\nu\alpha\beta}F^{\alpha\beta}/2$ is the dual of the electromagnetic field strength tensor $F^{\mu\nu}$. Using the relations given in the eqs. 2.5, one can write eq. 2.3 as in 2.6

$$T^{\mu\nu} = \frac{1}{\mu_0}\left[F^{\mu\alpha}F^{\nu}_{\alpha} - \frac{1}{4}g^{\mu\nu}F^{\alpha\beta}F_{\alpha\beta}\right], \tag{2.4}$$

$$\begin{aligned}T^{\mu\nu}T_{\mu\nu} &= 2\epsilon_0^2\left[\left(\mathbf{E}^2 - c^2\mathbf{B}^2\right)^2 + 2c^2(\mathbf{EB})^2\right] \\ &= 8\mathcal{L}_0^2 + \frac{4}{\mu_0^2}(\mathbf{EB})^2 \quad , \\ &= 4\left[\left(T_{00}\right)^2 - \frac{1}{c^2}\mathbf{S}^2\right] = -4T^{0\nu}T_{0\nu}\end{aligned} \tag{2.5}$$

$$\begin{aligned}\mathcal{L} &= \mathcal{L}_0 + \frac{2\alpha^2}{45}\frac{\lambda_e^4}{\hbar c}\left[-10\mathcal{L}_0^2 + \frac{7}{4}T^{\mu\nu}T_{\mu\nu}\right] \\ &= \mathcal{L}_0 + \frac{2\alpha^2}{45}\frac{\lambda_e^4}{\hbar c}\left[-10\mathcal{L}_0^2 + 7\left((T_{00})^2 - \frac{1}{c^2}\mathbf{S}^2\right)\right]\end{aligned}, \tag{2.6}$$

where $T^{\mu\nu}$ (eq. 2.4) is the stress-energy-momentum tensor of the free electromagnetic field, and $\mathbf{S}$ is the Poynting vector given by

$$\mathbf{S} = \frac{1}{\mu_0}\mathbf{E} \times \mathbf{B}, \tag{2.7}$$

The resulting Lagrangian is in fact non-linear which leads to non-linear corrections to the classical Maxwell equations. We can recognise from 2.6 that the Poynting vector provides us with interaction term between electromagnetic (photon). Euler and Kauckel also calculated the cross section of the photon-photon scattering for the first time and they find for photons of frequency $\hbar\omega \ll m_e c^2$:

$$\sigma \sim \alpha^4 \lambda_e^8 \left(\frac{\omega}{c}\right)^6, \tag{2.8}$$

this cross section turned out to be very small (10^{-30}cm^2 for γ -rays and of 10^{-70}cm^2 for visible light) which as pointed out by Euler makes it very difficult to observe this phenomenon experimentally. Almost one year later while working on Consequences of the Dirac Theory of Positrons Euler and Heisenberg indicated that the light-by-light scattering is related to the polarisation of the vacuum [46, 47].

2.3 Experimental approaches

The experimental effort to detect light-by-light scattering seems to have started in 1928 (even before Euler and Kockel calculations) by S. I. Vavilov [48]. In 1930 a similar attempt by A. L. Hughes and G. E. M. Jauncey [49] has been done using the light of the sun to try to detect collision between photons. No experimental sign of photon-photon collisions was found and Hughes and Jauncey give as bound for the cross section σ of photon photon scattering $\sigma < 3 \times 10^{-20}\text{cm}^2$. Afterwards, many experimental efforts were proposed to try to directly observe the scattering of photons by photons such as high power laser[50] and IR beams in vacuum, the layout of the latter setup is shown in Figure 2.2 [51]. No evidence of the process was observed and the limit on the cross section is shown in Figure 2.3. Another approach is the Compton back-scattered photons against laser photons in SLAC by colliding 19.5 GeV γ beam with a 4.66 eV laser light [52]. The differential cross section from the setup is shown in Figure 2.4. The later approach concluded with difficulty of the detection of the process and the need of a dedicated experiment as shown in Figure 2.5. Collisions of photons from microwave waveguides [53] or cavities [54] were also suggested but not experimentally tested as well as photon colliders. However no evidence of the process was observed. Which is well predicted and explained by the it's very small cross section. Only indirect measurements were actually possible, like measurements of the anomalous magnetic moment of the electron and muon [55, 56], where the LbyL it is predicted to contribute substantially. The $\gamma\gamma \to \gamma\gamma$ reaction has been measured in photon scattering in the Coulomb field of a nucleus (Delbrück scattering) [57–60] and in the photon splitting process [61]. A direct observation of the process is indeed as predicted by Euler and Heisenberg very challenging.

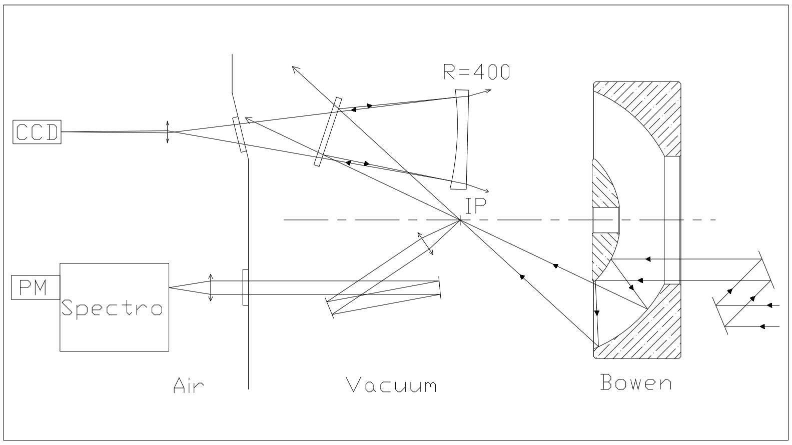

Figure 2.2: Layout of the experimental apparatus[51].

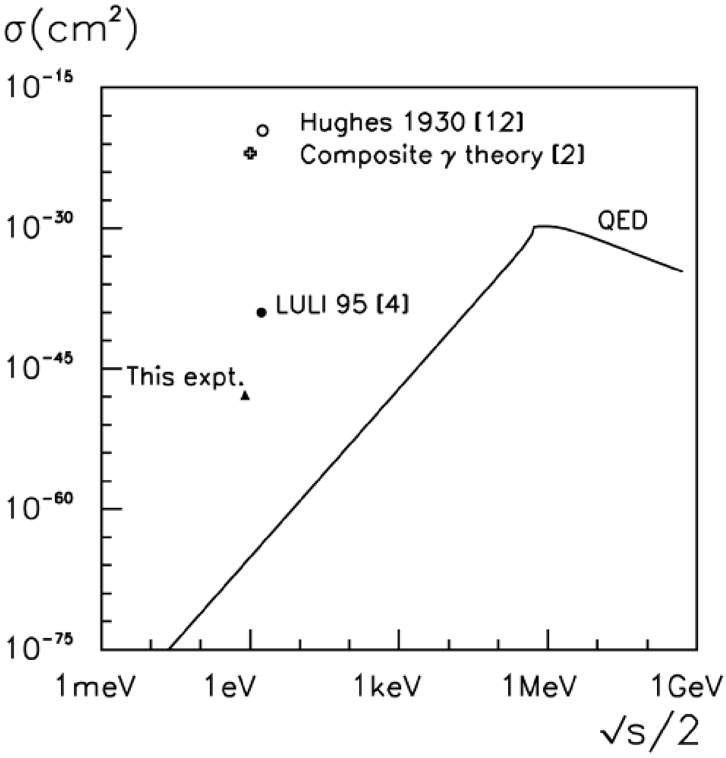

Figure 2.3: Elastic photon cross-section as a function of photon cms energy[51].

2.4 Light-by-light scattering at the LHC

In fundamental physics, it is more and more frequent that decades separate a prediction from its experimental confirmation for instance the Higgs boson, discovered in 2012 at the LHC, had been predicted in the 1960s, the gravitational waves, observed in 2015 by the LIGO / Virgo collaboration, had been postulated by Albert Einstein a century earlier, in 1916. In 2017, a phenomenon called magnetic birefringence of the vacuum had been highlighted, almost 80 years after two German physicists, Werner Heisenberg and Hans Heinrich Euler developed the theory which suggests its existence. This theory also predicted the existence of another process, elastic

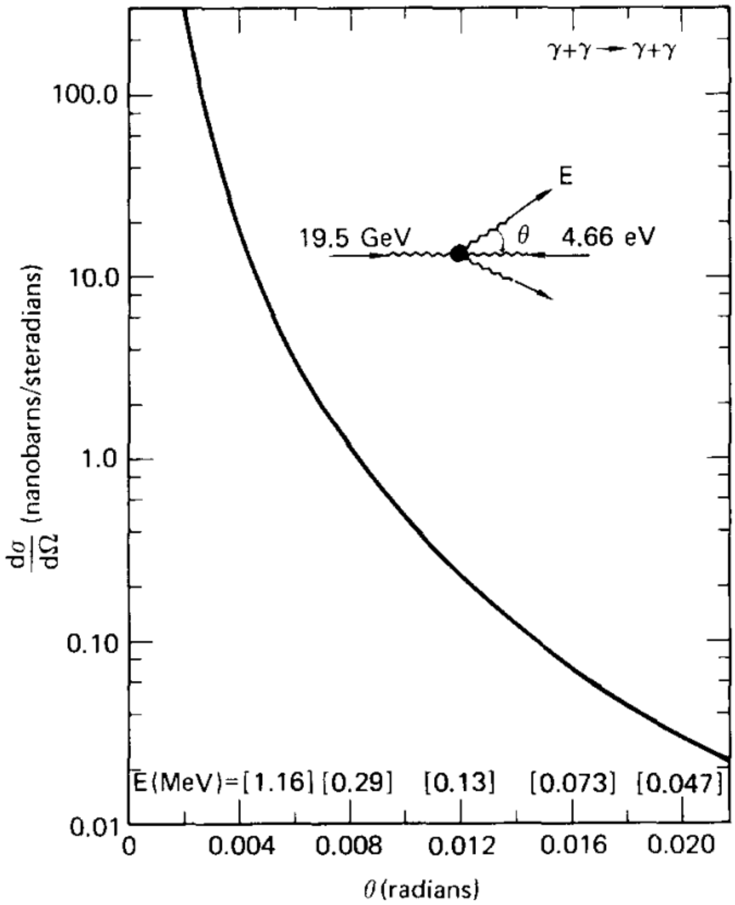

Figure 2.4: The differential cross section, dσ/dΩ, in nanobarns/ steradian, as a function of the scattering angle θ in radians.[52].

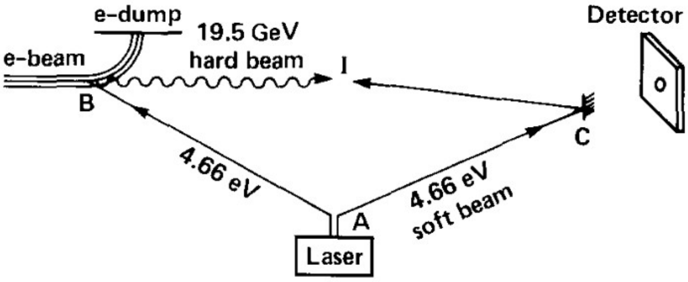

Figure 2.5: Schematic layout of a suggested$\gamma\gamma \to \gamma\gamma$ experiment that rely on a hard and soft beam [52].

photon-photon scattering, i.e the interaction of a photon with another photon. The experimental demonstration of this process as pointed earlier is however a challenge. Indeed, the probability that two photons interact in this way is very low and it takes a large flux of photons so that a single scattering possibly takes place. Even the most powerful lasers are not intense enough to make sure that one photon interact with another.

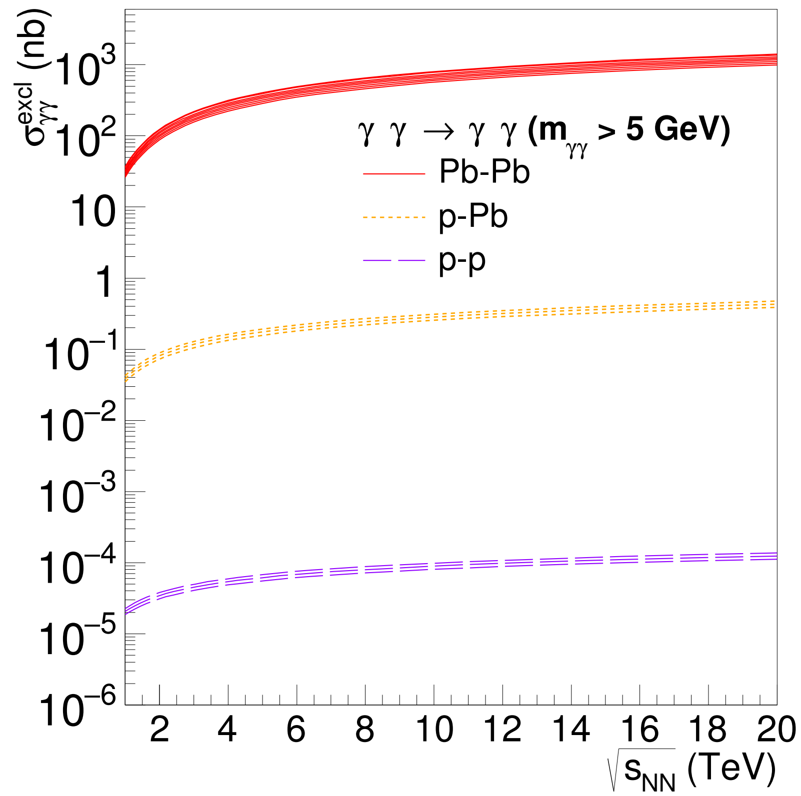

Figure 2.6: Cross sections for exclusive $\gamma\gamma \rightarrow \gamma\gamma$, with pair masses above 5 GeV, in ultraperipheral Pb -Pb (top curve), $\mathrm{p}-\mathrm{Pb}($ middle $)$ and $\mathrm{p}-\mathrm{p}($ bottom $)$ collisions as a function of the nucleon-nucleon c.m. energy in the range $\sqrt{s_{\mathrm{NN}}} = 1 - 20\mathrm{TeV}$ [62].

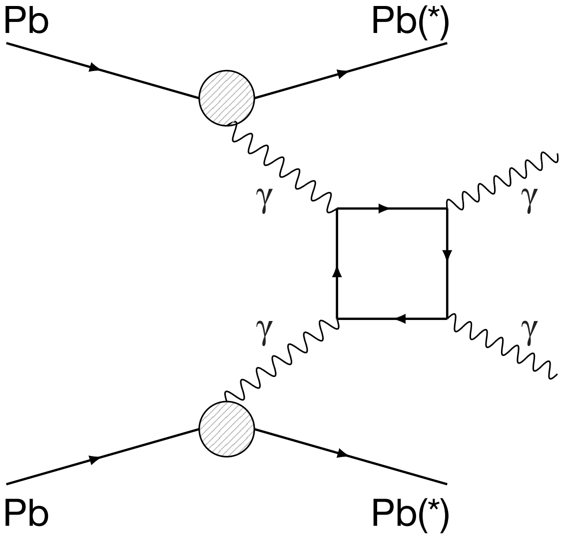

Figure 2.7: Schematic diagram of light-by-light scattering $\gamma\gamma \rightarrow \gamma\gamma$ in UPC Pb + Pb collisions. A potential electromagnetic excitation of the outgoing Pb ions is denotes by $(*)$. The loop contain contribution from quark and leptons at low mass and from W boson at high mass.

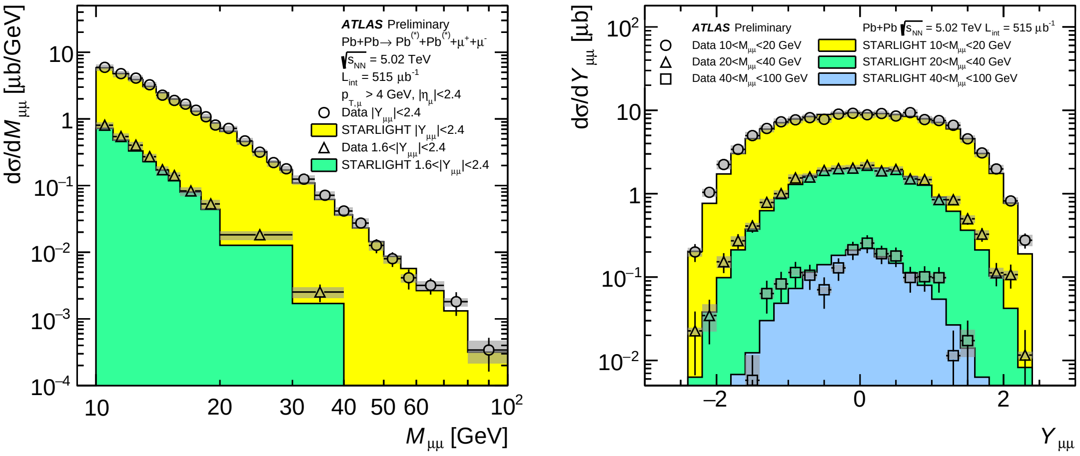

Figure 2.8: Cross section for dimuon production in UPC, as a function of pair mass (left) and pair rapidity (right). The data are indicated by the symbols while calculations are shown by solid histograms. The mass distribution is provided for two (overlapping) rapidity regions ($|Y_{\mu\mu}| < 2.4$ and $|Y_{\mu\mu}| > 1.6$) . The rapidity distribution is provided for three ranges ($10 < M_{\mu\mu} < 20\text{GeV}, 20 < M_{\mu\mu} < 40\text{GeV}, 40 < M_{\mu\mu} < 100\text{GeV}$) . Error bars indicate statistical uncertainties while the grey bands indicate the combined systematic uncertainties, including the 7% global luminosity uncertainty.

2.4.1 Exclusive production of lepton pairs and W bosons at the LHC

Ultra peripheral heavy ions collision have shown great feasibility in the study of the dilepton production by photon – photon interactions. Figure 2.8 shows the cross section for dimuon production in UPC, as a function of pair mass (left) and pair rapidity (right). This measurement was performed by the ATLAS collaboration [63]. Figure 2.9 shows the measurement of dielectron production in the CMS experiment [64]. This process is used in the analysis as a background and is studied in detail for the 2015 and 2018 data in chapter 5. Exclusive W^+W^- pair production as been observed in pp collision as shown in 2.10

The exclusive production of pairs of W bosons, $pp \to pp(\gamma\gamma) \to ppW^+W^-$, have been definitely observed in the LHC [65–67]. Figure 2.10 shows the kinematic distribution from the ATLAS measurement.

2.4.2 The first evidence of LbyL at the LHC

In 2016 a new approach [62] have been proposed to search for LbyL scattering at the LHC thanks to the large quasi-real photon fluxes available in electromagnetic interactions of protons (p) and lead (Pb) ions (Figure 2.7). This approach is based on the fact that all charges accelerated at high energies generate electromagnetic fields. Indeed each ion is accelerated to a speed close to that of light. The electromagnetic field which surrounds it, is then contracted in the plane perpendicular to the direction of displacement (due to the relativistic Lorentz transformations). As a result, the electromagnetic field of these relativistic ions in the equivalent photon approximation (EPA) [68–70] can be considered as a beam of photons with a small virtuality of $Q^2 < 1/R^2$, where R is the radius of the charge distribution and so $Q^2 < 10^{-3}\text{GeV}^2$. Then, the cross section for the reaction $\text{Pb} + \text{Pb}(\gamma\gamma) \to \text{Pb} + \text{Pb}\gamma\gamma$ can be calculated by convolving the respective photon flux with the elementary cross section for the

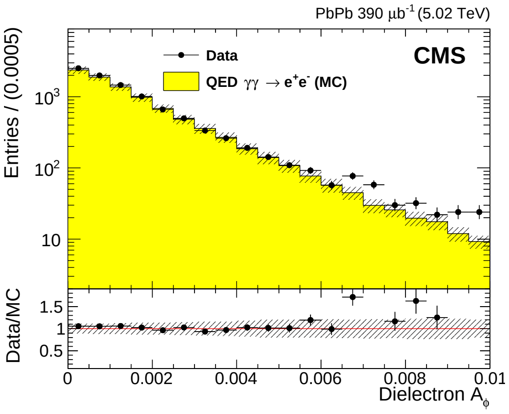

Figure 2.9: Comparison of data (circles) and STARLIGHT MC expectation (histogram) for the exclusive e^+e^- events passing all selection criteria, as a function of dielectron acoplanarity (left) and mass (right). Error bars around the data points indicate statistical uncertainties, and hashed bands around the histograms include systematic and MC statistical uncertainties added in quadrature. The horizontal bars around the data symbols indicate the bin size. The ratio of the data to the MC expectation is shown in the bottom panels.

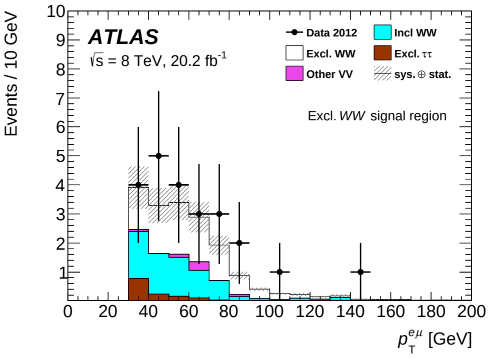

Figure 2.10: Kinematic distributions in the exclusive W^+W^- signal region comparing the simulation to data.

process $\gamma\gamma \to \gamma\gamma$. The expression of the cross section in a hadrons (A and B) collider and by using the equivalent photon approximation (also called Weizsäcker-Williams method) is given by :

$$\sigma^{\rm excl}_{\gamma\gamma\to\gamma\gamma} = \sigma({\rm AB} \xrightarrow{\gamma\gamma} {\rm A}\gamma\gamma{\rm B}) = \int {\rm d}\omega_1 {\rm d}\omega_2 \frac{{\rm f}_{\gamma/{\rm A}}\left(\omega_1\right)}{\omega_1}\frac{{\rm f}_{\gamma/{\rm B}}\left(\omega_2\right)}{\omega_2}\sigma_{\gamma\gamma\to\gamma\gamma}\left(\sqrt{{\rm S}_{\gamma\gamma}}\right), \tag{2.9}$$

where $\sigma_{\gamma\gamma\to\gamma\gamma}$ is the elementary cross section at $\sqrt{{\rm S}_{\gamma\gamma}}$ and ${\rm f}_{\gamma/{\rm A}}\left(\omega_1\right)$and ${\rm f}_{\gamma/{\rm B}}\left(\omega_2\right)$ are the photon fluxes at the energies ω_1 and ω_2 respictively. Furthermore, since lead ions have a high electrical charge (their nucleus contains 82 protons), the intensity of the electromagnetic field is high since the photon flux associated with each nucleus scales as Z^2, the cross section is extremely enhanced as compared to proton-proton (pp) collisions as shown in Figure 2.6.

In 2017 ATLAS experiment reported a first evidence of light-by-light scattering [71] using data from ultra-peripheral heavy ions collisions. 13 events were observed with an expected background of 2.6 ± 0.7 events. Figure 2.11 (left) shows the invariant mass of diphoton. Shortly after that the CMS collaboration also published

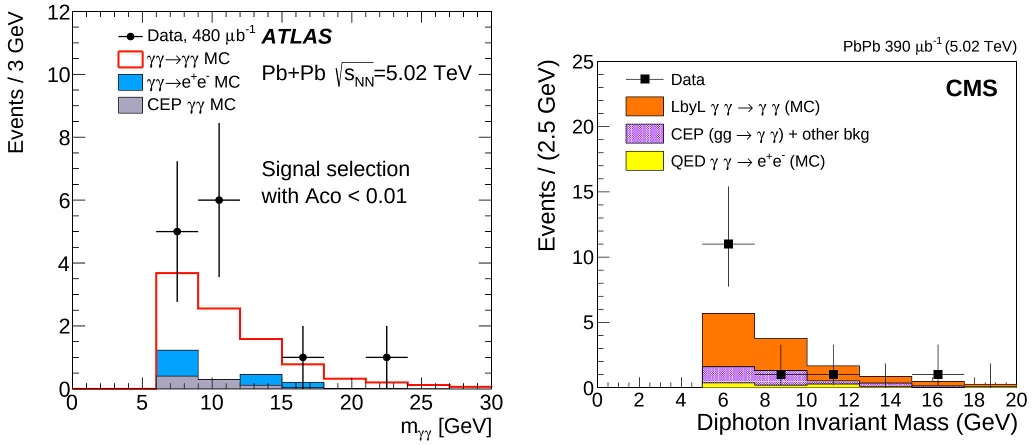

Figure 2.11: Diphoton invariant mass of the events observed after applying all selection criteria in ATLAS (left) and CMS (right) . Data (points) are compared to MC predictions (histograms). The statistical uncertainties on the data are shown as vertical bars.

the measurement of the same process [64]. 14 events were observed compared to expectations of 9.0 ± 0.9 (theo). The invariant mass of the diphoton is shown in the right side of Figure 2.11

2.5 light-by-light scattering beyond SM

In QED, the $\gamma\gamma \to \gamma\gamma$ reaction proceeds at lowest order in the fine structure constant via virtual one-loop box diagrams involving fermions (Figure 2.7), which is an $O(\alpha_{\text{em}}^4) \approx 3 \times 10^{-9}$ process. However, in various extensions of the Standard Model (SM), extra virtual contributions are possible, making the measurement of LbyL scattering sensitive to new physics Therefore either in collider (hadrons or photons) or laser experiment The light-by-light scattering via one loop can be very useful to perform many beyond SM searches. in this section we try to give a short overview of a couple of them.

2.5.1 Axion Like Particles

The existence of axions was initially postulated to solve the strong CP problem of QCD [72]. They are pseudo Nambu-Goldstone bosons associated with the (mostly) spontaneous breaking of a new global Peccei-Quinn (PQ) U(1) symmetry. They are good candidates for cold dark matter, since they were produced non-thermally. Axions considered in these models have small masses. More generally axion-like particles (ALPs), appear in theories with spontaneously broken global, approximate, symmetries as pseudo Nambu-Goldstone bosons with Independent coupling and mass and they can be of masses up to TeV scale. They also appear in supersymmetric extensions of the SM or string theory. Searching for axions or ALPs can be extremely challenging due to its extraordinarily feeble coupling to normal matter and radiation.The most promising approaches are the one related the photon coupling. From this came the fact that light-by-light scattering $\gamma\gamma \to \gamma\gamma$ can be a clean channel when looking for ALPs . Any particle directly coupling to photons could be produced in an s-channel process in photon–photon collisions, leading to a resonance peak in

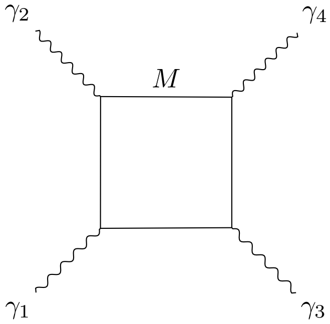

Figure 2.12: $\gamma\gamma \to \gamma\gamma$ via a virtual heavy monopole loop [75].

the invariant mass spectrum. One popular candidate for producing narrow diphoton resonances are axion-like particles (ALP) [73]. More details on chapter6.

2.5.2 Magnetic Monopoles

The magnetic monopole was introduced by Dirac [74] to explain the quantization of the electric charge of particles and to restore symmetry between electricity and magnetism. Due to the strong coupling of monopoles to photons searching for them at hadrons collider can be carried out in light-by-light scattering channel via a virtual heavy monopole loop (Figure 2.12). This effect can be observable at colliders with energies smaller than monopole masses [75].

2.5.3 Unparticles

Unparticles physics is a theory stipulating that there could be unseen sectors of the theory, which is exactly scale invariant and very weakly interacting with the rest of the standard model [76]. The light-by-light scattering can be used to hint unpartciles at TeV scale in collider like CLIC which can operate as photon collider [77].

2.5.4 Supersymmetric partners of SM particles

Non strongly interacting supersymmetric particles – sleptons, charginos, neutralinos, and charged Higgs bosons – are difficult to detect at the Large Hadron Collider. But there is a possibility of producing particles of this type in virtual $\gamma\gamma$ collisions at the LHC [78]. Since photons can be emitted from protons which do not break up in the radiation process, very clean events can be generated, compensating to some extent for the small event numbers. Higher rates are expected, at the expense of stray hadrons, for events in which one or two protons break up.

2.5.5 Low-scale gravity effects

The process $\gamma\gamma \to \gamma\gamma$ at TeV energies is an important test channel for Weak Scale Quantum Gravity (WSQG) theories, since the tree level gravity contribution to the process in these theories is expected to be significant, whereas the SM contributes only at the loop level. Ref [79] used the high energy limit SM helicity amplitudes and the gravity amplitudes from the lowest dimension WSQG effective Lagrangian to compute scattering cross sections. The SM + WSQG cross sections can significantly differ from those of the SM alone [79, 80]. Thus the effects of weak scale quantum gravity can be studied at the Next Linear Collider (NLC), in the photon collider mode.

2.5.6 Non-commutative interactions

The idea of non-commutative quantum field theory (NCQFT) is a generalization of the usual d-dimensional space, R^d, associated with commuting space-time coordinates to one which is non-commuting, R^d_θ. In such space, the conventional coordinates are represented by operators which no longer commute. This theory is derived from string/M-theory and it has been shown that it can lead to observable signatures in several $2 \to 2$ QED processes in e^+e^- collisions. In particular, pair annihilation, Moller and Bhabha scattering, as well as $\gamma\gamma \to \gamma\gamma$ scattering and show that non-commutative scales of order a TeV can be probed at high energy linear colliders [81].

Conclusion

In this chapter we give an overview of the theoretical background and motivation behind measurement of light-by-light scattering at the LHC. The light-by-light scattering was theoretically introduced in earliest days of QED however, the process persisted unobserved for so many years. Many experimental effort and suggestion were made to measure the process,but given its small cross section non of them were conclusive. The LHC heavy ions data opened the way toward the first measurement of the process. In this thesis we perform the measurement with more data collected in 2018 by the ATLAS detector.

Chapter 3

The ATLAS experiment at the Large Hadrons Collider

Contents

Introduction

Understanding the infinitely small, particles and their interactions is the goal today of all particle physicists. This research, however, can only be done with extremely well-performing equipment allowing not only the production of high energy physics processes, but also their detection, these steps being carried out by the particle accelerator-collider, like the LHC, and different detectors like ATLAS. In the first section of this chapter, the LHC is described, as well as its characteristics and performance in 2018 data taking period, the second Section introduces one of the four large detectors installed at the LHC, the ATLAS detector, its main sub-detectors , their performance and also describes more precisely its trigger system.

3.1 Motivation

The standard model has been tested to a greater degree of precision than any other model in science. So far, it withstands all tests and has been experimentally verified with tremendous precision. But, it is incomplete, and the search for the missing pieces of the puzzle is the prime motivation for building the LHC after the Higgs boson discovery. Indeed, the LHC program is much wider than a search for the Higgs. Alongside the 'general-purpose' detectors, known as ATLAS and CMS, the LHCb experiment will analyse the production of bottom quarks in LHC collisions. This rich system is the key to a better understanding of the phenomenon of CP violation and its connection to the dominance of matter over antimatter in the Universe. In addition, during dedicated runs in which lead ions will collide in the LHC instead of protons, the ALICE experiment alongside with ATLAS and CMS will study a phase of matter called quark–gluon plasma, which might have existed shortly after the Big Bang. The Large Hadron Collider (LHC) [82] at the European Laboratory for Particle Physics (CERN) near Geneva, Switzerland, is a hadrons accelerator(proton-proton pp and heavy-ion (Pb+Pb)) , designed to provide unprecedented centre-of-mass-energies and luminosities for the discovery of new physics. Furthermore, it allows the measurements of parameters of the Standard Model in hitherto inaccessible regions of phase space. The LHC is also known as the successor of the Large Electron Positron (LEP) which was built in the same tunnel (1989-2000). Up to the time of writing of these lines the LHC is the most powerful particle accelerator ever built.

3.2 Acceleration chain

3.2.1 LHC

The LHC is the last link in an acceleration chain made up of linear and circular accelerators, allowing proton at a centre-of-mass energy up to 14 TeV in the center frame of reference mass and heavy ions (lead nuclei) at 5.5 TeV per nucleon pair.

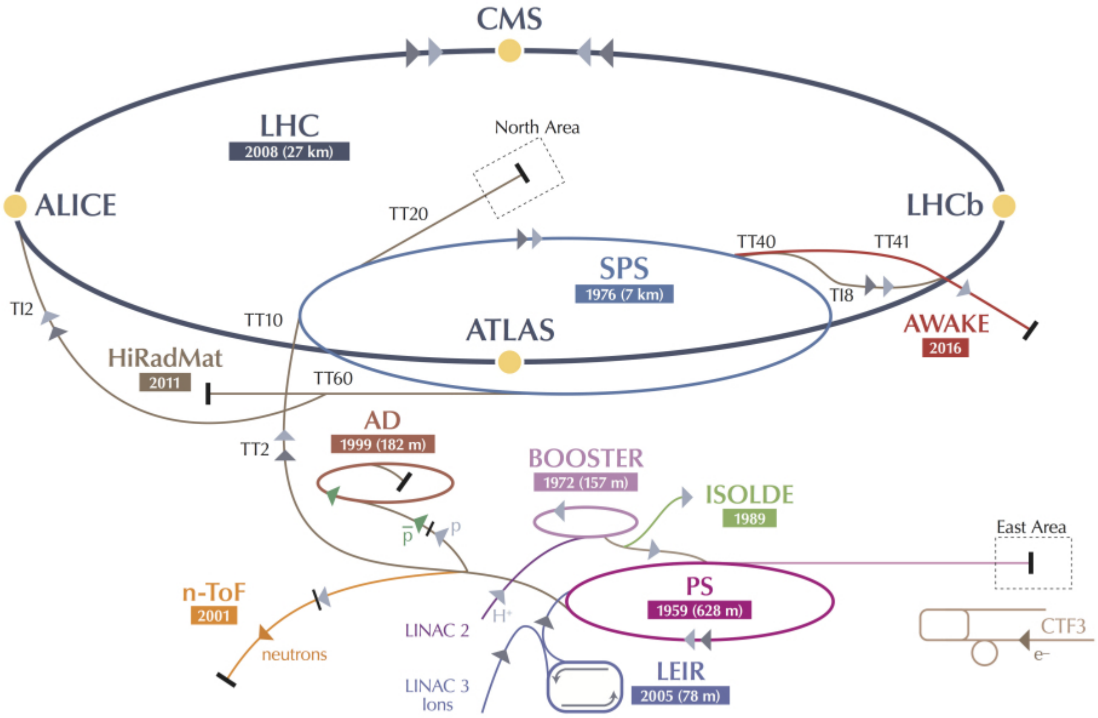

Figure 3.1: Schematic overview of CERN accelerator complex [87].

The entire chain is shown in Figure 3.1. The scheme of proton acceleration is shown in Figure 3.2. Protons are first extracted from ionized hydrogen and then brought to an energy of 50 MeV by a linear accelerator, LINAC2, before being injected into the first circular accelerator, BOOSTER which allows the rise energy to 1.4 GeV. Subsequently, the PS (Proton Synchrotron) and SPS (Super Proton Synchrotron) allows the energy increase up to 25 GeV and 450 GeV respectively. Protons are injected into the LHC where they are accelerated to an energy of 6.5 TeV (7 TeV for nominal configuration). They are divided into 1380 separate packages of 50 ns, each containing 1.7^{11} protons [83]. In order to reach such energies, the LHC is the largest (26.7 km in circumference) of the accelerations complex. It was installed in the same tunnel as the previous electron-positron collider (LEP). Hadrons being less affected than electrons by energy losses by radiation synchrotron 2, the energy reached can be much greater than in the case of a e^+e^- collider (209 GeV in the center of mass repository in the last year of LEP). The acceleration is produced by means of radio frequency cavities, the pulse frequency is 400 MHz, and the beam path is controlled by dipoles, quadrupoles or even sextu magnets poles and decapoles. At each turn of the ring, the protons can acquire, in nominal conditions, an energy of 450 keV, i.e. a total of 20 minutes necessary to reach the nominal energy (in 2015). Protons move in both directions (clockwise and counterclockwise) in two different vacuum tubes and the beams meet only at four points at which the ALICE[84], ATLAS (section 3.5), CMS[85] and LHCb[86] experiments are installed.

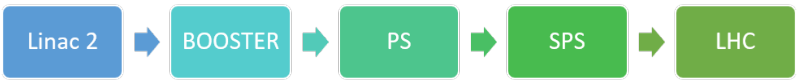

Figure 3.2: proton acceleration scheme.

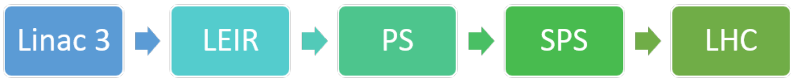

Figure 3.3: Heavy ions acceleration scheme.

3.2.2 LINAC

Linac 1 Linear Accelerator 1 (Linac 1) was designed in the early 1950s to serve as an injector for the Proton Synchrotron (PS). It accelerated its first beam in 1958 and was fully commissioned in 1959 when a beam of protons of 50 MeV made the tour of the PS for the first time. Linac 1 alone supplied protons to CERN synchrotrons until Linac 2 took over in 1978. Linac 1 accelerated light ions, such as deuterons and alpha particles, but also Oxygen or Sulfur ions, for 33 years until it stopped, in 1992. Since 1994, Linac 3 has been producing ions.

Linac 2 Linear accelerator 2 (Linac 2) is the starting point for the protons used in the experiments at CERN. Linear accelerators use radio frequency cavities to charge cylindrical conductors. The protons cross the conductors, which oscillate between positive charge and negative charge. The conductors thus exert alternately repulsion

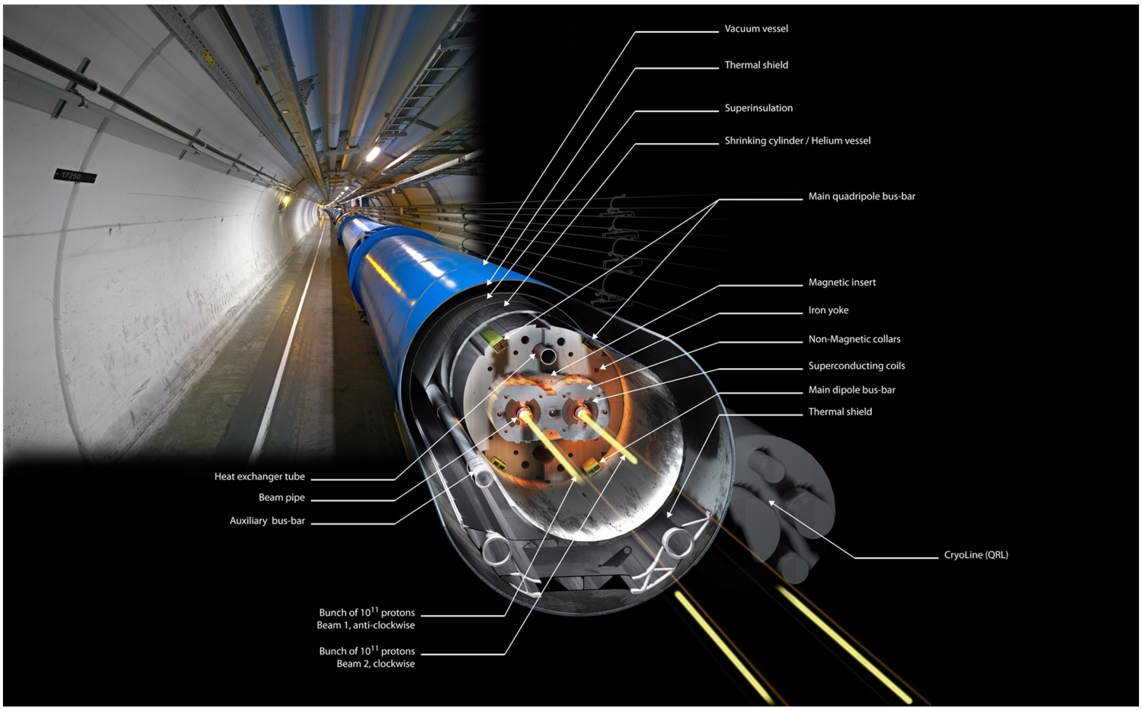

Figure 3.4: Cutout structure of the LHC [88] .

Figure 3.5: LHC running Schedule in 2018 [89].

and attraction on the particles, causing their acceleration. Small quadrupole magnets are used to tighten the proton beam.

The proton source is a bottle of gaseous hydrogen, located at the entrance to Linac 2. The hydrogen is subjected to an electric field, which pulls out its electrons so that only the protons enter the accelerator. By the time they reached the accelerator, the protons had reached the energy of 50 MeV and gained 5% of mass. They then enter the PS injector synchrotron (PSB), the next link in the CERN accelerator chain, which takes them to higher energy.

The proton beams are pulsed in increments of 100 microseconds maximum. The pulses are repeated until a sufficient number of protons is obtained.

The Linac 2 was put into service in 1978 after the Linac 1 was shut down. Initially, it was designed to provide higher intensity beams to the accelerators located downstream in the CERN accelerator complex. Linac 2 will be replaced by Linac 4 in 2020.

Linac 3 Linear accelerator 3 (Linac 3) is the starting point for the ions used in experiments at CERN. It provides lead ions for the Large Hadron Collider (LHC) and for fixed-target experiments. Researchers have requested that it produces other ions in the future, including argon and xenon.

Linear accelerators use radiofrequency cavities to charge cylindrical conductors. The ions pass through the conductors, which are alternately charged positive or negative. The conductors behind them push particles and the conductors ahead of them pull, causing the particles to accelerate. Superconducting magnets ensure particles remain in a tight beam.

The linear accelerators at CERN have swapped and changed roles over the years. After Linac 2 was built, Linac 1 was used to deliver ions for experiments at the Super Proton Synchrotron. There was soon pressure to provide heavier ions to study quark-gluon plasma, so the dedicated Linac 3 was built. It started up in 1994, providing ions to the Proton Synchrotron Booster. It injects now lead ions into the Low Energy Ion Ring, which prepares them for injection into the LHC.

Linac 3 uses up about 500 milligrams of lead per two weeks of operation. At the particles' origin and during acceleration through Linac 3, electrons are stripped away. Eventually, all of the electrons are removed and the lead is transformed into bare nuclei, which are easier to accelerate than whole ions.

Linac 3 is expected to be in use until at least 2022.

Linac 4 Linear accelerator 4 (Linac4) is designed to boost negative hydrogen ions to high energies. It is scheduled to become the source of proton beams for the Large Hadron Collider (LHC) after the long shutdown in 2019-2020.

Linac4 will accelerate negative hydrogen ions (H-, consisting of a hydrogen atom with an additional electron) to 160 MeV to prepare them to enter the Proton Synchrotron Booster, which is part of the LHC injection chain. Negative hydrogen ions are pulsed through the accelerator for 400 microseconds at a time.

Linear accelerators use radiofrequency cavities to charge cylindrical conductors. The ions pass through the conductors, which are alternately charged positive or negative. The conductors behind them push particles and the conductors ahead of them pull, causing the particles to accelerate. Quadrupole magnets ensure the hydrogen ions remain in a tight beam. The new machine comprises a H^- ion source and four types of accelerating structure: the particles are accelerated in several stages, first to 3 MeV by a radio-frequency quadrupole (RFQ), then to 50 MeV by drift tube linacs (DTLs), then to 100 MeV by coupled-cavity drift tube linacs (CCDTLs), and finally to 160 MeV by Pi-mode structures (PIMS). Linac 4's hardware also includes an equipment called a chopper line. Its role is to cut up the beam at the same frequency as that of the PS Booster.

The ions are stripped of their two electrons during injection from Linac 4 into the Proton Synchrotron Booster to leave only protons. This allows more particles to accumulate in the synchrotron, simplifies injection, reduces beam loss at injection and gives a more brilliant beam.

Linac 4 is 86 meters long and located 12 meters below ground. Beams have begun to be produced in 2013 and the milestone energy of 160 MeV was reached in 2016, after the commissioning of all the accelerating structures. During the long shutdown planned for 2019-20, it will replace Linac 2, which currently accelerates protons to 50 MeV. The Linac4 is a key element in the project to increase the luminosity of the LHC during the next decade.

3.2.3 LEIR

The Low Energy Ion Ring (LEIR) receives long pulses of lead ions from Linear accelerator 3 (Linac 3) and transforms them into short, dense bunches suitable for injection to the Large Hadron Collider (LHC). LEIR splits each long pulse from Linac 3 into four shorter bunches, each containing 2.2x108 lead ions. It takes about 2.5 seconds for LEIR to accelerate the bunches, in groups of two, from 4.2 MeV to 72 MeV. The ions are then at a suitable energy to be passed to the Proton Synchrotron (PS) for storage. Next, the lead ions are passed from accelerator to accelerator along the CERN complex to end up at their highest energy in the LHC. The LHC uses 592 bunches of ions per beam, so it takes around 10 minutes for LEIR to provide enough for a complete fill. LEIR was first proposed in 1993 as a conversion of a then-existing machine, the Low Energy Antiproton Ring (LEAR). The older machine was designed to decelerate antiprotons. Slowing and storing antimatter is now provided by the Antiproton Decelerator and the experiments ALPHA [90], AEGIS and ASACUSA. Work on the LEIR upgrade started in 2003, and by autumn 2006, the accelerator was being used to re-commission the PS to handle ions. In 2007 LEIR did the same for the Super Proton Synchrotron. Finally, in November 2010, the Low Energy Ion Ring carried out its primary role for the first time, providing lead ions for the very first ion collisions in the LHC.

3.2.4 PS

The Proton Synchrotron (PS) is a key component in CERN's accelerator complex, where it usually accelerates either protons delivered by the Proton Synchrotron Booster or heavy ions from the Low Energy Ion Ring (LEIR). In the course of its history it has juggled many different kinds of particles, feeding them directly to experiments or to more powerful accelerators. The PS first accelerated protons on 24 November 1959, becoming for a brief period the world's highest energy particle accelerator. The PS was CERN's first synchrotron. It was initially CERN's flagship accelerator, but when the laboratory built new accelerators in the 1970s, the PS's principal role became to supply particles to the new machines. Over the years, it has undergone many modifications and the intensity of its proton beam has increased a thousandfold. With a circumference of 628 meters, the PS has 277 conventional (room-temperature) electromagnets, including 100 dipoles to bend the beams round the ring. The accelerator operates at up to 25 GeV. In addition to protons, it has accelerated alpha particles (helium nuclei), Oxygen and sulfur nuclei, electrons, positrons and antiprotons.

3.2.5 SPS

The SPS originally operated as a hadron (more precisely, proton–antiproton) collider (as such it was called SppS) from 1981 to 1991„ when its beams provided the data for the UA1 and UA2 experiments, which resulted in the discovery of the W and Z bosons. These discoveries and a new technique for cooling particles led to a Nobel Prize for Carlo Rubbia and Simon van der Meer in 1984. Originally The SPS has been used to accelerate protons and antiprotons, electrons and positrons (for use as the injector for the Large Electron–Positron Collider (LEP)), and heavy ions. From 2006 to 2012, the SPS was used by the CNGS experiment to produce a neutrino stream to be detected at the Gran Sasso laboratory in Italy, 730 km from CERN.

3.3 The proton collisions

The proton collisions at the LHC are the main part of the LHC program, the precision measurement and the search for physics beyond the standard model are the motivation for this program, in fact the Higss discovery back in 2012 was done using data collected by ATLAS and CMS experiments from proton proton collisions

3.4 Heavy Ions collisions

The heavy ions program is essentially designed for probing the quark gluons plasma (QGP) which is a state predicted by QCD where the quarks and gluons are moving freely, this state is known as a state where the universe was shortly after the big-bang .the LHC rely mainly on ALICE experiment on studying those phenomena nevertheless, ATLAS and CMS also showed to be very useful to study this kind of collision. In fact through this thesis we will emphasis another use of this kind of collisions under the scope of the ATLAS experiment thus when the lead nuclei doesn't interact heads on which we call ultra peripheral collisions more details in chapter 5 of this thesis. In the study of heavy ion collisions, experimenters have only two quantities under their direct control: which two nuclei they collide and at what energies. The energies are known to high precision. However, knowing the colliding nuclei is not the same as knowing the colliding systems.Two general setups of the heavy-ion collision experiments can be distinguished, namely the fixed target and the collider. In the first one the beam of accelerated particles hits a fixed target. This kind of experimental approach is know for delivering high luminosities. In the other hand the colliders approach is more suitable for achieving higher energies which make them ideal for studying QGP.

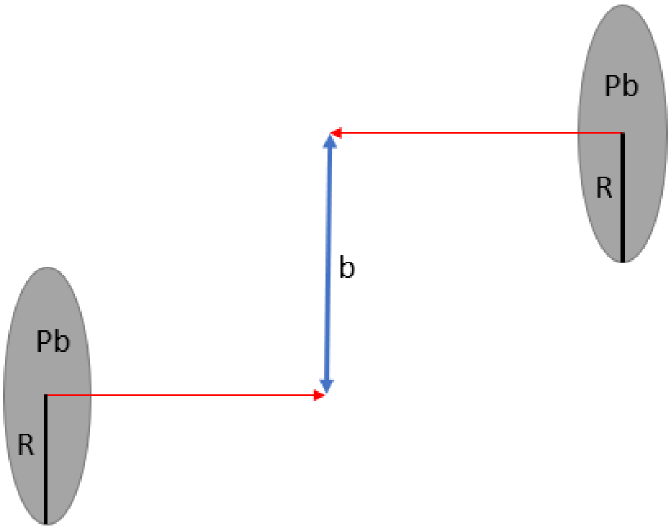

Figure 3.6: Scheme of a heavy ions collision. For ultra peripheral collisions collision b > 2R.

3.4.1 Properties

The heavy ions collisions are mostly characterised by 3 quantities :

- The impact parameter which characterise the centrality of the collision. we can distinguish 3 types of collision by relying on this parameter as shown in Table 3.1.
- The number of participant nucleons
- The number of collisions

Impact Parameter	collision type	Properties
Small	central	almost heads on collision
large	peripheral	partial collision
very large b > 2R	ultra peripheral	interact only through the photons created by the large electromagnetic field of the ions

Table 3.1: Collisions types and their properties.

3.4.2 Ultra peripheral collisions

Ultra peripheral collisions (UPC) (Figure 3.6) take place when the colliding ions pass by each other with an impact parameter higher enough so that they not interact hadronically , but also small enough so that the electromagnetic interaction occur. Allowing the study of photo-nuclear and two-photon interactions at energies above those available at fixed target experiment. The motivation behind studying such interaction in heavy ions comes from the fact that the photon flux scales as Z^2. For heavy ions, the couplings are large enough so that multi-photon interactions are possible, and higher order corrections are expected to be significant.

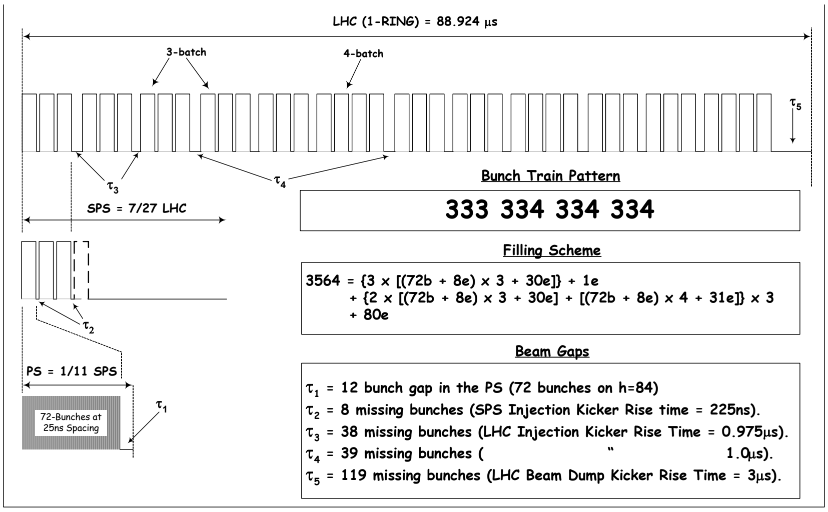

Figure 3.7: Schematic illustration of the LHC bunch distribution for a 25ns bunch spacing filling scheme [91].

3.4.3 The LHC bunch structure

The LHC can be operated with different filling schemes. In this section, a baseline scheme for the operation at 25 ns bunch spacing is described as an example. The information is largely based on reference [91]. All filling schemes must meet certain requirements; the most important one is a window of at least 3 μs without filled bunches to allow for the beam dump kicker rise time. This is known as the beam dump gap or abort gap. Figure 3.7 illustrates the filling scheme, where bunch 1 is defined to be the first bunch after the abort gap. In total, there are 3564 possible bunch positions, each with a length of 25 ns. The ring is filled in batches of 3 or 4 bunch trains – consisting of 72 bunches each – from the SPS with the following pattern:

333	334	334	334

which makes for 39 bunch trains in total and thus 2808 filled bunches. Within one batch, there is a spacing of 8 bunches between the trains (τ_2 2 in fig. 3.7), corresponding to the SPS injection kicker rise time. The batches are separated by 38 bunches (τ_3 , rise time of the LHC injection kicker) or by 39 bunches in between the 333 or 334 packets (τ_4). Finally, there is the abort gap, which comprises 119 empty bunches, corresponding to the rise time of the beam dump kicker (3 μs). In a filling scheme with 50 ns bunch spacing in the trains, the maximum number of filled bunches is 1380.

3.4.4 Luminosity

Proton bunches collisions involve quantities such as the instantaneous luminosity L expressed in cm^{-2}s^{-1} (or fb^{-1}s^{-1}). It allows to obtain the number of event for a given process X produced per second, N_X, given by:

$$N_X = L \times \sigma_X$$

where σ_X is the total cross section of the process X (expressed in fb). New Physics can manifest with low probability. Also, in order to maximize the number of potential

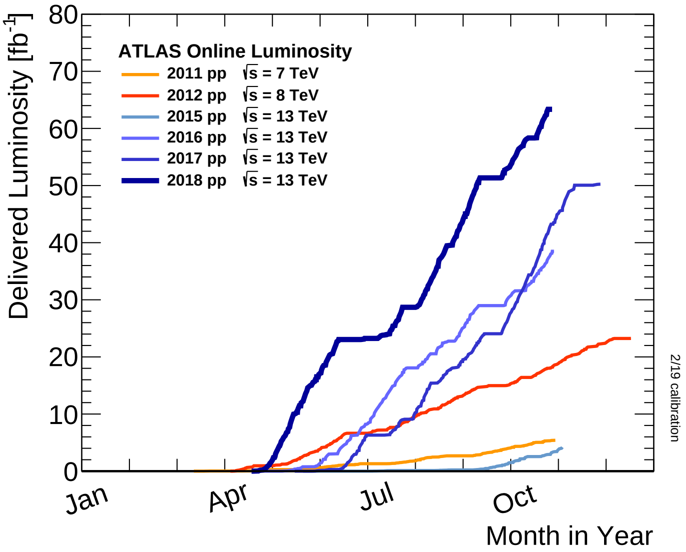

Figure 3.8: Integrated yearly luminosity between 2011 and 2018 for proton operation.

events for new phenomena, the ATLAS and CMS experiments require a very large instantaneous luminosity, leading to constraints on the proton beam, L depending only on its intrinsic parameters:

$$L = \frac{N_b^2 n_b f_{\text{rev}}\ \gamma}{4\pi\varepsilon_n\beta^*} \times F$$

In this equation, N_b is the number of protons per bunch, n_b the number of bunches per beam, f_{rev} their revolution frequency, γ the Lorentz factor of special relativity, ε_n the transverse emittance of the beam (corresponding to the dispersion of the beam in the phase space position-pulse in transverse plane), β^* the beta function at the point of collision (it quantifies the amplitude of the envelope of the beam) and F, a geometric factor depending essentially on the crossing angle of the beams. The instantaneous luminosity changes as collisions occur, in particular due to the decrease in the number of protons per packet, and its maximum value when taking data by the ATLAS detector is shown in Figure 3.2.

An analogous quantity, called integrated luminosity $\mathcal{L}$ corresponds to the integral of instantaneous luminosity over time, and makes it possible to quantify the total quantity of data delivered by the accelerator and / or recorded by an experiment, expressed in inverse femtobarns $\left(\text{fb}^{-1}\right)$. Its evolution for proton collision between 2011 and 2018 is presented in Figure 3.8 and for 2015 and 2018 heavy ions in Figure 3.9.

3.4.5 LHC experiments

The LHC delivers particle collisions to four experiments : ATLAS [92] (A Large Toroidal Lhc ApparatuS) and CMS [85] (Compact Muon Solenoid) these are so-called general purpose experiments, while LHCb [86] and ALICE [93] (A Large Ion Colliding Experiment) are specialized experiment in B physics and heavy ions respectively.

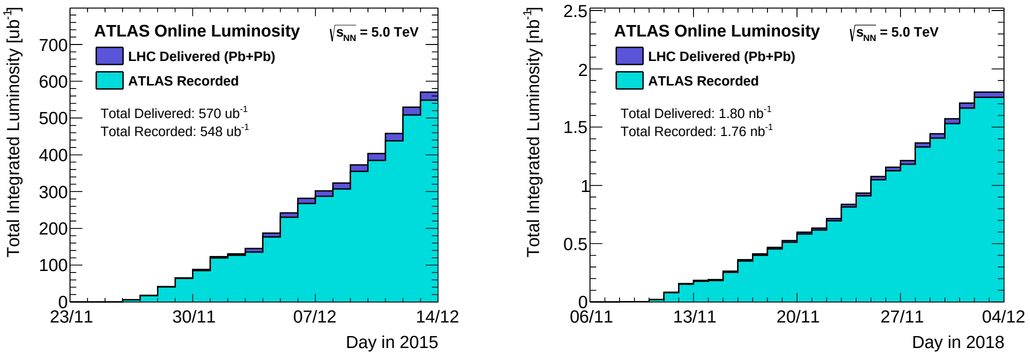

Figure 3.9: Integrated luminosity for 2015 and 2018 for Pb+Pb collision.

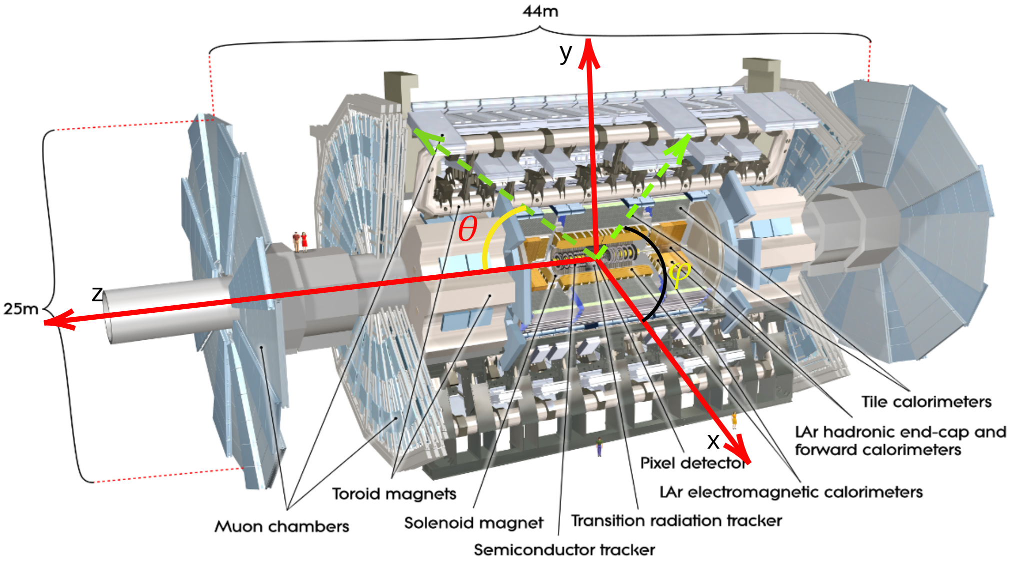

Figure 3.10: Overview of the ATLAS detector.

3.5 ATLAS Experiment

The ATLAS detector (A Toroidal LHC Apparatus) is one of two versatile detectors installed with the LHC, and has an acceptance of almost 4π sr. It is built, like other detectors of this type, of several sub-detectors such as internal detectors, dedicated to the determination of traces of charged particles, a calorimetric system, allowing the measurement of the energy of most particles, and finally a system of muon spectrometers which records their trajectories. In addition, it includes a set of solenoid and toroidal magnets used to bend the traces of charged particles and allow the measurement of their impulse. Despite this multiplicity of sub-detectors, all share the same coordinate system (Figure 3.10), used to characterize the position or momentum of an object.

3.5.1 The Coordinate System

The coordinate system of ATLAS is a right-handed coordinate system (Figure 3.10), the z axis being oriented along the beam axis, and the x and y axes defining the transverse plane of the detector. By convention, the axis x is oriented towards the center of the LHC. The angles θ and ϕ are used to characterize the angle relative to the z and x axis respectively. However, θ will be subsequently replaced by the quantity η, called pseudo-rapidity, and defined as:

$$\eta = -\ln\left(\tan\frac{\theta}{2}\right).,\tag{3.1}$$

This new quantity makes it possible to eliminate one of the indeterminacy inherent in hadronic colliders: the longitudinal component of the acceleration. Indeed, the partons which interact, carry only an unknown fraction of the energy of the protons, being able to lead to an asymmetry of the collision and to products not being at rest in the reference frame of the detector: boost . The difference in pseudo-rapidity $\Delta\eta$ is Lorentz invariant under boosts along the longitudinal axis. Finally, the difference between two particles in the plane (η, φ), denoted ΔR is defined as:

$$\Delta R = \sqrt{\Delta\varphi^2 + \Delta\eta^2},\tag{3.2}$$

will be used repeatedly in the coming chapters.

3.5.2 Internal detectors

Internal detectors are dedicated to measurement of the trajectory and the charge of charged particles, and play a major role in the reconstruction of primary and secondary vertexes, as well as in the identification of particles. Figure 3.11 shows their general structure. They are composed of three sub-detectors: the pixel detector, the silicon microstrip detector (SCT) and finally the radiation detector transition (TRT), all three bathed in the magnetic field generated by the solenoid magnet.

3.5.2.1 The Pixel Detector

The pixel detector is the closest to the beam since the first layer of pixels is located 5 cm of its axis. It includes two parts, the barrel part and the end-cap part, which allows coverage in the region $|\eta| < 2.5$ (Figure 3.12) The barrel part consists of three cylindrical pixels layers distant from the collision point between 5 and 12 cm comprising respectively 13, 22 and 31 million pixels of 50×400 μm^2 each. Each end-cap part is formed of three discs equipped with a total of 6.6 million pixels.

This geometry ensures that each charged particle emitted in the acceptance of the detector generates three pulses, one for each layer crossed. When a particle passes through a pixel, an electron-hole pair is created, and the presence of an electric field applied to the pixel allows the production of a measurable signal, determining the position of the particle, with an experimental resolution of 115 μm in the longitudinal direction, and of 10 μm in the direction $R - \varphi$.

In addition, due to its proximity to the point of interaction, this detector plays a fundamental role in the reconstruction of secondary vertices, necessary for the identification of jets coming from beauty hadrons, but is liable to be damaged by the radiations produced. during collisions. Radiation is mainly constituted of photons

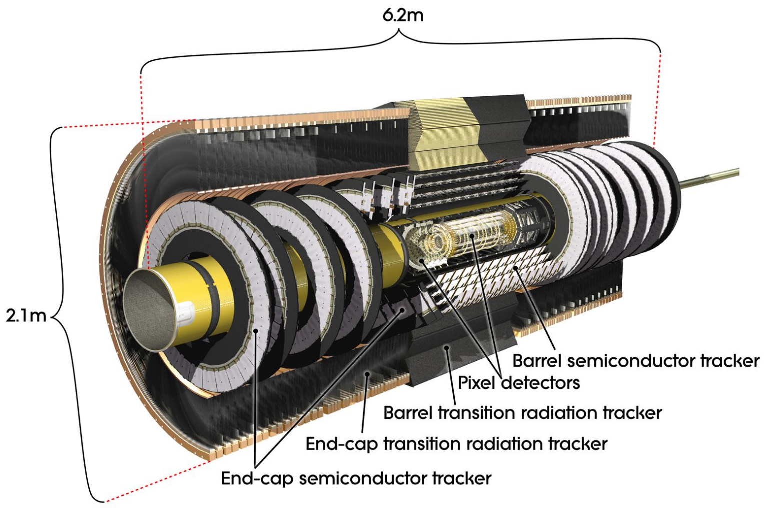

(a)

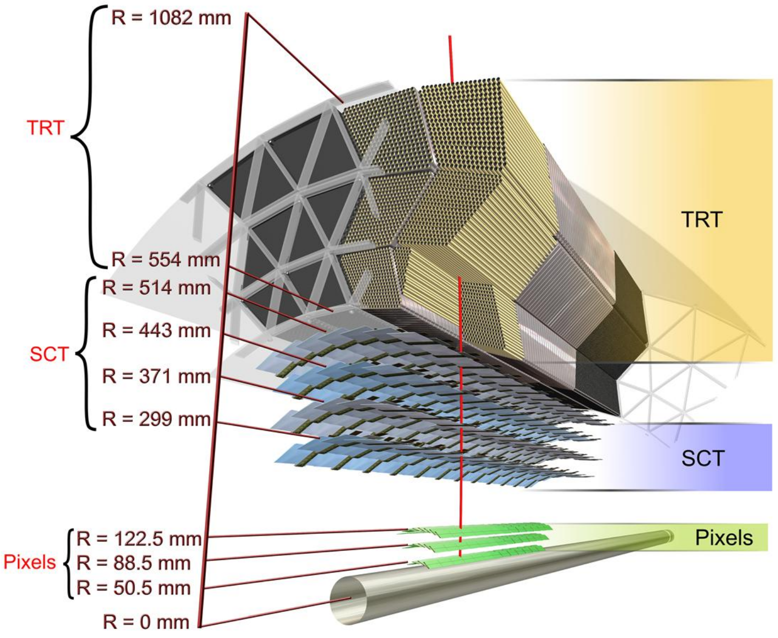

(b)

Figure 3.11: Diagrams of internal detectors. (a): whole of the barrel part of the detectors internal, with endcap parts. (b): transverse arrangement of the barrel part of the different sub-detectors (pixels, SCT and TRT).

and neutrons, and their fluxes depend on the region of the detector considered. For example, the inner detector layer closest to the beam undergoes a particle flow of about 40×10^6 Hz/cm^{-2}, against 10^5 Hz/cm^{-2} for the outermost layer.

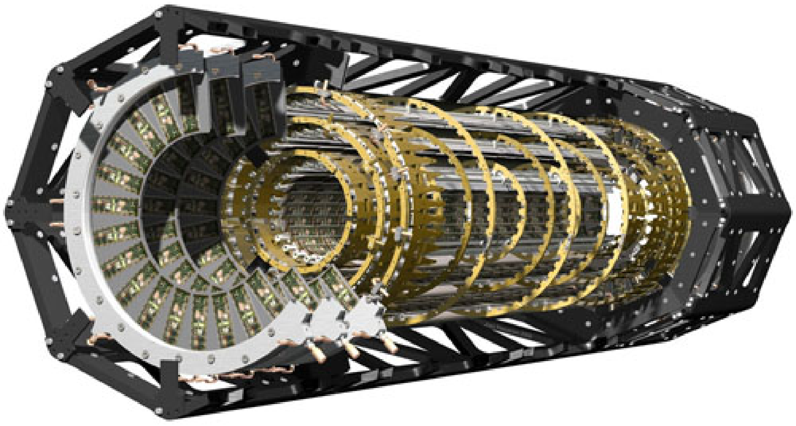

Figure 3.12: A cut-away view of the pixel detector. The barrel part consists of three cylinders coaxial. Each of the two endcap parts consists of three discs orthogonal to the axis of the beam.

3.5.2.2 The Semi-Conductor Tracker

The technology used here is very close to that of the pixel detector, the material used is Silicon, and the geometry is also comparable: four coaxial cylinders form the barrel part, while nine discs orthogonal to the beam constitute the end-cap part. The sensitive parts are then no longer pixels, but microscopic silicon tracks 80μm wide and 126 mm long. This technology leads to a resolution of 17 μm according to $r - \varphi$ and 580 μm in the longitudinal direction. On average, each charged particle located in the geometric acceptance of the detector ($|\eta| < 2.5$) will produce four pulses.

3.5.2.3 The Transition Radiation Tracker

The main component of this sub-detector is a set of polyimide tubes of 4mm in diameter, filled with a gas mixture (70% Xe $-27\%CO_2 + 3\%O_2$) with a slight overpressure. The axis of revolution of these tubes is an anode plated in gold and tungsten and they are surrounded by a material generating the emission of a so-called transition radiation. In particular, this material allows the differentiation between electrons and charged pions $\pi^{\pm}$ of low energy, the latter being little emitter of this type of radiation. Consequently, the photons emitted by the passage of an electron generate a greater ionization of the gas located in the tube, which is a greater signal amplitude for the electrons than for the charged pions.

The barrel part, long 160 cm covers the region $|\eta| < 0.7$ thanks to the tubes placed longitudinally, and the endcap part includes a set of nine discs orthogonal to the bundle in which the tubes are themselves perpendicular to the beam. The TRT offers an intrinsic resolution of 160 μm in the direction $R - \varphi$.

In the scoop of this sub-detector a dedicated study has been performed concerning performance of the emulation as an alternative of simulation and its effect on particle identification of the TRT. More details on this study is presented in chapter 4.

3.5.3 The calorimeter system

The particle energy is measured using a calorimetric system covering the region $|\eta| < 4.9$ and broken down into three parts (Figure 3.13): an **electromagnetic liquid argon calorimeter**, particularly sensitive to photons and electrons; a **had-**

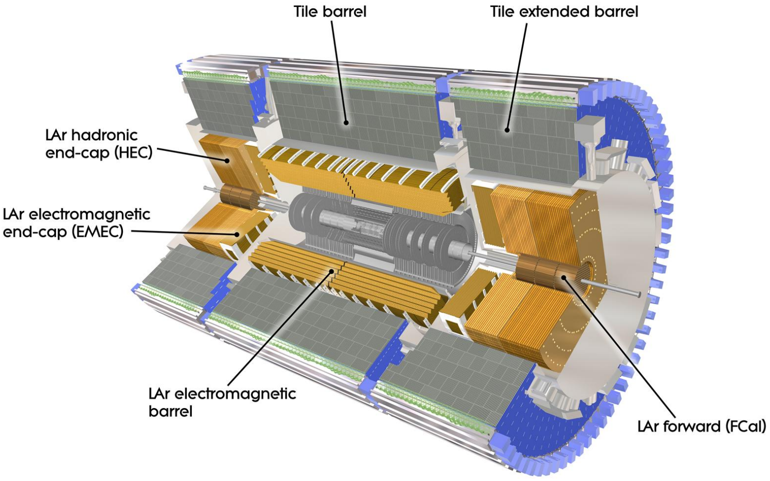

Figure 3.13: The ATLAS calorimeter system.

ronic calorimeter, sensitive to the jets and a **forward calorimeter** with a liquid argon makes it possible to detect at the same time hadrons and electrons / photons.

3.5.3.1 Electromagnetic liquid argon Calorimeter

The ATLAS electromagnetic calorimeter is a sampling calorimeter made of two parts: a barrel part ($|\eta| < 1.475$), (Figure 3.14) as well as an endcap part carrying acceptance up to $|\eta| < 3.2$ It is based on a lead / liquid argon set arranged in an accordion structure, allowing complete coverage in φ. Three detection layers are put in place in the region of the detector where the precision measurements are made ($|\eta| < 2.5$), then only two beyond [92, 94]. Both for the barrel part and for the caps, the liquid argon is kept at a constant temperature of 90K using cryostats (one for the barrel part and one for each cap part) to avoid the formation of bubbles.

The spatial segmentation in the plane (η, φ) depends on the value of $|\eta|$ and the calorimetric layer concerned (Figure 3.15). The first layer, measuring the beginnings of the development of the sheaf electromagnetic is segmented very finely into $\eta(\Delta\eta \times \Delta\varphi) = (0.0031 \times 0.1)$. The second and third layers allow a coarser segmentation: respectively $(\Delta\eta \times \Delta\varphi) = (0.025\times\ 0.025)$ and $(\Delta\eta \times \Delta\varphi) = (0.05 \times 0.025)$ for the central region.

Finally, the upstream energy losses of the electromagnetic calorimeter can be corrected by means of a portion of the calorimeter, called a pre-sampler whose spatial segmentation is $(\Delta\eta \times \Delta\varphi) = (0.025 \times 0.1)$. It is also made of liquid argon and located before the first layer of the electromagnetic calorimeter.

The structure of the electromagnetic calorimeter was particularly optimized for the search of the Higgs boson of the Standard Model in the channels $H \rightarrow \gamma\gamma$ and $H \rightarrow e^+e^-e^+e^-$, and its energy resolution, both in the barrel part and in the two End-cap is given by [92]:

$$\frac{\sigma_E}{E} = \frac{10\%}{\sqrt{E}} \oplus 0.7\%, \tag{3.3}$$

Given the distribution of materials in the EM calorimeter a presampler (Figure 3.14) is installed in order to correct for energy lose in the in front of the calorimeter.The barrel

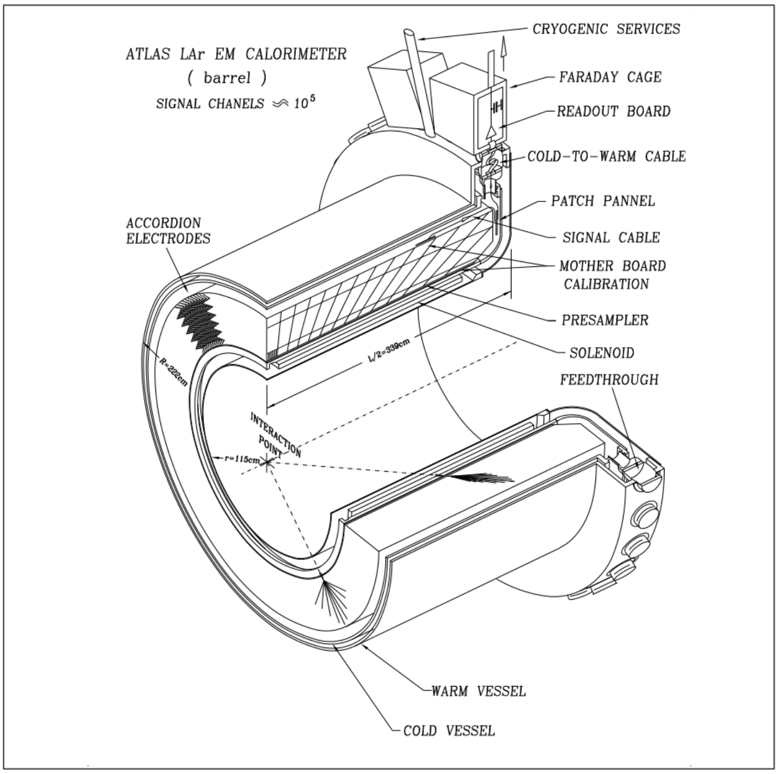

Figure 3.14: Perspective view of one half of the barrel the electromagnetic calorimeter.

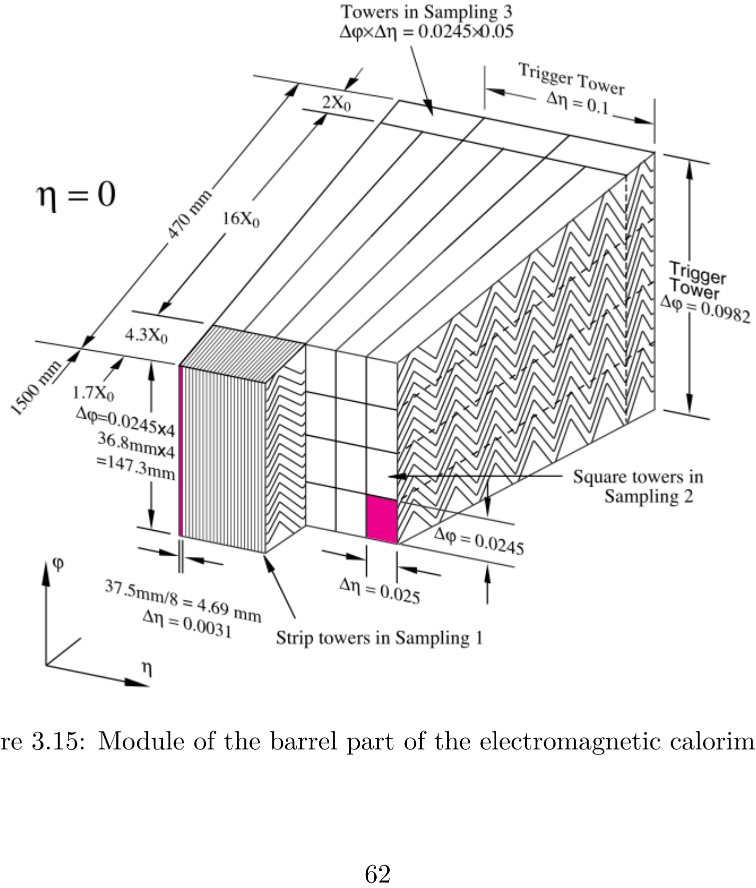

Figure 3.15: Module of the barrel part of the electromagnetic calorimeter.

(endcap) presampler feature, a 1 cm (5 mm) liquid argon active layer instrumented with electrodes roughly perpendicular (parallel) to the beam axis.

3.5.3.2 Hadronic Calorimeter

The hadronic calorimeter also consists of a barrel part and two End-cap. However, the technologies used for the two components are different. The barrel part corresponds to the **hadronic calorimeter with scintillating tiles** [95, 96] and the endcap part is based on a **copper / liquid argon sampling** [94]. This choice of technologies was imposed by the high sensitivity of the scintillating tiles to radiation, very high in the end-cap part, and also a compromise with respect to the price of the different configurations.

The hadronic tile calorimeter is a sampling calorimeter whose absorbing material is iron, and the active part is made of polystyrene wetters (sampling fraction of 4.7 for 1). The light emitted by the particles interacting with iron and scattered in the active material is captured by optical fibers with index shift to be processed by photomultiplier tubes. Decomposed into four, themselves divided into 64 trapezoidal modules in azimuth (with a segmentation $\Delta\varphi$ of approximately 0.1), this calorimeter covers the region $|\eta| < 1.7$, and represents a radial length of 7.4 interaction lengths [92] The detail of a module is given in Figure 3.16. The accessible energy resolution for pions is [92]:

$$\frac{\sigma_E}{E} = \frac{50\%}{\sqrt{E}} \oplus 3\%$$

The liquid argon hadronic calorimeter The two caps made of liquid argon allow the coverage of the region $1.5 < |\eta| < 3.2$, and reside in two wheels of 64 modules arranged in φ. These are " a copper / argon sampling calorimeter whose granularity in (η, φ) is variable according to the region of pseudo-rapidity: $(\Delta\eta \times \Delta\varphi) = (0.1 \times 0.1)$ for $1.5 < |\eta| < 2.5$ and $(\Delta\eta \times \Delta\varphi) = (0.2 \times 0.2)$ for $2.5 < |\eta| < 3.2$

3.5.3.3 Forward calorimeters

With a technology close to that of the electromagnetic liquid argon calorimeter, this detector covers the space for very large pseudo-velocities up to $|\eta| < 4.9$, ensuring the functions of electromagnetic and hadronic calorimetry. It is a set of four wheels, of which only three are equipped, the last serves as a shield for the muon chambers downstream. The first wheel is an electromagnetic calorimeter with copper / liquid argon sampling, while the second and third are made of tungsten and liquid argon, and correspond to hadronic calorimeters. The choice of these materials is explained by the desire to reduce the sensitivity to radiation, which is very strong in this region of the detector. In addition, tungsten allows a reduction in the dispersion of hadronic showers, a priori wider than electromagnetic showers. The set of wheels corresponds to approximately 10 interaction lengths [92].

The geometry of these calorimeters is however different from that used for the barrel and cap parts. Each instrumented wheel is formed by an absorber, pierced with holes of approximately 5 mm in diameter, in which are arranged metal tubes of 4.5 mm in diameter serving as an electrode. The remaining space is filled with liquid argon which is used as active material, and this space is particularly reduced in order to allow a rapid response of the detector thanks to a reduced drift time. Its

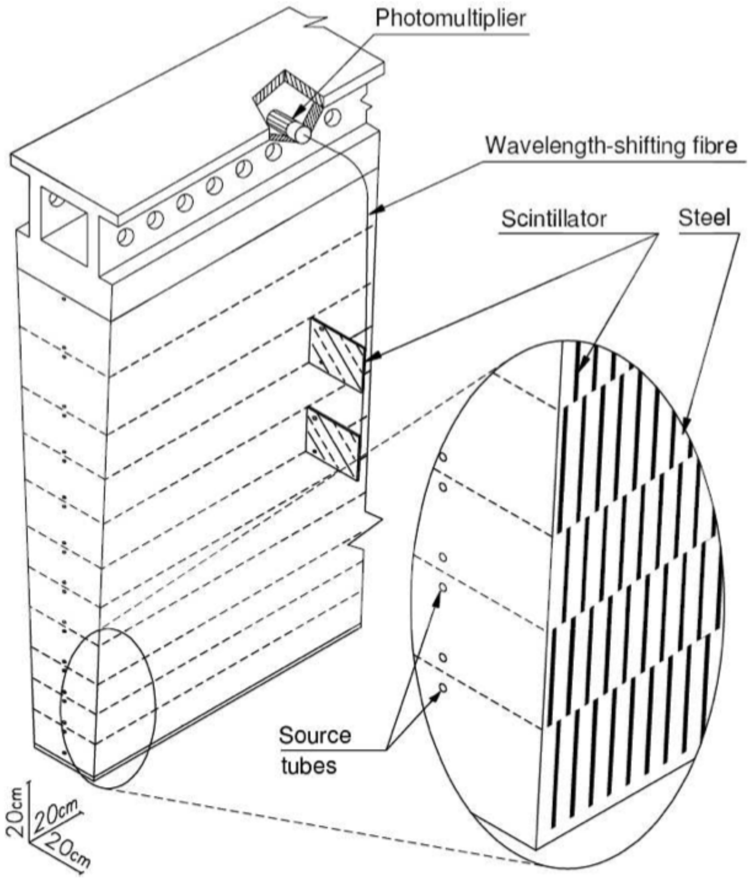

Figure 3.16: Schematic diagram of an ATLAS hadronic tile calorimeter.

energy resolution is given by [92]:

$$\frac{\sigma_E}{E} = \frac{100\%}{\sqrt{E}} \oplus 10\%$$

3.5.4 Muon spectrometers

Like all the sub-detectors mentioned so far, muon spectrometers [97] (Figure 3.17) have a barrel part, covering the central regions ($|\eta| < 1$) and a an end-cap part for detecting muons of greater pseudo-speed up to $|\eta| = 2.7$. These two sets are intended to determine the trajectories of the muons, curved by the magnetic field created by the toroïdal magnet (Section 3.5.5), allowing the measurement of their impulse.

In each of these parts, two types of detectors are present: a rapid response detector, used by the triggering system, and a precision detector, used for the measurement of muon properties (pulse and charge for example). The first type corresponds to RPC (Resistive Plate Chambers) and TGC (Thin Gap Chambers) detectors, while the second consists of MDT (Monitored Drift Tube) and CSC (Cathode Strip Chambers).

The MDTs are used in the barrel part and the cap part to cover the pseudorapidity region $|\eta| < 2.7$ and are formed of three layers, and based on the principle of a drift tube using an argon and carbon dioxide gas. The anode collecting the electrons generated by the passage of a muon consists of a tungsten-rhenium alloy wire.

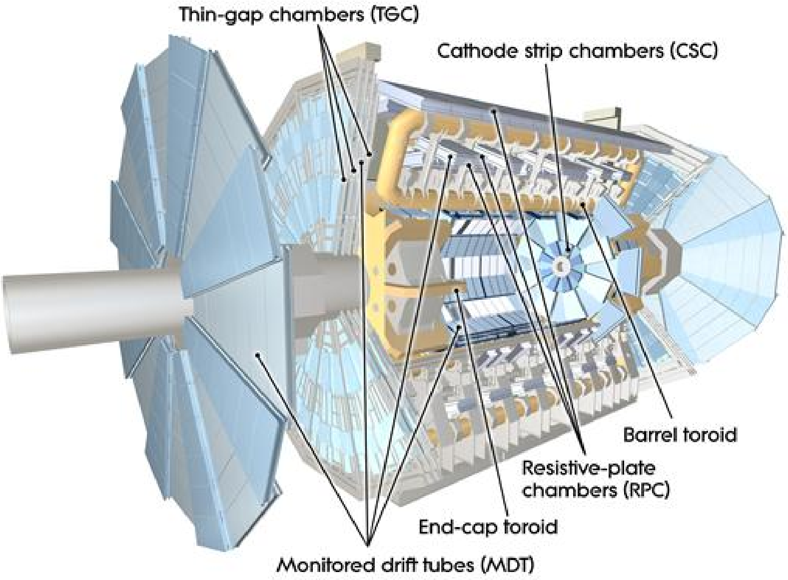

Figure 3.17: Muon spectrometer of the ATLAS detector.

The CSCs are multi-wire chambers in which the wires are subjected to a tension of 1900V and bathed in an argon / carbon dioxide mixture. These detectors are capable of enduring much larger particle flux than MDT (1000Hz/cm^{2}instead of150Hz/cm^2) **The RPCs** Located only in the barrel part, they are made of two plates between which a gas mixture is retained $(C_2H_2F_4/\text{Iso} - C_4H_{10}/SF_6)$, ionized when a muon passes. The applied potential difference (9.8 kV) allows the formation of an avalanche constituting a measurable electrical signal.

The TGCs use a technology similar to that of RPCs, but tolerate a higher flow of particles. They are therefore present only in the end-cap part of the muon spectrometer. The resolution in transverse pulse expected by this device is then $\frac{\sigma_{p_T}}{p_T} = 10\%$ for a transverse pulse of 1 TeV [92]

3.5.5 Magnet systems

The ATLAS detector is equipped with two systems of superconductive magnets curving the paths of charged particles, which allows their pulses to be measured. A solenoid magnet immerses the internal detector in a 2 T magnetic field, while the toroidal system allows to bend the trajectory of the muons at the level of the external part of the detector: the spectrometers to muons. Figure 3.18 shows the arrangement of the magnet systems. The solenoid magnet [98] is 5.8m length and a diameter between 2.46 and 2.56m, it allows to generate a field of about 2 T, thanks to a current intensity of 7730 kA. It is located between the internal detectors and the electromagnetic calorimeter and designed so that the quantity of material is minimal in order to ensure optimal performance of the electromagnetic calorimeter: it corresponds to approximately 0.66 length of radiation for a particle at normal incidence.

The toroïdal magnet [99, 100] is divided into two parts: the barrel part (for the central region of the detector $|\eta| < 1.2$) and the cap part ($|\eta| < 2.7$). For the barrel part, eight magnets of 25.3m and powered by an intensity of 20.5kA generate a field

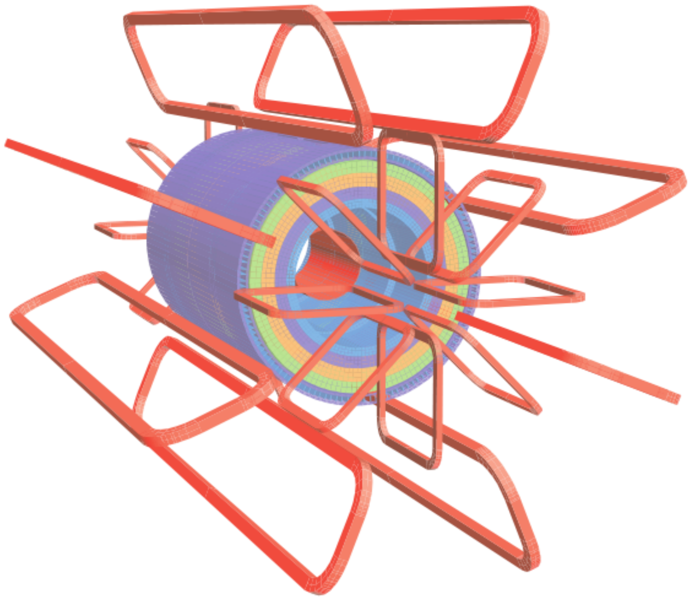

Figure 3.18: ATLAS detector magnet system with solenoid magnet (center), and magnet toroidal, whose magnetic field extends in muon trajectographs. The two side parts (called endcap) are also shown.

up to 2.5T, while the endcap parts , smaller, lead to a magnetic field up to 3.5T.

3.5.6 Trigger system

The nominal rate of collisions of 25 ns between each proton packet (50 ns in 2012) leads to an event frequency of 40 MHz (20 MHz in 2012). Most are of little interest, since they correspond to events produced with very little energy in the transverse plane, or towards the front for example.

In addition, the processing of the information from the various detectors, the reconstruction of events, as well as the storage of this information, requires a longer time than 25 ns. Consequently, an event filtering system, called the trigger system, or trigger [101, 102] is implemented. It allows the selection of events of interest for physics, and is based on the information provided by the various ATLAS subdetectors.

The architecture of the trigger system is shown in Figure 3.19. It is divided into two levels, depending on the nature and the precision of the information used.

3.5.6.1 The Level 1 trigger

This step [101] is based on calorimetric information and muon spectrometers (more specifically RPC and TGC). Regarding the calorimetric information, the granularity used is coarser than in the analyses (0.1×0.1 instead of 0.025×0.025 in the plane (η,φ) for example the electromagnetic calorimeter). This level makes it possible to define the regions of interest (ROI), formed of roughly reconstructed physical objects (leptons, jets for example). The number of objects reconstructed and their transverse energy make it possible to obtain the decision whether or not to transmit the event to the HLT. The processing time must not exceed 2.5 μs. Indeed, collisions being carried out under nominal conditions every 25 ns, the information is stored in the buffer

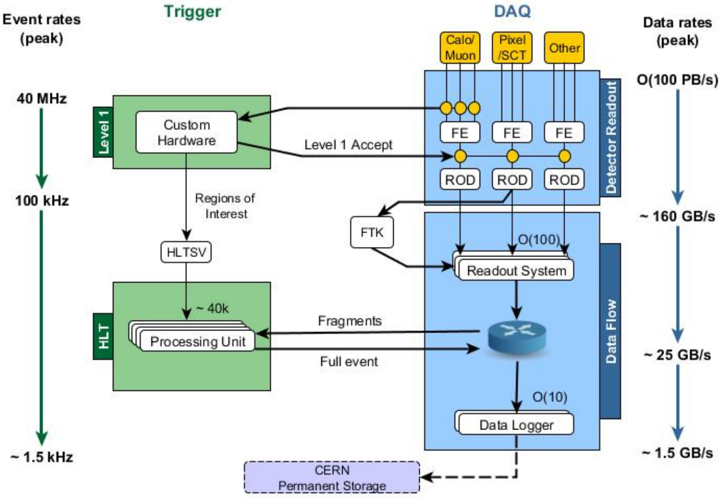

Figure 3.19: The ATLAS Trigger and Data Acquisition (TDAQ) System in LHC Run 2.

memory while waiting for its processing by the Level 1 system. They can be lost if the decision-making takes too long. This trigger level leads to a nominal frequency of events of 75kHz (65 kHz in 2012)

3.5.6.2 High-Level trigger

The HLT software is a fusion of the event filter and HLT used in Run-1 [103] the HLT uses software-based decision- making use of all detector information [102], and the reconstruction algorithms used take advantage of this additional granularity to refine the reconstruction of objects. In particular, the use of internal detectors allows improved identification of electrons. At the end of this step, the frequency of events is reduced to the order of 1kHz At the HLT, events are divided into different "streams", each containing the output from a number of different trigger chains. A single stream may contain, for example, all events passing an electron or muon trigger. Events may be added to several streams if they meet both L1 and HLT trigger requirements. The number and contents of the set of streams are decided at the beginning of a run. There is typically "debug" stream that is reserved for events that could not be evaluated in the allotted time for a trigger decision.

3.5.7 Special Systems

In addition to the main detectors described previously, the ATLAS detector is equipped with special parts dedicated to very large absolute values of pseudo-rapidity as well as systems providing information about the LHC beams.

3.5.7.1 MBTS

The Minimum Bias Trigger Scintillators (MBTS) [104] consists of 32 scintillator counters of 2cm thick each, organized into two disks with one on each side of the ATLAS detector (A and C). The scintillators are installed on the inner face of the end-cap calorimeter cryostats at $z = \pm 3560$mm such that the disk surface is

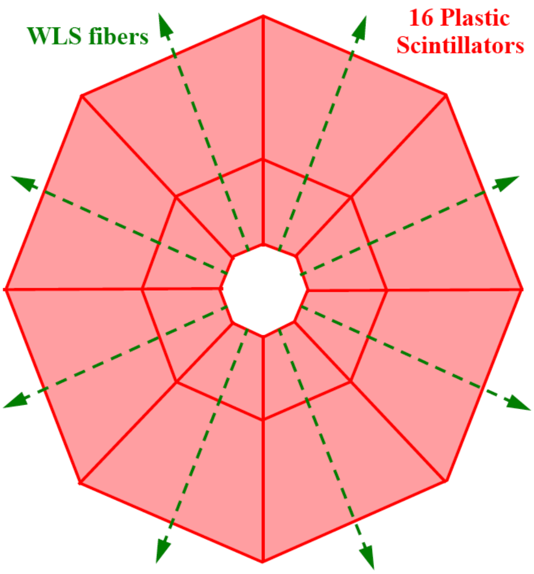

Figure 3.20: MBTS disk configuration with outer and inner rings.

perpendicular to the beam direction. Each disk is divided into an inner and an outer ring respectively covering the radial regions (153,426) mm and $(426, 890)$mm. In η these regions correspond to (3.84,2.82) and (2.82,2.09) respectively. Both the inner and the outer ring are organized into eight independent ϕ sectors, $2\pi/8$ radians wide each. These sectors are placed such that the first sector has its edges at $\phi = 0$ and $\phi = \pi/4$ radians (Figure 1). Light emitted by each scintillator counter is collected by wavelength-shifting optical fibers and guided to a photomultiplier tube (PMT). The PMT signals are read out by the Tile Calorimeter (TileCal) electronics. In the 2015 data used in this analysis a veto based on MBTS detector was used in the High Level Trigger.

3.5.7.2 ZDC

The Zero Degree Calorimeters (ZDCs) [105] are a compact calorimeters located at approximately zero degrees to the incident beams on either side (140 m far) of the interaction point Figure 3.21. Which is the point of transition between two separate beam pipes into one common straight section pipe as shown in Figure 3.22.

It consists of four modules - one electromagnetic (EM) module and 3 hadronic modules. For one arm the EM module is shown in Figure 3.23. It consists of 11 tungsten (W) plates 91.4mm wide, 180mm high, and 10mm thick in the beam region, with steel plates extending above for 290mm. 1.0 mm diameter Quartz rods penetrate the W plates parallel to the beam in an 8x12 matrix transverse to the beam. At the front end of the module the rods are bent 90° vertically and are viewed from above by multi-anode phototubes (MAPMTs). The hadronic modules shown in Figure 3.23 are similar, but while the EM module maps each of the 96 position measuring rods onto one pixel of the multi-anode phototube the hadronic modules maps clusters of four rods onto each pixel, and not all hadronic modules have position sensing rods (there is only one position sensing module per arm). Also, the hadronic modules only have one funnel.

The ZDC uses Tungsten plates as absorber material and quartz rods interspersed

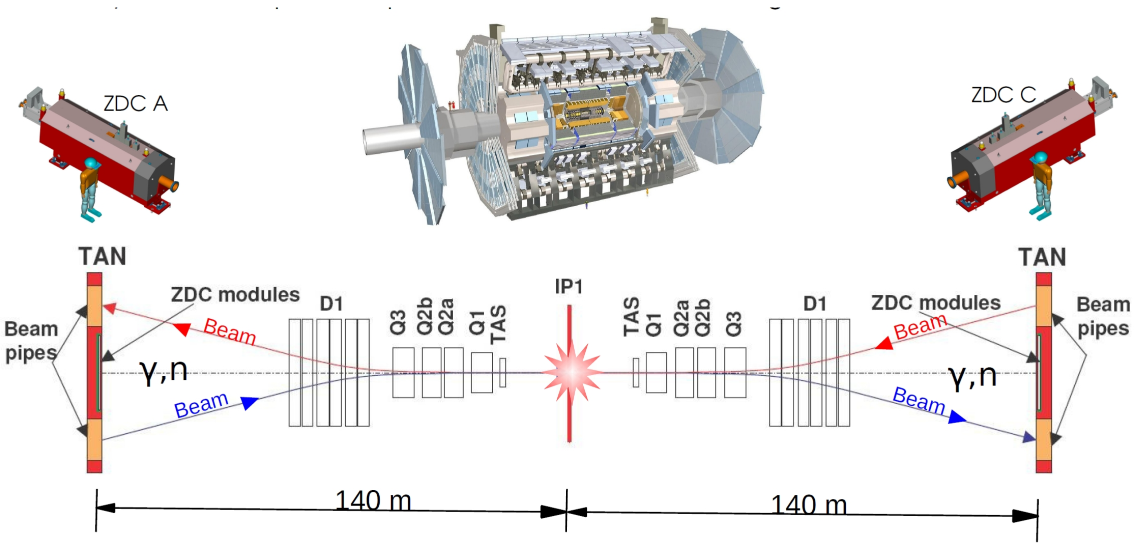

Figure 3.21: Plan view of the section between the interaction point (IP) and the ZDC. Due to the beam optics, charged particles are deflected while the neutral particles travel directly to the ZDCs (one at each side of the IP).

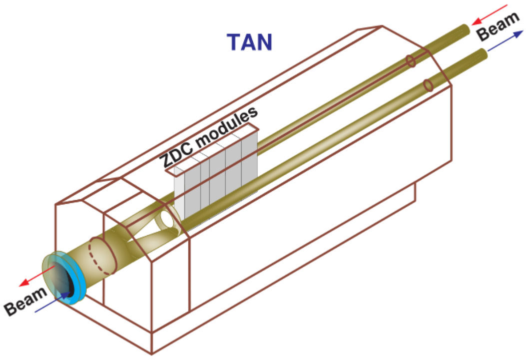

Figure 3.22: Emplacement of the ZDC modules .

in the absorber as active media. The energetic charged particles crossing the quartz rods produce Cherenkov light, which is then detected by photomultipliers and sent to the front end electronics for processing, in a total of 120 individual electronic channels. The position of the rods with Cerenkov light signal corresponds to the transverse position of the incident particle, and the intensity of the light reflects the energy of the particle. Both electromagnetic decaying neutral particles (π_0, η and K_S) and neutrons will be observed by ZDC, providing valuable measurements in a largely unknown kinematic region. The capability to measure both neutrons and π_0 will allow to observe also baryons as Λ and Σ and make ZDC an important instrument for forward physics studies.

The ZDCs play an important role in the characterization of events in heavy ions collisions. In fact when heavy ions are collided at the LHC only a portion of the ions participate in the collision these are called participant the others portion which pass without interaction are called spectators Figure 3.24. The ZDC take care of counting the spectator neutron. Measurement of the number of spectator neutrons is equivalent to measuring the magnitude of the impact parameter or centrality of

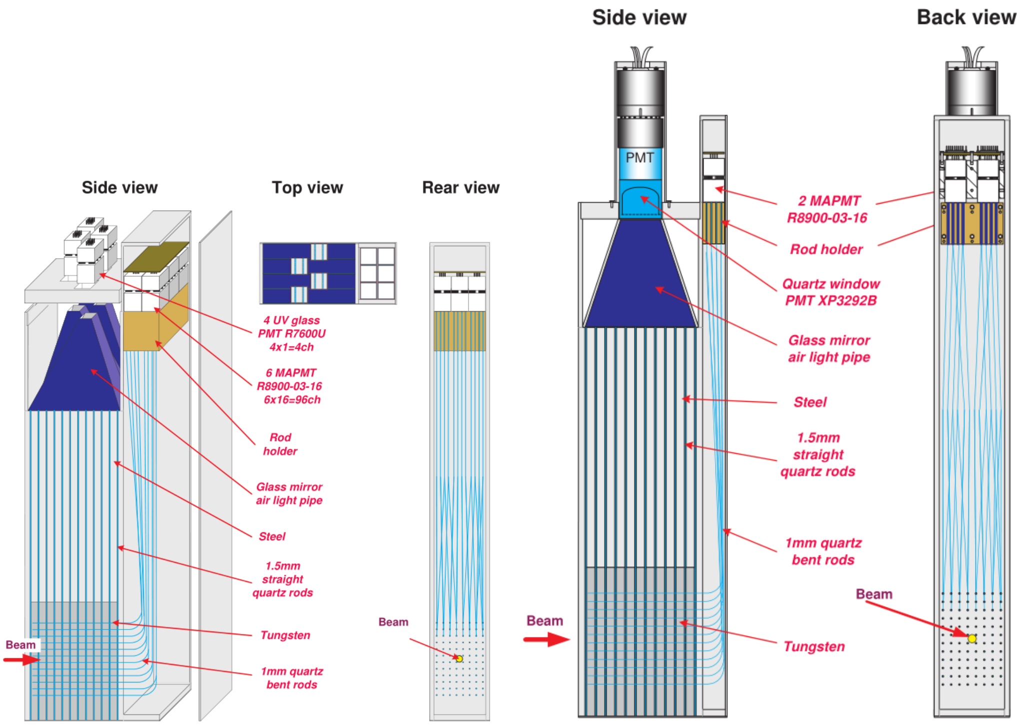

Figure 3.23: Left : Electromagnetic ZDC module, right : Hadronic ZDC modules.

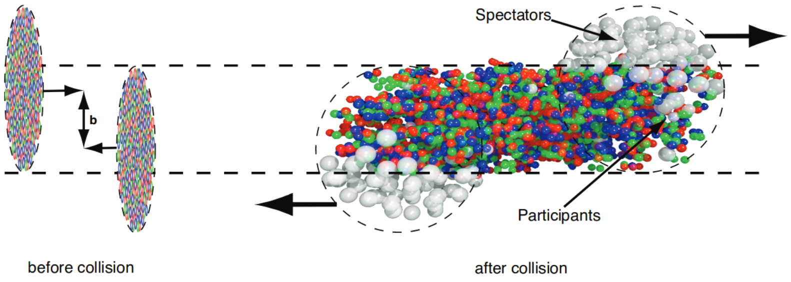

Figure 3.24: Simplified sketch of a heavy-ion collision. Left: Two ions before the collision with the impact parameter b. Right: Ions after collision divided into participants and spectators [106].

the collision since the more central the collision is, the larger the number of widely scattered particles is.

3.5.7.3 Luminosity detectors

LUCID (LUminosity measurement using a Cerenkov Integrating Detector) is The main online luminosity monitor for ATLAS and it is placed at a distance of 17m of each side of the interaction point, which detects inelastic pp scattering in the forward region. The ALFA detector (Absolute Luminosity For ATLAS) is located at 240 m from each side of the interaction point.

3.5.7.4 Beam Pickup Systems

A BPTX station is installed at each side of the ATLAS detector [107] 175 m from the interaction point, each station is made of four electrostatic button pick-up detectors. Those detector are used for synchronising the bunch clock sent by th LHC

3.5.7.5 Beam Conditions Monitors

The ATLAS Beam Conditions Monitor (BCM) consists of two stations of detectors .The stations are located symmetrically around the interaction point, positioning the diamond sensors at $z = \pm 184$ cm and $r = 55mm$ (a pseudo-rapidity of about 4.2). Each station is made with four modules. Each module includes two diamond sensors read out in parallel. The sensors are required to tolerate doses up to 500 kGy and in excess of 1015 charged particles per cm2 over the lifetime of the experiment [108].

3.5.8 Data, Simulation and Object Reconstruction

3.5.8.1 Data

The data whiten ATLAS experiment is collected as runs, each one has a unique run number and is divided into luminosity blocks. The luminosity blocks are flagged with data quality information these information can be used to build the good run list(GRL) that can be used in physics analysis. Once the data is collected, it get to the processing step that is handled by the ATLAS software framework called Athena [109], the same software is used in digitization and reconstruction of simulated event. After several steps that makes use [110] of the CERN computing resource for storage and processing. One of the final outputs of processing is Analysis Object Data (AOD) files which contains the information needed for physics analysis, i.e. objects like electrons, muons, and their properties like energy, momentum, position. The AOD files can eventually be used to produce Derived Analysis Object Data (DAOD) files such as the one used for the analysis presented in this work.

3.5.8.2 Simulation of the ATLAS detector

After the event generation stage, the role of the detector simulation is to simulate the interaction of the particles produced with the material that constitutes the detector and model the response of the detector electronics. The first step is carried out by considering a geometry of the detector, the decomposition of the latter into elementary volumes representing all the parts whether they are sensitive or not. The ATLAS detector is described by means of 4806839 volumes, almost uniformly distributed between the internal detectors (38%), the calorimeters (32%) and the muon spectrometers (30%)[111]. This geometry is modulated by the operating conditions of the real ATLAS detector, recorded at any time in an Oracle-type database, in order to allow the simulated detector to reproduce the faults of the real detector and allow a correct description of the data recorded.

The complete simulation of the ATLAS detector is based on GEANT4 [112] and provides an excellent description of the detector and the physics process but requires significant computation time. Also, given the large number of events generated (eg 15 million events for the pp $\rightarrow t\bar{t}$ process), a simplified procedure is also available, called ATLFASTII [113], allowing the calculation time to be reduced by a factor of 20 to 40 [111]. This last simulation, known as rapid, differs from the previous one by the description of the calorimetric system, and more particularly of the electromagnetic calorimeter with liquid Argon. Indeed, the interaction of particles with the detector is not simulated, but a library of electromagnetic and hadronic showers [114] is used. The latter is obtained by the complete simulation of nearly 30 million events, different by the longitudinal or transverse profiles of the sheaves. For simplicity, the electromagnetic showers are modeled from photons, and the hadronic showers from charged pions. At the end of this simplified detector simulation, the properties of the objects are very close to those obtained using the full detector simulation, namely with a difference in the energy scale of the jets from 1 to 2% [111].

The response of the simulated detector is then converted into a format exactly identical to that of actual data, so that the phase of reconstruction of physical objects, such as electrons, muons, jets and the missing transverse energy is carried out in an identical way in simulated and data samples.

3.5.8.3 Object Reconstruction

Whether in the Monte Carlo simulation or in the ATLAS data, the information transmitted by the detector's reading electronics cannot be used directly by physicists in the context of analyses. These use physical objects (electrons, muons, jets, missing transverse energy) obtained after using several reconstruction algorithms. These algorithms take advantage of all of ATLAS's sub-detectors, and therefore rely on the traces recorded by internal detectors and muon spectrometers, but also on calorimetric deposits, both in electromagnetic and hadronic calorimeters .The description given here is largely based on [115]. Only two objects are described in this section since the analysis presented in this work mostly make use of them :

Reconstruction of Electrons and Photons

The electrons and photons are reconstructed in the central region ($|\eta| < 2.5$) by the procedure described in Figure 3.25. This procedure is a replacement of the sliding window algorithm [116] which use fixed-size clusters of calorimeter cells. The new algorithm use dynamic, variable-size clusters (superclusters) and can be described in following steps:

Prepare tracks and clusters: it starts by forming proto-clusters in the EM and hadronic calorimeters using a set of noise thresholds in which the cell initiating the cluster is required to have significance $\left|s_{\text{cell}}^{\text{EM}}\right| \geq 4$, where

$$S_{\text{cell}}^{\text{EM}} = \frac{E_{\text{cell}}^{\text{EM}}}{\sigma_{\text{noise,cell}}^{\text{EM}}}$$

$E_{\text{cell}}^{\text{EM}}$ is the cell energy at the EM scale and $\sigma_{\text{noise cell}}^{\text{EM}}$ is the expected cell noise. The expected cell noise includes the known electronic noise and an estimate of the pile-up noise corresponding to the average instantaneous luminosity expected for Run 2. This energetic noise is specified for each cell. As soon as a seed cell is found, neighboring cells of the seed are iteratively added if their energy is twice as high as their noise level. after this step all neighboring cells with an energy above their noise level are added to form a topological calorimeter cluster. Next the selection of electromagnetic topological is carried out and then the reconstructed tracks and conversion-vertex from the inner detector are matched to the electromagnetic with a similar way of the one used in the sliding windows algorithm [116]. So far the reconstruction of the electron and photon proceeds simultaneously assuming a photon and an electron.

Build superclusters: the reconstruction of electron and photon superclusters proceeds independently For a photon, the minimal energy of a seed cluster is 1.5GeV. For electrons, a seed cluster must have a minimal energy of 1GeV and a matched track with at least four hits in the SCT. If a seed cluster is found, satellite clusters are added from all unused clusters. Such a satellite cluster is assumed to represent secondary electromagnetic showers from the same physics object. The energy of a satellite cluster is required to be below the energy of the seed cluster. In general, a cluster is added as satellite cluster if it lies within $\Delta\eta \times \Delta\phi = 0.075 \times 0.125$ around the barycentre of the seed cluster. Additionally for converted photons, clusters are added that share the same conversion vertex or any track from the conversion vertex of the seed cluster. For electrons, additional satellite clusters are searched for that lie within a window of $\Delta\eta \times \Delta\phi = 0.125 \times 0.3$ and whose best matched track is the same as that for the seed cluster.

Build analyis objects: after a supercluster is built, the next seed cluster is searched for, until all electromagnetic topological clusters are visited. Then, the supercluster energy is computed by only taking into account cells in the ECAL associated to this cluster. The supercluster size is restricted to three or five cells in η direction in the barrel or in the end-cap region, respectively, centred around the barycentre. This restriction excludes cells that do not contain a significant amount of the particles' energy, but potentially energy from other physics objects. Subsequently, the energy of the supercluster is calibrated using an [MVA] technique and the position of the barycentre is corrected [115]. Next, reconstructed tracks and conversion vertices are matched to the superclusters and the particle type is determined. As superclusters for photons and electrons are formed in parallel, ambiguities may occur which are tried to be resolved by a dedicated procedure. If an ambiguity cannot be resolved, the physics object is rejected in this analysis. As last step, the energy is recalibrated in dependence of the particle type following the procedure described in Ref [115].

More detail concerning the use of the calibration will be specified in the chapter 5.

Conclusion

In this chapter we present the experimental setup behind the data used in this thesis. The LHC accelerator complexes allows the acceleration and the collision of proton and heavy ions at four interaction points. The LHC deliver an immense amount of data for the four experiments. The ATLAS detector is a versatile detector with multiple sub-detectors. This chapter also provided detail on their functions. We also gave an overview of the data collection and simulation technique used in the scope of the ATLAS experiment. The next chapter present a study performed at the level of Transition Radiation Tracker which is the outermost part of the ATLAS inner detector. The study concerns the emulation technique and its performance in the simulation of the TRT.

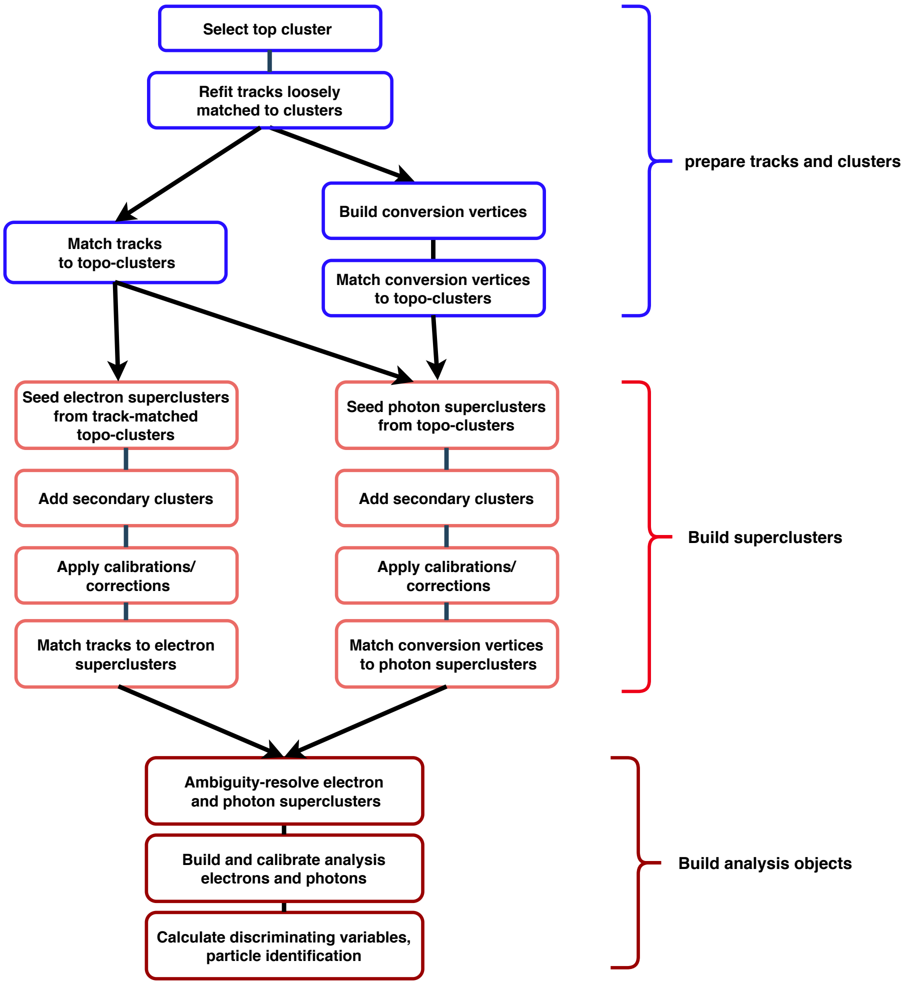

Figure 3.25: Flow diagram for the electron and photon reconstruction based on super cluster[115].

Chapter 4

Argon Emulation in The Simulation of the Transition Radiation tracker

Contents

Introduction

The Transition Radiation Tracker (TRT) is a straw tracker composed of approximately 300,000 carbon-fiber reinforced Kapton straws, arranged in two different geometries : The barrel section covers $560 < R < 1080$ mm and $|z| < 720$ mm and has the straws aligned with the direction of the beam axis [4]. The two end-cap sections cover $827 < |z| < 2744$ mm and $617 < R < 1106$ mm and have the straws arranged in planes composing wheels, aligned perpendicular to the beam axis, pointing outwards in the radial direction. The TRT extends to pseudo-rapidity $|\eta| = 2$. The average number of TRT hits per track is around 34, except in the transition region between barrel and end-caps and at the edge of the acceptance ($|\eta| = 1.7$) where it is reduced to approximately 25 hits.

Tracking information and TR signals are obtained for each straw using separate low and high threshold discriminators in the front-end electronics. The low level threshold (≈ 270 eV) is used for track position measurement in the straw, and the high level threshold (≈ 5 keV) is used to separate minimum ionizing particles from particles with high ionization or large Lorentz γ-factor due to transition radiation absorbed in the active gas. In this chapter, we look at the particle identification performance of the TRT under the emulation since it's the only one affected by the change of the gas geometry from xenon to the argon. more detail in [117].

4.1 TRT Particle Identification

4.1.1 Principle

Besides its tracking capabilities, the Transition Radiation Tracker also contribute in the ATLAS experiment to particle identification meanly electrons, since the time-structure and the amount of the energy deposited in a TRT straw when crossed by a particle, holds a great deal of information, usable both for tracking and particle identification. High threshold TRT hits indicate the presence of transition radiation (TR) photons. The probability of creating a high threshold hit depends on the Lorentz γ factor and the occupancy, and it's used to construct the likelihood that is needed to calculate the electron probability.

4.1.2 Effect of Argon mixture on PID

During Run I of the LHC, large leaks appeared in some of the tubing used to supply the active gas to the detector, due to mechanical stress and corrosion caused mainly by ozone. In Run II it has been decided to use an argon based gas mixture in places where the xenon losses are too high and therefore unaffordable, previous studies have been done and confirmed that argon based gas mixture does not affect the tracking performances of the detector, however the discrimination between electrons and charged pions is affected, this stems from the fact that the xenon have higher X-ray photon absorption cross section transition radiation than the argon. Figure 4.1 shows the difference in absorption length of X-ray in 3 noble gases with the xenon having a higher absorption than the argon.[118]. Studying the performance of the TRT under emulation in the PID level is a mandatory key to judge the emulation performance, which requires to check how different TRT PID observable respond to the emulation. In this study, we use the High Threshold probability and the electron probability as tools to investigate the emulation performance. [119]

4.2 Argon Emulation

4.2.1 Motivation

Saving computing resource and time is one of the most challenging issues of the ATLAS experiment globally and the simulation specially , The TRT as a part of ATLAS detector can contribute in facing this challenge by using the emulation method to simulate a new gas geometry when a change occurs in data taking periods, this will allow avoiding the start of a new simulation for the new gas geometry, the big gain of the emulation comes from the fact that it starts from the digitization stage

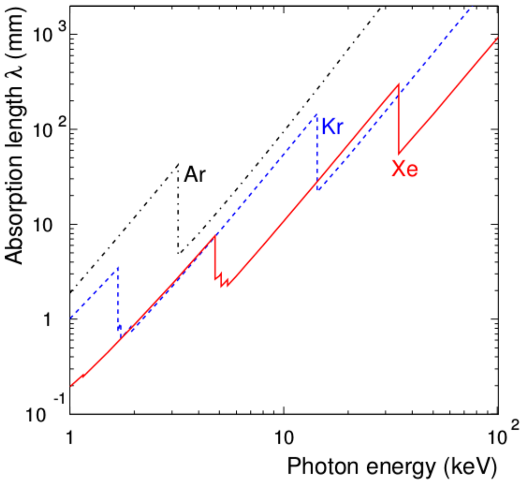

Figure 4.1: Absorption length of X-rays in noble gases in the relevant energy range of TR production.

of the ATLAS simulation which means skipping the generation and the simulation steps that require a lot of time and disk space to be accomplished.

4.2.2 ATLAS Simulation

In the ATLAS Experiment Simulation a number of steps need to be accomplished as shown in Figure 4.2. Starting from event generation with various generators (POWHEG, PYTHIA ...), then propagating the different particles through the different parts of the detector, the response of the detector to the particles is stored as a hits information, this information, are combined with estimates of internal noise and subjected to a parameterization of the known response of the detectors to produce simulated digital outputs (digits), the digits can be fed to the pattern recognition and track reconstruction as if they are real data in the reconstruction stage, finally from ESD files we can add or remove different information or objects depending on the need of each analysis [120].

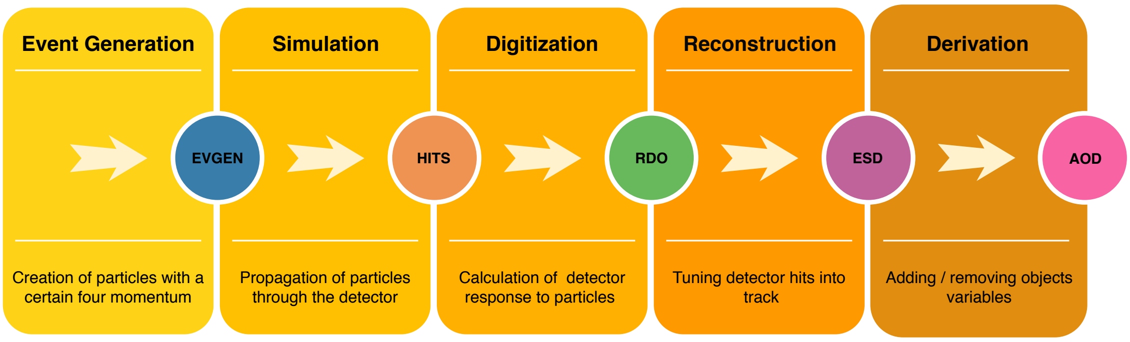

Figure 4.2: Descriptive scheme of the ATLAS Simulation chain.

4.2.3 TRT Digitization

The main task of the TRT digitization software is to generate a list of digits for each straw simulating the output of the read-out electronics of the real detector. The TRT digitization package is based on the energy deposits supplied by the simulation.The results of the simulation, in terms of a timed list of energy deposits, are propagated to the TRT digitization where they constitute the primary input. Using the known ionization potential, the content of the list is interpreted as clusters corresponding to a number of initial electrons at a given point in space and at a given time. The primary task of the digitization is to simulate the drift of these electrons to the anode wire, and to model the response of the front-end electronics to the signal thereby created [120].

4.2.4 Implementation and Tuning

To implement the emulation in the ATLAS simulation a new gas type definition is added to the database, in our case it's the emulated argon then, in the digitization stage of the ATLAS Simulation, we reduce the transition radiation by a reduction factor to pass from xenon to emulated argon, this is done in TRT_Digitization package. Figure 4.3 shows the difference between the argon and the xenon from the pHTmb level, this difference is what we try to quantify to pass from real xenon to emulated argon. Tuning emulation is done by producing an emulated sample (emulated argon) with a certain reduction factor then compare this sample to a control sample (real argon) using the pHTmb, eprob and ROC curves plots, different reduction factor as shown in Table 4.1 have been tested for emulating argon from xenon for barrel and end caps to ensure the best performance of emulation [121].

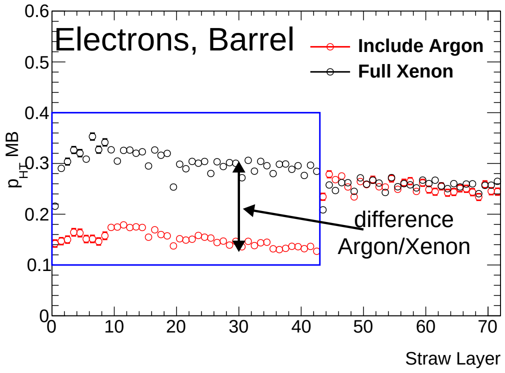

Figure 4.3: Difference between Xenon et Argon from the probability of the high threshold in the middle bit that is used to quantify the reduction factor to emulate the argon from xenon.

Barrel	0.05	0.06	0.07	0.08	0.09	0.10	0.11	0.12	0.13	0.14	0.15	0.16	0.18	0.20	1

End Caps	0.05	0.20	0.28	0.32	0.35	0.40	1

Table 4.1: The TRERF (Transition Radiation Efficiency Reduction Factor) that have been tested for emulating argon from xenon for Barrel and End Caps.

4.3 Results

The investigation of the performance of the emulation is carried out by two tools, the first one is the probability of the high threshold, and the second one is the electron probability, in this study we look at electrons and muons plots, the results are split to 3 parts, the first one for electrons, the second one for muons, and the last part is dedicated to the performance ROC curve that are built from the electron probability of electrons as a signal, and of muons as a background.

4.3.1 Samples and Cuts

For the production of the emulated samples two HITS files have been used :
Zee Stream : mc15_13TeV.361106.PowhegPythia8EvtGen_AZNLOCTEQ6L1_Zee.simul.HITS.e3601_s2874
Zmumu Stream : mc15_13TeV.361107.PowhegPythia8EvtGen_AZNLOCTEQ6L1_Zmumu.simul.HITS.e3601_s2874
both samples are simulated with full xenon geometry
For the validation two control samples simulated with the 2016 geometry Argon in Barrel (B0,B1) and in Endcaps (EA3,EA5,EC3,EC5,EC8) where used :
Zee Stream :
group.det-indet.361106.PowhegPythia8EvtGen_AZNLOCTEQ6L1_Zee.recon.TRTxAOD.e3601_s2876_r7886_trt098-00_EXT0
Zmumu Stream :
group.det-indet.361107.PowhegPythia8EvtGen_AZNLOCTEQ6L1_Zmumu.simul.TRTxAOD.e3601_s2876_r7886_trt095-02_EXT0
The TRT recommended analysis cuts have been used for this validation meanly for electrons and muons $pT > 10$ GeV and a track $pT_{trk} > 0.25 * pT$ to ensure that the tracks of electrons and muons passing with minimum pT still have a decent track pT we also require $|\eta| < 2.0$ and minimum 2 pixel hits and and 7 silicon hits and 15 TRT hits. All the plots presented are for the average number of interaction per bunch crossing $20 << \mu >< 23$.

4.3.2 Results for Electrons

The electron response to emulation was studied by comparing the HT probability, and the electron probability plots of the emulated produced samples (emulated argon) with the simulated sample (real argon), besides the visual comparison, a test of compatibility between the emulated and the control sample was carried out using the equation 4.1.

$$\chi = \frac{1}{n}\sum_{i=1}^{i=n}\frac{|Pemul_i - Pmc_i|}{Pmc_i}, \tag{4.1}$$

The equation compare for a given plot such as pHTmb versus straw layer or the electron probability the difference between the emulated sample labeled $Pemul$ and the control sample labeled Pmc bin per bin where n is the total number of bins and give the result for each TRERF, a minimum value of χ means a better agreement between the emulated and the control sample.
Figure 4.4 shows The pHTmb vs SL plots that are split to different regions of the detector, Barrel (a), End Cap A (b) and End Cap C (c), and also the results from pHTmb vs track η (d), the shown plots correspond to TRERF = 0.05 for Barrel and 0.20 for End Caps, these values were chosen after the production of many samples with different TRERF as shown in Table 4.1 and performing the test of compatibility.
Figure 4.5 shows the result of the compatibility test performed using the pHTmb vs SL plots for the three regions of the detector for different TRERF , in the barrel the plot points a minimum χ for TRERF = 0.05, and in the End Cap A and C the plots show a minimum χ for the TRERF = 0.20

The performance of the emulation is also studied using the electron probability which is mandatory for particle identification performance under the TRT. Figure

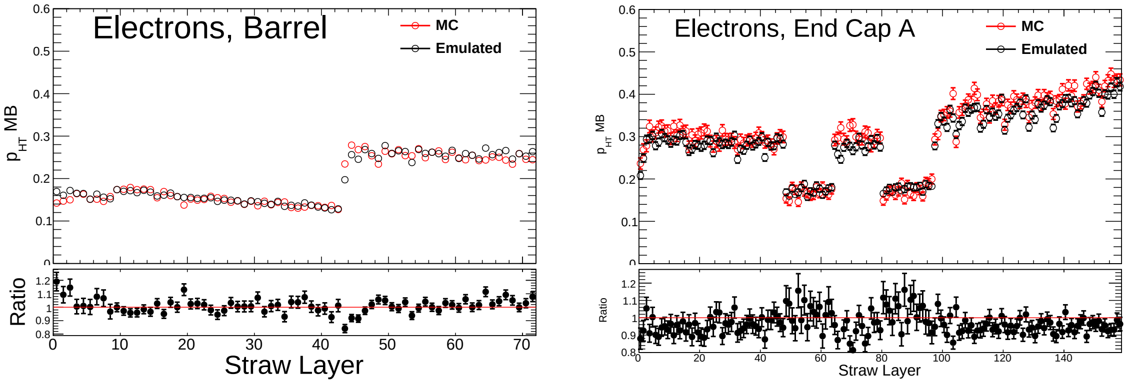

(a) Electron hits in the Barrel

(b) Electron hits in End-Cap A

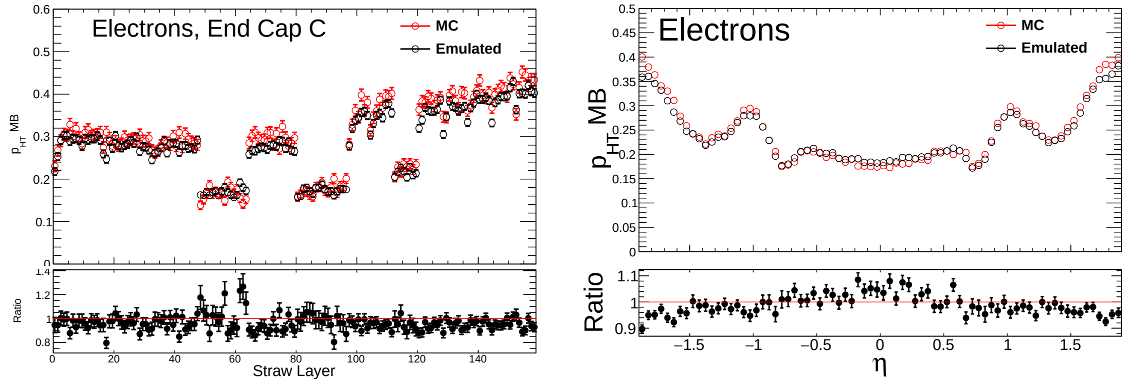

(c) Electron hits in End-Cap C

(d) Electrons η

Figure 4.4: HT probability versus straw layer for and track η distributions from electron tracks for both the produced emulated sample and the control full simulated sample with the 2016 geometry .

4.6 show the comparison of the electron probability of the emulated produced sample and the control full simulated sample for track in Barrel , End Cap A and End Cap C. The electron probability plots for the emulated samples with TRERF = 0.05 for Barrel and 0.20 for the End Cap show a good agreement with the control samples which confirm the result obtained from the pHTmb plots and the compatibility test.

4.3.3 Results for Muons

As for electrons the performance of emulation was studied using HT probability and electron probability of muons, except for this time we also used a muon momentum cut of 50 GeV to remove the Transition Radiation photons, the test of the compatibility was also done using the HT probability vs SL plots. Figure 4.7 shows the result of the comparison between the HT probability of muons hit in different regions of the TRT vs SL and track eta for the emulated and the full simulated samples, Figure 4.8 shows the electron probability of muons for the emulated and the full simulated sample in different region of the TRT, form these plots we can clearly see that the agreement between the emulated sample and the control sample for muons is less than the electrons, Figure 4.9 show the result of the compatibility test performed using the HT probability vs SL plots for different regions of the TRT, the three plots show that agreement isn't controlled by the TRERF factor as for the electrons, we also performed the production using a tag that preserve the emulation only for

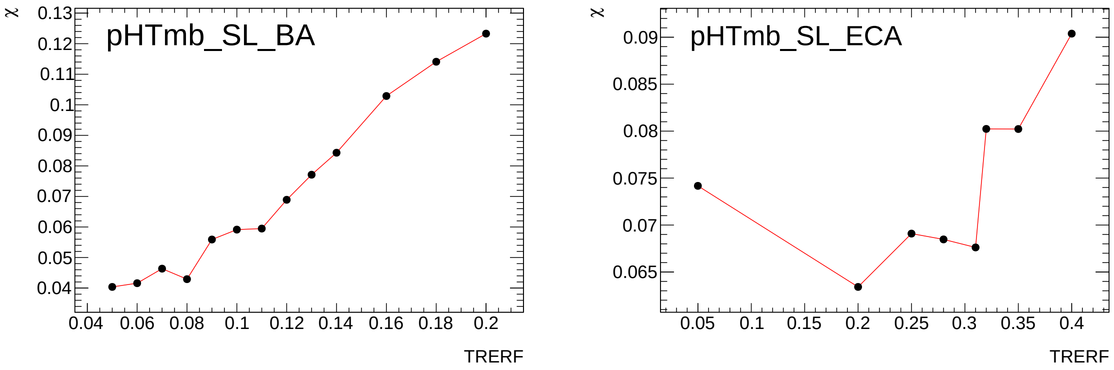

(a) TRERF vs χ for Barrel

(b) TRERF vs χ for End-Cap A

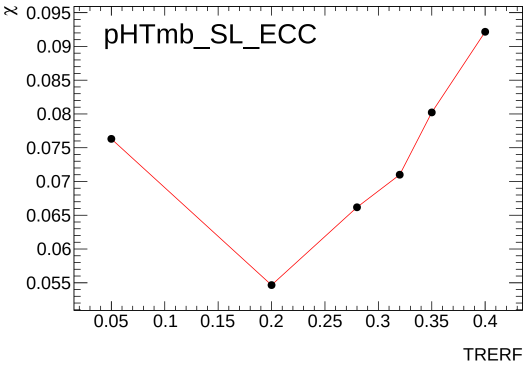

(c) TRERF vs χ for End-Cap C

Figure 4.5: Result of test of compatibility from pHTmb plot with corresponding TRERF for Barrel,End Cap A and End Cap C.

electrons but these result where not affected, then we conclude that the muons aren't responding to emulation in a sensitive way because they are heavier particles with less transition radiation production when crossing the TRT straws and also due to the muons momentum cut applied.

4.3.4 Results from ROC curves

In statistics a Receiver Operating Characteristic (ROC) Curve is a way to compare diagnostic tests. It is a plot of the true positive rate against the false positive rate. In the TRT PID we use the electron probability of electrons as signal (true rate) and the electron probability of muons as a background (false rate) to draw the ROC curves that describe the performance of the TRT PID. Figure 4.10 shows the ROC curves plotted from the electron probability in different TRT region from tracks in all occupancies, these plots show a good agreement between the emulated sample and the control sample as expected from the results of the electron probability sections 4.3.2 and 4.3.3.

4.4 Results from only straws filled with argon

The validation of the emulation results has also been done for only straws filled with argon, using the pHTmb vs SL plots, the layers filled with argon in the 2016

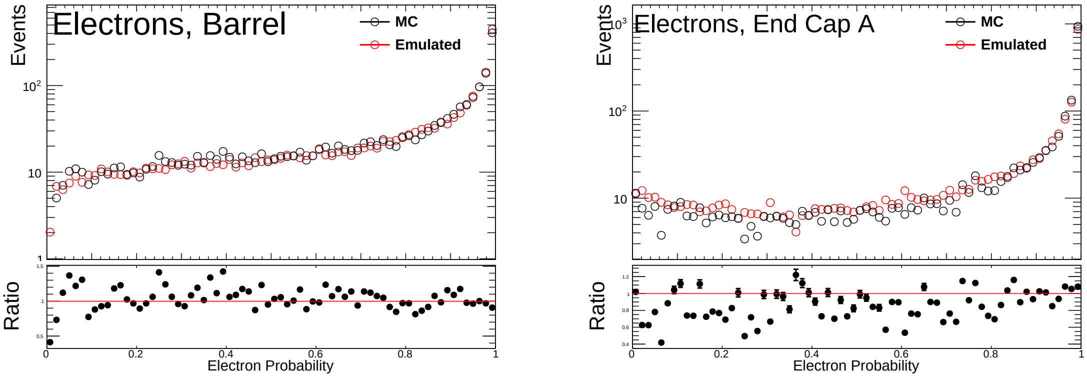

(a) Electron probability for electrons in Barrel

(b) Electron probability for electrons in End-Cap A

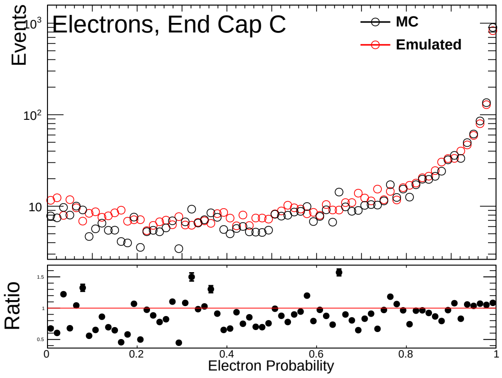

(c) Electron probability for electrons in End-Cap C

Figure 4.6: Electron probability for electrons for differnt regions of TRT.

geometry are : layer 0 and 1 from barrel and layer 3 and 5 from the End Cap A and layer 3,5 and 8 from the End Cap C, Figure 4.11 shows the results for different layers for electrons and Figure 4.12 shows the same results for muons, these plots give us a more precise look to the good agreement observed between the emulated and the control sample.

4.5 Results for $< \mu >$ range between 40 and 45

The validation was performed also for high $< \mu >$ range to check if the high occupancy affects the emulation performance, as in in the section 4.3 the result from pHTmb, electron probability for electrons and muons and the performance ROC curves are plotted in this section. All the plots produced for $20 << \mu >< 23$ were reproduced for $40 << \mu >< 45$ to check the performance of the emulation at high $< \mu >$ the result of pHTmb vs SL and eta for electrons are plotted in Figure 4.13 and in Figure 4.14 for only the straws filled with argon, Figure 4.15 and Figure 4.16 show the same results for muons.Figure 4.17 show the performance ROC curves for different regions of the detector for all occupancies. All the results are in agreement with the result for low $< \mu >$ range , this confirms that the emulation is performing well in high occupancy.

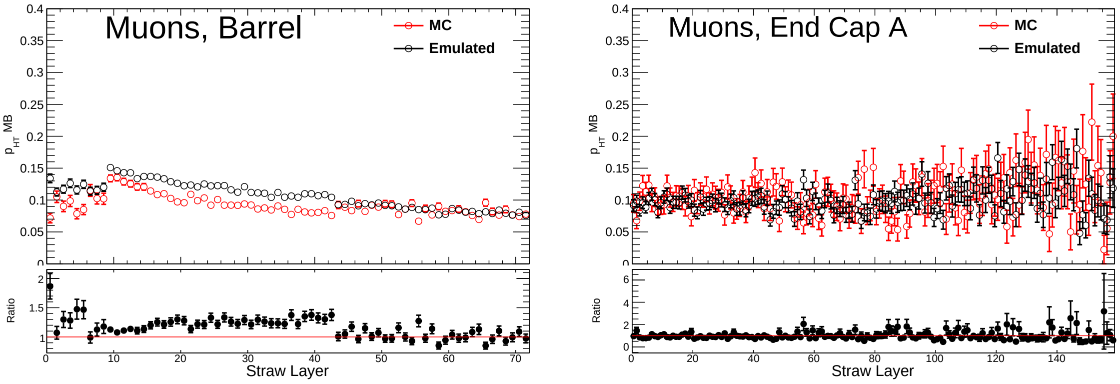

(a) Muon hits in the Barrel (b) Muon hits in End-Cap A

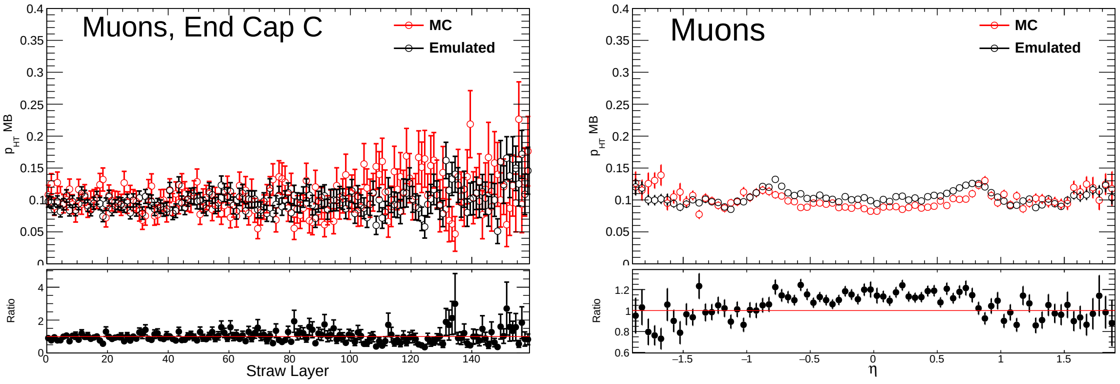

(c) Muon hits in End-Cap C (d) Muons η

Figure 4.7: HT probability versus straw layer for and track η distributions from muon tracks for both the produced emulated sample and the control full simulated sample with the 2016 geometry.

Conclusion

In this chapter the use and the performance of the emulation have been presented, the emulation is a possible solution to accommodate changes in the gas geometry of the ATLAS Transition Radiation Tracker, since it starts from the digitization step. This method will for sure help to save time and disk space within the ATLAS Simulation, since the gas geometry change from xenon to argon does not affect the tracking capabilities of the detector, emulation performance was studied using only the TRT PID observables such as the HT probability and the electron probability, a compatibility test was done to choose the best reduction factor to use to emulate argon from xenon (0.05 for Barrel and 0.20 for End Caps), these reduction factors are implemented in the TRT_Digitization stage, the performance was also studied using the comparison of the ROC curves built from the electron probability of electrons and muons, all the results show that the emulation is a method that we can trust and use with respect to the TRT PID observables. A second study concerning the PID performance in run3 was performed within the TRT group and its documented in Appendix A.

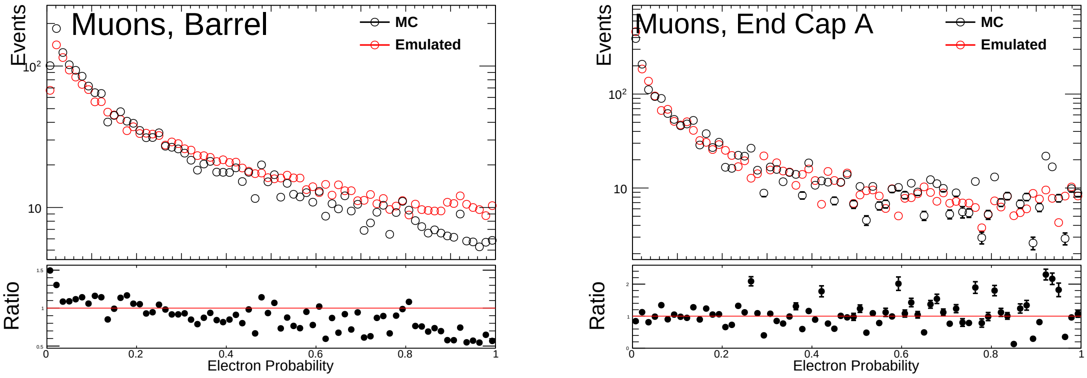

(a) Electron probability for muons in Barrel

(b) Electron probability for muons in End-Cap A

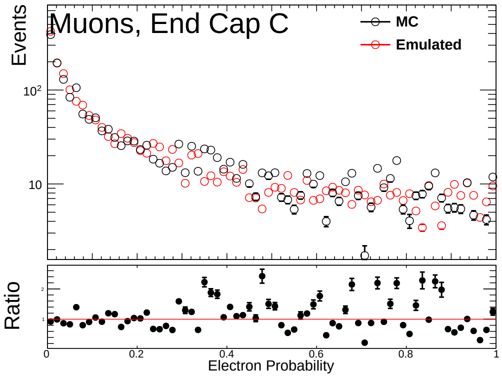

(c) Electron probability for muons in End-Cap C

Figure 4.8: Electron probability for muons in different region of the TRT.

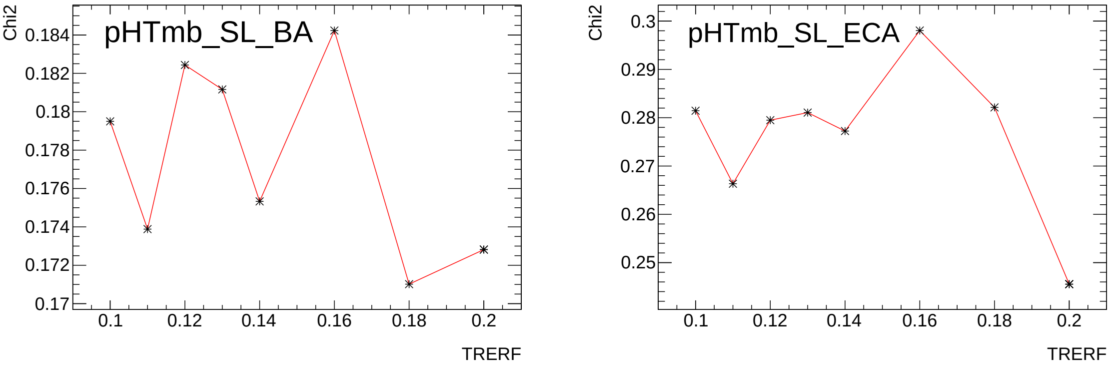

(a) TRERF vs χ for Barrel

(b) TRERF vs χ for End-Cap A

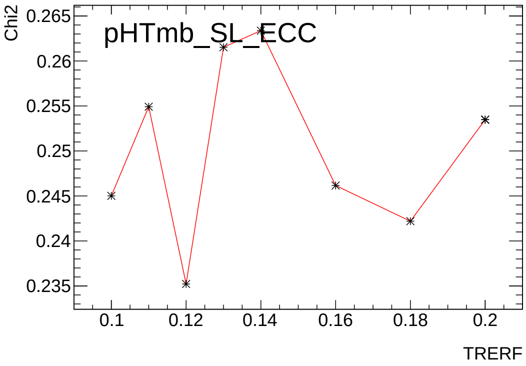

(c) TRERF vs χ for End-Cap C

Figure 4.9: Result of test of compatibility from pHTmb plot of muons with corresponding TRERF for Barrel,End Cap A and End Cap C.

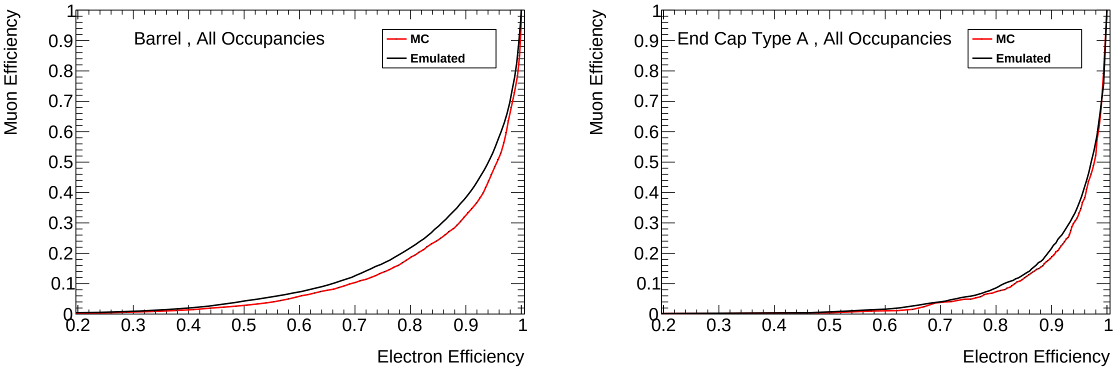

(a) Barrel All occupancies

(b) End-Cap A All occupancies

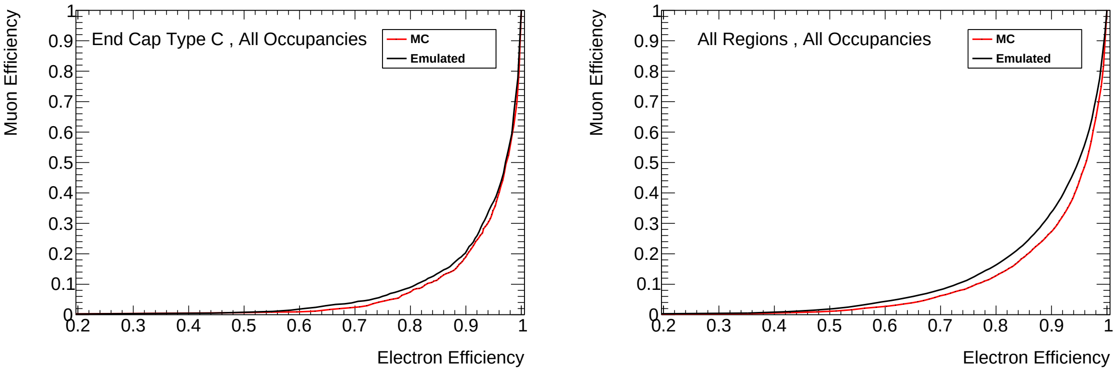

(c) End-Cap C All occupancies

(d) All regions, All occupancies

Figure 4.10: performance curves from full simulated sample and emulated samples generated from all occupancies tracks at different regions of the detector.

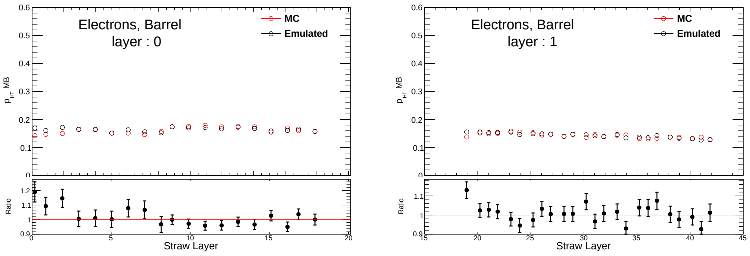

(a) Electron hits in the Layer 0 of the Barrel

(b) Electron hits in Layer 1 of the Barrel

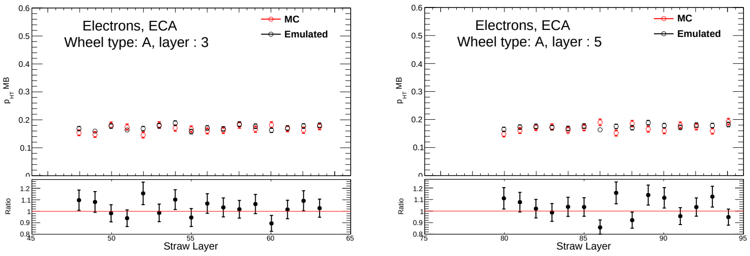

(c) Electron hits in layer 3 of End-Cap A

(d) Electron hits in layer 5 of End-Cap A

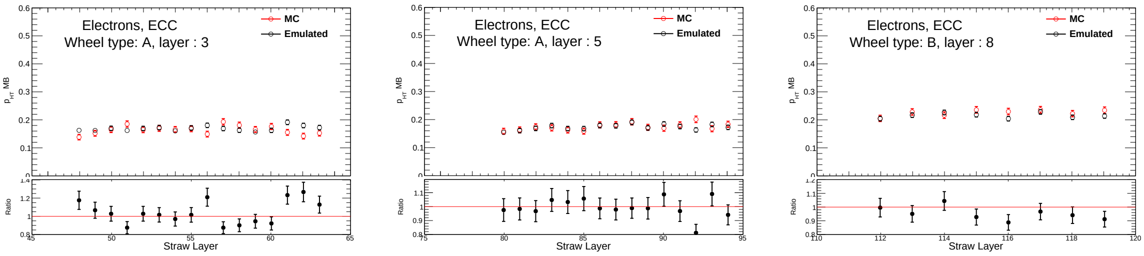

(e) Electron hits in in layer 3 of ECC

(f) Electron hits in in layer 3 of ECC

(g) Electron hits in in layer 8 of ECC

Figure 4.11: HT probability versus straw layer distributions from electron tracks for both full simulation and emulated sample for only layer filled with argon in the 2016 geometry .

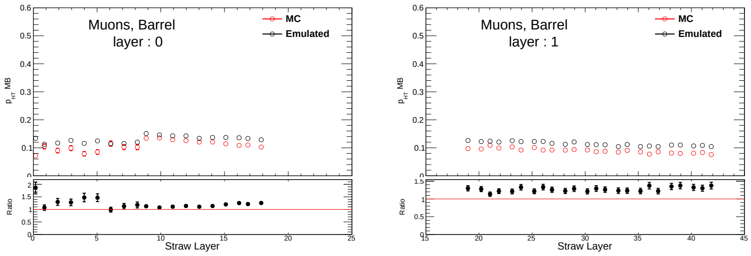

(a) Muon hits in Layer 0 of the Barrel (b) Muon hits in Layer 1 of the Barrel

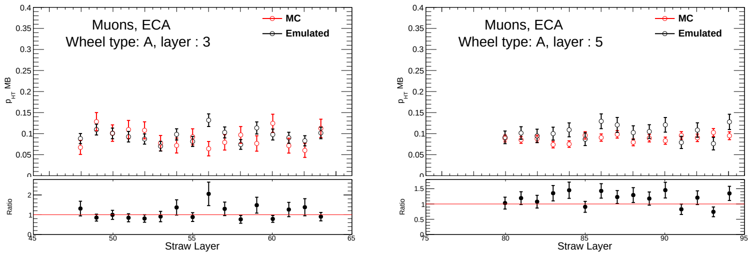

(c) Muon hits in layer 3 End-Cap A (d) Muon hits in layer 5 End-Cap A

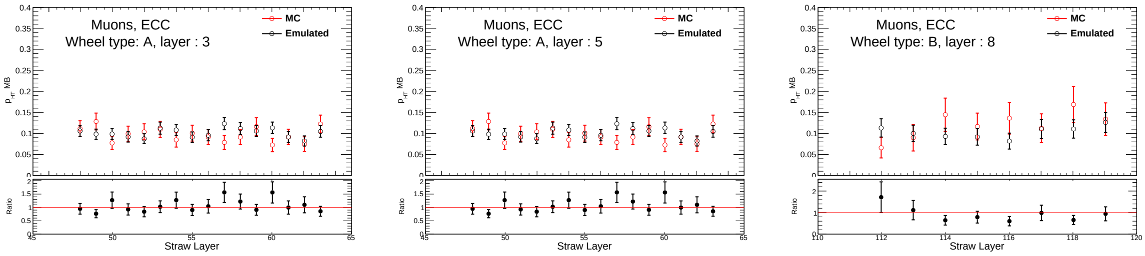

(e) Muon hits in Layer 3 ECC (f) Muon hits in Layer 5 ECC (g) Muon hits in Layer 8 ECC

Figure 4.12: HT probability versus straw layer distributions from muon tracks for both full simulation and emulated sample for only layer filled with argon in the 2016 geometry.

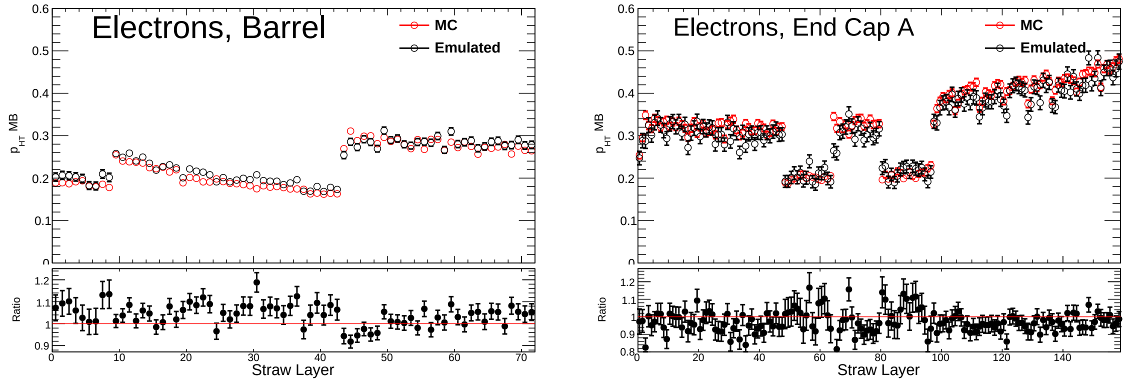

(a) Electron hits in the Barrel

(b) Electron hits in End-Cap A

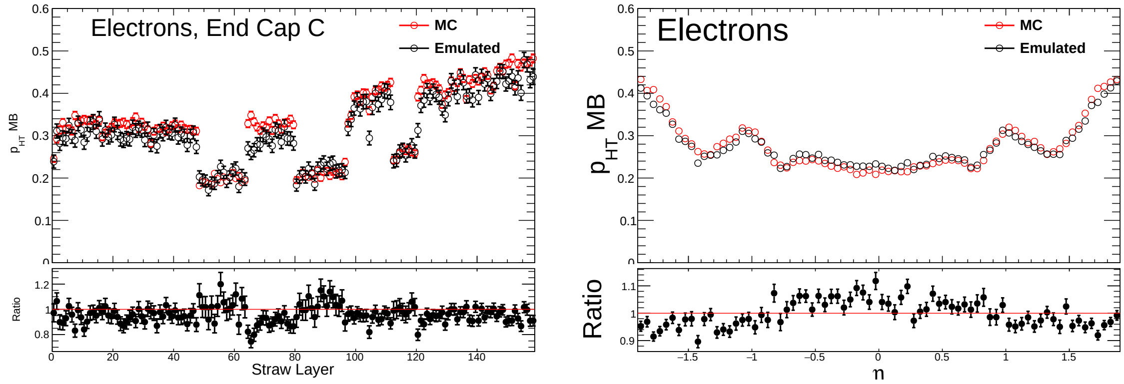

(c) Electron hits in End-Cap C

(d) Electrons η

Figure 4.13: HT probability versus straw layer and track η distributions from electron tracks for both full simulation of the 2015 geometry (with real argon, labeled “Baseline”) and emulated 2015 geometry.

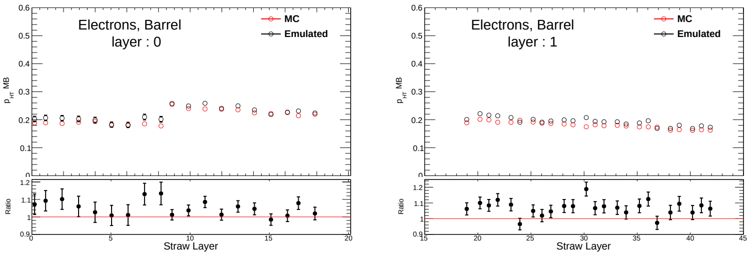

(a) Electron hits in the Layer 0 of the Barrel (b) Electron hits in Layer 1 of the Barrel

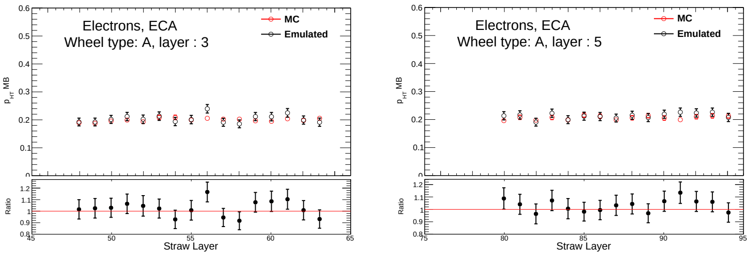

(c) Electron hits in layer 3 of End-Cap A (d) Electron hits in layer 5 of End-Cap A

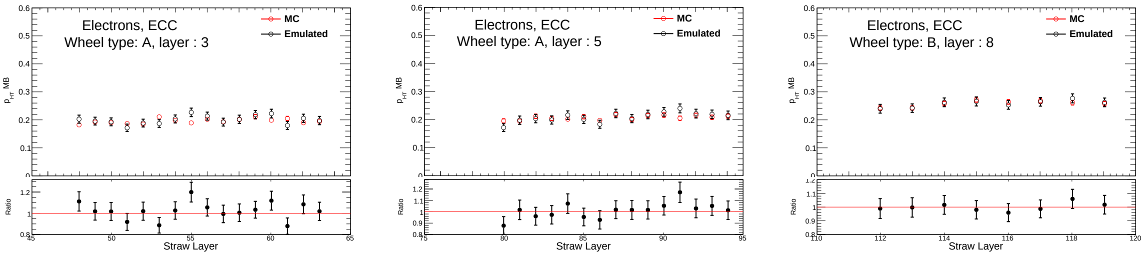

(e) Electron hits in in layer 3 of ECC (f) Electron hits in in layer 3 of ECC (g) Electron hits in in layer 8 of ECC

Figure 4.14: HT probability versus straw layer distributions from electron tracks for both full simulation and emulated sample for only layer filled with argon in the 2016 geometry .

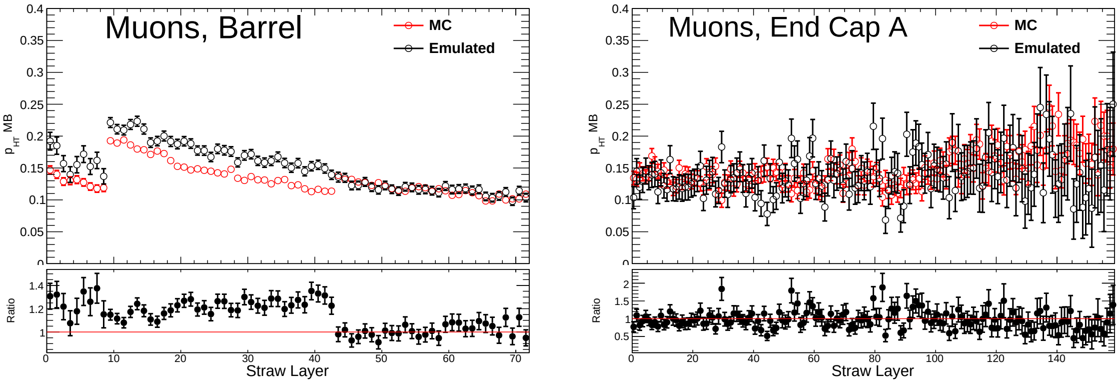

(a) Muon hits in the Barrel

(b) Muon hits in End-Cap A

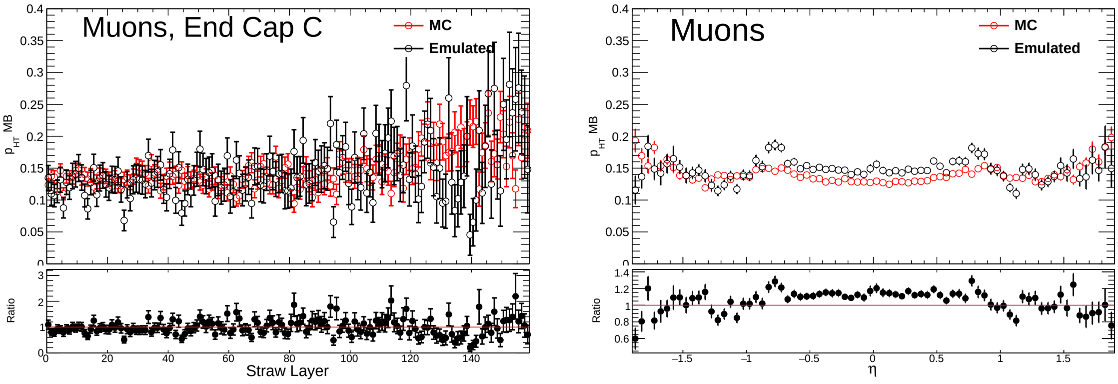

(c) Muon hits in End-Cap C

(d) Muons η

Figure 4.15: Height Threshold probability versus straw layer and track η distributions from muon tracks.

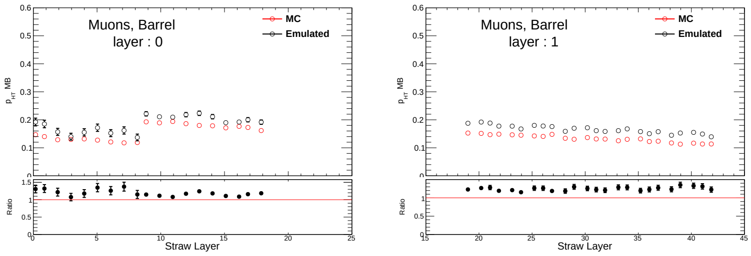

(a) Muon hits in Layer 0 of the Barrel (b) Muon hits in Layer 1 of the Barrel

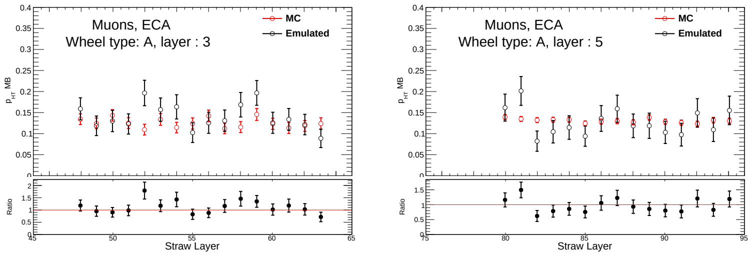

(c) Muon hits in layer 3 End-Cap A (d) Muon hits in layer 5 End-Cap A

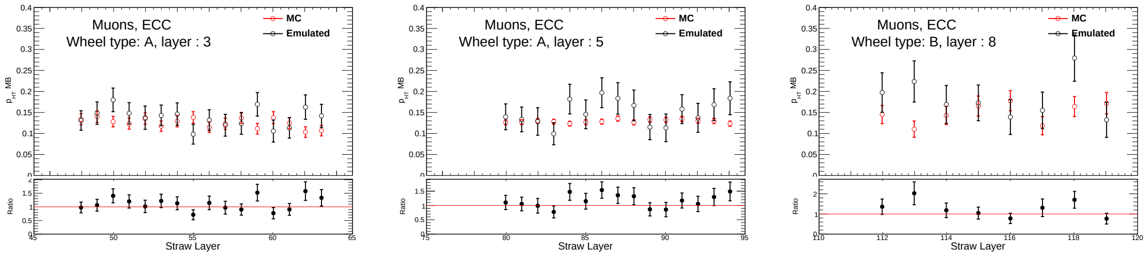

(e) Muon hits in Layer 3 ECC (f) Muon hits in Layer 5 ECC (g) Muon hits in Layer 8 ECC

Figure 4.16: HT probability versus straw layer distributions from muon tracks for both full simulation and emulated sample for only layer filled with argon in the 2016 geometry.

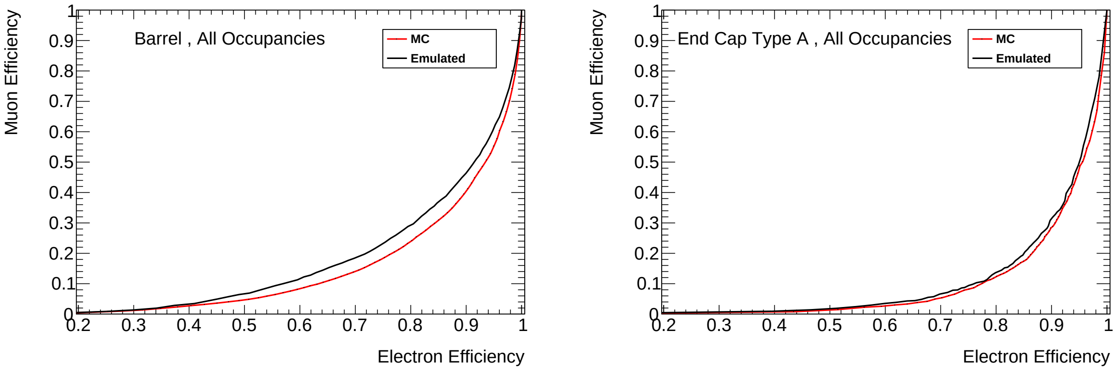

(a) Barrel All occupancies

(b) End-Cap A All occupancies

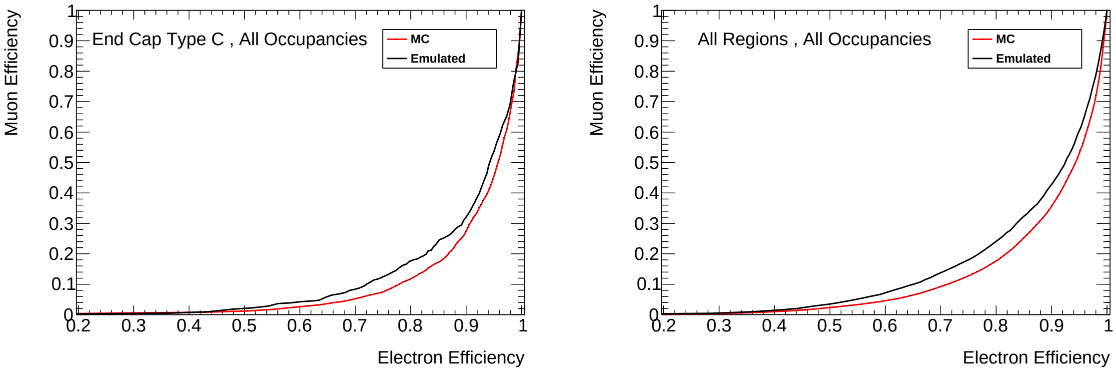

(c) End-Cap C All occupancies

(d) All regions, All occupancies

Figure 4.17: performance curves from full simulation and emulation samples generated from all occupancies tracks at different regions of the detector.

Chapter 5

Observation of light-by-light scattering in heavy-ion collisions with the ATLAS detector at the LHC

Contents

Introduction

In this analysis, the final-state signature of interest is the exclusive production of two photons, $\mathrm{Pb+Pb}\,(\gamma\gamma) \rightarrow \mathrm{Pb}^{(*)}\mathrm{+Pb}^{(*)}\,\gamma\gamma$ as shown in Figure 5.1 where the diphoton final-state is measured in the central detector, and the incoming Pb ions survive the EM interaction, with a possible EM excitation [122], denoted by (*). Hence, it is expected to detect two low-energy photons and no further activity in the detector, in particular no reconstructed charged-particle tracks originating from the Pb+Pb interaction point.

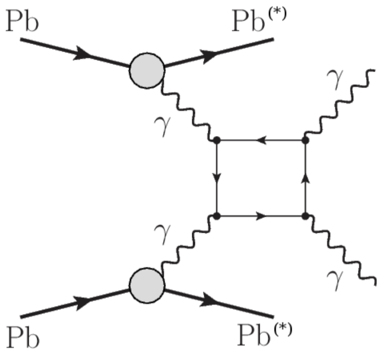

Figure 5.1: Schematic diagram of light-by-light scattering in UPC Pb+Pb collisions. A potential electromagnetic excitation of the outgoing Pb ions is denotes by (*).

5.1 Analysis strategy

In this analysis the same strategy followed in [71] is used and the analysis is carried out with 2018 data for fiducial cross section measurement and significance calculation and with combined 2018 and 2015 data for fiducial and differential cross section measurement and search for ALPs production

5.2 Data and Monte Carlo samples

5.2.1 Data

The data used in this analysis is from Pb+Pb collisions with a centre-of-mass energy of $\sqrt{s_{\mathrm{NN}}} = 5.02$ TeV, recorded in the 2015 and 2018 HI run at the LHC. Table 5.1 shows number of runs in each year , the integrated luminosity and the GRL used in each data set. The 2018 data set corresponds to an integrated luminosity of 1.7 nb^{-1} of Pb+Pb data, with an uncertainty of 4.1% while the 2015 data corrspond to 0.48 nb^{-1} with an uncertainty of 6% which make a total of 2.2 nb^{-1} with a total uncertainty of 3.2%. The 2015 data was reprocessed in release 21 of athena [111] software to make it compatible to combine it with the 2018 data.

Run numbers	Year (Integrated Luminosity)	GRL used
00286711, 00286717, 00286748, 00286767, 00286834, 00286854, 00286908, 00286967, 00286990, 00286995, 00287038, 00287044, 00287068, 00287222, 00287224, 00287259, 00287270, 00287281, 00287321, 00287330, 00287334, 00287378, 00287380, 00287382, 00287560, 00287594, 00287632, 00287706, 00287728, 00287827, 00287843, 00287866, 00287924, 00287931.	2015	data15_hi.periodAllYear_DetStatus-v105-pro22-13_Unknown_PHYS_HeavyIonP_All_Good.xml
00365602, 00365678, 00365681, 00365709, 00365752, 00365834, 00365914, 00365932, 00366011, 00366029, 00366092, 00366337, 00366383, 00366476, 00366526, 00366627, 00366805, 00366878, 00366994, 00367134, 00367165, 00367170, 00365498, 00365502, 00365512, 00365573, 00365627, 00366142, 00366268, 00366413, 00366528, 00366691, 00366754, 00366860, 00366919, 00366931, 00367023, 00367099, 00367233. 00367273, 00367318, 00367321, 00367363, 00367364, 00367365, 00367384.	2018	data18_hi.periodAllYear_DetStatus-v106-pro22-14_Unknown_PHYS_HeavyIonP_All_Good_ignore_TOROIDSTATUS.xml

Table 5.1: 2015 and 2018 Pb+Pb stable beam runs .

5.2.2 Monte Carlo samples

The samples used in this study are described in the following subsections and they all make use of a GEANT4 [112] based detector simulation [123]. The simulated events are reconstructed with the standard ATLAS reconstruction software. Details on each samples are shown in Table 5.2.

5.2.2.1 Signal

LbyL signal LbyL signal events are generated using SuperChic v3.0 [124]. They take into account box diagrams with leptons and quarks , and $W^{\pm}$ boson (such as the diagram in Fig. 5.1) . Alternatively, another LbyL signal sample is generated using calculations from Ref. [125]. In this case contributions from W-boson loops are omitted since they are only important for diphoton masses $m_{\gamma\gamma} > 2m_W$. These calculations are then folded with the Pb+Pb photon flux from the Starlight 2.0 Monte Carlo (MC) generator [126]. The theoretical uncertainty on the cross section is mainly due to limited knowledge of the nuclear (EM) form-factors and the related initial photon fluxes. This is extensively studied in Ref. [127] and the relevant uncertainty is estimated to be 10% within a fiducial phase space of the measurement. Higher-order corrections (not included in the calculations) are also part of the theoretical uncertainty and are of the order $1-3\%$ in the corresponding invariant mass range [128, 129].

5.2.2.2 Backgrounds

The major contribution to the background comes from the central exclusive production (CEP) ($gg \to \gamma\gamma$) process, followed by the ($\gamma\gamma \to e^+e^-$) and ($\gamma\gamma \to q\bar{q}$) processes.

CEP $gg \to \gamma\gamma$ the exclusive diphoton final state can be also produced via the strong interaction through a quark loop in the exchange of two gluons in a colour-singlet state. This CEP process, $gg \to \gamma\gamma$, is modelled using SuperChic v3.0.

$\gamma\gamma \to e^+e^-$ the $\gamma\gamma \to e^+e^-$ background contribution is modelled with the Starlight 2.0 MC generator [126], in which the cross section is computed by combining the Pb+Pb photon flux with the leading-order formula for $\gamma\gamma \to e^+e^-$.

$\gamma\gamma \to q\bar{q}$ Two-photon production of quark–antiquark pairs is estimated using HERWIG++ 2.7.1 [130] where the pp photon fluxes are implemented. The sample is then normalised to cover the differences in equivalent photon fluxes between the Pb+Pb and pp cases.

Process	Number of event	Generator
LbyL Signal	100k	SuperChic v3.0 [124]
Alternative LbyL	100k	STARLIGHT [126]
$\gamma\gamma \to e^+e^-$ ($3.6 < M_{\text{inv}} < 8$ GeV)	1.5 M	STARLIGHT [126]
$\gamma\gamma \to e^+e^-$ ($M_{\text{inv}} > 8$ GeV)	0.5 M	STARLIGHT [126]
CEP	100k	SuperChic v3.0 [124]
$\gamma\gamma \to q\bar{q}$	100k	Herwig++ 2.7.1 [131]
ALPs	10k per mass	STARLIGHT [126]

Table 5.2: MC samples and number of event used in the analysis.

5.3 Event selection

This section describes all the criteria that applied to the events to satisfy the light by light signal region. Figure 5.2 shows a typical cut-flow of this analysis.

5.3.1 GRL

Dedidacted GRL list have ben used in this analysis one for the 2015 data and another for the 2018 data. Concerning the latter and given the data taking conditions a

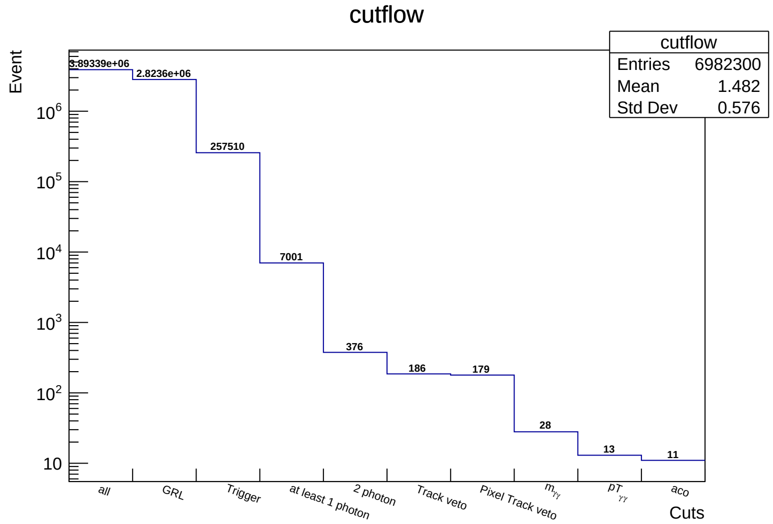

Figure 5.2: A typical cut-flow from the 2015 data. Details of the cuts are given in the text.

dedicated study have been performed to decide the GRL to use. The study is described bellow. subsectionStudies of toroid-off data

During the 2018 heavy ions run period, the ATLAS Toroid magnets system was down for the last 7 runs, from run 367273 till run 367384, while the Toroid system was on during the first 39 runs, from run 365498 till run 367233 as shown in Table 5.3. Therefore, it is important to verify if the period of Toroid off does not affect the results of the analysis presented in this work, which makes use of the full statistics accumulated. In practice, we check whether the exclusive e^+e^- selection is affected by this detector effect or not. We prove that the effect is negligible by comparing event numbers and several observables relevant for the e^+e^- exclusive selection with toroid on and off. We have realized run by run comparisons using runs with similar luminosities. First, we have considered the run 367023 (Toroid on) and a luminosity of 64.9 μb^{-1} with the run 367321 (Toroid off) and a luminosity of 65.6 μb^{-1}. As both runs have similar luminosities, we expect that both runs lead to similar event numbers after the exclusive e^+e^- selection. For the selection, we follow the standard requirements of the exclusive di-lepton analysis described in the analysis: we consider

Toroid on runs	Toroid off runs
00365602, 00365678, 00365681, 00365709, 00365752, 00365834, 00365914, 00365932, 00366011, 00366029, 00366092, 00366337, 00366383, 00366476, 00366526, 00366627, 00366805, 00366878, 00366994, 00367134, 00367165, 00367170, 00365498, 00365502, 00365512, 00365573, 00365627, 00366142, 00366268, 00366413, 00366528, 00366691, 00366754, 00366860, 00366919, 00366931, 00367023, 00367099, 00367233.	00367273, 00367318, 00367321, 00367363, 00367364, 00367365, 00367384.

Table 5.3: 2018 Pb+Pb stable beam runs .

2 loose electrons with $p_T > 2.5$ GeV and 2 tracks. Results are presented in Fig. 5.3 where the transverse momentum of the final state e^+e^- system is shown, as well as the sum of the transverse momentum of each leptons. We observe that shapes of the distributions are similar and that the number of events are close: 1248 events for run 367321 to be compared to 1263 events for run 367023. Then, we can conclude that the Toroid off effect is negligible.

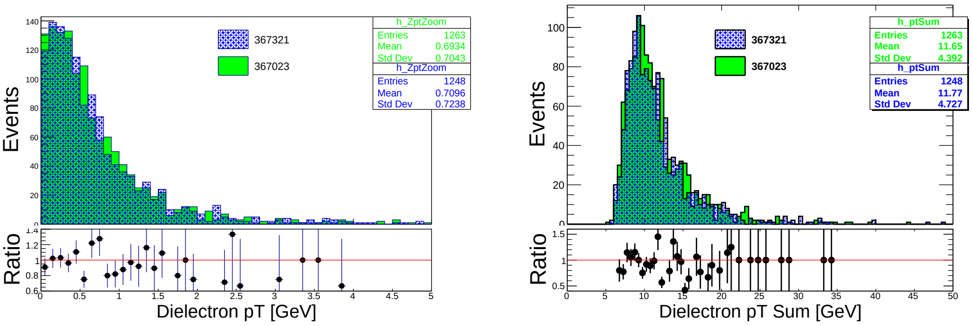

Figure 5.3: Transverse momentum of the final state e^+e^- system (left). Sum of the transverse momentum for each lepton (right). We superimpose the results obtained for the run with Toroid on and the run with Toroid off (see text).

We have repeated the procedure for another run with Toroid on, the run 366860, corresponding to a luminosity of 65.3 μb^{-1}, very close to the value for the run with Toroid off (run 367321). Comparisons are presented in Fig. 5.4, which prove also that the effect of the Toroid off condition is negligible.

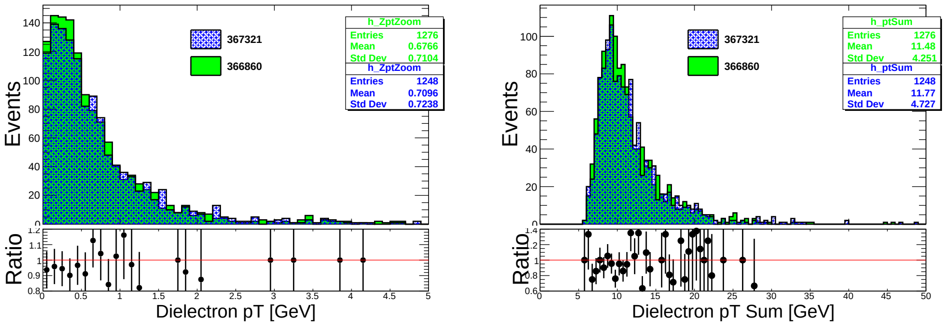

Figure 5.4: Transverse momentum of the final state e^+e^- system (left). Sum of the transverse momentum for each lepton (right). We superimpose the results obtained for the run with Toroid on and the run with Toroid off (see text).

In order to test potential effect on the shapes of the distributions presented above that we would not notice with only one run, we have made the comparison for the full period of Toroid on with the full period with Toroid off, normalized to the number of events. Results are presented in Figure 5.5. No effect is observable, which confirms that the Toroid off condition is of no importance for the analysis presented in this work.

Of course, if we select specifically muons, we expect some differences between the 2 periods as shown in Figure 5.6.

This study endorsed the decision to use the 2018 GRL list that ignore the toroid condition as shown in table

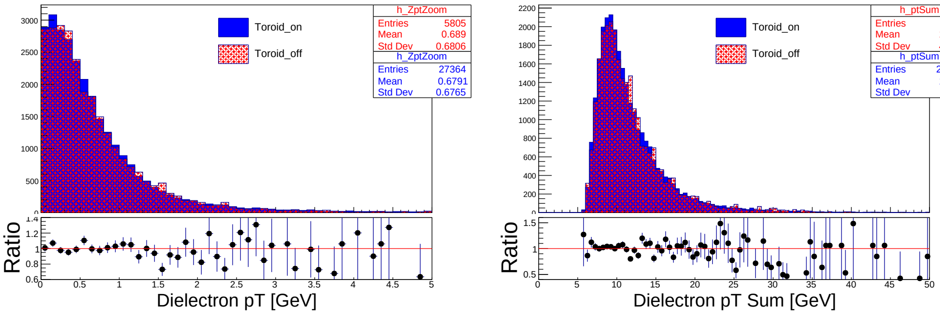

Figure 5.5: Transverse momentum of the final state e^+e^- system (left). Sum of the transverse momentum for each lepton (right) The results for all runs with Torioid off are compared to all runs with Toroid on.

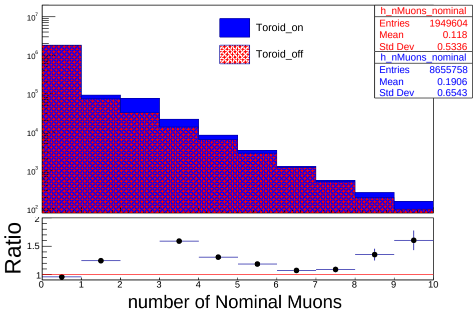

Figure 5.6: Number of muons reconstructed for the full period with Toroid on compared to the full period with Toroid off.

5.3.2 Event cleaning

Additional cleaning is applied to the remaining events to discard corrupted events and ensure that candidate's informations are completely measured by the whole ATLAS sub-detectors. The different sources of bad event measurements are described as follow:
Tile calorimeter corrupted events: since run-I TileCal has suffered from the photomultiplier tubes (PMTs) that are not properly powered in some consecutive trip modules. In case of one unpowered module, trips issue is signed as tolerable defect by the data quality group and the events are recovered by extrapolating information from its neighbouring modules. On the other hand, if the problem exists in several consecutive modules, the issue is signed-off as intolerable defect and the events are rejected [132].
LAr calorimeter's noise bursts: The LAr calorimeter is affected by the large noise bursts due to the high instantaneous luminosity delivered by the LHC. This noise is observed for a short time of about $0.5s$ with about 90% found to be less than $5\mu s$ This issue is treated by applying a time-window veto [115] procedures. Once the noise burst is identified data in a time window ($1\ ms$) around the burst is vetoed. In case of many noise events the entire LB is rejected [133].
Semiconductor Tracker corrupted events: The high energetic particles that pass through the SCT's junction creates electron-hole pairs by interacting with the

atom of silicon. Some of those pairs are recombined forming a short current pulse leading to soft errors called single event upset (SEU) [134] producing a bit flip where data with 1 bit becoming 0 bit or vice versa in the memory. To mitigate this defect the data quality group reset the event counters automatically once the error is detected in a SCT module. In this analysis, the affected candidates by single event upsets are rejected.

5.3.3 Trigger

The trigger strategy is different between 2015 and 2018 data

2015 data

For 2015, the trigger configuration was:

- `HLT_gg_upc_L1TE5_VTE200`

and it is based on the following requirements:

- A Level-1 seed requires total E_{T} between 5 and 200 GeV in the entire calorimeter,
- MBTS veto, i.e. maximum one hit in the inner ring of the MBTS detector,
- Low activity in the ID, defined by a maximum number of 10 hits in the Pixel Detector (imposed in `hi_gg_upc`).

2018 data

Candidate diphoton events were recorded in the Pb+Pb run in 2018 using a dedicated trigger for events with moderate activity in the calorimeter but little additional activity in the entire detector. The primary trigger for low-E_{T} diphoton events uses a logical OR of two dedicated triggers having different Level-1 seeds and the same HLT selection. These two triggers are:

- `HLT_hi_upc_FgapAC3_hi_gg_upc_L1TAU1_TE4_VTE200`
- `HLT_hi_upc_FgapAC3_hi_gg_upc_L12TAU1_VTE50`.

They include three sets of requirements:

- A Level-1 seed is one of the following:
  - `L1_TAU1_TE4_VTE200`, requiring coincidence of minimum one EM cluster of $E_{\mathrm{T}} > 1$ GeV and total E_{T} between 4 and 200 GeV in the entire calorimeter,
  - `L1_2TAU1_VTE50`, requiring at least 2 EM clusters of $E_{\mathrm{T}} > 1$ GeV and total E_{T} in the entire calorimeter below 50 GeV,
- FCal veto, i.e. rejection of events with $\Sigma E_T^{\mathrm{FCal}} > 3$ GeV on any side of FCal (imposed in `hi_upc_FgapAC3`),
- Low activity in the ID, defined by a maximum number of 15 hits in the Pixel Detector (imposed in `hi_gg_upc`).

5.3.4 Photon reconstruction

Photons are reconstructed from EM clusters in the calorimeter and tracking information provided by the ID, which allows the identification of photon conversions [135]. Selection requirements are applied to remove EM clusters with a large amount of energy from poorly functioning calorimeter cells, and a timing requirement is made to reject out-of-time candidates. An energy calibration specifically optimised for photons [136] is applied to the candidates to account for upstream energy loss and both lateral and longitudinal shower leakage. A dedicated correction [135] is applied for photons in MC samples to correct for potential mismodelling of quantities which describe the properties of the associated EM showers.

5.3.5 Photon particle-identification

The photon particle-identification (PID) in this analysis is based on several shower-shape variables, which are summarized in Table 5.4. Only photons with $E_{\mathrm{T}} > 2.5$ GeV and $|\eta| < 2.37$, excluding the calorimeter transition region $1.37 < |\eta| < 1.52$, are considered. The pseudorapidity requirement ensures that the photon candidates pass through regions of the EM calorimeter where the first layer is segmented into narrow strips, allowing for good separation between genuine prompt photons and photons coming from the decay of neutral hadrons. A constant photon PID efficiency of 95% as a function of η with respect to reconstructed photon candidates is maintained. The identification is based on a neural network trained on background photons extracted from data and photons from the signal MC. The PID allows for a rejection of EM energy clusters induced by the calorimeter noise and cosmic-ray muons with 95% efficiency.

Variable name	Definition
$w_{\eta 2}$	Lateral width of the shower in the second layer of the EM calorimeter
E_{ratio}	Ratio of the energy difference associated with the largest and second largest energy deposits to the sum of these energies in the first layer
f_1	Fraction of energy reconstructed in the first layer with respect to the total energy of the cluster
R_η	Ratio of the energy in3×7 $\eta \times \phi$ cells over the energy in 7×7 cells centered around the photon cluster position
R_{had1}	Ratio of E_{T} in the first layer of the hadronic calorimeter to E_{T} of the EM cluster
R_{had}	Ratio of E_{T} in the hadronic calorimeter to E_{T} of the EM cluster

Table 5.4: Definition of shower-shape variables which are used to define photon PID requirements.

5.3.6 Final selection

Preselected events are required to have exactly two photons satisfying the above selection criteria, with a diphoton invariant mass greater than 5 GeV. In order to suppress the $\gamma\gamma \to e^+e^-$ background, a veto on charged-particle tracks (with $p_{\mathrm{T}} > 100$ MeV, $|\eta| < 2.5$, at least one hit in the Pixel detector and at least six silicon hits in total) is imposed. In order to constrain poorly reconstructed electron tracks, candidate events are required to have no “pixel tracks”, which are reconstructed based on the information only from the Pixel detector. Candidate pixel tracks are required to have $p_{\mathrm{T}} > 50$ MeV, $|\eta| < 2.5$, and at least three hits in the Pixel detector. In order to suppress fake pixel tracks due to noise in the Pixel detector, only pixel tracks with $\Delta\eta < 0.5$ from the photons are considered.

These requirements reduce the fake photon background from the dielectron final state by a factor of 10^4, according to simulation. They have minor impact on $\gamma\gamma \to \gamma\gamma$ signal events (93% efficiency for track veto and 99% for pixel track veto), since the probability of photon conversion in the Pixel detector is relatively small and the converted photons are initially suppressed at very low-E_{T} by the photon reconstruction algorithm due to the presence of low-momentum electron tracks.

To reduce other fake photon backgrounds (involving mainly calorimeter noise and cosmic-ray muons), the transverse momentum of the diphoton system ($p_{\mathrm{T}}^{\gamma\gamma}$) is required to be below 1 GeV for $m_{\gamma\gamma} < 12$ GeV and below 2 GeV for $m_{\gamma\gamma} > 12$ GeV. To reduce real photon background from CEP $gg \to \gamma\gamma$ reactions, an additional requirement on acoplanarity, $\mathrm{Aco} = (1 - \frac{|\Delta\phi_{\gamma\gamma}|}{\pi})$, is used. Due to its exclusive nature, the CEP $gg \to \gamma\gamma$ production is expected to be the dominant source of background with two photons in the final state [71, 127].

Exclusive dielectron pairs from the reaction Pb+Pb $(\gamma\gamma) \to \mathrm{Pb}^{(*)}$+$\mathrm{Pb}^{(*)}\, e^+e^-$ are used for various aspects of the nominal analysis, in particular to validate the EM calorimeter energy scale and resolution. To select these $\gamma\gamma \to e^+e^-$ candidates, events are required to pass the same trigger as in the diphoton selection. Each electron is reconstructed from EM energy cluster in the calorimeter matched to a track in the inner detector [137]. The electrons are required to have a transverse energy $E_{\mathrm{T}} > 2.5$ GeV and pseudorapidity $|\eta| < 2.47$ with the calorimeter transition region $1.37 < |\eta| < 1.52$ excluded. They are also required to meet *loose* identification criteria based on shower shape and track-quality variables [137]. The $\gamma\gamma \to e^+e^-$ events are selected by requiring exactly two oppositely charged electrons, no further charged-particle tracks coming from an interaction region (with the selection requirements as described above), and dielectron acoplanarity, $\mathrm{Aco} < 0.01$.

Figure 5.7 and 5.8 presents kinematic distributions of the dielectron system after applying the e^+e^- event selection for the 2018 and 2015 data respectively. The egamma resolution and scale uncertainties (as provided by the EGamma CP group [138]) are shown as shaded band. In total, about 30000 candidate events are observed in 2018 data and 7000 in 2015 data. Reasonable agreement between the data and the STARlight prediction is observed.

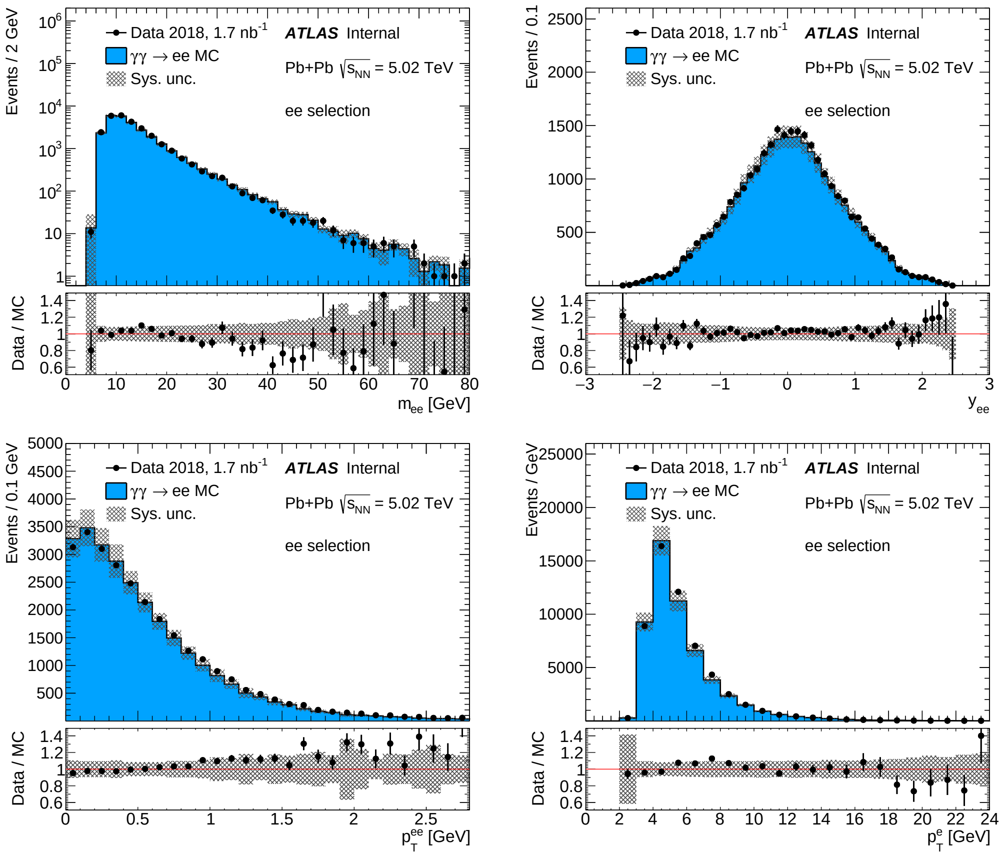

Figure 5.7: Kinematic distributions for Pb+Pb $(\gamma\gamma) \rightarrow$ Pb$^{(*)}$+Pb$^{(*)}$ e^+e^- event candidates in 2018: (a) dielectron mass, (b) dielectron rapidity, (c) dielectron p_T and (d) electron transverse energy. Data (points) are compared to MC expectations (histograms). Electrons with $E_T > 2.5$ GeV and $|\eta| < 2.47$ excluding the calorimeter transition region $1.37 < |\eta| < 1.52$ are considered. The egamma resolution, egamma scale, trigger efficiency and scale factor uncertainties are shown as shaded band. The $es2017\_R21\_ofc0\_v1$ calibration is used.

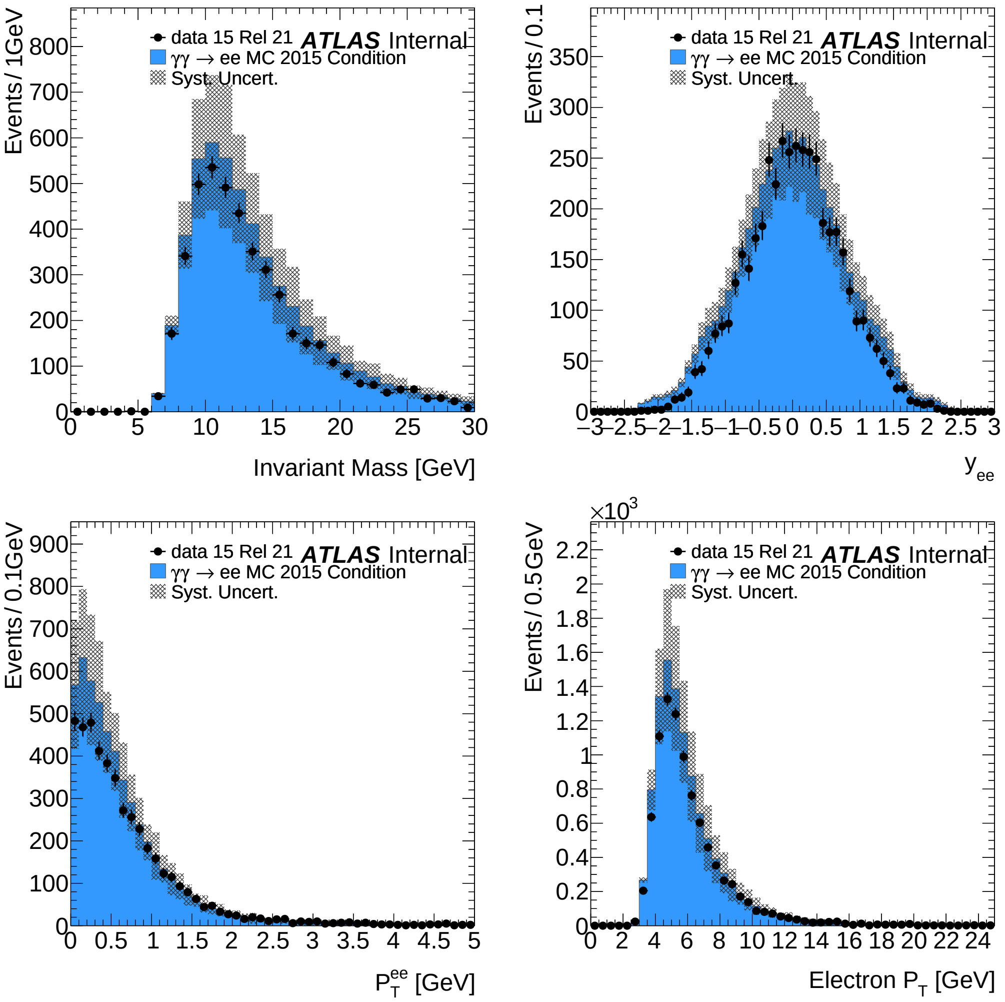

Figure 5.8: Kinematic distributions for Pb+Pb $(\gamma\gamma) \rightarrow$ Pb$^{(*)}$+Pb$^{(*)}$ e^+e^- event candidates in 2015: (a) dielectron mass, (b) dielectron rapidity, (c) dielectron p_T and (d) electron transverse energy. Data (points) are compared to MC expectations (histograms). Electrons with $E_\mathrm{T} > 2.5$ GeV and $|\eta| < 2.47$ excluding the calorimeter transition region $1.37 < |\eta| < 1.52$ are considered. The egamma resolution and scale uncertainties are shown as shaded band. The $es2017\_R21\_ofc0\_v1$ calibration is used.

5.4 Detector calibration

5.4.1 Trigger efficiency

The trigger sequence used in the analysis consists of three independent requirements: Level-1, MBTS/FCal veto, as well as the requirement on low activity in the ID. The efficiency determination of all three contributions is discussed in the following.

The Level-1 trigger efficiency has been estimated with $\gamma\gamma \to e^+e^-$ events passing one of the independent supporting triggers. These triggers are designed to select events with single or double dissociation of Pb nuclei and small activity in the ID. They are based on a coincidence of signals in one or both ZDC sides with a requirement on the total E_T in the calorimeter to be below 50 GeV. Dielectron event candidates are required to have exactly two reconstructed tracks and two EM clusters, each with a minimum E_T of 1 GeV and $|\eta| < 1.37$ or $1.52 < |\eta| < 2.47$. The electron identification requirements are not used in order to accept more events in this very low-E_T region, where the efficiencies to reconstruct and identify electrons are low. Furthermore, to reduce possible background, each pair of charged-particle tracks is required to have small acoplanarity below 0.01. The extracted Level-1 trigger efficiency is provided as a function of a sum of E_T of two EM clusters ($E_\mathrm{T}^\mathrm{cluster1}$ $+E_\mathrm{T}^\mathrm{cluster2}$). This efficiency, shown in Fig. 5.9, reaches 65% for $(E_\mathrm{T}^\mathrm{cluster1} + E_\mathrm{T}^\mathrm{cluster2}) =$ 5 GeV and 80% for $(E_\mathrm{T}^\mathrm{cluster1} + E_\mathrm{T}^\mathrm{cluster2}) = 6$ GeV for 2018 trigger settings. Due to higher trigger thresholds in 2015, the Level-1 trigger efficiency is about 25% for $(E_\mathrm{T}^\mathrm{cluster1}+E_\mathrm{T}^\mathrm{cluster2}) = 7$ GeV and 90% for $(E_\mathrm{T}^\mathrm{cluster1}+E_\mathrm{T}^\mathrm{cluster2}) = 9$ GeV. The efficiency plateau is reached around $(E_\mathrm{T}^\mathrm{cluster1} + E_\mathrm{T}^\mathrm{cluster2}) = 10$ GeV for the 2015 data-taking period and around $(E_\mathrm{T}^\mathrm{cluster1} + E_\mathrm{T}^\mathrm{cluster2}) = 9$ GeV for the 2018 one. The efficiency is parameterised using an error function fit that is used to reweight the MC simulation. The statistical uncertainty is estimated based on the variation of fit parameters by their uncertainty values. The systematic uncertainty is estimated using modified $\gamma\gamma \to e^+e^-$ selection criteria.

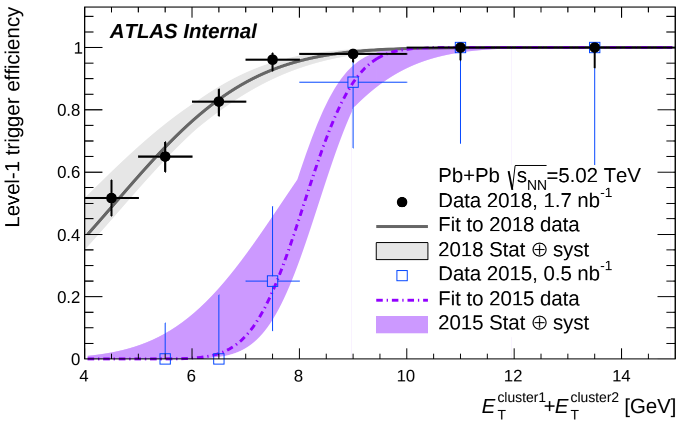

Figure 5.9: The Level-1 trigger efficiency extracted from $\gamma\gamma \to e^+e^-$ events that pass the supporting triggers. Data are shown as points, separately for two data-taking periods: 2015 (open squares) and 2018 (full circles). The efficiency is parameterised using the error function fit, shown as a dashed (2015) or solid (2018) line. Shaded bands denote total (statistical and systematic) uncertainty.

The MBTS and FCal veto efficiencies are estimated using $\gamma\gamma \to e^+e^-$ events recorded by supporting triggers. The MBTS veto efficiency is estimated to be $(98 \pm 2)\%$ and the FCal veto efficiency is found to be $(99.1 \pm 0.6)\%$.

Due to low conversion probability of signal photons in the Pixel detector and very high hit reconstruction efficiency for converted photons, any inefficiency of the Pixel-veto requirement at the trigger level is found to be negligible for diphoton event candidates.

For events satisfying the $\gamma\gamma \to e^+e^-$ selection the efficiency of the Pixel-veto requirement is evaluated using a dedicated supporting trigger selected events with at most 15 tracks at the HLT, out of which at least two had $p_\mathrm{T} > 1$ GeV. At Level-1, the same trigger condition was applied as in the diphoton trigger. Also the FCal veto requirement was imposed at the HLT. The Pixel-veto efficiency is parameterised using a second order polynomial as a function of dielectron rapidity, y_ee. The efficiency reaches 80–85% for dielectron rapidity $|y_\mathrm{ee}| < 1$ and drops to 45–50% at $|y_\mathrm{ee}| \sim 2.5$. This efficiency correction is applied to the $\gamma\gamma \to e^+e^-$ MC simulation.

5.4.2 Photon reconstruction and identification

The photon reconstruction efficiency is extracted from data using $\gamma\gamma \to e^+e^-$ events, where one of the electrons emits a hard-bremsstrahlung photon due to interaction with the material of the detector. The tag-and-probe method is used and the analysis is performed for events with exactly one identified electron and exactly two reconstructed charged-particle tracks. The electron is considered a tag if it can be matched to one of the tracks with a $\Delta R < 1.0$ requirement. The electron E_T^e is required to be above 4 GeV and the track that is unmatched with the electron (trk2) should have $p_\mathrm{T} > 1.5$ GeV. The electron–trk2 transverse momentum difference is treated as a probe, since the additional hard-bremsstrahlung photon is expected to have $E_\mathrm{T}^\gamma \approx (E_\mathrm{T}^\mathrm{e} - p_\mathrm{T}^\mathrm{trk2})$. The $p_\mathrm{T}^\mathrm{trk2} < 1.5$ GeV requirement ensures a sufficient ΔR separation between the expected photon and the second electron. Any additional background contribution to the exclusive $\gamma\gamma \to e^+e^-$ reaction is found to be very small in Pb+Pb collisions [139], therefore it is considered negligible.

The data sample contains 2905 $\gamma\gamma \to e^+e^-(\gamma)$ bremsstrahlung photons and is used to extract the photon reconstruction efficiency, which is presented in Fig. 5.10. The efficiency in data is approximately 60% for $E_\mathrm{T}^\gamma = 2.5$ GeV and reaches 90% at $E_\mathrm{T}^\gamma = 6$ GeV. Reasonable agreement between data and simulation is found. The distribution from Fig. 5.10 is used to obtain the data-to-simulation scale factors used to correct the MC simulation.

High-p_T exclusive dilepton production ($\gamma\gamma \to l^+l^-$ with $\ell^\pm = e^\pm, \mu^\pm$) with final-state radiation (FSR) is used for data-driven measurement of the photon PID efficiency, defined as the probability for a reconstructed photon to pass the identification criteria. Events with exactly two oppositely-charged tracks with $p_\mathrm{T} > 0.5$ GeV are selected in UPC events. In addition a requirement to reconstruct a photon candidate with $E_\mathrm{T}^\gamma > 2.5$ GeV and $|\eta| < 1.37$ or $1.52 < |\eta| < 2.37$ is imposed. A photon candidate is required to be separated from each track, with the requirement $\Delta R > 0.3$. This condition avoids the leakage of the photon cluster to electron clusters from the $\gamma\gamma \to e^+e^-$ process. The mass of the dilepton system is required to be above 1.5 GeV. The FSR event candidates are identified using a $p_\mathrm{T}^{\mathrm{tt}\gamma} < 1$ GeV requirement, where $p_\mathrm{T}^{\mathrm{tt}\gamma}$ is the transverse momentum of the three body system consisting of two oppositely-charged tracks and a photon. The FSR sample consists of 1333 (212)

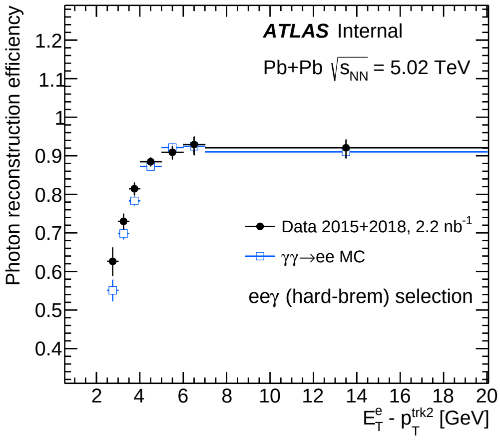

Figure 5.10: Photon reconstruction efficiency as a function of photon E_{T}^{γ} (approximated with $E_{\mathrm{T}}^{e} - p_{\mathrm{T}}^{\mathrm{trk2}}$) extracted from $\gamma\gamma \to e^{+}e^{-}$ events with a hard-bremsstrahlung photon. Data (full symbols) are compared with $\gamma\gamma \to e^{+}e^{-}$ MC simulation (open symbols).

photon candidates in the 2018 (2015) data set.

Figure 5.11 shows the photon PID efficiency as a function of reconstructed photon E_{T} for 2018 (left) and 2015 (right) data. The measurement from data is compared to the one extracted from the signal MC sample. Photon efficiencies in MC simulation reflecting 2018 and 2015 data taking conditions are in good agreement. In the 2018 data for photon $E_{\mathrm{T}} < 5$ GeV, the PID efficiency is 4% lower compared to MC simulation, while for 2015 data, it is found 5% higher than in the MC simulation. Based on these studies, MC simulated events are corrected using photon E_{T}-dependent data-to-simulation scale factors separately for the 2018 and 2015 data sets.

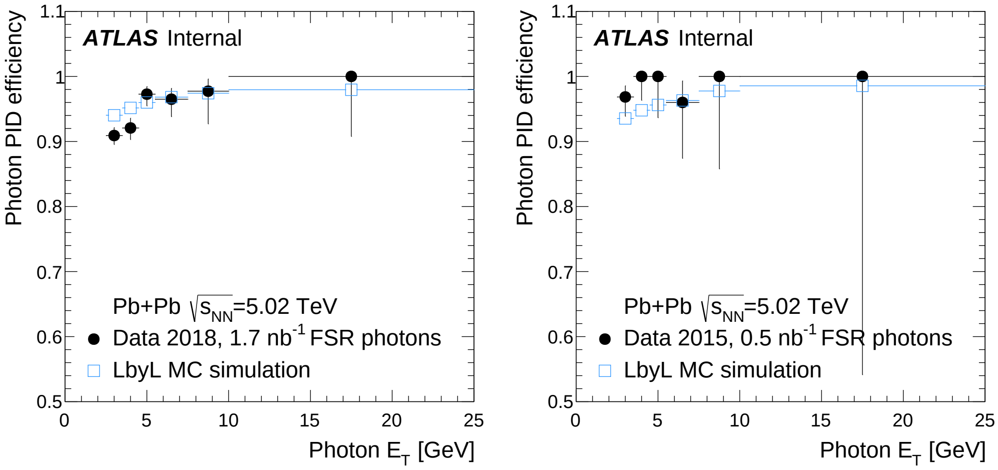

Figure 5.11: Photon PID efficiency as a function of photon E_{T} extracted from FSR event candidates in 2018 (left) and 2015 (right) data (full symbols) and signal MC sample (open symbols).

5.4.3 Photon energy calibration

The performance of EM energy scale and resolution is validated in data using $\gamma\gamma \rightarrow e^+e^-$ events. The electrons from the $\gamma\gamma \rightarrow e^+e^-$ reaction are well balanced in their transverse momenta, with very small initial (theoretical) smearing $\sigma^{\mathrm{theory}}_{p_{\mathrm{T}}^{e+}-p_{\mathrm{T}}^{e-}} < 30$ MeV, much smaller than the expected EM calorimeter energy resolution. Therefore by measuring $(E_{\mathrm{T}}^{\mathrm{cluster1}} - E_{\mathrm{T}}^{\mathrm{cluster2}})$ distributions in $\gamma\gamma \rightarrow e^+e^-$ events, one can extract $\sigma_{E_{\mathrm{T}}^{\mathrm{cluster}}}$ that follows the formula:

$$\sigma_{E_{\mathrm{T}}^{\mathrm{cluster}}} \approx \frac{\sigma_{(E_{\mathrm{T}}^{\mathrm{cluster1}}-E_{\mathrm{T}}^{\mathrm{cluster2}})}}{\sqrt{2}} \; , , \tag{5.1}$$

where $E_{\mathrm{T}}^{\mathrm{cluster1}}$ and $E_{\mathrm{T}}^{\mathrm{cluster2}}$ are the transverse energies of the two clusters. At low electron-E_{T} (below 10 GeV) the $\sigma_{E_{\mathrm{T}}^{\mathrm{cluster}}}/E_{\mathrm{T}}^{\mathrm{cluster}}$ is observed to be 8–10% in data, which agrees well with the resolution from simulation.

The EM energy scale is cross-checked using the ratio of electron cluster E_{T} and electron track p_{T}. It is observed that the simulation provides good description of the $E_{\mathrm{T}}^{\mathrm{e}}/p_{\mathrm{T}}^{\mathrm{trk}}$ distribution.

5.4.4 Energy calibration studies

The analysis uses a newly developed tag of egamma calibration labelled es2017_R21_ofc0_v1 applicable for low pileup data reconstructed in release 21.

5.4.4.1 Analysis of 2018 data

The electron/photon energy resolution can be extracted from data using $\gamma\gamma \rightarrow e^+e^-$ event properties. For this purpose, electrons passing the `LHloose` identification with $p_{\mathrm{T}} > 2.5\,\mathrm{GeV}$ are selected. Additionally, the associated tracks are required to pass the recommended `tight` track quality requirements defined by the Tracking CP group [140][141]:

- d_0 significance < 5
- at least 9 silicon hits for $|\eta| < 1.65$, otherwise at least 11 silicon hits
- no pixel holes
- at least one hit in the IBL and BLayer if hits are expected

The electrons from the $\gamma\gamma \rightarrow e^+e^-$ reaction are well balanced in their transverse momenta, with very small initial (truth) smearing $\sigma^{MCtruth}_{p_{\mathrm{T}}^{e1}-p_{\mathrm{T}}^{e2}} < 0.03$ GeV, much smaller than the expected egamma energy resolution. Therefore by measuring $E_{\mathrm{T}}^{\mathrm{cluster1}} - E_{\mathrm{T}}^{\mathrm{cluster2}}$ distributions in $\gamma\gamma \rightarrow e^+e^-$ events, one can extract $\sigma_{E_{\mathrm{T}}^{\mathrm{cluster}}}$ that follows the formula:

$$\sigma_{E_{\mathrm{T}}^{\mathrm{cluster}}} \approx \frac{\sigma_{E_{\mathrm{T}}^{\mathrm{cluster1}}-E_{\mathrm{T}}^{\mathrm{cluster2}}}}{\sqrt{2}} \; ., \tag{5.2}$$

Figure 5.12 shows the $E_{\mathrm{T}}^{\mathrm{cluster1}} - E_{\mathrm{T}}^{\mathrm{cluster2}}$ distributions in different $E_{\mathrm{T}}^{\mathrm{e}}$ bins. The transverse energy resolution in data agrees with simulated resolution within resolution uncertainties which are provided by the EGamma CP tool [138]. Moreover, the $\sigma_{E_{\mathrm{T}}^{\mathrm{cluster}}}/E_{\mathrm{T}}^{\mathrm{cluster}}$ is observed to be $\approx 8-10\%$ at low-E_{T}.

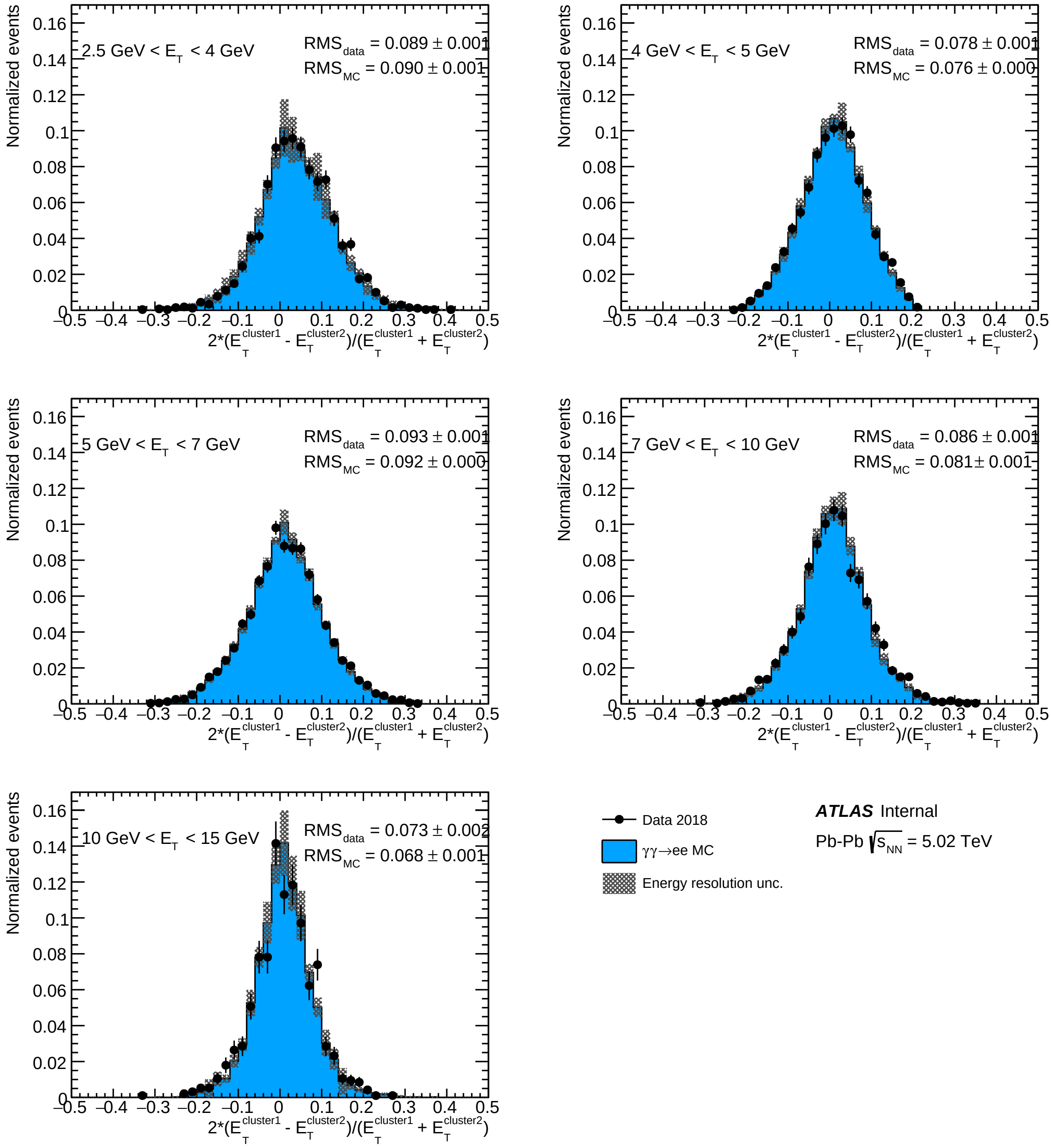

Figure 5.12: Transverse momentum difference of egamma clusters associated with identified electrons in $\gamma\gamma \to e^+e^-$ events. Different cluster E_{T} bins are shown. Data (black points) is compared to $\gamma\gamma \to e^+e^-$ MC (blue histograms). The band denotes energy resolution uncertainty (as provided by the egamma tool). The $es2017\_R21\_ofc0\_v1$ calibration is used.

The energy scale calibration of calorimeter clusters in MC simulation is cross checked using electrons and the measured transverse momenta of their associated tracks.

For all selected electrons the calibrated electron transverse energy E_{T} is divided by the transverse momentum of the associated track $p_{\mathrm{T}}^{\mathrm{trk}}$. The distribution is expected to follow a Landau distribution with a peak slightly above unity due to collinear photon radiation of the electrons in the detector material. Collinearly radiated photons lowers the measured track momentum but not the measured cluster energy. The $E_{\mathrm{T}}^{\mathrm{e}}/p_{\mathrm{T}}^{\mathrm{trk}}$ distributions obtained from data and simulation are compared in Fig. 5.13 in several bins of cluster energy E_{T} in the range $2.5 < E_{\mathrm{T}} < 15\,\mathrm{GeV}$. Within the energy scale uncertainties provided by the EGamma CP tool [138], the data and MC agree reasonably well.

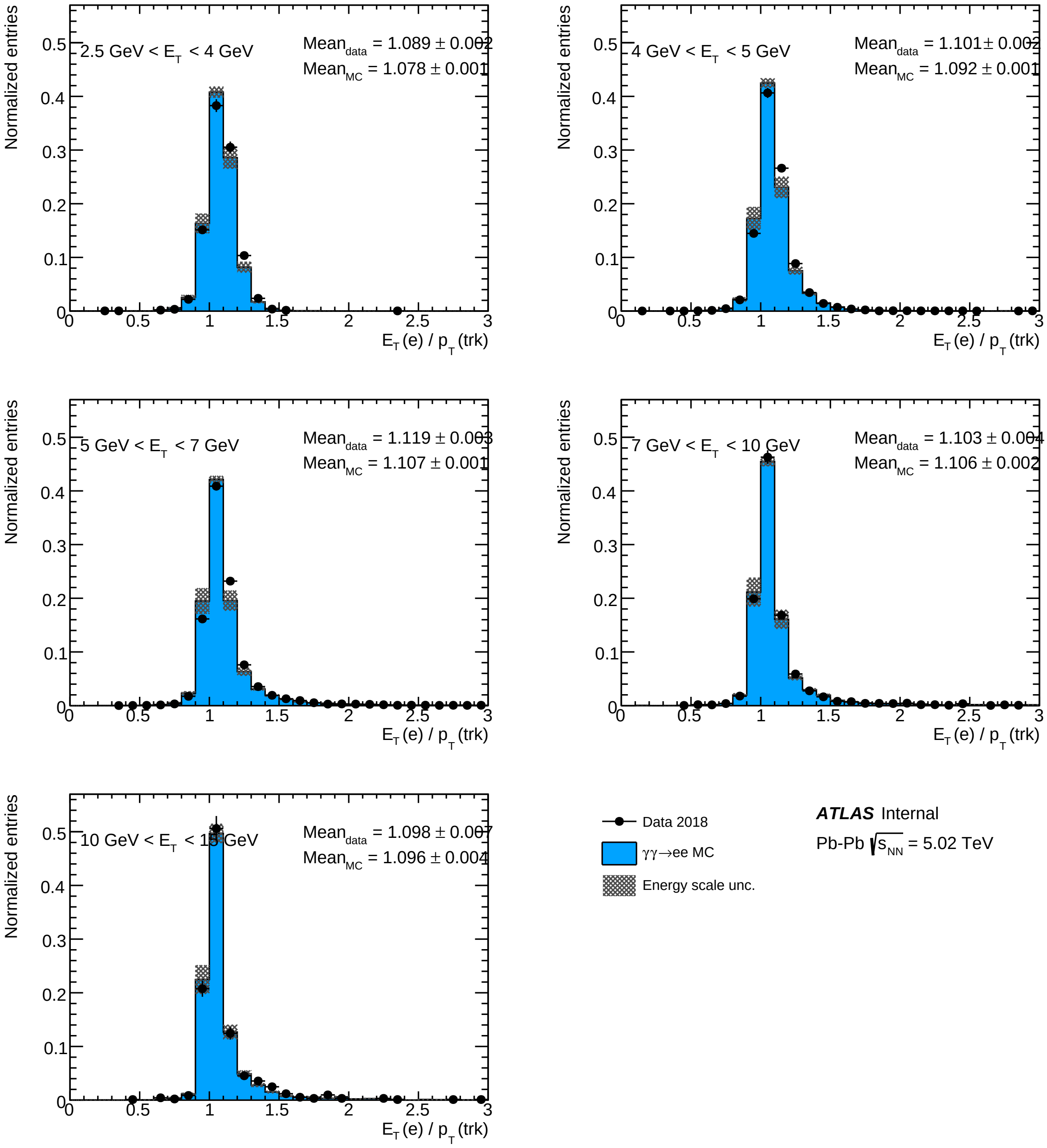

Figure 5.13: E_T^e/p_T^{trk} for electrons from $\gamma\gamma \to e^+e^-$ process. Different cluster E_T bins are shown. Data (black points) is compared to $\gamma\gamma \to e^+e^-$ MC (blue histograms). The band denotes energy scale uncertainty (as provided by the egamma tool). The $es2017\_R21\_ofc0\_v1$ calibration is used.

5.4.4.2 Analysis of 2015 data

The same procedure described in the previous section is applied this time to perform comparison between 2015 data reprocessed in the release 21 and MC simulation with the 2015 detector conditions. Figure 5.14 shows the $E_{\mathrm{T}}^{\mathrm{cluster1}} - E_{\mathrm{T}}^{\mathrm{cluster2}}$ distributions in 2015 data and MC for different E_{T}^{e} bins. The transverse energy resolution in data agrees reasonably with the MC simulation.

The $E_{\mathrm{T}}^{e}/p_{\mathrm{T}}^{\mathrm{trk}}$ distributions obtained from 2015 data and simulation are compared in several bins of cluster energy E_{T} in the range $2.5 < E_{\mathrm{T}} < 15\,\mathrm{GeV}$.

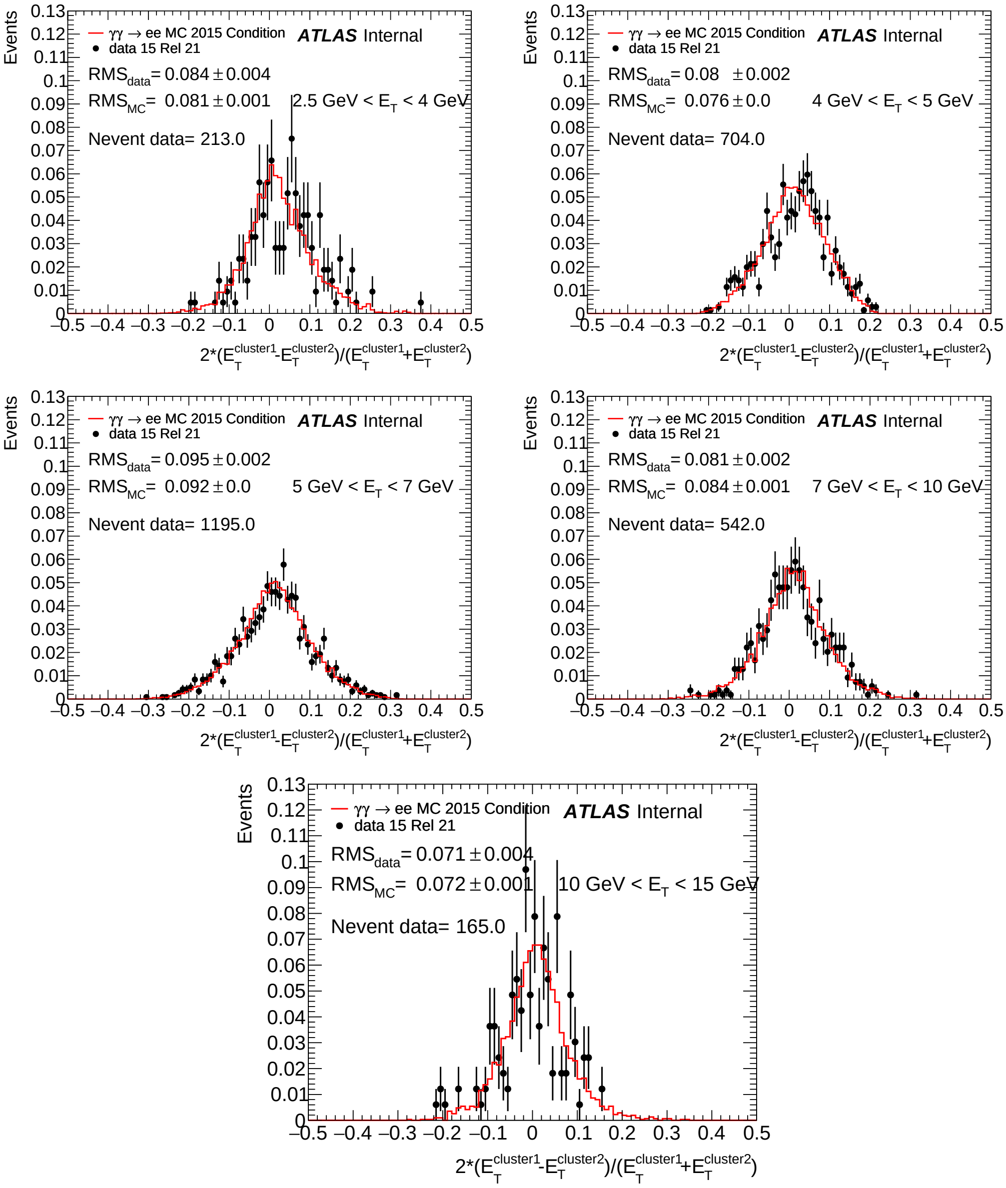

Figure 5.14: Transverse momentum difference of egamma clusters associated with identified electrons in $\gamma\gamma \to e^+e^-$ events. Different cluster E_{T} bins are shown. Data (black points) is compared to $\gamma\gamma \to e^+e^-$ MC (red histograms).

The energy scale calibration of calorimeter clusters in MC simulation is cross checked using electrons and the measured transverse momenta of their associated

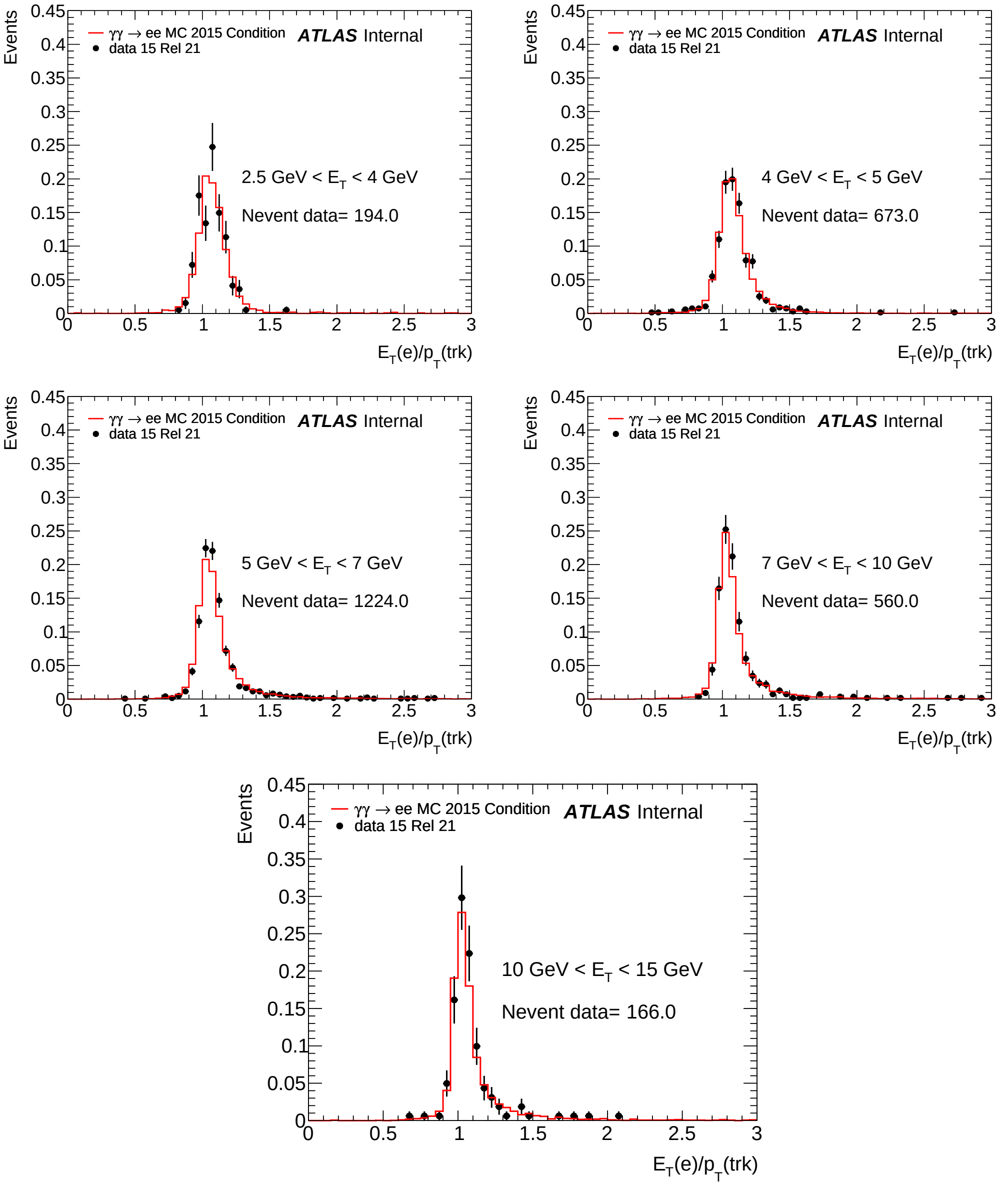

Figure 5.15: E_T^e/p_T^{trk} for electrons from $\gamma\gamma \rightarrow e^+e^-$ process. Different cluster E_T bins are shown. Data (black points) is compared to $\gamma\gamma \rightarrow e^+e^-$ MC (red histograms).

tracks.

The $E_{\mathrm{T}}^{e}/p_{\mathrm{T}}^{\mathrm{trk}}$ distributions obtained from data and simulation are compared in Fig. 5.15 in several bins of cluster energy E_{T} in the range $2.5 < E_{\mathrm{T}} < 15\,\mathrm{GeV}$. The data and MC are in a reasonable agreement.

Control region name	Purpose	Selection
Aco > 0.01 CR	CEP $gg \to \gamma\gamma$ normalization	signal selection, except Aco > 0.01
$N_{\rm MST} > 0$ CR	Fake photon background estimate	signal selection + $N_{\rm MST} > 0$
CR($N_{\rm Trk} = 2$)	e^+e^- yield cross-check after preselection	Preselection + $N_{\rm Trk} = 2$
CR($N_{\rm Trk} = 1$)	e^+e^-: $p^{\rm e}_{\rm mistag}$ evaluation	Preselection + $N_{\rm Trk} = 1$ + Aco < 0.01
CR($N_{\rm PixTrk} = 1$)	e^+e^-: yield evaluation	signal selection, except allowing 1 pixel track
CR($N_{\rm PixTrk} = 2$)	e^+e^-: yield evaluation	signal selection, except allowing 2 pixel tracks

Table 5.5: Definitions of various control regions used to determine different types of background. The MST acronym denotes Muon spectrometer track particle.

5.5 Background estimation

The main sources of background in this analysis are: $\gamma\gamma \to e^+e^-$, CEP $gg \to \gamma\gamma$, and fake diphoton events due to cosmic-ray muons and calorimeter noise. These background sources are estimated using data-driven techniques with several control regions, which are summarized in Table 5.5.

Figure 5.16 presents the $N_{\rm Trk}$ distribution for diphoton events after preselection ($m_{\gamma\gamma} > 5$ GeV). The distribution in data is compared to $\gamma\gamma \to e^+e^-$ simulation. It is clear that at this stage of the selection the background is fully dominated by $\gamma\gamma \to e^+e^-$ events.

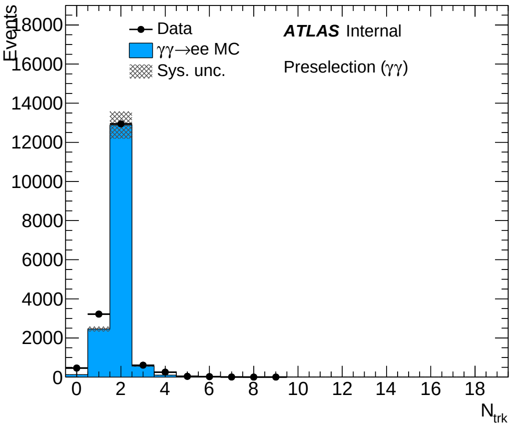

Figure 5.16: $N_{\rm Trk}$ distribution for diphoton events after preselection ($m_{\gamma\gamma} > 5$ GeV). Data (points) are compared to MC expectations for $\gamma\gamma \to e^+e^-$ process (histogram). Systematic uncertainties associated with photon energy scale and resolution uncertainties are shown as shaded band.

5.5.1 Dielectron final states

Due to its relatively high rate, the $\gamma\gamma \to e^+e^-$ process can be a source of fake diphoton events. The electron→photon misidentification can occur when the electron track is not reconstructed or the electron emits a hard bremsstrahlung photon.

In order to cross-check the simulation, a control region with exactly two reconstructed charged-particle tracks and two photons, is defined (denoted as CR($N_{\rm Trk} = 2$)). This control region is expected to be dominated by $\gamma\gamma \to e^+e^-$ background. Figure 5.17 shows the diphoton mass and $p_{\rm T}$ distributions for data and $\gamma\gamma \to e^+e^-$ MC in this control region. Good agreement is observed between data and MC, with small mismodelling for $p_{\mathrm{T}}^{\gamma\gamma} > 1$ GeV. This mismodelling is due to missing QED FSR corrections in $\gamma\gamma \to e^+e^-$ simulation. The $\gamma\gamma \to e^+e^-$ MC correctly describes dielectron yields up to the pixel track veto selection, where some discrepancies are observed, as indicated below.

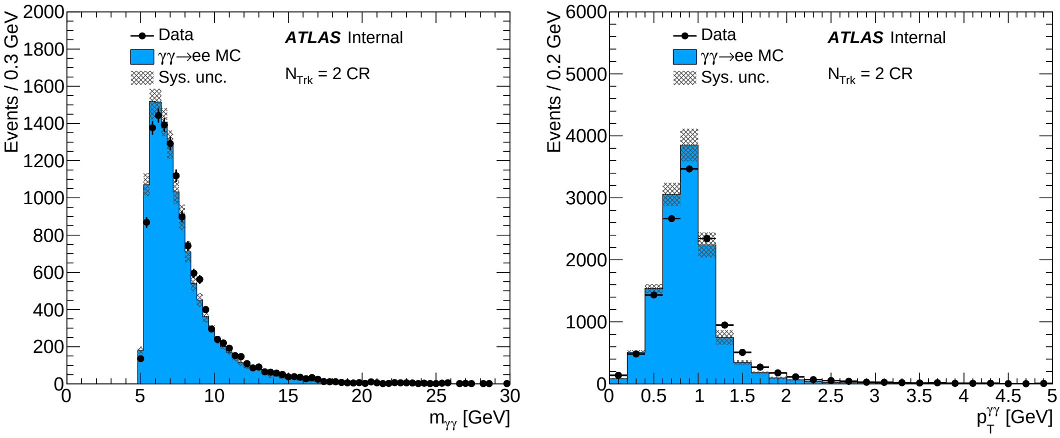

Figure 5.17: Diphoton mass (left) and diphoton transverse momentum (right) distributions for $N_{\mathrm{Trk}} = 2$ control region. Data (points) are compared to MC expectations for $\gamma\gamma \to e^+e^-$ process (histogram). Systematic uncertainties associated with photon energy scale and resolution uncertainties are shown as shaded band. No other sources of background are considered in this control region.

Figure 5.18 shows the pixel track multiplicity distribution for events satisfying signal selection except allowing at least one pixel track. There is a clear mismodelling observed, which points to the bad modelling of pixel track reconstruction efficiencies in simulation.

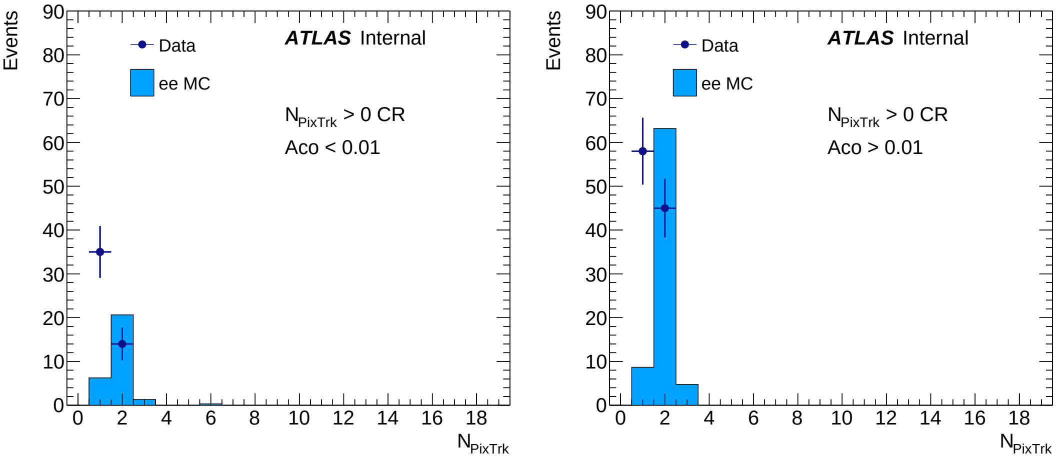

Figure 5.18: Pixel track multiplicity distribution for events satisfying signal selection except allowing at least one pixel track and Aco < 0.01 (left) or Aco > 0.01 (right). Data (points) are compared to MC expectations for $\gamma\gamma \to e^+e^-$ process (histogram).

Therefore, a data driven background estimation is introduced. In this method the following extra control regions are defined:

- CR($N_{\mathrm{Trk}} = 1$): 1 track, any number of pixel tracks, Aco < 0.01
- CR($N_{\mathrm{PixTrk}} = 2$): signal selection except allowing 2 pixel tracks
- CR($N_{\mathrm{PixTrk}} = 1$): signal selection except allowing 1 pixel track

From CR($N_{\mathrm{Trk}} = 1$), the conditional probability $p^{\mathrm{e}}_{\mathrm{mistag}}$ to miss one electron pixel track if the standard track is not reconstructed, is extracted. This is done by comparing the $N_{\mathrm{PixTrk}} = 1$ to $N_{\mathrm{PixTrk}} = 2$ relative event yields in this region (tag-and-probe method), as presented in Fig. 5.19. It is found that $p^{\mathrm{e}}_{\mathrm{mistag}} = 45\%$ for data, to be compared with $p^{\mathrm{e}}_{\mathrm{mistag}} = 10\%$ for $\gamma\gamma \to e^+e^-$ simulation. To evaluate the systematic uncertainty on $p^{\mathrm{e}}_{\mathrm{mistag}}$, the definition of CR($N_{\mathrm{Trk}} = 1$) was modified by dropping the acoplanarity requirement (Aco < 0.01), which leads to 8% change of $p^{\mathrm{e}}_{\mathrm{mistag}}$. As a further cross-check, the $p^{\mathrm{e}}_{\mathrm{mistag}}$ is studied as a function of pixel track pseudorapidity and charge. No deviations above quoted uncertainty are observed.

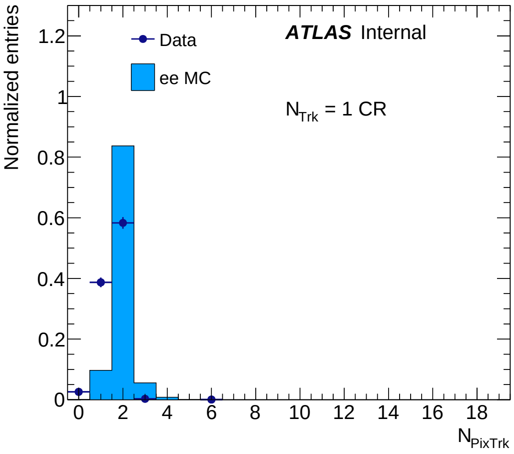

Figure 5.19: Pixel track multiplicity distribution for events with exactly one standard track (CR($N_{\mathrm{Trk}} = 1$)). Data (points) are compared to MC expectations for $\gamma\gamma \to e^+e^-$ process (histogram).

Using this conditional probability to mis-reconstruct electron pixel track, the event probabilities for different misidentification scenarios can be calculated:

$$p^{\mathrm{event}}_{N_{\mathrm{Pix}}=2} = \left(1 - p^{\mathrm{e}}_{\mathrm{mistag}}\right)^2 \tag{5.3}$$

$$p^{\mathrm{event}}_{N_{\mathrm{Pix}}=1} = 2 \cdot p^{\mathrm{e}}_{\mathrm{mistag}} \cdot (1 - p^{\mathrm{e}}_{\mathrm{mistag}}) \tag{5.4}$$

$$p^{\mathrm{event}}_{N_{\mathrm{Pix}}=0} = \left(p^{\mathrm{e}}_{\mathrm{mistag}}\right)^2 . \tag{5.5}$$

Then, by using the number of events in CR($N_{\mathrm{PixTrk}} = 1$) and CR($N_{\mathrm{PixTrk}} = 2$) together with these probabilities, the expected number of background events in the signal region can be extrapolated. The central value is calculated using the mean number of events in the two control regions:

$$SR_{\mathrm{expected}} = (N^{\mathrm{events}}_{\mathrm{CR}(N_{\mathrm{PixTrk}}=1)} + N^{\mathrm{events}}_{\mathrm{CR}(N_{\mathrm{PixTrk}}=2)}) \cdot \frac{p^{\mathrm{event}}_{N_{\mathrm{Pix}}=0}}{1 - p^{\mathrm{event}}_{N_{\mathrm{Pix}}=0}} \;, , \tag{5.6}$$

	Data nominal	$p^{\text{e}}_{\text{mistag}}$ variation	CR variation 1	CR variation 2	MC
$p^{\text{e}}_{\text{mistag}}$	44.80 %	36.87 %	44.80 %	44.80 %	9.87 %
$p^{\text{event}}_{N_{\text{Pix}}=2}$	30.47 %	39.85 %	30.47 %	30.47 %	81.23 %
$p^{\text{event}}_{N_{\text{Pix}}=1}$	49.46 %	46.55 %	49.46 %	49.46 %	17.79 %
$p^{\text{event}}_{N_{\text{Pix}}=0}$	20.07 %	13.59 %	20.07 %	20.07 %	0.97 %
CR($N_{\text{PixTrk}} = 1$)	31	31	31	31	6.23
CR($N_{\text{PixTrk}} = 2$)	15	15	15	15	22.45
SR	11.55	7.23	9.88	12.58	0.28

Table 5.6: Summary of the results from the data driven e^+e^- background studies. The number of extrapolated e^+e^- events in SR is shown in last row.

	Data nominal	$p^{\text{e}}_{\text{mistag}}$ variation	CR variation 1	CR variation 2	MC
$p^{\text{e}}_{\text{mistag}}$	44.80 %	36.87 %	44.80 %	44.80 %	9.87 %
$p^{\text{event}}_{N_{\text{Pix}}=2}$	30.47 %	39.85 %	30.47 %	30.47 %	81.23 %
$p^{\text{event}}_{N_{\text{Pix}}=1}$	49.46 %	46.55 %	49.46 %	49.46 %	17.79 %
$p^{\text{event}}_{N_{\text{Pix}}=0}$	20.07 %	13.59 %	20.07 %	20.07 %	0.97 %
CR($N_{\text{PixTrk}} = 1$, aco> 0.01)	53	53	53	53	9.35
CR($N_{\text{PixTrk}} = 2$, aco> 0.01)	45	45	45	45	69.74
CEP norm. region	24.61	15.42	21.51	29.64	0.78

Table 5.7: Summary of the results from the data driven e^+e^- background studies in the Aco > 0.01 region (CEP normalization region).

while the lower and upper CR variations are given by:

$$SR_{\text{expected,low}} = N^{\text{events}}_{\text{CR}(N_{\text{PixTrk}}=1)} \cdot \frac{p^{\text{event}}_{N_{\text{Pix}}=0}}{p^{\text{event}}_{N_{\text{Pix}}=1}} \tag{5.7}$$

$$SR_{\text{expected,high}} = N^{\text{events}}_{\text{CR}(N_{\text{PixTrk}}=2)} \cdot \frac{p^{\text{event}}_{N_{\text{Pix}}=0}}{p^{\text{event}}_{N_{\text{Pix}}=2}} \tag{5.8}$$

The results of these data-driven studies for signal region (Aco < 0.01) are summarized in Table 5.6. The number of $\gamma\gamma \to e^+e^-$ events in the signal region is estimated to be $N_{\gamma\gamma\to ee} = 12 \pm 5$, where the uncertainty includes the $p^{\text{e}}_{\text{mistag}}$ uncertainty and limited statistics of CR($N_{\text{PixTrk}} = 1,\ 2$). This uncertainty also covers the differences if the $\gamma\gamma \to e^+e^-$ yield is extrapolated from event yields for individual pixel track multiplicities ($N_{\text{PixTrk}} = 1$ or $N_{\text{PixTrk}} = 2$).

To estimate the e^+e^- background within the Aco > 0.01 region (CEP background normalization region) the same technique was used, however the cut on acoplanarity was inverted to Aco> 0.01 for the control regions with one or two pixel tracks. Everything else in the method is the same (as discussed above). The results for the e^+e^- background in the Aco > 0.01 region are given in Table 5.7. The number of $\gamma\gamma \to e^+e^-$ events in the Aco > 0.01 region is estimated to be $N_{\gamma\gamma\to ee} = 25 \pm 10$.

Figure 5.20 shows the pixel track multiplicity distribution for events satisfying signal selection except allowing at least one pixel track, where the data is compared to data-driven prediction for e^+e^- estimate. The results are shown for the Aco < 0.01 region (left plot) and Aco > 0.01 region (right plot). Good agreement is observed.

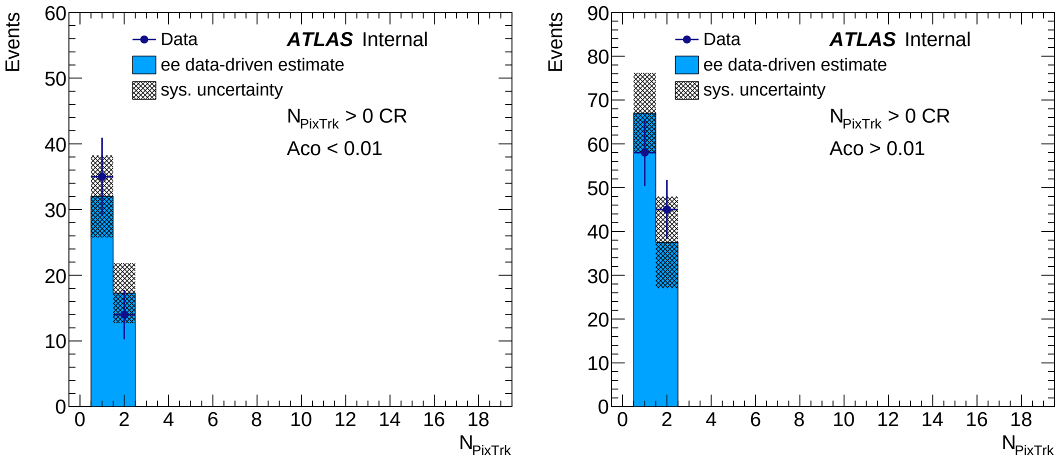

Figure 5.20: Pixel track multiplicity distribution for events satisfying signal selection except allowing at least one pixel track and Aco < 0.01 (left) or Aco > 0.01 (right). Data (points) are compared to data-driven expectations for $\gamma\gamma \to e^+e^-$ process (histogram). Systematic band denotes the uncertainty on $p^{\mathrm{e}}_{\mathrm{mistag}}$.

5.5.2 Central exclusive diphoton production

The CEP $gg \to \gamma\gamma$ background is estimated from simulation (SuperChic3 generator), with additional normalization of this process performed in the Aco > 0.01 control region. The normalisation is performed using the condition:

$$N_{\mathrm{data}}(\mathrm{Aco} > 0.01) = N_{gg\to\gamma\gamma}(\mathrm{Aco} > 0.01) + N_{\mathrm{sig}}(\mathrm{Aco} > 0.01) + N_{\gamma\gamma\to ee}(\mathrm{Aco} > 0.01)\;,, \tag{5.9}$$

where N_{data} denotes the number of observed events, $N_{gg\to\gamma\gamma}$ is the expected CEP $gg \to \gamma\gamma$ event yield, N_{sig} is the expected number of signal events and $N_{\gamma\gamma\to ee}$ is the e^+e^- background yield. Diphoton acoplanarity distribution for events satisfying signal region selection, but before applying Aco < 0.01 requirement is shown in Fig. 5.34. The predictions provide a fair description of the shape of the data distribution in the Aco > 0.01 region.

Control distributions for various diphoton kinematic distributions in the Aco $>$ 0.01 control region are presented in Fig. 5.22. Good agreement is found for the shapes of the kinematic distributions.

The uncertainty on the CEP $gg \to \gamma\gamma$ background process takes into account limited statistics in the Aco > 0.01 control region (11%), as well as experimental and modelling uncertainties. It is found that all experimental uncertainties have negligible impact on the CEP $gg \to \gamma\gamma$ background estimate. The impact of the shape MC modeling is estimated using alternative SuperChic MC sample with extra gluon interactions (no absorptive effects). This leads to 22% change in CEP background yield in the signal region, which is taken as systematic uncertainty. The effect of experimental systematic variations, as well as modeling uncertainty (Superchic2 vs Superchic3) on diphoton acoplanarity shape for CEP MC is shown in Fig. 5.23. Additional check is done by varying parton distribution function (PDF) of the gluon. The differences between MMHT 2014 [142], CT14 [143] and NNPDF3.1 [144] PDF sets have negligible impact on the shape of the diphoton acoplanarity distribution.

The background due to CEP is estimated to be 13 ± 3 counts.

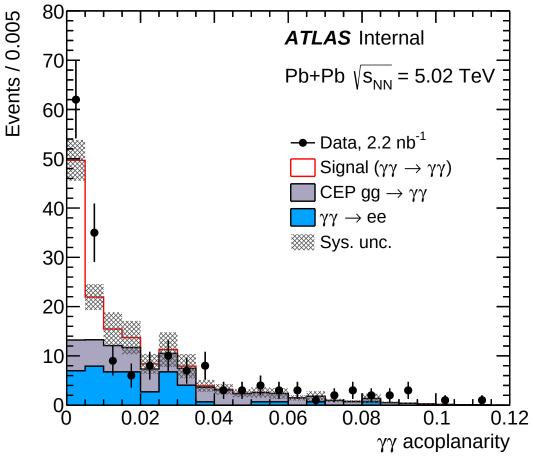

Figure 5.21: The diphoton acoplanarity distribution for events satisfying signal region selection, but before applying Aco < 0.01 requirement. The CEP $gg \to \gamma\gamma$ background is normalized in the Aco > 0.01 control region. Data are shown as points with statistical error bars, while the histograms represent the expected signal and background levels. The shaded band represents the uncertainties on signal and background predictions, excluding the uncertainty on the luminosity.

5.5.3 Fake photon background

Fake diphoton events can occur due to noise in the calorimeter or cosmic-ray muons that do not cross the Pixel detector (no reconstructed charged-particle tracks). Such fake photons are characterised by differences in the shower shape variables [145]. The contribution from such events in the signal region, is estimated using the control region with at least one track reconstructed in MS ($N_{\mathrm{MST}} > 0$, where MST denotes Muon Spectrometer Track Particle). Template N_{MST} distribution is built from events triggered on empty bunches. The template is then normalized using $N_{\mathrm{MST}} > 0$) control region, for each step of the event selection. The N_{MST} template distribution from empty bunch events is shown in Fig. 5.24, together with example N_{MST} distribution for events in $N_{\mathrm{MST}} > 0$ control region for selected diphoton events after applying $N_{\mathrm{trk}} = 0$ requirement. Approximately 60% of fake-diphoton events are expected to have $N_{\mathrm{MST}} > 0$, and the number of fake-photon events after applying $N_{\mathrm{trk}} = 0$ requirement is estimated to be 60 ± 40 (stat.). However, after applying $p_{\mathrm{T}}^{\gamma\gamma}$ requirements, no events with $N_{\mathrm{MST}} > 0$ are found in data, therefore the background due to other fake photons is found to be negligible in the signal region.

As a further cross-check, the reconstructed photon cluster time distribution is studied. It is observed that after applying $p_{\mathrm{T}}^{\gamma\gamma}$ requirements, the photon time distribution is consistent with prompt photons and no out-of-time photon candidates are present in data. Comparison of photon time distribution between fake photons triggered on empty bunches, and photons from Aco > 0.01 control region is shown in Fig. 5.25. Fake photons have random time distribution (as expected), whereas the photons in Aco > 0.01 control region are fully consistent with prompt photons from simulation.

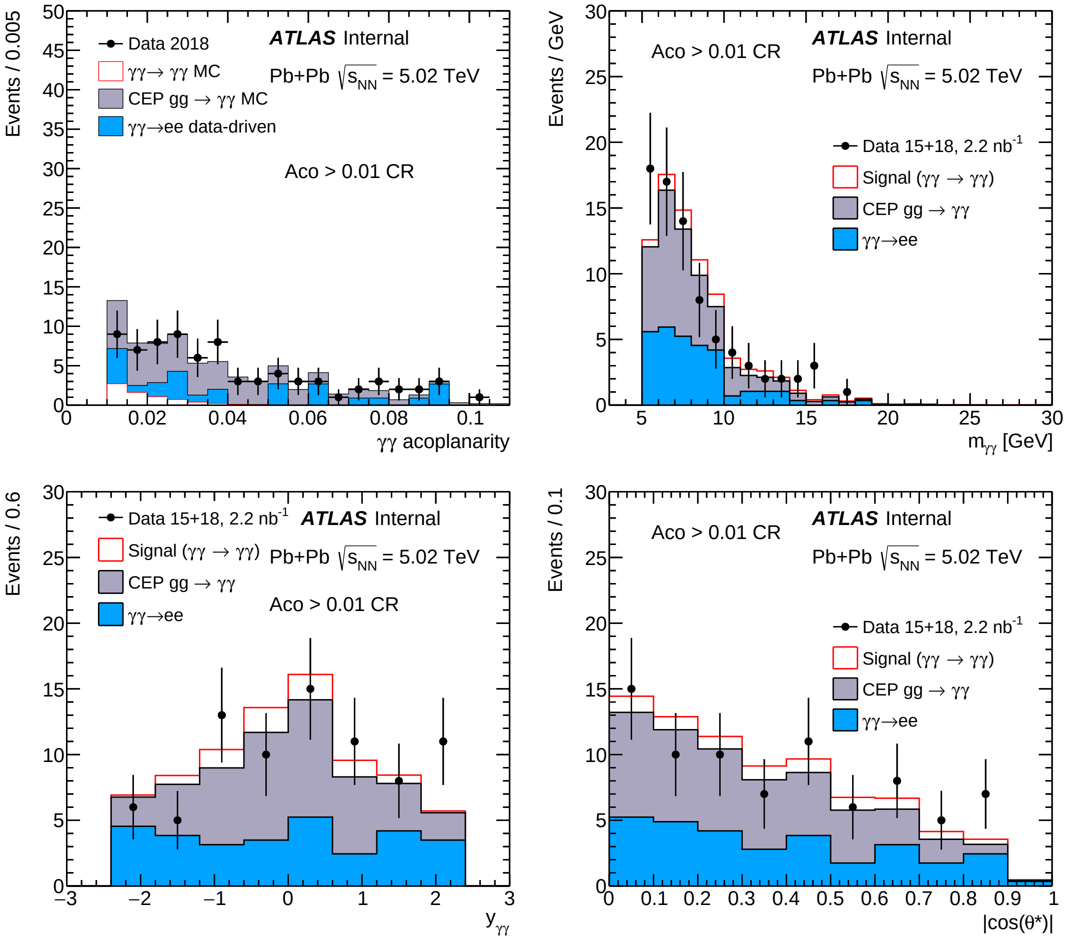

Figure 5.22: Control distributions for events in Aco > 0.01 control region. Diphoton acoplanarity (top left), diphoton invariant mass (top right), diphoton rapidity (bottom left) and photon pseudorapidity difference (bottom right) are shown. The CEP $gg \to \gamma\gamma$ background is normalized to data in this control region.

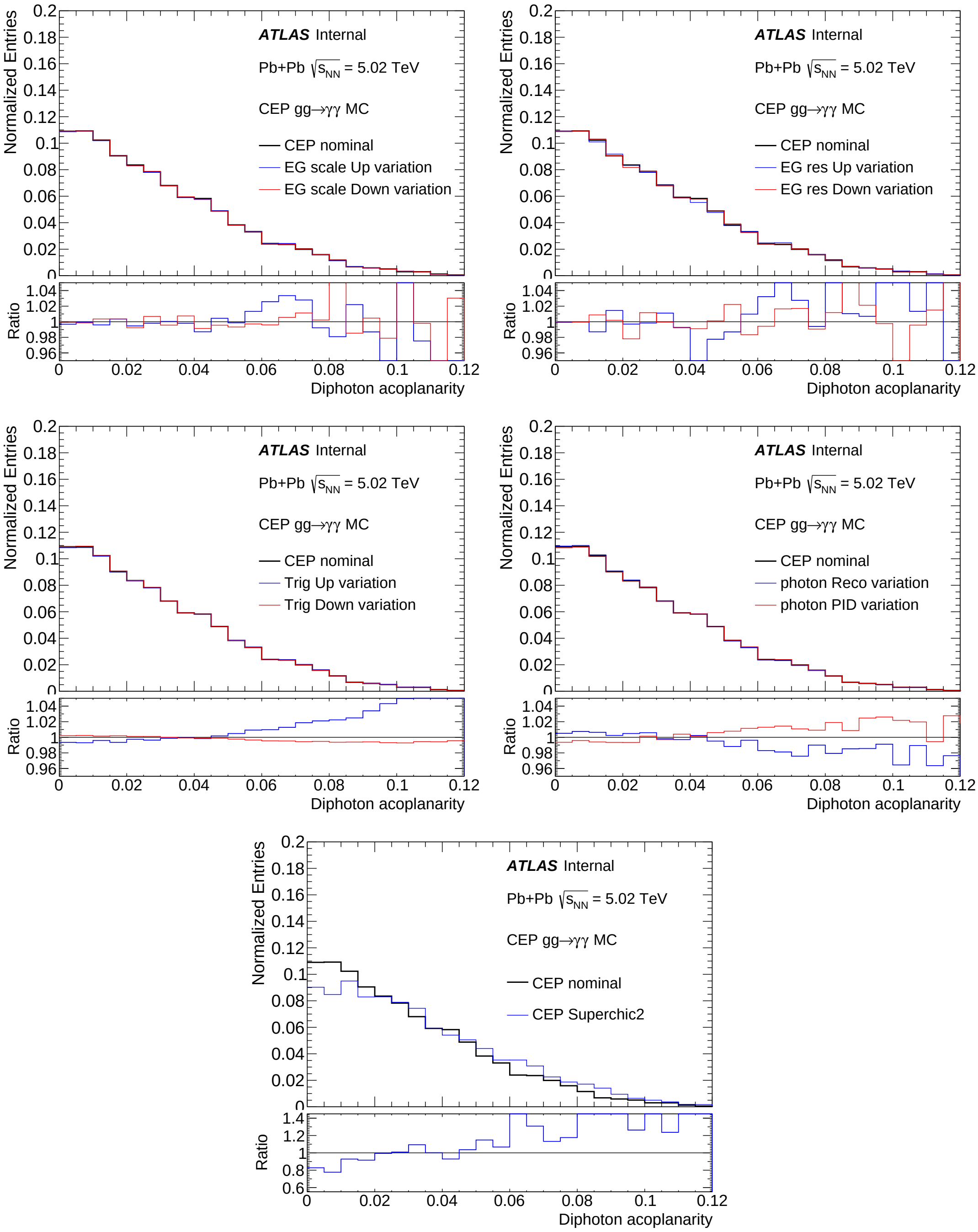

Figure 5.23: Effect of experimental and modeling systematic variations on diphoton acoplanarity shape in CEP MC for 2.5 GeV selection. Different variations are shown (from left to right and top to bottom): EG scale, EG resolution, trigger efficiency, photon reconstruction and PID efficiencies and Superchic2 vs Superchic3 variation.

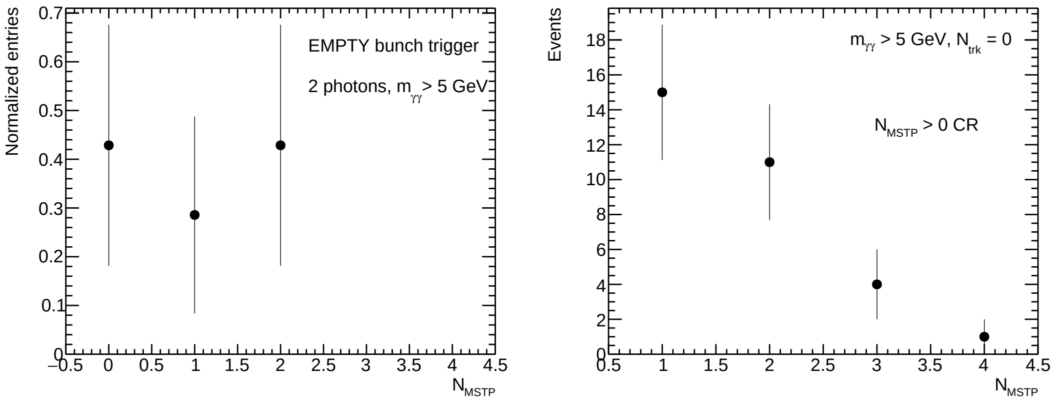

Figure 5.24: Muon spectrometer track particle (MST) multiplicity for diphoton events triggered on empty bunches (left), and in $N_{\text{MST}} > 0$ control region for selected diphoton events after applying $N_{\text{trk}} = 0$ requirement (right).

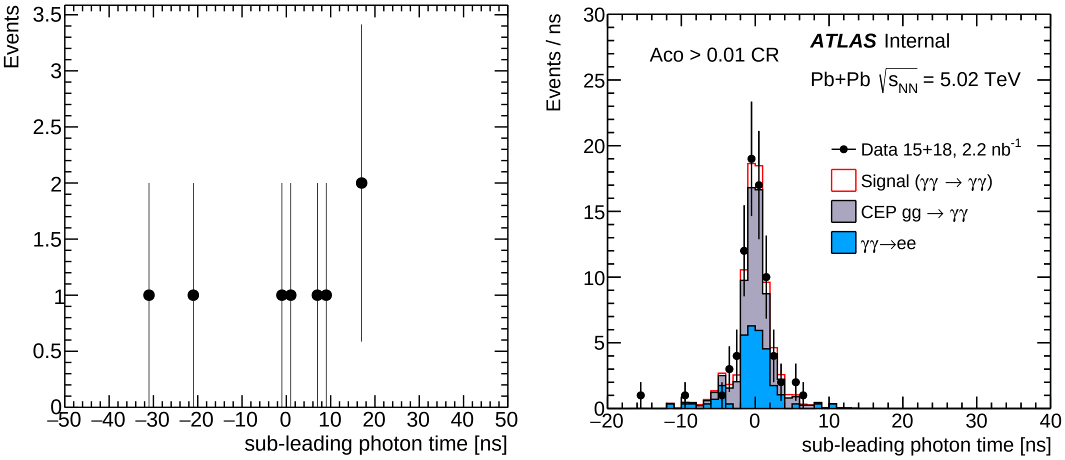

Figure 5.25: Photon time distribution for fake photons triggered on empty bunches (left), and photons from Aco > 0.01 control region (right). In the right figure, data is also compared to MC simulation.

Background	Evaluation method	Event yield in SR
$\gamma\gamma \to e^+e^-$	Data-driven method (Sec. 5.5.1)	12 ± 5
Fake photons (calo noise, cosmics)	Data-driven method (Sec. 5.5.3)	<1
CEP $gg \to \gamma\gamma$	Shape from MC, norm. in Aco $>$ 0.01 CR (Sec. 5.5.2)	13 ± 3
$\gamma\gamma \to qq$	MC simulation [130]	<0.1
$\gamma\gamma \to ee\gamma\gamma$	MC simulation [151]	<0.5
$\gamma\gamma \to \eta_b \to \gamma\gamma$ + γPb $\to \Upsilon \to \gamma\eta_b \to 3\gamma$	Calculations from Refs. [152, 153] + STARlight	negligible
Ion bremsstrahlung	Calculations from Ref. [154]	negligible
Exclusive meson pairs	Calculations from Refs. [147–150]	negligible

Table 5.8: Summary of various background contributions to the signal region, together with short description of the estimation methods.

5.5.4 Other background processes

Quark and gluon final states

Low-p_{T} dijet events can produce multiple π^0 mesons that could potentially mimic diphoton events. The contribution from $\gamma\gamma \to q\bar{q}$ production is estimated using MC simulation (Herwig++). Since low-energy jets usually produce $\mathcal{O}(10)$ charged-particle tracks with $p_{\mathrm{T}} > 100$ MeV, none of the 10^5 simulated events ($m_{q\bar{q}} > 4$ GeV) pass the $N_{\mathrm{Trk}} = 0$ requirement.

Exclusive meson pair production

Exclusive two-meson production can be a potential source of background for LbyL events, mainly due to their similar back-to-back topology. Mesons can fake photons either by their intermediate decay to photons (neutral mesons: π^0, η, η') or by misreconstructed charged-particle tracks for charged mesons ($\pi^+\pi^-$ states). Exclusive meson pairs are usually produced via resonant production at low invariant masses (e.g. $\rho^0(770) \to \pi^+\pi^-$) and the cross sections are suppressed for invariant masses above 5 GeV [146], where only continuum processes are involved. The contribution from $\gamma\gamma \to \pi^+\pi^-$ and $\gamma\gamma \to \pi^0\pi^0$ production is estimated in Refs. [147, 148] and is found to be negligible for $m_{\pi\pi} > 4$ GeV. The $\sigma(gg \to \pi^0\pi^0)/\sigma(gg \to \gamma\gamma)$ ratio is calculated to be below 1% for $p_{\mathrm{T}}^{\pi} > 3$ GeV and $|\eta^{\pi}| < 2.5$ [149]. The CEP ratio of $\sigma(gg \to \eta^{(\prime)}\eta^{(\prime)})$ to $\sigma(gg \to \gamma\gamma)$ is estimated in Ref. [150] to be below 10% for mesons with $p_{\mathrm{T}} > 2.5$GeV. Since the cross sections for exclusive two-meson production are estimated to be very small, these processes are considered to have a negligible contribution to the signal region.

5.5.5 Summary of background estimation in the signal region

Table 5.8 shows the summary of various background contributions to the signal region, together with short description of the estimation methods.

In total, the number of estimated background events in the signal region is: $N_{\mathrm{bkg}} = 25 \pm 6$. Summary of the impact of individual systematic variations on the expected number of background events in the signal region is shown in Table 5.9.

Source of uncertainty	Relative variation
CEP Aco > 0.01 CR stat uncertainty	± 0.08
CEP Superchic2 vs Superchic3 uncertainty	± 0.16
ee CR stat uncertainty	± 0.05
ee CR variation uncertainty	± 0.09
ee $p^{\mathrm{e}}_{\mathrm{mistag}}$ variation uncertainty	± 0.08
EG scale uncertainty	± 0.002
EG resolution uncertainty	± 0.002
Photon angular resolution uncertainty	± 0.01
Trigger uncertainty	± 0.007
photon reco uncertainty	± 0.005
photon PID uncertainty	± 0.004
Total	± 0.22

Table 5.9: Impact of individual systematic variations on the expected number of background events in the signal region.

5.6 Systematic uncertainties

5.6.1 Trigger efficiency

The trigger efficiency has been estimated with $\gamma\gamma \to e^+e^-$ events originating from exclusive e^+e^- production. Three event selection criteria are used in order to estimate a mean value of the trigger efficiency and its systematic uncertainty: nominal, loose and tight. Each selection requires two opposite-sign tracks, two egamma clusters matched to tracks and $\Sigma\ E_{\mathrm{T}}{}^{\mathrm{FCal}}$ lower than noise level + 4σ on each side of FCal. Other requirements are summarized in Table 5.10.

	Track WP	minimum $p_{\mathrm{T}}{}^{\mathrm{track}}$ [GeV]	ΔR	maximum Aco
loose	all	1	0.7	0.2
nominal	HILoose	1	0.5	0.01
tight	HILoose	2	0.3	0.01

Table 5.10: Summary of requirements used for loose, nominal and tight e^+e^- candidate selections for trigger efficiency measurements.

The statistical uncertainties are estimated based on the variation of fit parameters by their respective σ values. The systematic uncertainties are estimated using the loose and tight e^+e^- selection criteria. The upper uncertainty is the absolute value of the difference between fits for nominal and tight selections while the lower uncertainty is an absolute value of the difference between fits for nominal and loose selections. Figure 5.26 presents the relative uncertainties of Level-1 trigger efficiency, which for $(E_{\mathrm{T}}^{\mathrm{cluster1}} + E_{\mathrm{T}}^{\mathrm{cluster2}}) > 7\,\mathrm{GeV}$ do not exceed 4%.

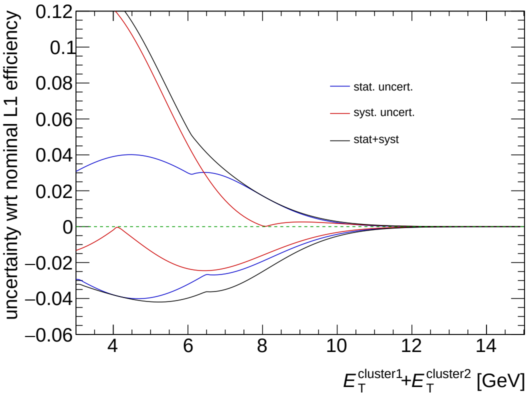

Figure 5.26: Relative statistical and systematic uncertainties of Level-1 trigger efficiency.

As an extra cross-check, the efficiency of the Level-1 trigger is also derived as a function of absolute rapidity of the electron pair. For this purpose, an additional requirement of $E_{\mathrm{T}}^{\mathrm{cluster1}} + E_{\mathrm{T}}^{\mathrm{cluster2}} > 5$ GeV is imposed in the event selection. Given the low number of e^+e^- candidates recorded by the supporting triggers, the result for the nominal selection shown in Fig. 5.27, is presented in three bins in $|y_{\mathrm{ee}}|$. The efficiency is flat in $|y_{\mathrm{ee}}|$ within statistical uncertainties.

In total, the impact of Level-1 trigger efficiency uncertainty on signal is 6%.

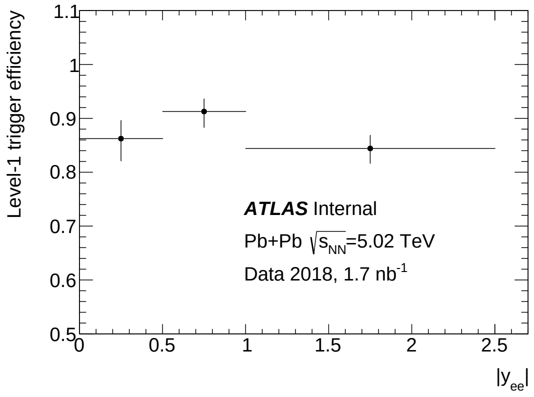

Figure 5.27: Level-1 trigger efficiency as a function of absolute rapidity of the electron pair for $\gamma\gamma \rightarrow e^+e^-$ events passing one of the supporting triggers.

5.6.2 Photon reconstruction efficiency

The uncertainty on the photon reconstruction and PID efficiencies is estimated by parameterizing the scale factors as a function of the photon pseudorapidity, instead of the photon transverse momentum (see Figures 5.29 and 5.31). This impacts C factor by 5% for photon reconstruction corrections and by 1% for photon PID corrections, which is taken as systematic uncertainty. As an additional check, the photon PID efficiency correction factors derived from FSR photon sample are compared to the correction factors built using $\gamma\gamma \rightarrow e^+e^-(\gamma)$ bremsstrahlung photons (Figure 5.28). The difference, propagated to the overall correction factor, is below 1% and is taken as systematic uncertainty. The statistical uncertainty on photon reconstruction and PID efficiency corrections is propagated using the pseudo-experiment method in which the correction factors are randomly shifted in an ensemble of pseudo-experiments according to the mean and standard deviation of the correction factor. This gives negligible impact on C.

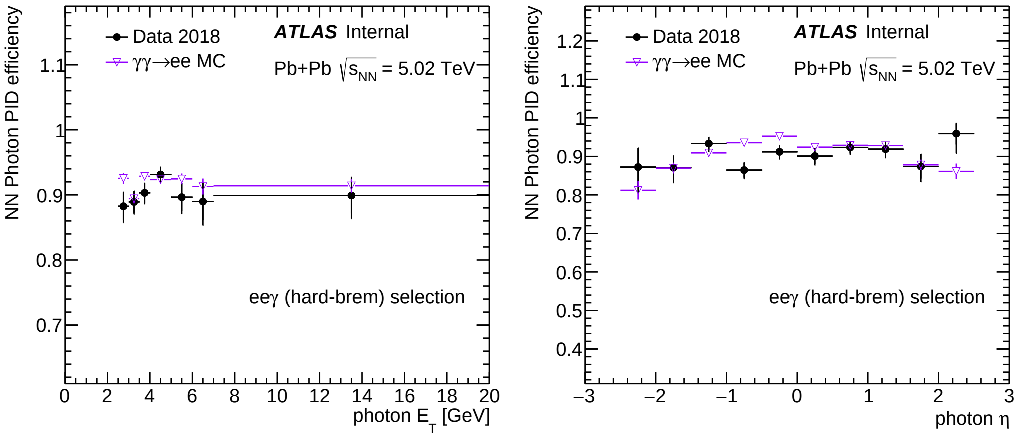

Figure 5.28: Photon PID efficiency as a function of photon E_{T} (left) and photon η (right) extracted from hard bremsstrahlung photon sample from $\gamma\gamma \rightarrow e^+e^-$ process. Data (black points) are compared with $\gamma\gamma \rightarrow e^+e^-$ MC (open points).

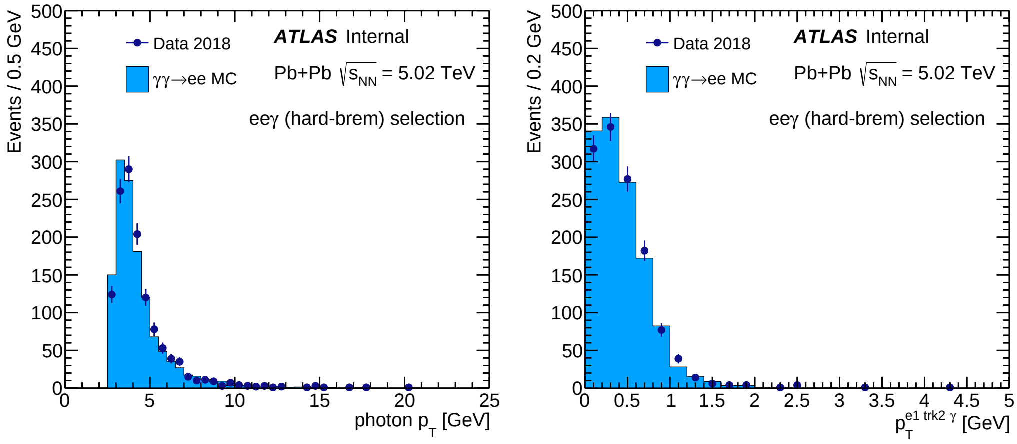

Figure 5.29: Hard-bremsstrahlung photon properties from $\gamma\gamma \to e^+e^-$ events: E_{T} distribution (left) and transverse momentum of $ee\gamma$ system (right).

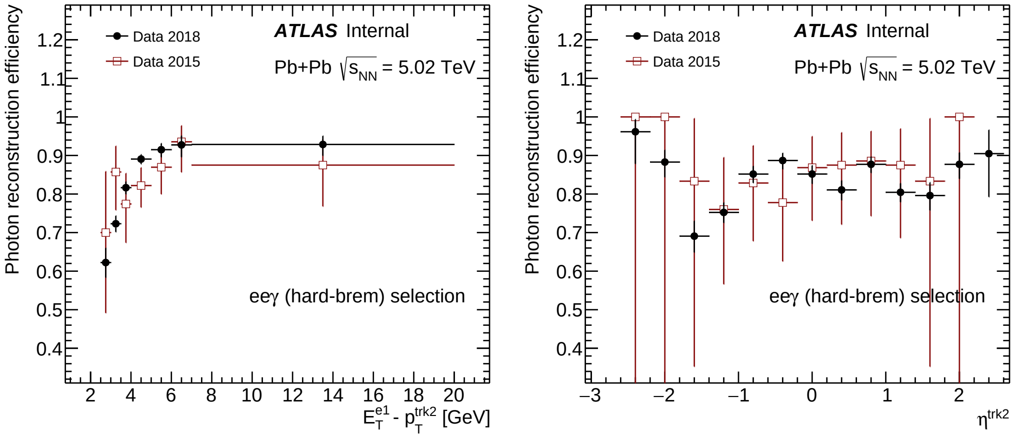

Figure 5.30: Photon reconstruction efficiency in data as a function of photon E_{T} (left, approximated with $E_{\mathrm{T}}^{e} - p_{\mathrm{T}}^{trk2}$) and photon η (right, approximated with η^{trk2}) extracted from $\gamma\gamma \to e^+e^-$ events with hard bremsstrahlung photon. Data 2018 (black points) are compared with data 2015 (dark red squares).

5.6.3 Photon energy scale and energy resolution

The uncertainties related to the photon energy scale and resolution are taken from the official EGamma CP tool [138]. The impact of the relevant variations on the simulated signal yield is 1% for energy scale variations and 2% for energy resolution variations.

5.6.4 Photon angular resolution

The uncertainty due to the knowledge of photon angular resolution is estimated using electron clusters from $\gamma\gamma \to e^+e^-$ process.

The electrons from the $\gamma\gamma \to e^+e^-$ reaction are well balanced in their transverse momenta, with very small initial (truth) smearing $\sigma^{MCtruth}_{\phi^{e1}-\phi^{e2}} < 0.001$, much smaller than the expected angular resolution of the cluster.

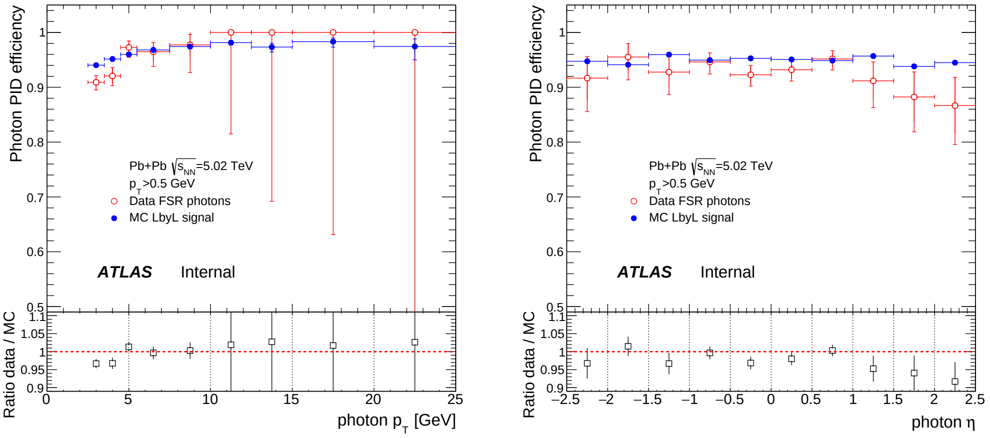

Figure 5.31: Very loose photon PID efficiency as a function of photon p_{T} (left) and η (right) extracted from FSR event candidates in 2018 data (open markers) and MC simulation (full markers). A ratio of the data over MC simulation is given in the lower panel.

By measuring $(|\phi^{\text{cluster1}} - \phi^{\text{trk1}}| - |\phi^{\text{cluster2}} - \phi^{\text{trk2}}|)$ distributions in $\gamma\gamma \to e^+e^-$ events and assuming that tracking angular resolution is much smaller than the calorimeter angular resolution, one can extract $\sigma_{\phi^{\text{cluster}}}$ that follows the formula:

$$\sigma_{\phi^{\text{cluster}}} \approx \frac{(|\phi^{\text{cluster1}} - \phi^{\text{trk1}}| - |\phi^{\text{cluster2}} - \phi^{\text{trk2}}|)}{\sqrt{2}} ., \tag{5.10}$$

Figure 5.32 shows the $(|\phi^{\text{cluster1}} - \phi^{\text{trk1}}| - |\phi^{\text{cluster2}} - \phi^{\text{trk2}}|)/\sqrt{2}$ distributions in different electron E_{T} bins. At low electron E_{T}, extra tails are visible, which are due to hard-bremsstrahlung emissions. After fitting to the central peak of the spectrum (which should correspond to the "proper" electron cluster without hard-bremstrahlung emissions) the single-electron cluster phi resolution is $\sigma_{\phi}^{e\text{ cluster}} \approx 0.011 - 0.013$ in data and $\sigma_{\phi}^{e\text{ cluster}} \approx 0.010 - 0.011$ in MC. When subtracting these numbers of quadrature, this translates into extra $\sigma_{\phi} \approx 0.006$ single-cluster smearing which is needed in ee MC to describe the data.

After applying the extra $\sigma_{\phi} \approx 0.006$ smearing to photons in signal MC, the detector correction factor changes by 2%, which is taken as systematic uncertainty. The impact of this variation on CEP acoplanarity shape is minor, resulting in a 1% variation of the expected CEP event yield in the signal region.

5.6.5 Alternative signal MC sample

The uncertainty due to the choice of signal MC generator is estimated by using alternative signal MC sample, as detailed in Section 5.2. A difference in the C-factor value between these samples is 1%, which is taken as systematic uncertainty.

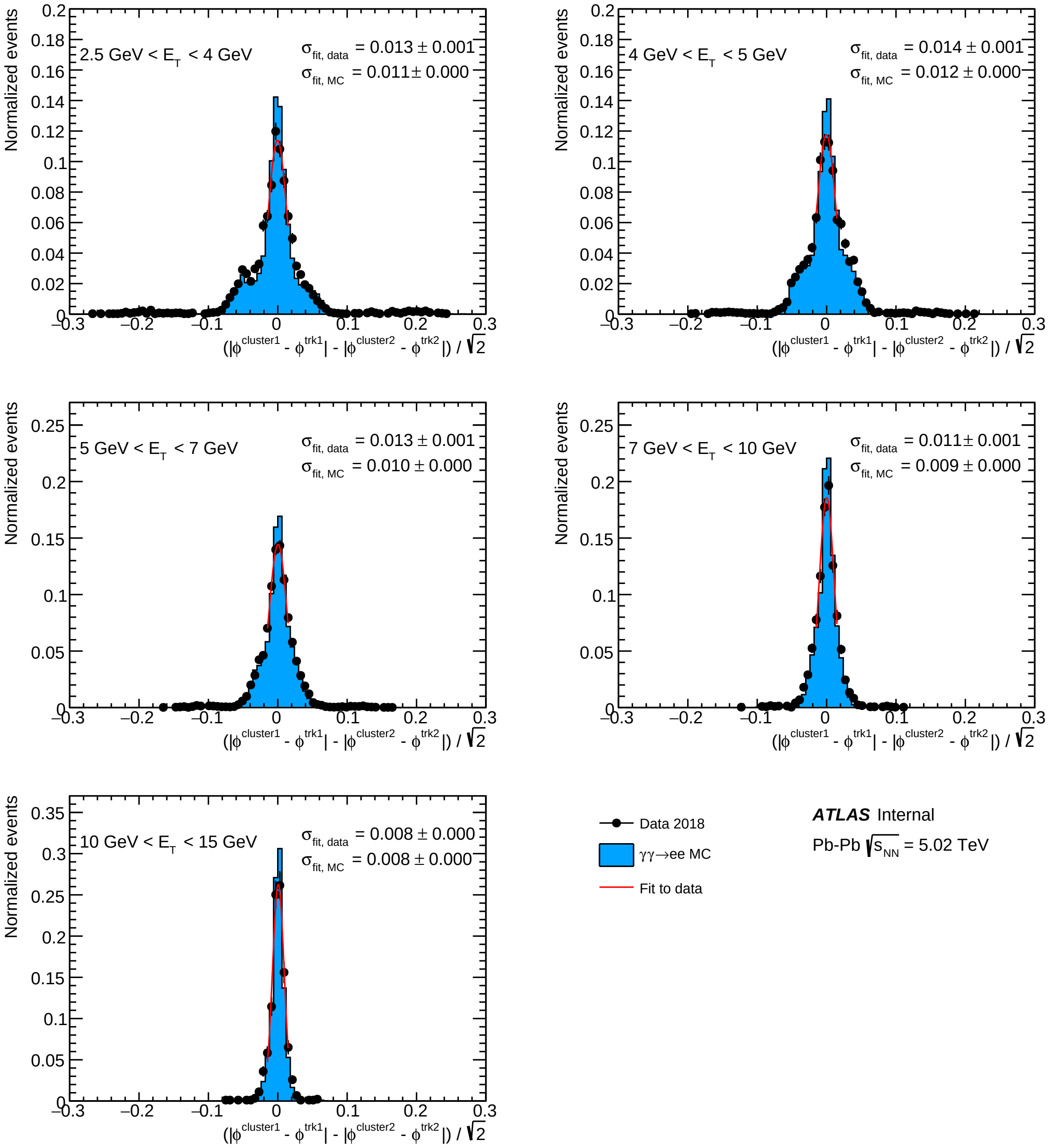

Figure 5.32: $(|\phi^{\text{cluster1}} - \phi^{\text{trk1}}| - |\phi^{\text{cluster2}} - \phi^{\text{trk2}}|)/\sqrt{2}$ distribution for electrons in $\gamma\gamma \to e^+e^-$ events. Different electron E_{T} ranges are shown. Data (black points) is compared to $\gamma\gamma \to e^+e^-$ MC (blue histograms). The gaussian fit to the data in the central part of each spectrum is shown as red line.

5.7 Results

5.7.1 Results with the 2018 data

5.7.1.1 Kinematic distributions

After applying the signal selection, 59 events are observed in the data where 30 ± 4 signal events and 12 ± 3 background events are expected. The compatibility of

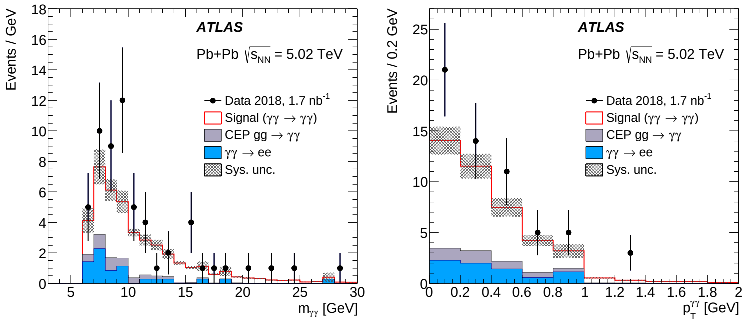

(a) (b)

Figure 5.33: (a) Diphoton invariant mass and (b) diphoton transverse momentum for events satisfying the signal selection. Data (points) are compared with the sum of signal and background expectations (histograms). Systematic uncertainties of the signal and background processes, excluding that of the luminosity, are shown as shaded bands.

the data with the background-only hypothesis has been evaluated in a narrower $0 < \text{Aco} < 0.005$ range, which in studies using simulated data was found to be most sensitive. In this region, 42 events are observed in the data where 25 ± 3 signal events and 6 ± 2 background events are expected. The data excess is quantified by calculating the p -value using a profile likelihood-ratio test statistic [155], resulting in an observed (expected) statistical significance of 8.2(6.2) standard deviations. Photon kinematic distributions for events satisfying all selection criteria are shown in Figure 5.33.

5.7.1.2 Cross section measurement

The cross section for the $\gamma\gamma \rightarrow \gamma\gamma$ process is measured in a fiducial phase space, defined by the following requirements on the diphoton final state, reflecting the selection at reconstruction level: Both photons have to be within $|\eta| < 2.4$ with a transverse energy of $E_{\mathrm{T}} > 3$ GeV. The invariant mass of the di-photon system has to be $m_{\gamma\gamma} > 6\,\text{GeV}$ with a transverse momentum of $p_{\mathrm{T}}^{\gamma\gamma} < 1$ GeV. In addition, the photons must be back-to-back, i.e. fulfil an acoplanarity requirement of $1 - \frac{\Delta\phi_{\gamma\gamma}}{\pi} < 0.01$. Experimentally, the fiducial cross section is given by

$$\sigma_{\text{fid}} = \frac{N_{\text{data}} - N_{\text{bkg}}}{C \times \int L dt} \text{ , ,} \tag{5.11}$$

where $N_{\text{data}} = 59$ is the number of selected events in data, $N_{\text{bkg}} = 12 \pm 3$ is the number of background events, $\int L dt = 1.73 \pm 0.07\ \text{nb}^{-1}$ is the integrated luminosity of the data sample and C is the overall correction factor that accounts for efficiencies and resolution effects. The C factor is defined as the ratio of the number of reconstructed MC signal events passing the selection to the number of generated MC signal events satisfying the fiducial requirements.

The value of C is found to be: $C = 0.350 \pm 0.024$. The main source of the inefficiency is due to the trigger and photon reconstruction inefficiencies. These requirements together are 40% efficient. The photon PID efficiency gives 85% efficiency (for both photons). The track and pixel track veto are 93% efficient, and the $p_{\mathrm{T}}^{\gamma\gamma}$ requirements are 92% efficient. The uncertainty on C is estimated by varying

Source of uncertainty	Detector correction (C)
	0.350
Trigger efficiency	2%
Photon reco efficiency	4%
Photon PID efficiency	2%
Photon energy scale	2%
Photon energy resolution	2%
Photon angular resolution	2%
Alternative signal MC	1%
Signal MC statistics	1%
Total	7%

Table 5.11: The detector correction factor, C, and its uncertainties.

the data/MC correction factors within their uncertainties, in particular for the photon reconstruction/PID efficiency, photon energy scale/resolution and trigger efficiency.

An overview of the various uncertainties on C is given in Table 5.12.

The measured fiducial cross section is $\sigma_{\text{fid}} = 78 \pm 13$ (stat.) ± 7 (syst.) ± 3 (lumi.) nb. which can be compared to the predicted values of 51 ± 5 nb from Ref. [125] and 50 ± 5 nb from SuperChic3 MC [124].

5.7.1.3 Significance

The compatibility of the data with the background-only hypothesis has been evaluated in the region $0 <$ Aco < 0.005, which corresponds to the first bin of diphoton acoplanarity distribution from Fig. 5.34. A test statistic, t_μ, based on the asymptotic approximation of the profile likelihood ratio [155] is used to evaluate the signal strength parameter, μ (defined as the scaling of the signal histogram which produces the best agreement with data). The scan of the profile likelihood $-2\Delta \ln L$ is plotted

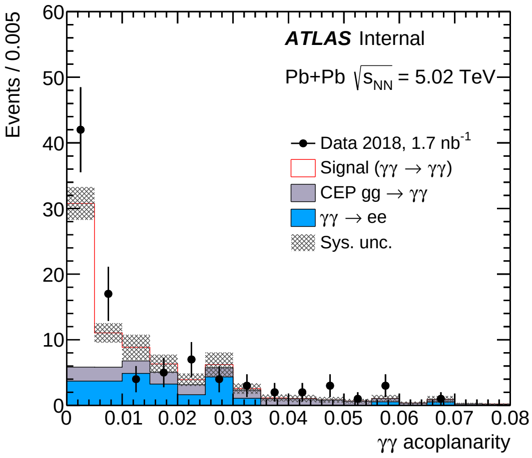

Figure 5.34: The diphoton acoplanarity distribution for events satisfying signal region selection, but before applying Aco < 0.01 requirement. The CEP $gg \to \gamma\gamma$ background is normalized in the Aco > 0.01 control region. Data are shown as points with statistical error bars, while the histograms represent the expected signal and background levels. The shaded band represents the uncertainties on signal and background predictions, excluding the uncertainty on the luminosity.

in Fig. 5.35 as a function of μ for both the observed data, and the signal and background expectation.

The p-value for the null (background-only) hypothesis is $\approx 10^{-16}$, which corresponds to $\mu = 0$ in Fig. 5.35 and a significance of 8.2σ.

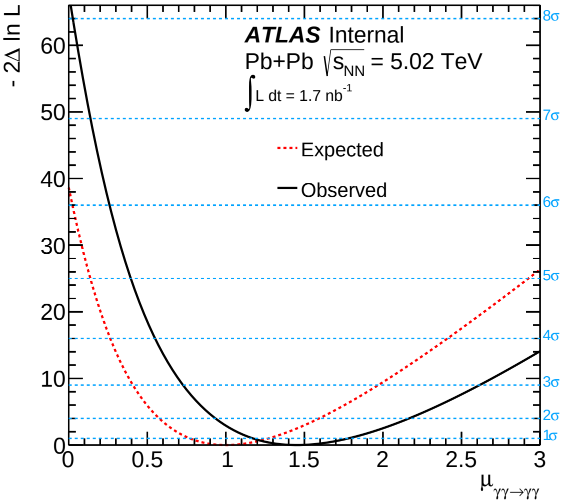

Figure 5.35: Scan of the profile likelihood as a function of the signal strength, μ, relative to the expectation for the process $\gamma\gamma \to \gamma\gamma$. The observed significance for the background only hypothesis ($\mu = 0$) is 8.2σ, whilst the expected significance is 6.2σ.

5.7.2 Results with the combined 2018 and 2015 data

5.7.2.1 Kinematic distributions

Photon kinematic distributions comparing the selected data with a sum of signal and background processes in the signal region are shown in Fig. 5.36. In total, 97 events are observed in data where 45 signal events and 27 background events are expected. Fair agreement between data and expectations is observed for the shapes of various kinematic distributions whereas the overall normalisation is predicted slightly lower than observed. An event display of the highest invariant mass (29GeV) event is shown in Figure 5.37

5.7.2.2 Fiducial cross section

The inclusive cross section for the $\gamma\gamma \to \gamma\gamma$ process is measured in a fiducial phase space, defined by the following requirements on the diphoton final state, reflecting the selection at reconstruction level: both photons have to be within $|\eta| < 2.4$ with a transverse momentum of $p_{\mathrm{T}} > 2.5$ GeV. The invariant mass of the diphoton system has to be $m_{\gamma\gamma} > 5\,\mathrm{GeV}$ with transverse momentum of $p_{\mathrm{T}}^{\gamma\gamma} < 1$ GeV. In addition, the photons must fulfil an acoplanarity requirement of Aco < 0.01.

The fiducial cross section is obtained as follows:

$$\sigma_{\text{fid}} = \frac{N_{\text{data}} - N_{\text{bkg}}}{C \times \int Ldt}\,,, \tag{5.12}$$

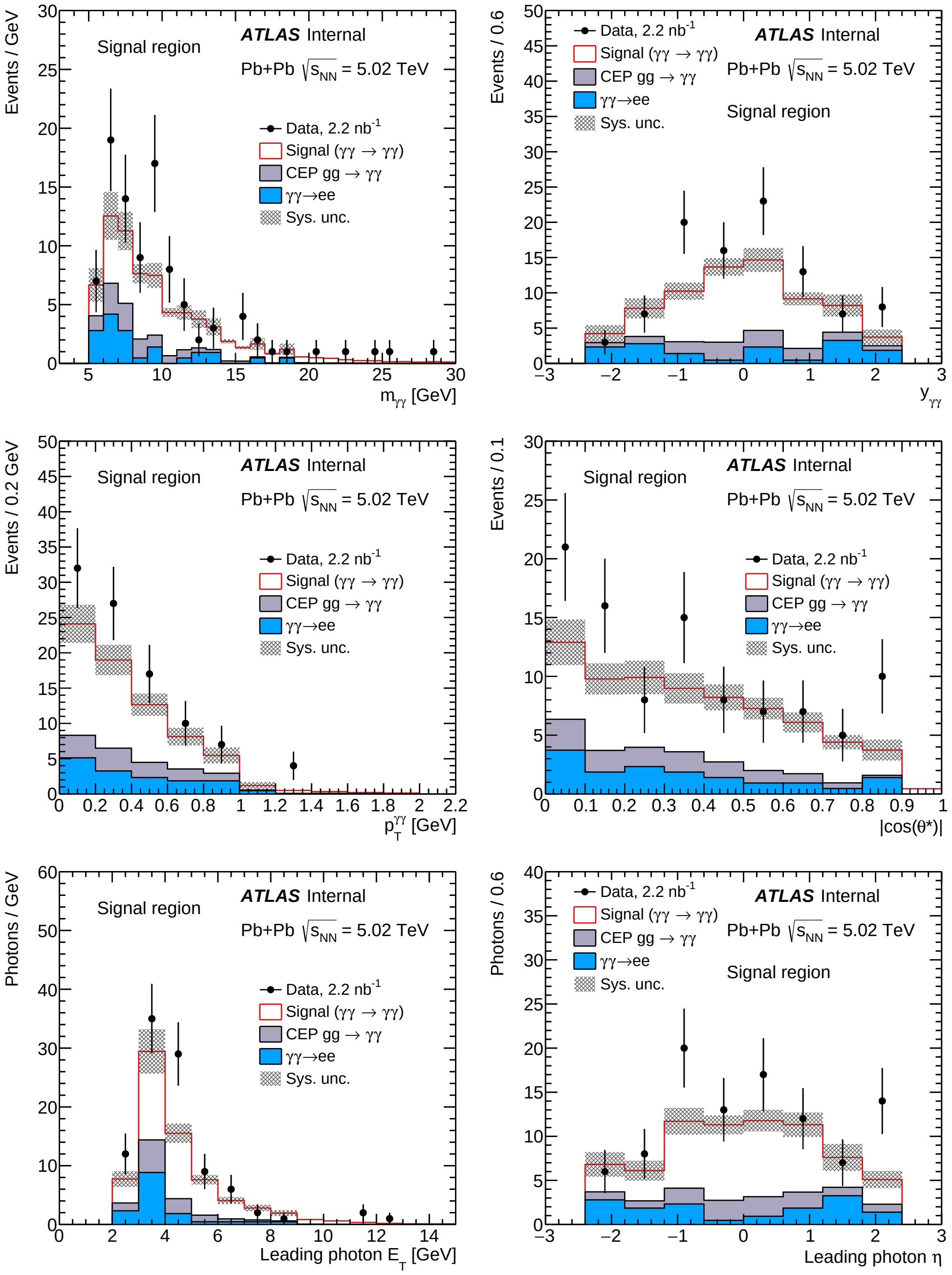

Figure 5.36: Kinematic distributions for $\gamma\gamma \to \gamma\gamma$ event candidates: diphoton invariant mass (top-left), diphoton rapidity (top-right), diphoton transverse momentum (mid-left), diphoton $|\cos(\theta^{*})|$ (mid-right) leading photon transverse energy (bottom-left) and photon pseudorapidity (bottom-left). Data (points) are compared to the sum of signal and background expectations (histograms). Systematic uncertainties on the signal and background processes, excluding that on the luminosity, are denoted as shaded bands.

where $N_{\text{data}} = 97$ is the number of selected events in data, $N_{\text{bkg}} = 27 \pm 5$ is the number of background events, $\int L dt = 2.22 \pm 0.07$ nb^{-1} is the integrated luminosity of the data sample and $C = 0.263 \pm 0.021$ is the overall correction factor that accounts for efficiencies and resolution effects. The C factor is defined as the ratio of the number of reconstructed MC signal events passing the selection to the number of

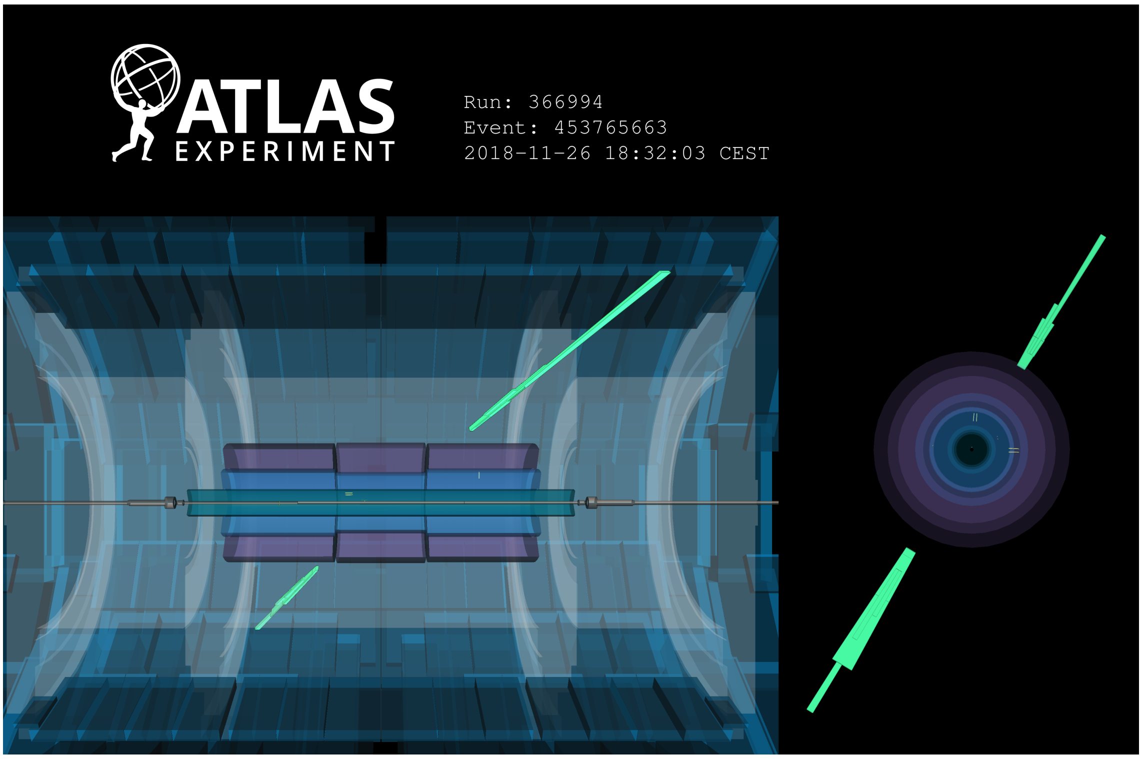

Figure 5.37: Event display for an exclusive $\gamma\gamma \to \gamma\gamma$ candidate. Event 453765663 from run 366994 recorded on 2018.11 .26 at 18: 32: 03 is shown. Two back-to-back photons $\left(E_{\mathrm{T}}^{\gamma 1} = 11\mathrm{GeV}\right.$ and $\left.E_{\mathrm{T}}^{\gamma 2} = 10\mathrm{GeV}\right)$ with an invariant mass of 29GeV and no additional activity in the detector are presented. All calorimeter cells with various E_{T} thresholds are shown: $E_{\mathrm{T}} > 250\mathrm{MeV}$ for EMB, EMEC and Tile, $E_{\mathrm{T}} > 800\mathrm{MeV}$ for HEC, and $E_{\mathrm{T}} > 1000\mathrm{MeV}$ for FCal.

Source of uncertainty	Detector correction (C)
	0.263
Trigger efficiency	5%
Photon reco. efficiency	4%
Photon PID efficiency	2%
Photon energy scale	1%
Photon energy resolution	2%
Photon angular resolution	2%
Alternative signal MC	1%
Signal MC statistics	1%
Total	8%

Table 5.12: The detector correction factor, C, and its uncertainties for the fiducial cross-section measurement.

generated MC signal events satisfying the fiducial requirements.

The uncertainty on C is estimated by varying the data/MC correction factors within their uncertainties as described in Section 5.6, in particular for the photon reconstruction and PID efficiencies, photon energy scale and resolution and trigger efficiency. An overview of the various uncertainties on C is given in Table 5.12.

The measured fiducial cross section is $\sigma_{\text{fid}} = 120 \pm 17\ (\text{stat.}) \pm 13\ (\text{syst.}) \pm 4\ (\text{lumi.})$

nb, which can be compared to the predicted values of 80 ± 8 nb from Ref. [125] and 78 ± 8 nb from SuperChic3 MC [124].

5.7.2.3 Differential cross sections

Differential cross sections as a function of diphoton invariant mass, diphoton absolute rapidity, average photon transverse momentum and diphoton $|\cos\theta^*|$ where :

$$|\cos(\theta^*)| = \left|\tanh\left(\frac{\Delta\eta_{\gamma\gamma}}{2}\right)\right|, \tag{5.13}$$

are unfolded to particle level in the fiducial phase space described in the previous section.

The differential cross sections are determined using an iterative Bayesian unfolding method [156] with one iteration for all distributions. The unfolding procedure corrects for bin migrations between particle- and detector-level distributions due to detector resolution effects, and applies reconstruction efficiency as well as fiducial corrections. The reconstruction efficiency corrects for events inside the fiducial region that are not reconstructed in the signal region due to detector inefficiencies; the fiducial corrections take into account events that are reconstructed in the signal region, but originate from outside the fiducial region. The backgrounds are subtracted from data prior to unfolding.

The statistical uncertainty of the data is estimated using 1000 Poisson-distributed pseudo-data sets, constructed by smearing the observed number of events in each bin of the detector-level distribution. The root mean square of the differences between the resulting unfolded distributions and the unfolded data is taken as the statistical uncertainty in each bin. In the measurement of differential cross sections, a full set of experimental systematic uncertainties is considered as described in Section 5.6. In addition, uncertainties due to the unfolding procedure and the modelling of the signal process are considered by repeating the cross-section extraction with modified inputs. This is estimated by reweighting the distribution at generator level to improve the agreement between data and simulation after event reconstruction. The obtained prediction at detector level, which is then very similar to data, is unfolded with the input of the default unfolding and the difference from the reweighted prediction at generator level is considered as an uncertainty. The impact of statistical uncertainties in the signal simulation is estimated using pseudo-data.

The unfolded differential cross-sections are shown in Fig. 5.38. They are compared with the predictions from SuperChic v3.0, which provide a fair description of the data, except for the overall normalisation differences. Global χ^2 comparisons are carried out for the shapes of differential distributions. They do not display any significant differences between predictions and data with the largest χ^2 per degree of freedom being 5.8/4 when comparing the shape of $|\cos(\theta^*)|$ distribution.

The cross sections for all distributions shown here, including normalised differential cross sections, are available in HepData [157].

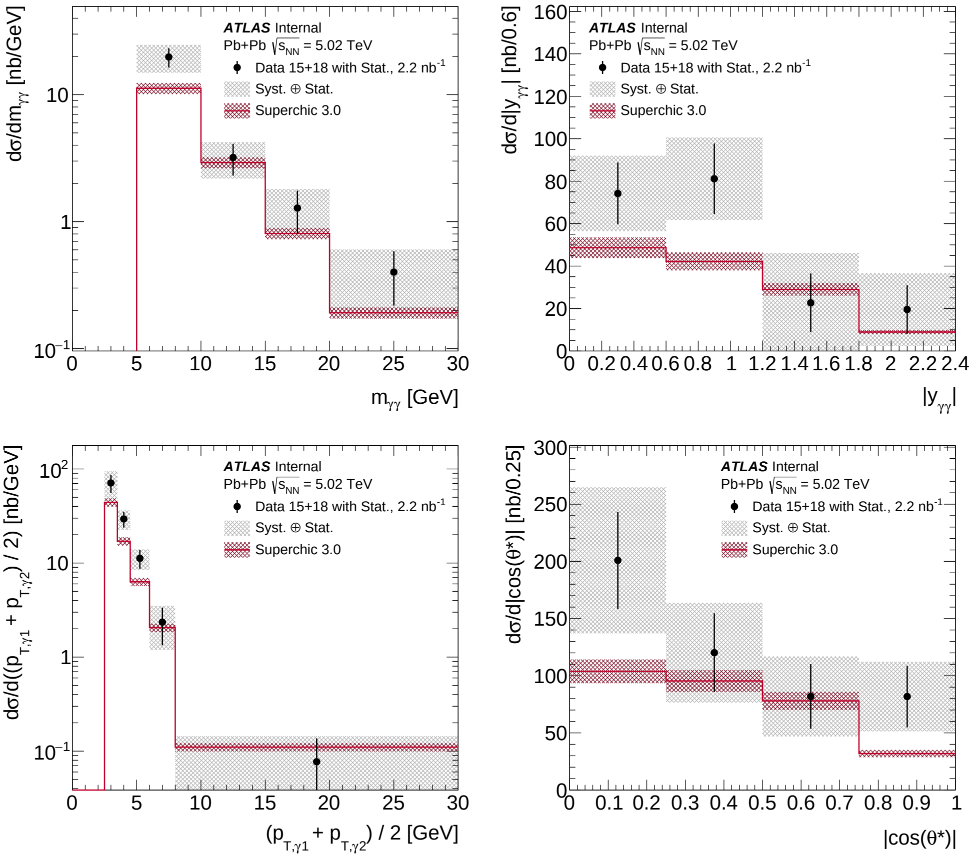

Figure 5.38: Measured differential cross sections of $\gamma\gamma \to \gamma\gamma$ production in Pb+Pb collisions at $\sqrt{s_{\mathrm{NN}}} = 5.02$ TeV for four observables (from left to right and top to bottom): diphoton invariant mass, diphoton absolute rapidity, average photon transverse momentum and diphoton $|\cos(\theta^{*})|$. The measured cross-section values are shown as points with error bars giving the statistical uncertainty and grey bands indicating the size of the total uncertainty. The results are compared with the prediction from the SuperChic v3.0 MC generator (solid line) with bands denoting the theoretical uncertainty.

Conclusion

This chapter describes the observation of the light-by-light scattering process in quasi-real photon interactions from ultra-peripheral Pb+Pb collisions at $\sqrt{s_{\mathrm{NN}}} = 5.02$ TeV by the ATLAS experiment. The analysis was carried out with 2015 and 2018 data sets. The 2018 data set corresponds to an integrated luminosity of 1.7 nb^{-1}. After applying all selection criteria to the data, 59 events are observed in the data where 30 ± 4 signal events and 12 ± 3 background events are expected. The dominant background processes, i.e. CEP $gg \to \gamma\gamma$, $\gamma\gamma \to e^+e^-$ as well as other fake-photon backgrounds, are estimated using data-driven methods. The significance is determined to be 8.2 standard deviations. After background subtraction and analysis corrections, the cross section of the $\gamma\gamma \to \gamma\gamma$ process for photon transverse momentum, $E_{\mathrm{T}} > 2.5$ GeV, photon pseudorapidity, $|\eta| < 2.4$, invariant mass of the diphoton system, $m_{\gamma\gamma} > 6$ GeV, diphoton transverse momentum, $p_{\mathrm{T}}^{\gamma\gamma} < 1$ GeV and diphoton acoplanarity below 0.01 is measured to be 78±13 (stat.)±7 (syst.)±3 (lumi.) nb.

A second measurement based on the full Run 2 dataset (2015+2018) corresponding to 2.2 nb^{-1}have been performed. After the final selection criteria are applied to the data, 97 events are observed, while 27 ± 5 background events are expected. The dominant background processes are estimated using data-driven methods.

After background subtraction and corrections for all detector effects, the fiducial cross section of the $\gamma\gamma \to \gamma\gamma$ process for photon transverse momentum, $E_{\mathrm{T}} > 2.5$ GeV, photon pseudorapidity, $|\eta| < 2.4$, invariant mass of the diphoton system, $m_{\gamma\gamma} > 5$ GeV, diphoton transverse momentum, $p_{\mathrm{T}}^{\gamma\gamma} < 1$ GeV and diphoton acoplanarity below 0.01 is measured to be $\sigma_{\mathrm{fid}} = 120 \pm 17$ (stat.) ± 13 (syst.) ± 4 (lumi.) nb. Differential cross sections are measured as a function of several variables of the final-state photons and are compared with theory predictions. Data and theory show fair agreement for all differential distributions, except for the overall normalisation differences. The measurement precision is limited in all kinematic regions by statistical uncertainties. The measured diphoton invariant mass distribution is used to search for axion-like particles and set new exclusion limits on their production. To date, the derived exclusion limits are best over the mass range of $6 < m_{\mathrm{a}} < 100$ GeV.

Chapter 6

Search for axion like particle

Contents

Introduction

QCD suggests that if you reverse a particle's charge and parity (i.e., reverse its electrical charge and look at it in a mirror), it would no longer follow exactly the same physical laws. Yet, nothing in the experimental results indicates this is the case. This conflict between theory and experiments constitutes a serious enigma, a crack in the beautiful edifice of the Standard Model, our best model of particle physics. This crack constitutes the "strong CP problem". The QCD Lagrangian includes a CP-violating term :

$$\mathcal{L}_{\text{strong}}\ \text{CP} = -\bar{\theta}\frac{\alpha_s}{8\pi}G^{\mu\nu a}\tilde{G}^{a}_{\mu\nu}, \tag{6.1}$$

where $-\pi \leq \bar{\theta} \leq +\pi$ is the effective θ parameter after diagonalizing quark masses, $G^{\mu\nu a}$ is the color field strength tensor, and $\tilde{G}^{a}_{\mu\nu} \equiv \frac{1}{2}\epsilon^{\mu\nu\lambda\rho}G^{a}_{\lambda\rho}$, with $\varepsilon^{0123} = 1$, its dual.

An Axion is a hypothetical particle introduced by Peccei and Quinn in 1977 to solve CP problem in quantum chromodynamics [72]. The axion being the pseudo Nambu-Goldstone boson responsible for breaking the global Peccei-Quinn symmetry by its anomalous triangle coupling to gluons.

$$\mathcal{L} = \left(\frac{\phi_A}{f_A} - \bar{\theta}\right)\frac{\alpha_s}{8\pi}G^{\mu\nu a}\tilde{G}^{a}_{\mu\nu}, \tag{6.2}$$

In this chapter we gives a short overview about Axion Like Particles (ALPs) which are also pseudo-scalar, but unlike axion they don't intend solving the QCD problem. Section 6.1 is dedicated to introduce ALPs, while in section 6.2 were present experimental approaches for searching for ALPs. Sections 6.3 and 6.4 are dedicated to the ALPs search at the LHC and results of the later using heavy ions collisions respectively.

6.1 Axion Like Particles (ALPs)

ALPs share many of the theoretical and phenomenological aspects of axions. ALPs are also pseudo Nambu-Goldstone bosons, however, they do not interact via the PQ mechanism (breaking the global Peccei-Quinn symmetry). Thus don't solve the QCD CP violation problem. They can get mass from other dynamics. Most of the cases they are predicted to couple to photons, electrons or nucleons.

6.2 Experimental approaches

Constraint on axion and ALPs have been made essentially from three approaches

6.2.1 terrestrials approaches

Two main experimental techniques are used to search for ALPs on earth. Light-shining-through-a-wall (LSW), helioscope and haloscopes experiments.

6.2.1.1 Light-shining-through-a-wall (LSW)

These experiments (Figure 6.1) aim for producing and detecting axions in the laboratory. They do not rely on cosmological or astrophysical assumptions. In the first section of such an experiment, laser light is shone through a strong magnetic field, where axions can be generated via a reverse process. A second section of the experiment is separated from the first one by a light- tight wall which can only be surpassed by axions. These particles would stream through a strong magnetic field behind the wall allowing for a re-conversion into photons. This effect will give the impression of light-shining-through-a-wall (LSW).

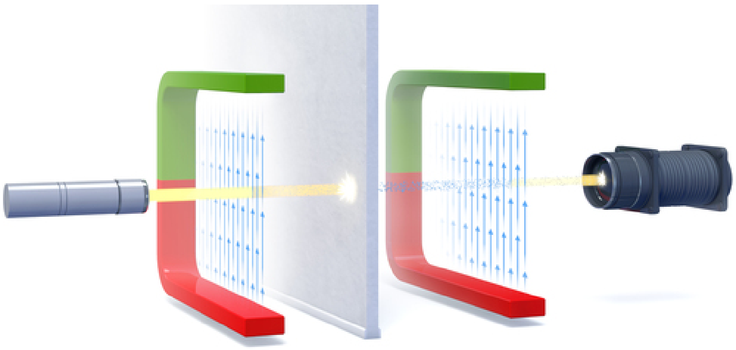

Figure 6.1: Scheme of a light-shining-through a wall experiment: light, typically from a strong laser, is shone into a magnetic field.

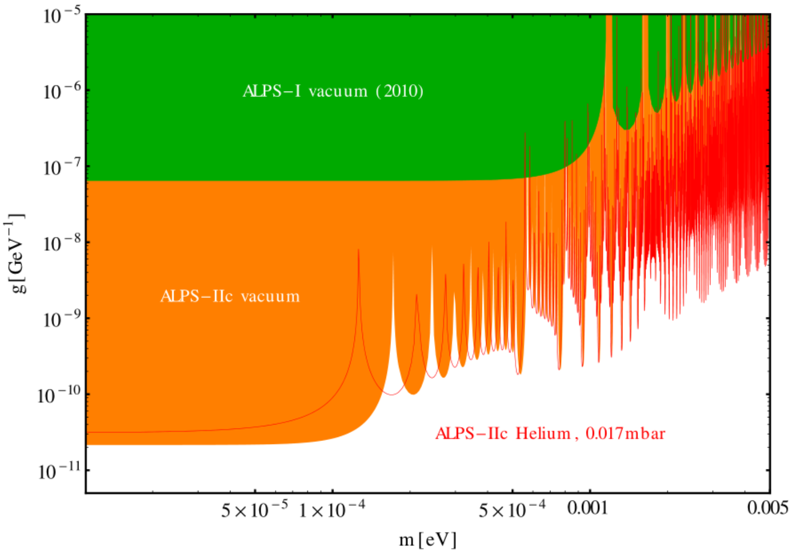

Figure 6.2: Prospective sensitivity reach for axion-like particles in the final stage of the ALPs-experiment, ALPs-IIc.

6.2.1.2 Haloscopes and helioscope

Haloscopes are designed to search for dark matter candidate particles in our galaxy by relying on the axion photon coupling. This is mostly known as the inverse Primakoff effect[158, 159]. As their name indicates the haloscopes are designed to look for dark matter axion in the galactic halo[160]. The first experiment was proposed in 1983 [159]. The detection principle is simple, when an axion enter a magnetized volume it may convert into photon. This will generate the power P given by

$$P = \eta g_{a\gamma\gamma}^{2} \left(\frac{\rho_a}{m_a} \right) B^2 V P B$$

where η is the efficiency, $g_{a\gamma\gamma}$ is axion-photon coupling, ρ_a is the local dark matter axion number density, m_a is the axion mass, B is the magnetic field strength, V the volume and PB the power built-up factor of the resonant amplification. Typical value of the conversion power is very low (10^{-22} watts) which makes it very challenging. The most sensitive experiment built so far is Axion Dark Matter eXperiment (ADMX) at Lawrence Livermore National Laboratory which was able to set limits in the μeV mass region[161] as shown in Figure 6.3. However the covered mass range in ADMX is limited due to tuning cavities. The Magnetized Disc and Mirror Axion (MADMAX) experiment (Figure 6.4) [162] is expected to be an alternative approach with a movable booster of dielectric disks embedded in a high field dipole magnet. MADMAX will be sited at DESY in Hamburg and could be installed by 2026.

Helioscopes also uses magnetic field to convert axion to X-rays photons. However they looks for axion in the solar core so they are designed to track the Sun. Axions are converted into photons with energy of several keV, reflecting temperature of the solar core. Helioscopes basically consist of a tracking system, a superconducting magnet, and an X-ray detector. The typical mass coverage of such detectors extends from 0 up to about 1 eV. The probability to observe an axion-to-photon conversion

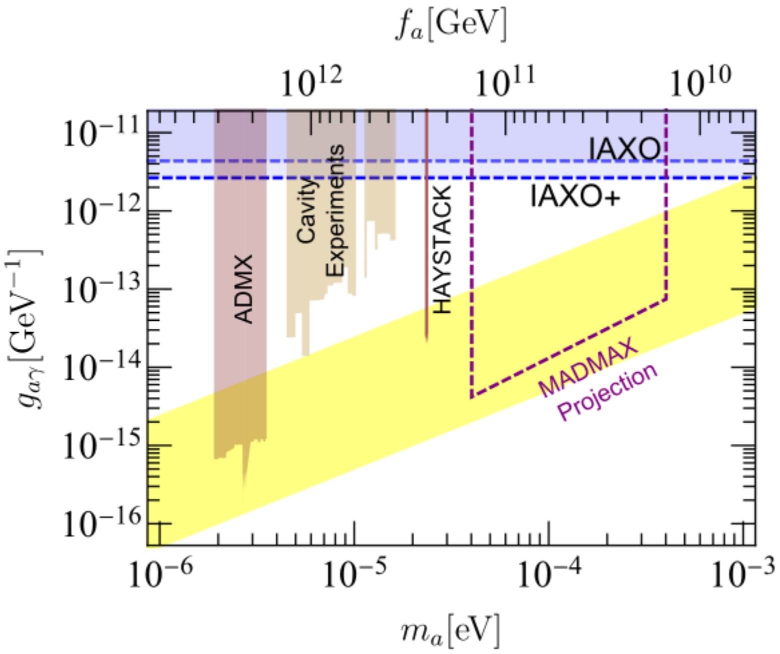

Figure 6.3: Haloscopes results and projected sensitivities.

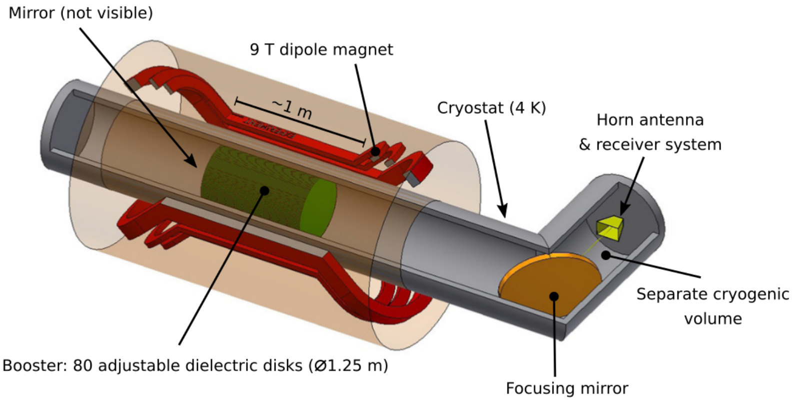

Figure 6.4: Conceptual sketch of the MADMAX experiment.

is given by

$$P_{a\to\gamma} = A g_{a\gamma\gamma}^2 B^2 \left(\frac{\sin(qL/2)}{q}\right)^2 \quad \text{with } q = \frac{m_a^2}{2E}$$

with A being the aperture area of the magnet bore, L the length of the magnetic field B and E the energy of the solar axion. For $q \ll 1$ the equation reduces to

$$P_{a\to\gamma} = A g_{a\gamma\gamma}^2 B^2 L^2/4.$$

Three helioscopes have been built, in Brookhaven [163], Tokyo [164] and at CERN [165]. Up to now, CERN Axion Solar Telescope (CAST) experiment at CERN has performed the most sensitive search for solar axions [166]. A new generation of axion helioscope is in the way to allow the exploration of wider mass ranges. The International Axion Observatory (IAXO) [167] will be the successor of CAST being able to check for the astrophysical hints mentioned above and to explore the QCD axion in the mass range around 1meV, which is not accessible by any other technology right now. This helioscope will use a huge 20m long toroidal superconducting magnet (Figure 6.5). IAXO is expected to increase the sensitivity on $g_{a\gamma\gamma}$ 20 times compared to CAST. A first step toward building this experiment will be the BabyIAXO prototype to mainly test the magnet concept, new X-ray optics and detectors. However, it will also have a physics reach more than a factor 3 beyond CAST and could be ready in 2024. DESY in Hamburg is the potential host for BabyIAXO and IAXO.

The same experiments are also sensitive to axion produced in the Sun via their couplings to electrons as shown in Figure 6.6.

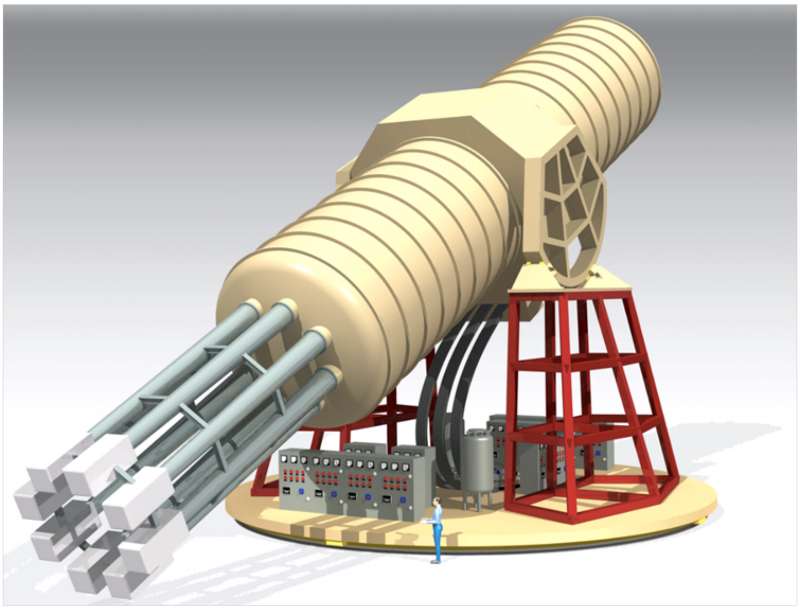

Figure 6.5: Conceptual layout of IAXO experiment.

6.2.2 Cosmological approach

Cosmological measurement such as the distribution of Large Scale Structures (LSS) [168] and Cosmic Microwave Background (CMB) anisotropies [169] can be used to constraints axions and ALPs properties. They can be combined with terrestrial and stellar observations using previously cited experiment. Since axions are a dark matter candidate they could play a role in the cosmological evolution of the universe. They are also related to other cosmological phenomena such as dark energy and inflation.

Diverse mechanisms are suggested as a source for axion production in cosmology.

6.2.2.1 Thermal production

The non-thermally produced axions are thought to have a greater role than thermally produced axions as especially as a cold dark matter constituent, but it is possible to have an additional populations of axions as thermal relics from the primordial plasma thermal scatterings of pions and nucleons such as $\pi + \pi \rightarrow \pi + a$ in the early Universe [170, 171] could produce relativistic (hot) axions. Being hot these QCD axions would contribute as dark radiation at early times. Bounds on thermal axions can be evaded by relaxing the assumption of a standard thermal history, like in scenarios with a low reheating temperature [172], but are quite robust with respect

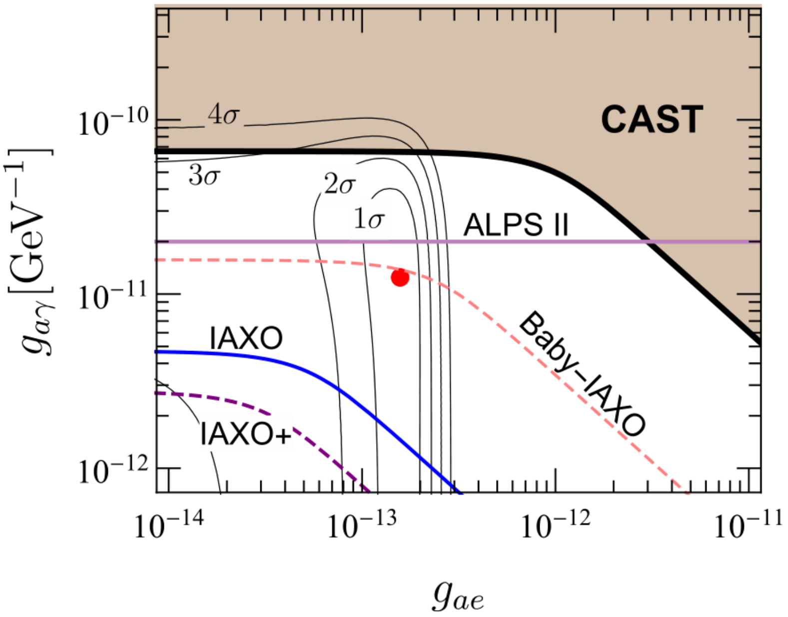

Figure 6.6: Hinted regions in the ALP parameter space from stellar observations. The experimental potential is also shown.

to assumptions about the underlying inflationary model [173, 174]. Thermal axions also affect structure formation at late times, suppressing small-scale fluctuations in a similar way to neutrinos. Together, these two effects can be used to constrain the abundance of relativistic axions and thus their mass. The most recent constraints comes from the temperature and polarization measurements of the Planck satellite experiment, which sets a limit $m_a < 0.54\mathrm{eV}$ at 95%CL for thermal QCD axions [174]. Future observations are expected to improve the sensitivity, and might be able to detect $m_a \simeq 0.15\mathrm{eV}$ at high significance, from a combination of CMB and LSS observations [175]. Thermal axions could also produced in the primordial QGP.

6.2.2.2 Decay of topological defects

Topological defects such as strings and domain walls[176] could produce a large number of axions in cosmological scenario where the PQ symmetry is broken. The decay of a heavy particle also usually produces relativistic axions, and thus dark radiation. In fact, the presence of an axion population from moduli decay is a generic prediction of string and M-theory [177, 178].

6.2.2.3 The misalignment mechanism

The axion field begins to coherently oscillate around the minimum of the potential at the time of QCD phase transition. This coherent oscillation of the axion field behaves as a cold matter in the universe. The critical point of the misalignment mechanism is that the axion field a_0 begins to coherently oscillate around the minimum of the potential the potential at the time of QCD phase transition. Since the axion mass vanishes at sufficiently high temperature, the value of a 0 is not necessarily zero at $t \lesssim t_1$. Then, a_0 begins to roll down to zero when the axion mass m_a is turned on.

6.2.3 Astrophysics approach

The existence of axion or ALPs can have many implications in astrophysics, thus it can have effect in many Very High Energy phenomena here we give a glance about them.

6.2.3.1 Active galactic nuclei (AGNs)

An active galactic nucleus (AGN) is a compact region at the center of a galaxy that has a high luminosity over at least some portion of the electromagnetic spectrum with characteristics indicating that the luminosity is not produced by stars. Photons traveling long astronomical distances and traversing galactic or inter-galactic magnetic fields could convert into ALPs and lead to observable effects. The most interesting one is an effective reduction in the γ -ray opacity (optical depth Figure 6.7) of the intergalactic medium , possibly leading to the observation of distant sources that could be obscured otherwise, this is similar to setting up a LSW experiment at intergalactic scale. Indeed the observation of very high energy (VHE) photons from distant AGNs by imaging atmospheric Cherenkov telescopes (IACT) like HESS [179] or MAGIC [180] triggered the first studies of this effect.

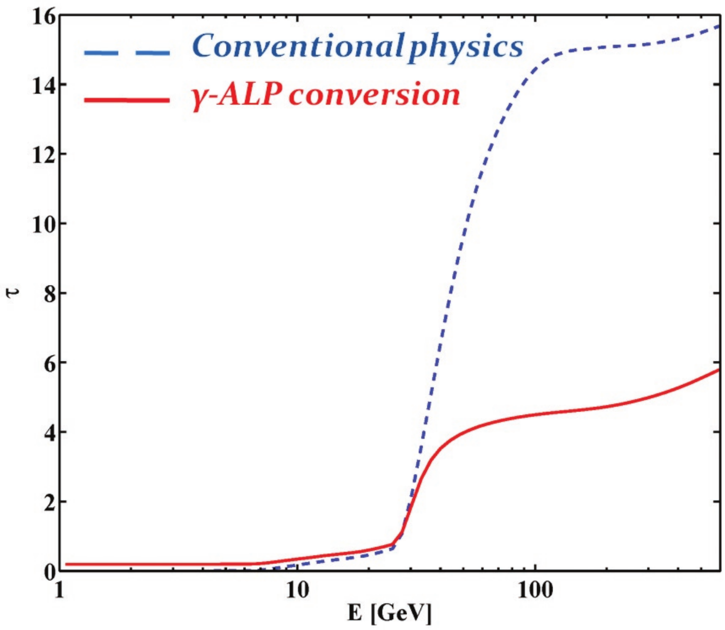

Figure 6.7: The broad line region optical depth τ in the standard case and with photon-ALP interaction for flat spectrum radio quasars : $g_{a\gamma\gamma} \simeq 10^{-11}\text{GeV}^{-1}$ and $m_a < \mathcal{O}\left(10^{-10}\text{eV}\right)$ [181].

6.2.3.2 Black holes

The existence of ALPs has spectacular effects on black holes with radii comparable to their Compton wavelength. The phenomenon of black hole superradiance can radiate extremely efficiently the black hole's angular momentum into ALPs [182], therefore the existence of black holes with large angular momentum can be used to strongly disfavour ALPs minimally coupled to gravity. This argument excludes ALPs in the band $6 \times 10^{-13}\text{eV} < m_a < 2 \times 10^{-11}\text{eV}$ [183]. The ALP cloud around the blackhole can become so dense that ALPs can annihilate into monochromatic gravitational waves that can be detected by gravitational wave interferometers [183]. The bounds are robust against uncertainties in the black hole.

6.2.3.3 Galaxy cluster

Data from gamma-ray astronomy experiment such as Fermi Large Area Telescope [184] can be used to constrain Photon-ALP coupling. Indeed Photon-ALP interactions could leave an imprint on $\gamma-$ray spectra, provided that the ALP mass is sufficiently small, $m_a \lesssim \mu$eV. Above a critical energy photon ALP mixing becomes maximal, leading to a reduction of the photon flux [185, 186]. This critical energy naturally falls in the gamma ray energy range. The photon-ALP beam can also have effect on extra-galactic space [187], and main sequence and evolved stars [188].

6.3 ALPs at the LHC

All the previous approaches from dedicated ALPs experiment are limited to low masses. The high mass search is accessible at hadrons colliders. However, searching for a particle relying only on its coupling to photons is not an easy task at a lepton or hadron collider. Bounds obtained from the LEP, Tevatron and LHC in tri-photon, di-photon and mono-photon final states reach the highest masses, but are not very sensitive. An interesting approach is the one proposed in [189] which rely on the same event topology as for the light-by-light scattering (Figure 6.8).

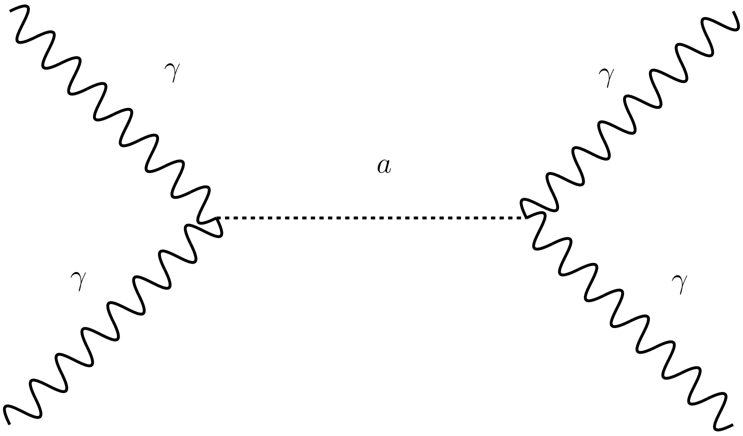

Figure 6.8: Feynman diagram of the light-by-light scattering mediated by an axion like particle (ALP) .

6.4 Search for Axion Like Particles production

As introduced in chapter 2 the light-by-light scattering channel can be used to perform search for axion like particles (ALP) . The measured invariant mass spectrum, as shown in Fig. 5.36, is used to extract limits on the cross section of the reaction $\gamma\gamma \to a \to \gamma\gamma$, where a denotes the ALP. The LbyL, $\gamma\gamma \to e^+e^-$ and CEP $gg \to \gamma\gamma$ processes described in Sec. 5.5 are considered as background.

Events for ALP signal are generated using STARlight v2.0 for ALP masses (m_a) ranging between 5 and 100 GeV. For $5 < m_\mathrm{a} < 30$ GeV, a 1 GeV mass spacing is applied, while for $m_\mathrm{a} > 30$ GeV a 10 GeV mass spacing is used.

At every bin of interest a 'cut and count' experiment is performed to estimate the expected numbers of background and signal events as well as the number of measured data events. The signal contribution is fitted using a maximum likelihood fit [155, 190], which is then used to estimate the limit on the signal strength μ at 95% confidence level (CL). The bin width is chosen to contain at least 80% of the expected ALP signal and ranges from 3 GeV at low masses to 20 GeV at $m_{\gamma\gamma} = 100$ GeV.

Experimental systematic uncertainties to the ALP signal model originate from the trigger, PID and photon reconstruction efficiencies and photon energy scale and resolution. The systematic uncertainties are evaluated identically to the treatment in the integrated cross-section measurement, described in Section 5.6. The theoretical uncertainty on the calculated ALP signal cross section is 10% in the full mass range due to the limited knowledge of the initial photon fluxes [191]. This uncertainty is considered uncorrelated to other sources of uncertainties. The luminosity uncertainty of the recorded data set is 3.2% [192].

The obtained limits on the signal strength μ are transformed into limits on the cross section $\sigma_{\gamma\gamma\to a\to\gamma\gamma} = \mu_{\mathrm{CLs}} \cdot \sigma^{\mathrm{MC}}_{\mathrm{gen}}$. Additionally limits on the photon ALP coupling ($1/\Lambda_\mathrm{a}$) are calculated following $1/\Lambda^{\mathrm{CLs}}_{\mathrm{a}} = \sqrt{\mu^{\mathrm{CLs}}} \cdot 1/\Lambda^{\mathrm{gen}}_{\mathrm{a}}$, where $\sigma^{\mathrm{MC}}_{\mathrm{gen}}$ and $\Lambda^{\mathrm{gen}}_{\mathrm{a}}$ are the cross section and coupling use in the MC generator. The observed and expected 95% CL limits on the ALP production cross section and ALP coupling to photons are presented in Fig. 6.9. The largest deviation from the background-only hypothesis, corresponding to a local excess of 2.1 standard deviations, is observed near a mass of 10 GeV.

Assuming the 100% ALP decay branching fraction to photons the derived constraints on the ALP mass and its coupling to photons are compared in Fig. 6.10 to those obtained from various experiments [127, 193]. The exclusion limits from this analysis are best so far over the mass range of $6 < m_\mathrm{a} < 100$ GeV.

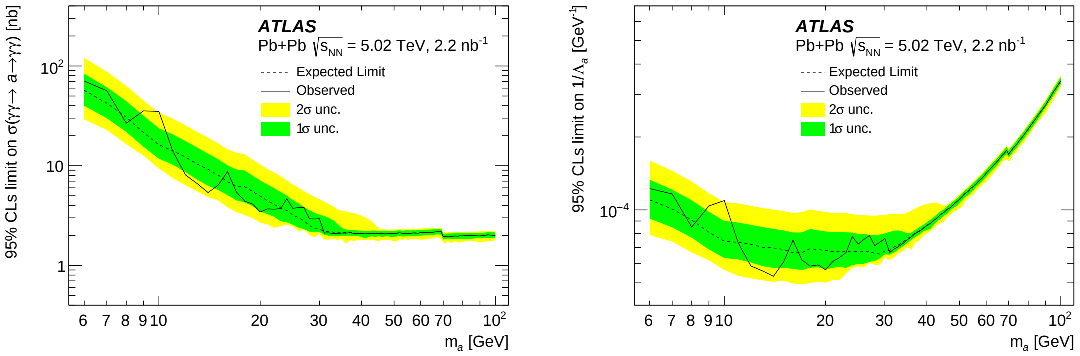

Figure 6.9: The 95% CL upper limit on the ALP production cross section (left) and ALP coupling $1/\Lambda_\mathrm{a}$ (right) for the $\gamma\gamma \to a \to \gamma\gamma$ process as a function of ALP mass m_a. The observed upper limit is shown as a solid black line and the expected upper limit is shown by the dashed black line, with a green $\pm 1\sigma$ and a yellow $\pm 2\sigma$ band. The discontinuity at $m_\mathrm{a} = 70$ GeV is caused by the increase of the mass-bin width which brings an increase in signal acceptance.

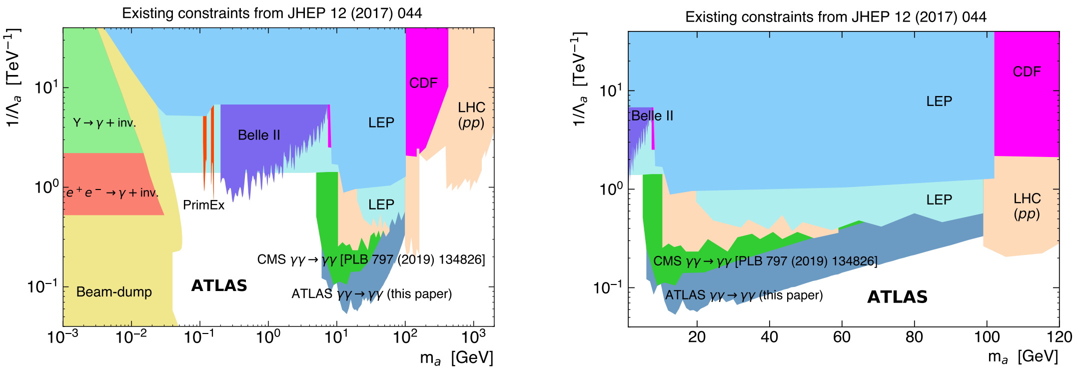

Figure 6.10: Compilation of exclusion limits at 95% CL in the ALP-photon coupling ($1/\Lambda_{\mathrm{a}}$) versus ALP mass (m_{a}) plane obtained by different experiments. The existing limits, derived from Refs. [127, 193] are compared to the limits extracted from this measurement. The plot on the right is a zoomed version over the range $1 < m_{\mathrm{a}} < 120$ GeV.

Conclusion

Despite not yet having been found, axion and ALPs models have been well studied for over 40 years, giving time for physicists to develop insight into axion (ALPs) effects that might be detected. Several experimental searches for axions and/or ALPs by relying on interaction with photons in strong magnetic fields. Axions are also one of the few remaining candidates for dark matter particles, and might be discovered in some dark matter experiments. In these chapter we present a search carried out with ultra peripheral heavy ions collision data collected by the ATLAS detector by looking at the mass range $6 < m_{\mathrm{a}} < 100$ GeVof the diphoton invariant mass. No significant excess beyond the background-only hypothesis is observed and limit on the ALP production cross section (left) and ALP coupling are sets in the same mass range.

Conclusion

This thesis was carried out within the ATLAS collaboration and it cover two topics the first which is technical, it concerns the Argon emulation in the simulation of the ATLAS Transition Radiation Tracker which is the outermost part of the ATLAS detector using a mixture of Argon and Xenon gases. The study consist of tuning parameters allowing to pass from xenon to argon configuration at the digitization stage of the simulation of the TRT. Making it possible to gain time and disk space by skipping the simulation step. The study was carried out by several PID observable given that the PID is the only aspect affected by the change of the gas geometry from xenon to argon while the tracking capabilities of the detector are intact. The study has been done by producing emulated samples with different emulation parameters and then comparing them to fully simulated ones. The results presented shows that emulation can be useful and reliable to switch from xenon to argon configuration at the digitization level of the TRT simulation. The final parameters were injected in the *athena* software for future possible usage.

The second one concerns the light-by-light scattering which is a quantum-mechanical process proven theoretically in early stages of QED by Euler and Heisenberg and was carried out within the scoop of ultra peripheral heavy ion collision (UPC). The analysis was performed with the 2015 and 2018 data set recorded with the ATLAS detector at center-of-mass energy of $\sqrt{s_{NN}} = 5.02$ TeV. This analysis presents the observation of the process, the measurement of its fiducial and differential cross section and the interpretation in the light of ALPs production. More specifically the analysis was done in two stages the first one with only the 2018 data where te number of event observed was 59 events where 30 ± 4 signal events and 12 ± 3 background events are expected. The statistical significance against the background-only hypothesis is found to be 8.2 standard deviations. The measured fiducial cross section is $\sigma_{\text{fid}} = 78 \pm 13$ (stat.) $\pm$ 7 (syst.) $\pm$ 3 (lumi.) nb. The second stage make uses of the combined 2015 and 2018 data sets. Where the number of event observed is 97 events, while 27 ± 5 background events are expected. The measured fiducial cross section is $\sigma_{\text{fid}} = 120 \pm 17$ (stat.) $\pm$ 13 (syst.) $\pm$ 4 (lumi.) nb. Differential cross sections are measured as a function of several variables of the final-state photons and are compared with theory predictions. The measured diphoton invariant mass distribution is used to search for axion-like particles and set new exclusion limits on their production. To date, the derived exclusion limits are the best over the mass range of $6 < m_{\text{a}} < 100$ GeV.

The 2018 heavy ions data taking was the last stage of the LHC run2. The LHC is now in the long shutdown mode with all detectors and the LHC itself going through upgrade to be ready for the run3. The latter is planned to start on 2021 which will be the start of the HL-LHC era. In run3 the luminosity is expected to be 2 time highers than run2.

Thought up to date the LHC data has delivered many answer and precise measurement of the Standard Model processes. The light-by-light scattering is one of them. In the same time it keep rising more question concerning physics beyond the standard model such as dark matter and supersymmetry. Hopefully the run 3 data and HL-LHC will bring more light to this dark side of our universe.

As perspective and while waiting for new data we could try to use this new measurement in making interpretation for other BSM predictions such as Effective Field Theory (EFT) and Born-Infeld Theory or any of BSM extension listed in section 2.5.

Appendix A

TRT PID Performance

The aim of this study is to help understanding the expected particle ID performance for run-3, i.e. at Average $\langle \mu \rangle$ or higher. This is an extremely important task for the TRT and ATLAS in general as it will help to decide which gas configuration to use. In particular, it will help to understand whether the information from the TRT PID is still relevant enough, so that the high running costs of loosing the Xenon gas in the leaks is justified. The study is performed by:

- Looking to High occupancy MC samples Zee and Zmumu
- Checking ROC curves for different occupancy slices
- Check the separation electrons/muons with HT and ToT in straw filled with argon using real data

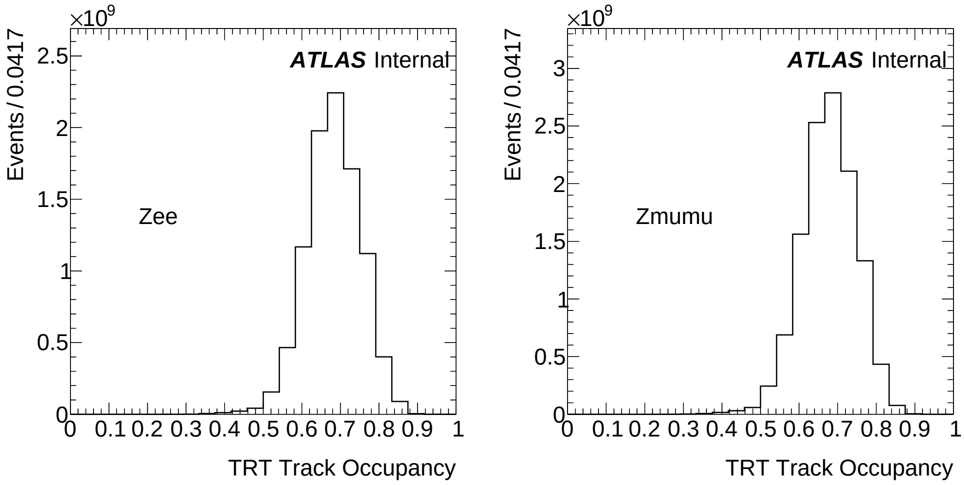

Figure A.1: TRT Track occupancy from High Occupancy MC samples right : Zmumu sample, left : Zee sample .

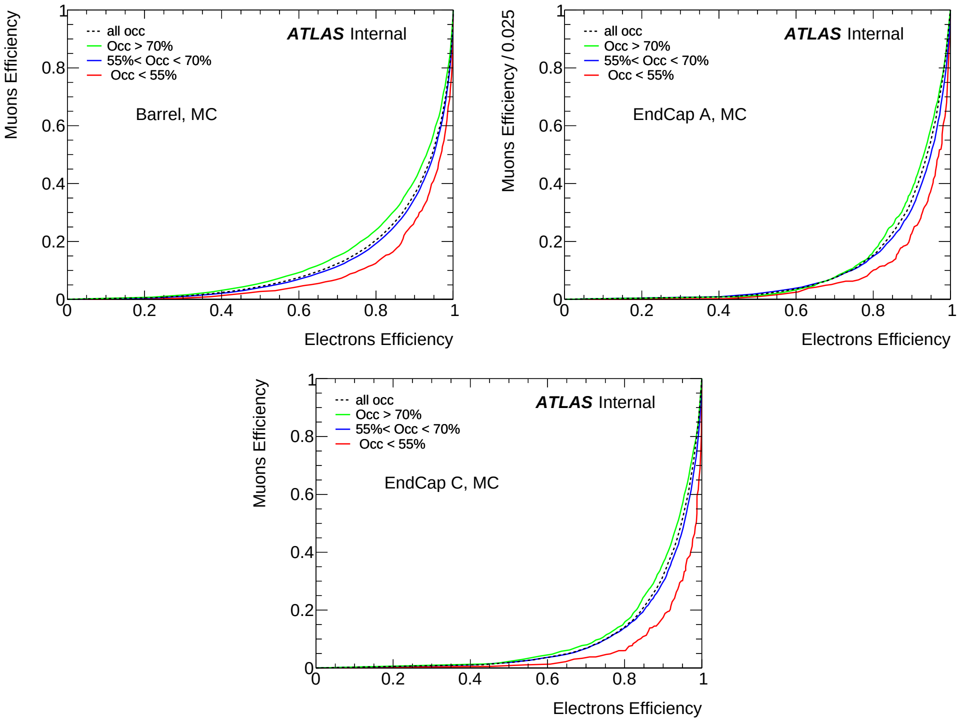

Figure A.2: ROC Curve from the MC samples in Barrel, EndCap A and C for different occupancies slices .

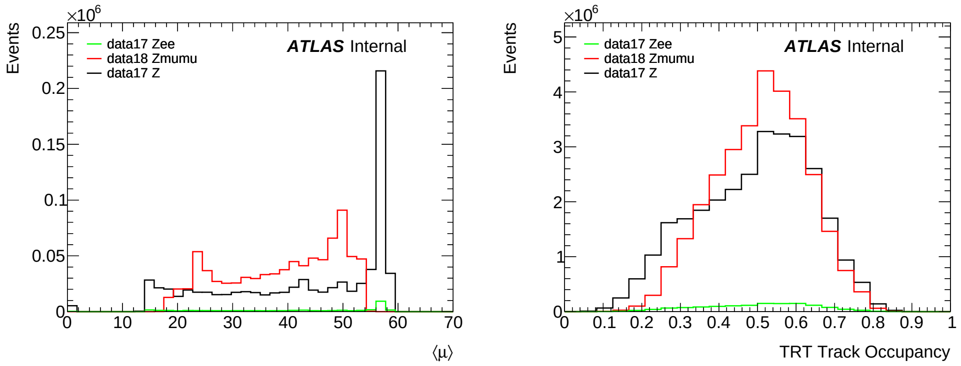

Figure A.3: Average $\langle \mu \rangle$ (left) and Track Occupancy (right) .

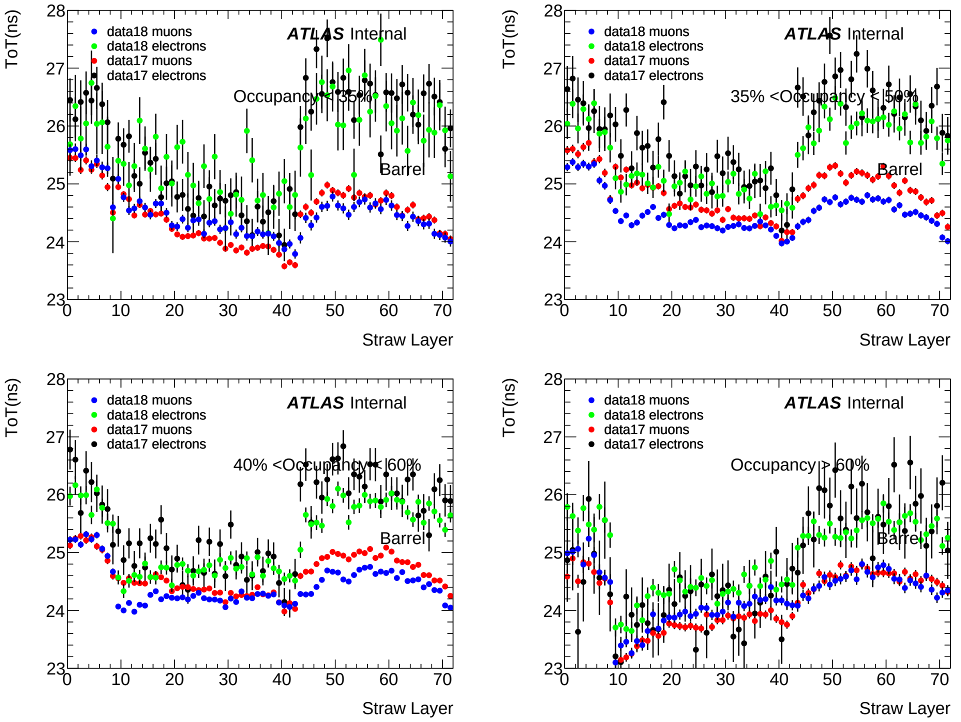

Figure A.4: ToT vs SL Barrel for different occupancy slices from data samples with Argon .

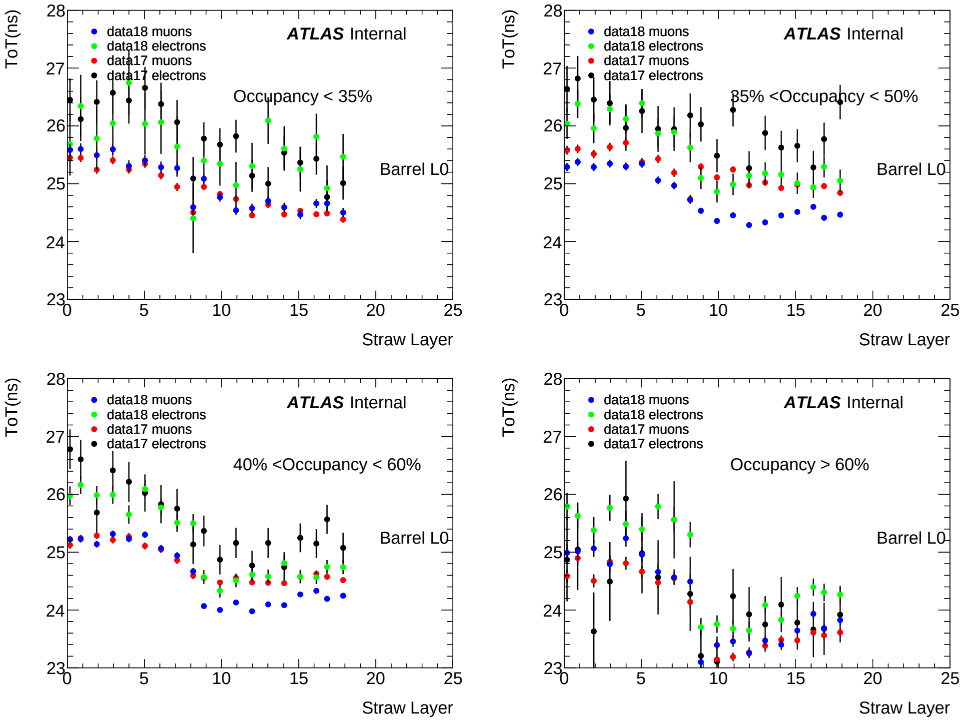

Figure A.5: ToT vs SL Barrel L0 for different occupancy slices from data samples with Argon .

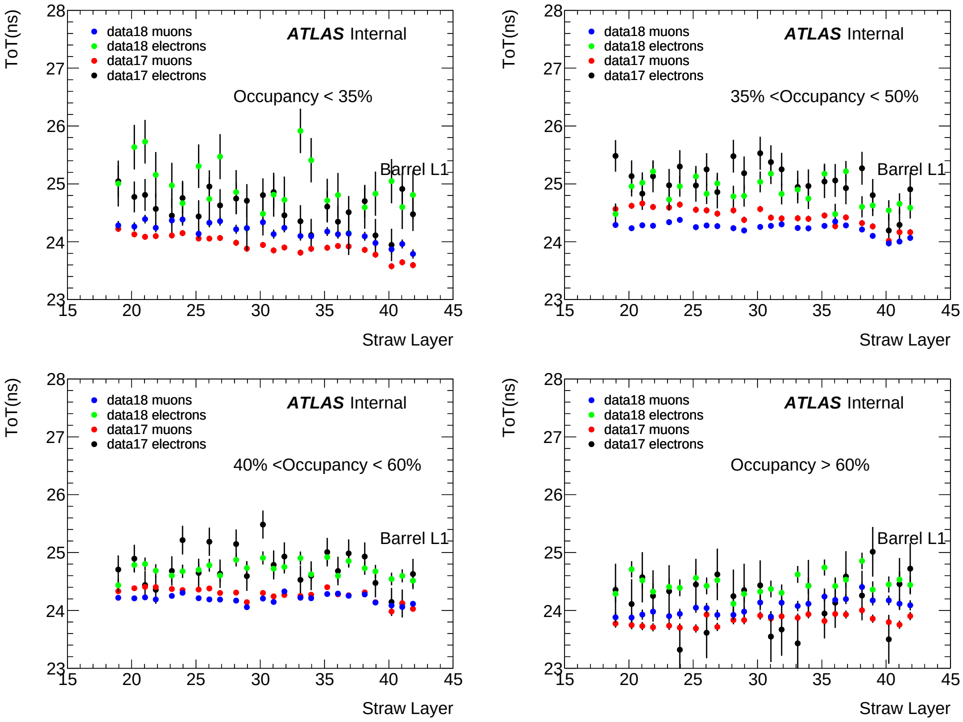

Figure A.6: ToT vs SL Barrel L1 for different occupancy slices from data samples with Argon .

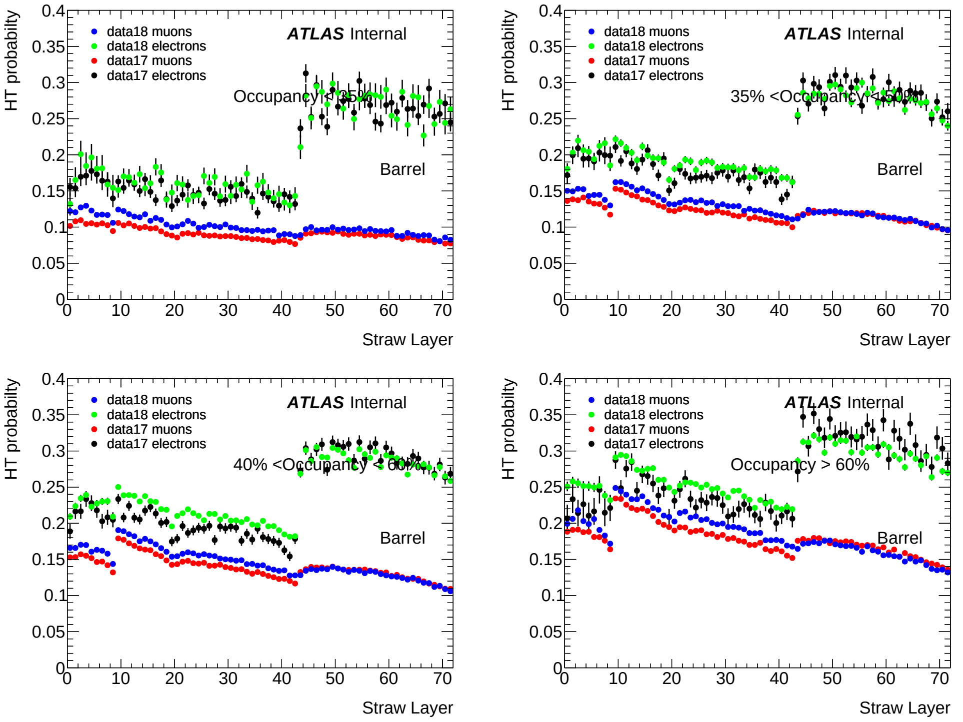

Figure A.7: HT vs SL Barrel for different occupancy slices from data samples with Argon .

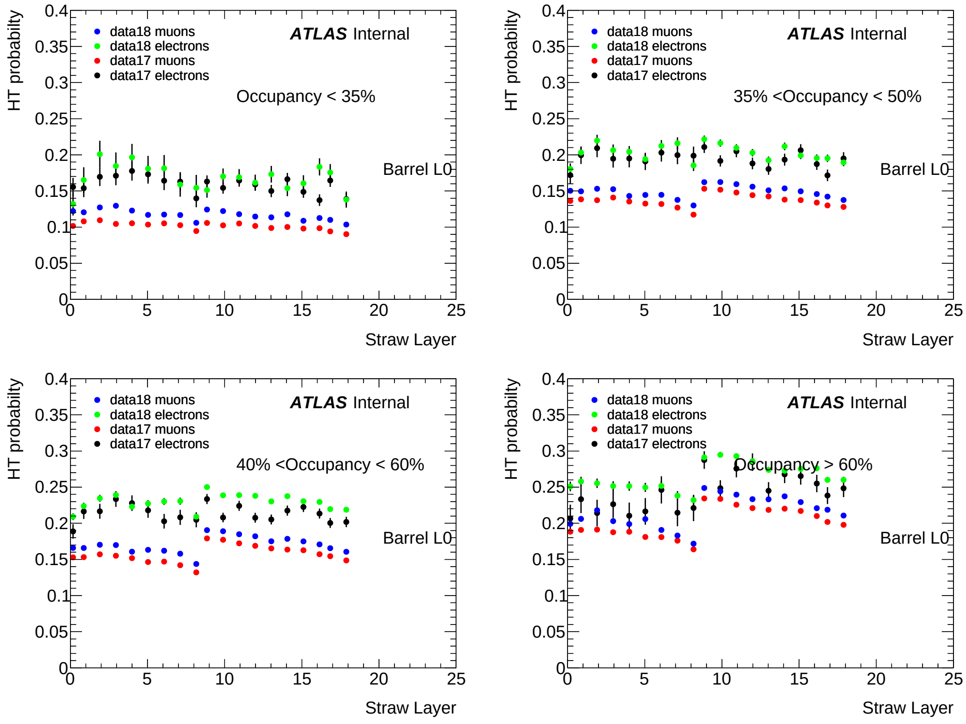

Figure A.8: HT vs SL Barrel L0 for different occupancy slices from data samples with Argon .

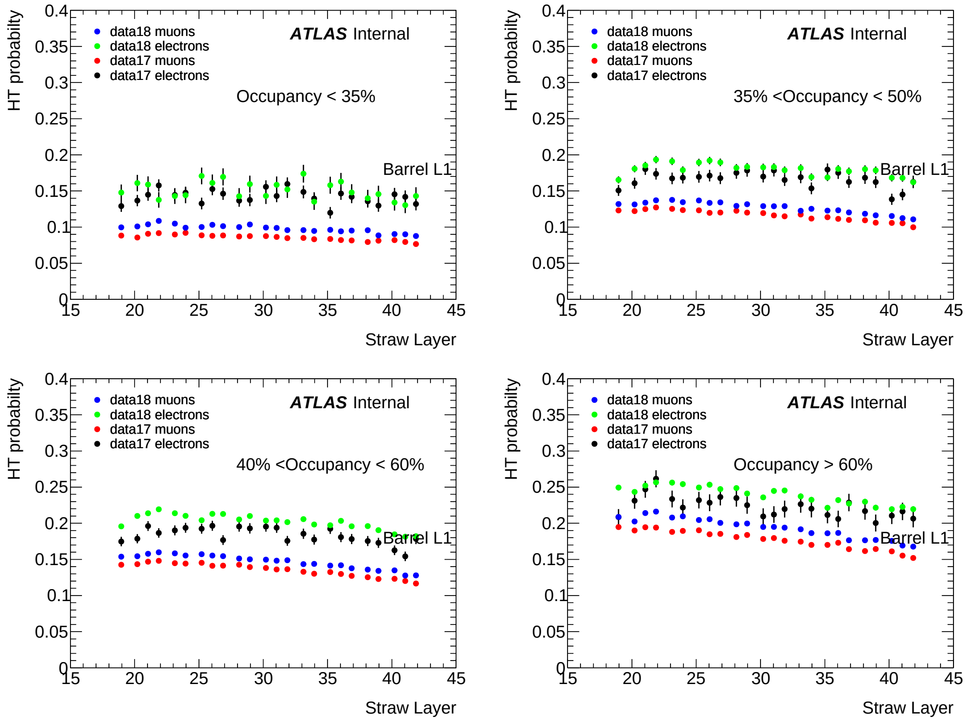

Figure A.9: HT vs SL Barrel L1 for different occupancy slices from data samples with Argon .

Bibliography

[1] ATLAS Collaboration. 'Observation of a new particle in the search for the Standard Model Higgs boson with the ATLAS detector at the LHC'. In: *Phys. Lett. B* 716 (2012), p. 1. DOI: `10.1016/j.physletb.2012.08.020`. arXiv: `1207.7214 [hep-ex]`.

[2] G. Zweig. 'An SU_3 model for strong interaction symmetry and its breaking; Version 2'. In: CERN-TH-412 (Feb. 1964), 80 p. URL: `https://cds.cern.ch/record/570209`.

[3] M. Gell-Mann. 'A Schematic Model of Baryons and Mesons'. In: *Phys. Lett.* 8 (1964), pp. 214–215. DOI: `10.1016/S0031-9163(64)92001-3`.

[4] J. Beringer et al. 'Review of Particle Physics (RPP)'. In: *Phys. Rev.* D86 (2012), p. 010001. DOI: `10.1103/PhysRevD.86.010001`.

[5] J. J. Thomson. 'Cathode rays'. In: *Phil. Mag. Ser.5* 44 (1897), pp. 293–316. DOI: `10.1080/14786449708621070`.

[6] F. Reines and C. L. Cowan. 'The neutrino'. In: *Nature* 178 (1956), pp. 446–449. DOI: `10.1038/178446a0`.

[7] E. D. Bloom et al. 'High-Energy Inelastic e p Scattering at 6-Degrees and 10-Degrees'. In: *Phys. Rev. Lett.* 23 (1969), pp. 930–934. DOI: `10.1103/PhysRevLett.23.930`.

[8] J. C. Street and E. C. Stevenson. 'New Evidence for the Existence of a Particle of Mass Intermediate Between the Proton and Electron'. In: *Phys. Rev.* 52 (1937), pp. 1003–1004. DOI: `10.1103/PhysRev.52.1003`.

[9] G. Danby et al. 'Observation of High-Energy Neutrino Reactions and the Existence of Two Kinds of Neutrinos'. In: *Phys. Rev. Lett.* 9 (1962), pp. 36–44. DOI: `10.1103/PhysRevLett.9.36`.

[10] J. E. Augustin et al. 'Discovery of a Narrow Resonance in e^+e^- Annihilation'. In: *Phys. Rev. Lett.* 33 (1974). [Adv. Exp. Phys.5,141(1976)], pp. 1406–1408. DOI: `10.1103/PhysRevLett.33.1406`.

[11] M. L. Perl et al. 'Evidence for Anomalous Lepton Production in e+ - e- Annihilation'. In: *Phys. Rev. Lett.* 35 (1975), pp. 1489–1492. DOI: `10.1103/PhysRevLett.35.1489`.

[12] K. Kodama et al. 'Observation of tau neutrino interactions'. In: *Phys. Lett.* B504 (2001), pp. 218–224. DOI: `10.1016/S0370-2693(01)00307-0`. arXiv: `hep-ex/0012035 [hep-ex]`.

[13] F. Abe et al. 'Observation of top quark production in $\bar{p}p$ collisions'. In: *Phys. Rev. Lett.* 74 (1995), pp. 2626–2631. DOI: `10.1103/PhysRevLett.74.2626`. arXiv: `hep-ex/9503002 [hep-ex]`.

[14] S. W. Herb et al. 'Observation of a Dimuon Resonance at 9.5-GeV in 400-GeV Proton-Nucleus Collisions'. In: *Phys. Rev. Lett.* 39 (1977), pp. 252–255. DOI: `10.1103/PhysRevLett.39.252`.

[15] M. E. Peskin and D. V. Schroeder. *An introduction to quantum field theory*. Includes exercises. Boulder, CO: Westview, 1995. URL: `https://cds.cern.ch/record/257493`.

[16] E. Noether. 'Invariant variation problems'. In: *Transport Theory and Statistical Physics* 1.3 (Jan. 1971), pp. 186–207. ISSN: 1532-2424. DOI: `10.1080/00411457108231446`. URL: `http://dx.doi.org/10.1080/00411457108231446`.

[17] J. C. Maxwell. 'A dynamical theory of the electromagnetic field'. In: *Philosophical Transactions of the Royal Society of London* 155 (1865), pp. 459–513.

[18] S. L. Glashow. ‘Partial Symmetries of Weak Interactions’. In: *Nucl. Phys.* 22 (1961), pp. 579–588. DOI: 10.1016/0029-5582(61)90469-2.

[19] S. Weinberg. ‘A Model of Leptons’. In: *Phys. Rev. Lett.* 19 (1967), pp. 1264–1266. DOI: 10.1103/PhysRevLett.19.1264.

[20] F. Englert and R. Brout. ‘Broken Symmetry and the Mass of Gauge Vector Mesons’. In: *Phys. Rev. Lett.* 13 (1964), pp. 321–323. DOI: 10.1103/PhysRevLett.13.321.

[21] P. W. Higgs. ‘Broken symmetries, massless particles and gauge fields’. In: *Phys. Lett.* 12 (1964), pp. 132–133. DOI: 10.1016/0031-9163(64)91136-9.

[22] P. W. Higgs. ‘Broken Symmetries and the Masses of Gauge Bosons’. In: *Phys. Rev. Lett.* 13 (1964), pp. 508–509. DOI: 10.1103/PhysRevLett.13.508.

[23] CMS Collaboration. ‘Observation of a new boson at a mass of 125 GeV with the CMS experiment at the LHC’. In: *Phys. Lett. B* 716 (2012), p. 30. DOI: 10.1016/j.physletb.2012.08.021. arXiv: 1207.7235 [hep-ex].

[24] ATLAS Collaboration. ‘Evidence for the spin-0 nature of the Higgs boson using ATLAS data’. In: *Phys. Lett. B* 726 (2013), p. 120. DOI: 10.1016/j.physletb.2013.08.026. arXiv: 1307.1432 [hep-ex].

[25] CMS Collaboration. ‘Study of the Mass and Spin-Parity of the Higgs Boson Candidate Via Its Decays to Z Boson Pairs’. In: *Phys. Rev. Lett.* 110 (2013), p. 081803. DOI: 10.1103/PhysRevLett.110.081803. arXiv: 1212.6639 [hep-ex].

[26] T. A. collaboration. ‘Updated coupling measurements of the Higgs boson with the ATLAS detector using up to 25 fb^{-1} of proton-proton collision data’. In: (2014).

[27] ‘Combined measurements of the mass and signal strength of the Higgs-like boson with the ATLAS detector using up to 25 fb^{-1} of proton-proton collision data’. In: (2013).

[28] G. Arnison et al. ‘Experimental Observation of Isolated Large Transverse Energy Electrons with Associated Missing Energy at s**(1/2) = 540-GeV’. In: *Phys. Lett.* 122B (1983), pp. 103–116. DOI: 10.1016/0370-2693(83)91177-2.

[29] G. Arnison et al. ‘Experimental Observation of Lepton Pairs of Invariant Mass Around 95-GeV/c**2 at the CERN SPS Collider’. In: *Phys. Lett.* 126B (1983), pp. 398–410. DOI: 10.1016/0370-2693(83)90188-0.

[30] S. P. Martin. ‘A Supersymmetry primer’. In: (1997). [Adv. Ser. Direct. High Energy Phys.21,1(2010); Adv. Ser. Direct. High Energy Phys.18,1(1998)], pp. 1–98. DOI: 10.1142/9789812839657_0001,10.1142/9789814307505_0001. arXiv: hep-ph/9709356 [hep-ph].

[31] M. Roos. *Dark Matter: The evidence from astronomy, astrophysics and cosmology.* 2010. arXiv: 1001.0316 [astro-ph.CO].

[32] *Standard Model Summary Plots Summer 2019.* Tech. rep. ATL-PHYS-PUB-2019-024. Geneva: CERN, July 2019. URL: http://cds.cern.ch/record/2682186.

[33] F. Gabbiani et al. ‘A complete analysis of FCNC and CP constraints in general SUSY extensions of the standard model’. In: *Nuclear Physics B* 477.2 (Oct. 1996), pp. 321–352. ISSN: 0550-3213. DOI: 10.1016/0550-3213(96)00390-2. URL: http://dx.doi.org/10.1016/0550-3213(96)00390-2.

[34] A. Collaboration. ‘ATLAS News: Highlights from EPS 2019 - SUSY Summary Plot July 2019’. General Photo. July 2019. URL: https://cds.cern.ch/record/2683428.

[35] T. KALUZA. ‘On the Unification Problem in Physics’. In: *International Journal of Modern Physics D* 27.14 (Oct. 2018), p. 1870001. ISSN: 1793-6594. DOI: 10.1142/s0218271818700017. URL: http://dx.doi.org/10.1142/S0218271818700017.

[36] O. Klein. ‘Quantum Theory and Five-Dimensional Theory of Relativity. (In German and English)’. In: *Z. Phys.* 37 (1926), pp. 895–906. DOI: 10.1007/BF01397481.

[37] L. Randall and R. Sundrum. ‘Large Mass Hierarchy from a Small Extra Dimension’. In: *Physical Review Letters* 83.17 (Oct. 1999), pp. 3370–3373. ISSN: 1079-7114. DOI: 10.1103/physrevlett.83.3370. URL: http://dx.doi.org/10.1103/PhysRevLett.83.3370.

[38] N. Arkani-Hamed, S. Dimopoulos and G. Dvali. ‘Phenomenology, astrophysics, and cosmology of theories with submillimeter dimensions and TeV scale quantum gravity’. In: *Physical Review D* 59.8 (Mar. 1999). ISSN: 1089-4918. DOI: `10.1103/physrevd.59.086004`. URL: `http://dx.doi.org/10.1103/PhysRevD.59.086004`.

[39] N. Arkani–Hamed, S. Dimopoulos and G. Dvali. ‘The hierarchy problem and new dimensions at a millimeter’. In: *Physics Letters B* 429.3-4 (June 1998), pp. 263–272. ISSN: 0370-2693. DOI: `10.1016/s0370-2693(98)00466-3`. URL: `http://dx.doi.org/10.1016/S0370-2693(98)00466-3`.

[40] I. Antoniadis et al. ‘New dimensions at a millimeter to a fermi and superstrings at a TeV’. In: *Physics Letters B* 436.3-4 (Sept. 1998), pp. 257–263. ISSN: 0370-2693. DOI: `10.1016/s0370-2693(98)00860-0`. URL: `http://dx.doi.org/10.1016/S0370-2693(98)00860-0`.

[41] A. Pomarol. *Beyond the Standard Model*. 2012. arXiv: `1202.1391 [hep-ph]`.

[42] W. D. Goldberger and M. B. Wise. ‘Modulus Stabilization with Bulk Fields’. In: *Physical Review Letters* 83.24 (Dec. 1999), pp. 4922–4925. ISSN: 1079-7114. DOI: `10.1103/physrevlett.83.4922`. URL: `http://dx.doi.org/10.1103/PhysRevLett.83.4922`.

[43] K. Agashe et al. ‘CERN LHC signals from warped extra dimensions’. In: *Physical Review D* 77.1 (Jan. 2008). ISSN: 1550-2368. DOI: `10.1103/physrevd.77.015003`. URL: `http://dx.doi.org/10.1103/PhysRevD.77.015003`.

[44] H. Euler. ‘Über die Streuung von Licht an Licht nach der Diracschen Theorie’. In: *Annalen der Physik* 418.5 (1936), pp. 398–448. DOI: `10.1002/andp.19364180503`. eprint: `https://onlinelibrary.wiley.com/doi/pdf/10.1002/andp.19364180503`. URL: `https://onlinelibrary.wiley.com/doi/abs/10.1002/andp.19364180503`.

[45] H. Euler. ‘On the scattering of light by light according to Dirac’s theory’. In: *Annalen Phys.* 26.5 (1936). [Annalen Phys.418,no.5,398(1936)], pp. 398–448. DOI: `10.1002/andp.19364180503`.

[46] W. Heisenberg and H. Euler. ‘Folgerungen aus der Diracschen Theorie des Positrons’. In: *Zeitschrift fur Physik* 98.11 (1936), pp. 714–732. DOI: `10.1007/BF01343663`.

[47] W. Heisenberg and H. Euler. *Consequences of Dirac Theory of the Positron*. 2006. arXiv: `physics/0605038 [physics.hist-ph]`.

[48] S. I. Vavilov. *Remarks on the empirical accuracy of the optical superposition principle [Engl. transl. of Zh. Russk. Fiz.-Khim. Obshch., Ch. Fiz. 60(1928)555]*. 2017. arXiv: `1708.06817 [physics.hist-ph]`.

[49] A. L. Hughes and G. E. M. Jauncey. ‘An Attempt to Detect Collisions of Photons’. In: *Phys. Rev.* 36 (4 Aug. 1930), pp. 773–777. DOI: `10.1103/PhysRev.36.773`. URL: `https://link.aps.org/doi/10.1103/PhysRev.36.773`.

[50] E. Lundström et al. ‘Using High-Power Lasers for Detection of Elastic Photon-Photon Scattering’. In: *Physical Review Letters* 96.8 (Mar. 2006). ISSN: 1079-7114. DOI: `10.1103/physrevlett.96.083602`. URL: `http://dx.doi.org/10.1103/PhysRevLett.96.083602`.

[51] D. Bernard et al. ‘Search for stimulated photon-photon scattering in vacuum’. In: *The European Physical Journal D* 10.1 (Mar. 2000), pp. 141–145. ISSN: 1434-6060. DOI: `10.1007/s100530050535`. URL: `http://dx.doi.org/10.1007/s100530050535`.

[52] K. O. Mikaelian. ‘Detection of elastic light-by-light scattering at SLAC’. In: *Physics Letters B* 115.3 (1982), pp. 267–269. ISSN: 0370-2693. DOI: `https://doi.org/10.1016/0370-2693(82)90660-8`. URL: `http://www.sciencedirect.com/science/article/pii/0370269382906608`.

[53] G. Brodin, M. Marklund and L. Stenflo. ‘Proposal for Detection of QED Vacuum Nonlinearities in Maxwell’s Equations by the Use of Waveguides’. In: *Phys. Rev. Lett.* 87 (17 Oct. 2001), p. 171801. DOI: `10.1103/PhysRevLett.87.171801`. URL: `https://link.aps.org/doi/10.1103/PhysRevLett.87.171801`.

[54] D. Eriksson et al. ‘Possibility to measure elastic photon-photon scattering in vacuum’. In: *Phys. Rev. A* 70 (1 July 2004), p. 013808. DOI: 10.1103/PhysRevA.70.013808. URL: https://link.aps.org/doi/10.1103/PhysRevA.70.013808.

[55] R. S. Van Dyck, P. B. Schwinberg and H. G. Dehmelt. ‘New high-precision comparison of electron and positron g factors’. In: *Phys. Rev. Lett.* 59 (1 July 1987), pp. 26–29. DOI: 10.1103/PhysRevLett.59.26.

[56] Muon g-2 Collaboration, H. N. Brown et al. ‘Precise measurement of the positive muon anomalous magnetic moment’. In: *Phys. Rev. Lett.* 86 (2001), pp. 2227–2231. DOI: 10.1103/PhysRevLett.86.2227. arXiv: hep-ex/0102017 [hep-ex].

[57] R. R. Wilson. ‘Scattering of 1.33 Mev Gamma-Rays by an Electric Field’. In: *Phys. Rev.* 90 (1953), pp. 720–721. DOI: 10.1103/PhysRev.90.720.

[58] G. Jarlskog et al. ‘Measurement of Delbruck Scattering and Observation of Photon Splitting at High Energies’. In: *Phys. Rev. D* 8 (11 Dec. 1973), pp. 3813–3823. DOI: 10.1103/PhysRevD.8.3813.

[59] M. Schumacher et al. ‘Delbruck Scattering of 2.75-MeV Photons by Lead’. In: *Phys. Lett.* B59 (1975), pp. 134–136. DOI: 10.1016/0370-2693(75)90685-1.

[60] S. Z. Akhmadaliev et al. ‘Delbruck scattering at energies of 140-450 MeV’. In: *Phys. Rev. C* 58 (Nov. 1998), pp. 2844–2850. DOI: 10.1103/PhysRevC.58.2844.

[61] S. Z. Akhmadaliev et al. ‘Experimental investigation of high-energy photon splitting in atomic fields’. In: *Phys. Rev. Lett.* 89 (2002), p. 061802. DOI: 10.1103/PhysRevLett.89.061802. arXiv: hep-ex/0111084 [hep-ex].

[62] D. d’Enterria and G. G. da Silveira. ‘Observing Light-by-Light Scattering at the Large Hadron Collider’. In: *Physical Review Letters* 111.8 (Aug. 2013). ISSN: 1079-7114. DOI: 10.1103/physrevlett.111.080405. URL: http://dx.doi.org/10.1103/PhysRevLett.111.080405.

[63] *Measurement of high-mass dimuon pairs from ultraperipheral lead-lead collisions at $\sqrt{s_{\mathrm{NN}}} = 5.02$ TeV with the ATLAS detector at the LHC.* Tech. rep. ATLAS-CONF-2016-025. Geneva: CERN, June 2016. URL: http://cds.cern.ch/record/2157689.

[64] A. Sirunyan et al. ‘Evidence for light-by-light scattering and searches for axion-like particles in ultraperipheral PbPb collisions at sNN=5.02TeV’. In: *Physics Letters B* 797 (Oct. 2019), p. 134826. ISSN: 0370-2693. DOI: 10.1016/j.physletb.2019.134826. URL: http://dx.doi.org/10.1016/j.physletb.2019.134826.

[65] S. Chatrchyan et al. ‘Search for Exclusive or Semi-Exclusive Photon Pair Production and Observation of Exclusive and Semi-Exclusive Electron Pair Production in pp Collisions at $\sqrt{s} = 7$ TeV’. In: *JHEP* 11 (2012), p. 080. DOI: 10.1007/JHEP11(2012)080. arXiv: 1209.1666 [hep-ex].

[66] A. Collaboration. *Measurement of exclusive $\gamma\gamma \to W^+W^-$ production and search for exclusive Higgs boson production in pp collisions at $\sqrt{s} = 8$ TeV using the ATLAS detector.* 2016. arXiv: 1607.03745 [hep-ex].

[67] V. Khachatryan et al. ‘Evidence for exclusive $\gamma\gamma \to W^+W^-$ production and constraints on anomalous quartic gauge couplings in pp collisions at $\sqrt{s} = 7$ and 8TeV’. In: *Journal of High Energy Physics* 2016.8 (Aug. 2016). ISSN: 1029-8479. DOI: 10.1007/jhep08(2016)119. URL: http://dx.doi.org/10.1007/JHEP08(2016)119.

[68] E. Fermi. ‘On the Theory of Collisions between Atoms and Electrically Charged Particles’. In: *Electromagnetic Probes of Fundamental Physics* (Sept. 2003). DOI: 10.1142/9789812704214_0026. URL: http://dx.doi.org/10.1142/9789812704214_0026.

[69] E. J. Williams. ‘Nature of the High Energy Particles of Penetrating Radiation and Status of Ionization and Radiation Formulae’. In: *Phys. Rev.* 45 (10 May 1934), pp. 729–730. DOI: 10.1103/PhysRev.45.729. URL: https://link.aps.org/doi/10.1103/PhysRev.45.729.

[70] C. von Weizsacker. ‘Radiation emitted in collisions of very fast electrons’. In: *Z. Phys.* 88 (1934), pp. 612–625. DOI: 10.1007/BF01333110.

[71] ATLAS Collaboration. 'Evidence for light-by-light scattering in heavy-ion collisions with the ATLAS detector at the LHC'. In: *Nature Phys.* 13.9 (2017), pp. 852–858. DOI: 10.1038/nphys4208. arXiv: 1702.01625 [hep-ex].

[72] R. Peccei and H. R. Quinn. 'CP Conservation in the Presence of Instantons'. In: *Phys. Rev. Lett.* 38 (1977), pp. 1440–1443. DOI: 10.1103/PhysRevLett.38.1440.

[73] S. Knapen et al. 'Searching for axion-like particles with ultra-peripheral heavy-ion collisions'. In: (2016). arXiv: 1607.06083 [hep-ph].

[74] P. A. M. Dirac. 'The Theory of Magnetic Poles'. In: *Phys. Rev.* 74 (7 Oct. 1948), pp. 817–830. DOI: 10.1103/PhysRev.74.817. URL: https://link.aps.org/doi/10.1103/PhysRev.74.817.

[75] I. F. Ginzburg and A. Schiller. *Search for a heavy magnetic monopole at the Fermilab Tevatron and CERN LHC.* 1998. arXiv: hep-ph/9802310 [hep-ph].

[76] H. Georgi. 'Unparticle Physics'. In: *Physical Review Letters* 98.22 (May 2007). ISSN: 1079-7114. DOI: 10.1103/physrevlett.98.221601. URL: http://dx.doi.org/10.1103/PhysRevLett.98.221601.

[77] O. Çakır and K. Ozansoy. 'Unparticle searches through gamma–gamma scattering'. In: *The European Physical Journal C* 56.2 (July 2008), pp. 279–285. ISSN: 1434-6052. DOI: 10.1140/epjc/s10052-008-0658-7. URL: http://dx.doi.org/10.1140/epjc/s10052-008-0658-7.

[78] J. Ohnemus, T. Walsh and P. Zerwas. '$\gamma\gamma$ production of non-strongly interacting SUSY particles at hadron colliders'. In: *Physics Letters B* 328.3-4 (June 1994), pp. 369–373. ISSN: 0370-2693. DOI: 10.1016/0370-2693(94)91492-3. URL: http://dx.doi.org/10.1016/0370-2693(94)91492-3.

[79] H. Davoudiasl. '$\gamma\gamma \to \gamma\gamma$ as a test of weak scale quantum gravity at the NLC'. In: *Phys. Rev.* D60 (1999), p. 084022. DOI: 10.1103/PhysRevD.60.084022. arXiv: hep-ph/9904425 [hep-ph].

[80] K. Cheung. 'Diphoton signals for low scale gravity in extra dimensions'. In: *Physical Review D* 61.1 (Dec. 1999). ISSN: 1089-4918. DOI: 10.1103/physrevd.61.015005. URL: http://dx.doi.org/10.1103/PhysRevD.61.015005.

[81] J. L. Hewett, F. J. Petriello and T. G. Rizzo. 'Signals for noncommutative interactions at linear colliders'. In: *Physical Review D* 64.7 (Sept. 2001). ISSN: 1089-4918. DOI: 10.1103/physrevd.64.075012. URL: http://dx.doi.org/10.1103/PhysRevD.64.075012.

[82] 'LHC Guide'. Mar. 2017. URL: http://cds.cern.ch/record/2255762.

[83] J. Wenninger. 'Operation and Configuration of the LHC in Run 2'. In: (Mar. 2019). URL: https://cds.cern.ch/record/2668326.

[84] K. Aamodt et al. 'The ALICE experiment at the CERN LHC'. In: *JINST* 3 (2008), S08002. DOI: 10.1088/1748-0221/3/08/S08002.

[85] CMS Collaboration. 'The CMS experiment at the CERN LHC'. In: *JINST* 3 (2008), S08004. DOI: 10.1088/1748-0221/3/08/S08004.

[86] A. A. Alves Jr. et al. 'The LHCb Detector at the LHC'. In: *JINST* 3 (2008), S08005. DOI: 10.1088/1748-0221/3/08/S08005.

[87] E. Mobs. 'The CERN accelerator complex. Complexe des accélérateurs du CERN'. In: (July 2016). General Photo. URL: https://cds.cern.ch/record/2197559.

[88] *Cross section of an LHC dipole in the tunnel.* https://www.flickr.com/photos/arselectronica/5980837642.

[89] *LHC Schedule 2018.* https://beams.web.cern.ch/sites/beams.web.cern.ch/files/schedules/LHC_Schedule_2018.pdf.

[90] W. Bertsche et al. ‘A magnetic trap for antihydrogen confinement’. In: *Nuclear Instruments and Methods in Physics Research Section A: Accelerators, Spectrometers, Detectors and Associated Equipment* 566.2 (2006), pp. 746–756. ISSN: 0168-9002. DOI: https://doi.org/10.1016/j.nima.2006.07.012. URL: http://www.sciencedirect.com/science/article/pii/S0168900206012617.

[91] R. Bailey and P. Collier. *Standard Filling Schemes for Various LHC Operation Modes*. Tech. rep. LHC-PROJECT-NOTE-323. Geneva: CERN, Sept. 2003. URL: https://cds.cern.ch/record/691782.

[92] ATLAS Collaboration. ‘The ATLAS Experiment at the CERN Large Hadron Collider’. In: *JINST* 3 (2008), S08003. DOI: 10.1088/1748-0221/3/08/S08003.

[93] T. A. Collaboration. In: 3.08 (Aug. 2008), S08002–S08002. DOI: 10.1088/1748-0221/3/08/s08002. URL: https://doi.org/10.1088%2F1748-0221%2F3%2F08%2Fs08002.

[94] *ATLAS liquid-argon calorimeter: Technical Design Report*. Technical Design Report ATLAS. Geneva: CERN, 1996. URL: https://cds.cern.ch/record/331061.

[95] *ATLAS tile calorimeter: Technical Design Report*. Technical Design Report ATLAS. Geneva: CERN, 1996. URL: https://cds.cern.ch/record/331062.

[96] ATLAS Collaboration. ‘Readiness of the ATLAS Tile Calorimeter for LHC collisions’. In: *Eur. Phys. J. C* 70 (2010), p. 1193. DOI: 10.1140/epjc/s10052-010-1508-y. arXiv: 1007.5423 [hep-ex].

[97] *ATLAS muon spectrometer: Technical Design Report*. Technical Design Report ATLAS. Geneva: CERN, 1997. URL: https://cds.cern.ch/record/331068.

[98] A. Yamamoto et al. ‘The ATLAS central solenoid’. In: *Nucl. Instrum. Meth.* A584 (2008), pp. 53–74. DOI: 10.1016/j.nima.2007.09.047.

[99] J. P. Badiou et al. *ATLAS barrel toroid: Technical Design Report*. Technical Design Report ATLAS. Electronic version not available. Geneva: CERN, 1997. URL: https://cds.cern.ch/record/331065.

[100] *ATLAS magnet system: Technical Design Report, 1*. Technical Design Report ATLAS. Geneva: CERN, 1997. URL: https://cds.cern.ch/record/338080.

[101] *ATLAS level-1 trigger: Technical Design Report*. Technical Design Report ATLAS. Geneva: CERN, 1998. URL: http://cds.cern.ch/record/381429.

[102] P. Jenni et al. *ATLAS high-level trigger, data-acquisition and controls: Technical Design Report*. Technical Design Report ATLAS. Geneva: CERN, 2003. URL: https://cds.cern.ch/record/616089.

[103] ‘The ATLAS Data Acquisition and High Level Trigger system’. In: *Journal of Instrumentation* 11.06 (June 2016), P06008–P06008. DOI: 10.1088/1748-0221/11/06/p06008. URL: https://doi.org/10.1088%2F1748-0221%2F11%2F06%2Fp06008.

[104] A. Sidoti. ‘Minimum Bias Trigger Scintillators in ATLAS Run II’. In: *JINST* 9.10 (2014), p. C10020. DOI: 10.1088/1748-0221/9/10/C10020.

[105] P. Jenni, M. Nessi and M. Nordberg. *Zero Degree Calorimeters for ATLAS*. Tech. rep. CERN-LHCC-2007-001. LHCC-I-016. Geneva: CERN, Jan. 2007. URL: http://cds.cern.ch/record/1009649.

[106] R. Snellings. ‘Collective expansion at the LHC: selected ALICE anisotropic flow measurements’. In: *Journal of Physics G: Nuclear and Particle Physics* 41.12 (Nov. 2014), p. 124007. ISSN: 1361-6471. DOI: 10.1088/0954-3899/41/12/124007. URL: http://dx.doi.org/10.1088/0954-3899/41/12/124007.

[107] C. Ohm and T. Pauly. ‘The ATLAS beam pick-up based timing system’. In: *Nuclear Instruments and Methods in Physics Research Section A: Accelerators, Spectrometers, Detectors and Associated Equipment* 623.1 (Nov. 2010), pp. 558–560. ISSN: 0168-9002. DOI: 10.1016/j.nima.2010.03.069. URL: http://dx.doi.org/10.1016/j.nima.2010.03.069.

[108] V. Cindro et al. 'The ATLAS beam conditions monitor'. In: *JINST* 3 (2008), P02004. DOI: 10.1088/1748-0221/3/02/P02004.

[109] G. Duckeck et al. 'ATLAS computing: Technical design report'. In: (2005).

[110] I. Bird et al. 'LHC computing Grid. Technical design report'. In: (2005).

[111] ATLAS Collaboration. 'The ATLAS Simulation Infrastructure'. In: *Eur. Phys. J. C* 70 (2010), p. 823. DOI: 10.1140/epjc/s10052-010-1429-9. arXiv: 1005.4568 [physics.ins-det].

[112] S. Agostinelli et al. 'GEANT4: A Simulation toolkit'. In: *Nucl. Instrum. Meth.* A506 (2003), pp. 250–303. DOI: 10.1016/S0168-9002(03)01368-8.

[113] E. Richter-Was, D. Froidevaux and L. Poggioli. 'ATLFAST 2.0 a fast simulation package for ATLAS'. In: (1998).

[114] E. Barberio et al. 'Fast shower simulation in the ATLAS calorimeter'. In: *Journal of Physics: Conference Series* 119.3 (July 2008), p. 032008. DOI: 10.1088/1742-6596/119/3/032008. URL: https://doi.org/10.1088%2F1742-6596%2F119%2F3%2F032008.

[115] G. Aad et al. 'Electron and photon performance measurements with the ATLAS detector using the 2015–2017 LHC proton-proton collision data'. In: *Journal of Instrumentation* 14.12 (Dec. 2019), P12006–P12006. ISSN: 1748-0221. DOI: 10.1088/1748-0221/14/12/p12006. URL: http://dx.doi.org/10.1088/1748-0221/14/12/P12006.

[116] M. Aaboud et al. 'Electron reconstruction and identification in the ATLAS experiment using the 2015 and 2016 LHC proton–proton collision data at $\sqrt{s} = 13$TeV'. In: *The European Physical Journal C* 79.8 (Aug. 2019). ISSN: 1434-6052. DOI: 10.1140/epjc/s10052-019-7140-6. URL: http://dx.doi.org/10.1140/epjc/s10052-019-7140-6.

[117] ATLAS Collaboration. 'Performaaance of the ATLAS Transition Radiation Tracker in Run 1 of the LHC: tracker properties'. In: *JINST* (2017). DOI: 10.1088/1748-0221/12/05/P05002.

[118] ALICE Collaboration. 'The ALICE Transition Radiation Detector: construction, operation, and performance'. In: *NIM-A* (2017). DOI: 10.1016/j.nima.2017.09.028.

[119] ATLAS Collaboration. 'ATLAS Transition Radiation Tracker (TRT): Straw Tubes for Tracking and Particle Identification at the Large Hadron Collider'. In: *NIM-A* (2016). DOI: 10.1016/j.nima.2016.04.026.

[120] A. Basalaev, Z. Marshall and A. Collaboration. 'The Fast Simulation Chain for ATLAS'. In: *Journal of Physics: Conference Series* 898.4 (2017), p. 042016. DOI: 10.1088/1742-6596/898/4/042016.

[121] D. Davis. *Gas Type Emulation in the Simulation of the ATLAS Transition Radiation Tracker*. Tech. rep. ATL-COM-INDET-2017-001. Geneva: CERN, Dec. 2016. URL: https://cds.cern.ch/record/2241907.

[122] ALICE Collaboration, B. Abelev et al. 'Measurement of the Cross Section for Electromagnetic Dissociation with Neutron Emission in Pb-Pb Collisions at $\sqrt{s_{NN}} = 2.76$ TeV'. In: *Phys. Rev. Lett.* 109 (2012), p. 252302. DOI: 10.1103/PhysRevLett.109.252302. arXiv: 1203.2436 [nucl-ex].

[123] ATLAS Collaboration. 'The ATLAS Simulation Infrastructure'. In: *Eur. Phys. J.* C70 (2010), pp. 823–874. DOI: 10.1140/epjc/s10052-010-1429-9. arXiv: 1005.4568 [physics.ins-det].

[124] L. A. Harland-Lang, V. A. Khoze and M. G. Ryskin. 'Exclusive LHC physics with heavy ions: SuperChic 3'. In: *Eur. Phys. J.* C79.1 (2019), p. 39. DOI: 10.1140/epjc/s10052-018-6530-5. arXiv: 1810.06567 [hep-ph].

[125] M. Kłusek-Gawenda, P. Lebiedowicz and A. Szczurek. 'Light-by-light scattering in ultraperipheral Pb-Pb collisions at energies available at the CERN Large Hadron Collider'. In: *Phys. Rev.* C93.4 (2016), p. 044907. DOI: 10.1103/PhysRevC.93.044907. arXiv: 1601.07001 [nucl-th].

[126] S. R. Klein and J. Nystrand. 'Photoproduction of quarkonium in proton proton and nucleus nucleus collisions'. In: *Phys. Rev. Lett.* 92 (2004), p. 142003. DOI: 10.1103/PhysRevLett.92.142003. arXiv: hep-ph/0311164 [hep-ph].

[127] CMS Collaboration. ‘Evidence for light-by-light scattering and searches for axion-like particles in ultraperipheral PbPb collisions at $\sqrt{s_{\mathrm{NN}}} = 5.02$ TeV’. In: (2018). arXiv: 1810.04602 [hep-ex].

[128] Z. Bern et al. ‘QCD and QED corrections to light by light scattering’. In: *JHEP* 11 (2001), p. 031. DOI: 10.1088/1126-6708/2001/11/031. arXiv: hep-ph/0109079 [hep-ph].

[129] M. Kłusek-Gawenda, W. Schaefer and A. Szczurek. ‘Two-gluon exchange contribution to elastic $\gamma\gamma \to \gamma\gamma$ scattering and production of two-photons in ultraperipheral ultrarelativistic heavy ion and proton-proton collisions’. In: (2016). DOI: 10.1016/j.physletb.2016.08.059. arXiv: 1606.01058 [hep-ph].

[130] M. Bahr et al. ‘Herwig++ Physics and Manual’. In: *Eur. Phys. J.* C58 (2008), pp. 639–707. DOI: 10.1140/epjc/s10052-008-0798-9. arXiv: 0803.0883 [hep-ph].

[131] J. Bellm et al. ‘Herwig++ 2.7 Release Note’. In: (Oct. 2013). arXiv: 1310.6877 [hep-ph].

[132] URL: https://twiki.cern.ch/twiki/bin/viewauth/Atlas/TileTripReader.

[133] T. A. collaboration. ‘Monitoring and data quality assessment of the ATLAS liquid argon calorimeter’. In: *Journal of Instrumentation* 9.07 (July 2014), P07024–P07024. DOI: 10.1088/1748-0221/9/07/p07024. URL: https://doi.org/10.1088%2F1748-0221%2F9%2F07%2Fp07024.

[134] A. Dafinca, J. Henderson and A. R. Weidberg. *Single Event Upset Studies Using the ATLAS SCT*. Tech. rep. ATL-COM-INDET-2013-064. TWEPP proceedings deadline is 1/11/13. Geneva: CERN, Oct. 2013. URL: https://cds.cern.ch/record/1607080.

[135] ATLAS Collaboration. ‘Measurement of the photon identification efficiencies with the ATLAS detector using LHC Run 2 data collected in 2015 and 2016’. In: *Submitted to: Eur. Phys. J.* (2018). arXiv: 1810.05087 [hep-ex].

[136] ATLAS Collaboration. ‘Electron and photon energy calibration with the ATLAS detector using 2015-2016 LHC proton-proton collision data’. In: *Submitted to: JINST* (2018). arXiv: 1812.03848 [hep-ex].

[137] ATLAS Collaboration. ‘Electron reconstruction and identification in the ATLAS experiment using the 2015 and 2016 LHC proton-proton collision data at $\sqrt{s} = 13$ TeV’. In: (2019). arXiv: 1902.04655 [physics.ins-det].

[138] ATLAS egamma CP group. *Egamma CP recommendations*. https://twiki.cern.ch/twiki/bin/viewauth/AtlasProtected/ElectronPhotonFourMomentumCorrection. 2018.

[139] E. Abbas et al. ‘Charmonium and e^+e^- pair photoproduction at mid-rapidity in ultra-peripheral Pb-Pb collisions at $\sqrt{s_{\mathrm{NN}}}$=2.76 TeV’. In: *Eur. Phys. J.* C73.11 (2013), p. 2617. DOI: 10.1140/epjc/s10052-013-2617-1. arXiv: 1305.1467 [nucl-ex].

[140] ATLAS Collaboration. *Track Reconstruction Performance of the ATLAS Inner Detector at $\sqrt{s} = 13$ TeV*. ATL-PHYS-PUB-2015-018. 2015. URL: https://cds.cern.ch/record/2037683.

[141] ATLAS tracking CP group. *Tracking CP recommendations*. https://twiki.cern.ch/twiki/bin/view/AtlasProtected/TrackingCPRecsRun2Final. 2018.

[142] L. A. Harland-Lang et al. ‘Parton distributions in the LHC era: MMHT 2014 PDFs’. In: *Eur. Phys. J. C* 75.5 (2015), p. 204. DOI: 10.1140/epjc/s10052-015-3397-6. arXiv: 1412.3989 [hep-ph].

[143] S. Dulat et al. ‘New parton distribution functions from a global analysis of quantum chromodynamics’. In: *Phys. Rev. D* 93.3 (2016), p. 033006. DOI: 10.1103/PhysRevD.93.033006. arXiv: 1506.07443 [hep-ph].

[144] R. D. Ball et al. ‘Parton distributions from high-precision collider data’. In: *Eur. Phys. J. C* 77.10 (2017), p. 663. DOI: 10.1140/epjc/s10052-017-5199-5. arXiv: 1706.00428 [hep-ph].

[145] ATLAS Collaboration. *Reconstruction of collinear final-state-radiation photons in Z decays to muons in $\sqrt{s} = 7$ TeV proton–proton collisions*. ATLAS-CONF-2012-143. 2012. URL: https://cds.cern.ch/record/1491697.

[146] D. d'Enterria and G. G. Silveira. 'Observing light-by-light scattering at the Large Hadron Collider'. In: *Phys. Rev. Lett.* 111 (2013). [Erratum: Phys. Rev. Lett.116,no.12,129901(2016)], p. 080405. DOI: 10.1103/PhysRevLett.111.080405,10.1103/PhysRevLett.116.129901. arXiv: 1305.7142 [hep-ph].

[147] M. Klusek-Gawenda and A. Szczurek. 'Exclusive production of large invariant mass pion pairs in ultraperipheral ultrarelativistic heavy ion collisions'. In: *Phys. Lett. B* 700 (2011), pp. 322–330. DOI: 10.1016/j.physletb.2011.05.015. arXiv: 1104.0571 [nucl-th].

[148] M. Kłusek-Gawenda. 'Importance of mesons in light-by-light scattering in ultraperipheral lead-lead collisions at the LHC'. In: *15th International Workshop on Meson Physics (MESON 2018) Kraków, Poland, June 7-12, 2018.* 2018. arXiv: 1809.03823 [hep-ph].

[149] L. A. Harland-Lang et al. 'Central exclusive meson pair production in the perturbative regime at hadron colliders'. In: *Eur. Phys. J.* C71 (2011), p. 1714. DOI: 10.1140/epjc/s10052-011-1714-2. arXiv: 1105.1626 [hep-ph].

[150] L. A. Harland-Lang et al. 'Central exclusive production as a probe of the gluonic component of the eta' and eta mesons'. In: *Eur. Phys. J.* C73 (2013), p. 2429. DOI: 10.1140/epjc/s10052-013-2429-3. arXiv: 1302.2004 [hep-ph].

[151] J. Alwall et al. 'The automated computation of tree-level and next-to-leading order differential cross sections, and their matching to parton shower simulations'. In: *JHEP* 07 (2014), p. 079. DOI: 10.1007/JHEP07(2014)079. arXiv: 1405.0301 [hep-ph].

[152] D. Ebert, R. N. Faustov and V. O. Galkin. 'Properties of heavy quarkonia and B_c mesons in the relativistic quark model'. In: *Phys. Rev. D* 67 (2003), p. 014027. DOI: 10.1103/PhysRevD.67.014027. arXiv: hep-ph/0210381 [hep-ph].

[153] J. Segovia et al. 'Bottomonium spectrum revisited'. In: *Phys. Rev. D* 93.7 (2016), p. 074027. DOI: 10.1103/PhysRevD.93.074027. arXiv: 1601.05093 [hep-ph].

[154] C. A. Bertulani and G. Baur. 'Electromagnetic Processes in Relativistic Heavy Ion Collisions'. In: *Phys. Rept.* 163 (1988), p. 299. DOI: 10.1016/0370-1573(88)90142-1.

[155] G. Cowan et al. 'Asymptotic formulae for likelihood-based tests of new physics'. In: *Eur. Phys. J.* C71 (2011). [Erratum: Eur. Phys. J.C73,2501(2013)], p. 1554. DOI: 10.1140/epjc/s10052-011-1554-0,10.1140/epjc/s10052-013-2501-z. arXiv: 1007.1727 [physics.data-an].

[156] G. D'Agostini. 'A Multidimensional unfolding method based on Bayes' theorem'. In: *Nucl. Instrum. Meth. A* 362 (1995), pp. 487–498. DOI: 10.1016/0168-9002(95)00274-X.

[157] *High Energy Physics Data Repository.* URL: https://hepdata.net.

[158] H. Primakoff. 'Photo-Production of Neutral Mesons in Nuclear Electric Fields and the Mean Life of the Neutral Meson'. In: *Phys. Rev.* 81 (5 Mar. 1951), pp. 899–899. DOI: 10.1103/PhysRev.81.899. URL: https://link.aps.org/doi/10.1103/PhysRev.81.899.

[159] P. Sikivie. 'Experimental Tests of the "Invisible" Axion'. In: *Phys. Rev. Lett.* 51 (16 Oct. 1983), pp. 1415–1417. DOI: 10.1103/PhysRevLett.51.1415. URL: https://link.aps.org/doi/10.1103/PhysRevLett.51.1415.

[160] A. Helmi. 'The stellar halo of the Galaxy'. In: *The Astronomy and Astrophysics Review* 15.3 (Apr. 2008), pp. 145–188. ISSN: 1432-0754. DOI: 10.1007/s00159-008-0009-6. URL: http://dx.doi.org/10.1007/s00159-008-0009-6.

[161] N. Du et al. 'Search for Invisible Axion Dark Matter with the Axion Dark Matter Experiment'. In: *Physical Review Letters* 120.15 (Apr. 2018). ISSN: 1079-7114. DOI: 10.1103/physrevlett.120.151301. URL: http://dx.doi.org/10.1103/PhysRevLett.120.151301.

[162] P. Brun et al. 'A new experimental approach to probe QCD axion dark matter in the mass range above 40 μeV'. In: *Eur. Phys. J. C* 79.3 (2019), p. 186. DOI: 10.1140/epjc/s10052-019-6683-x. arXiv: 1901.07401 [physics.ins-det].

[163] D. Lazarus et al. 'A Search for solar axions'. In: *Phys. Rev. Lett.* 69 (1992), pp. 2333–2336. DOI: 10.1103/PhysRevLett.69.2333.

[164] R. Ohta et al. 'The Tokyo axion helioscope'. In: *Nuclear Instruments and Methods in Physics Research Section A: Accelerators, Spectrometers, Detectors and Associated Equipment* 670 (Apr. 2012), pp. 73–78. ISSN: 0168-9002. DOI: 10.1016/j.nima.2011.12.027. URL: http://dx.doi.org/10.1016/j.nima.2011.12.027.

[165] K. Zioutas et al. 'A decommissioned LHC model magnet as an axion telescope'. In: *Nuclear Instruments and Methods in Physics Research Section A: Accelerators, Spectrometers, Detectors and Associated Equipment* 425.3 (Apr. 1999), pp. 480–487. ISSN: 0168-9002. DOI: 10.1016/s0168-9002(98)01442-9. URL: http://dx.doi.org/10.1016/S0168-9002(98)01442-9.

[166] 'New CAST limit on the axion–photon interaction'. In: *Nature Physics* 13.6 (May 2017), pp. 584–590. ISSN: 1745-2481. DOI: 10.1038/nphys4109. URL: http://dx.doi.org/10.1038/nphys4109.

[167] E. Armengaud et al. 'Conceptual design of the International Axion Observatory (IAXO)'. In: *Journal of Instrumentation* 9.05 (May 2014), T05002–T05002. ISSN: 1748-0221. DOI: 10.1088/1748-0221/9/05/t05002. URL: http://dx.doi.org/10.1088/1748-0221/9/05/T05002.

[168] V. Desjacques, A. Kehagias and A. Riotto. 'The impact of ultra-light axion self-interactions on the large scale structure of the Universe'. In: *Physical Review D* 97 (Sept. 2017). DOI: 10.1103/PhysRevD.97.023529.

[169] M. A. Fedderke, P. W. Graham and S. Rajendran. 'Axion dark matter detection with CMB polarization'. In: *Physical Review D* 100.1 (July 2019). ISSN: 2470-0029. DOI: 10.1103/physrevd.100.015040. URL: http://dx.doi.org/10.1103/PhysRevD.100.015040.

[170] E. W. Kolb and M. S. Turner. *The Early Universe.* Vol. 69. 1990. ISBN: 978-0-201-62674-2.

[171] A. Salvio, A. Strumia and W. Xue. 'Thermal axion production'. In: *Journal of Cosmology and Astroparticle Physics* 2014.01 (Jan. 2014), pp. 011–011. ISSN: 1475-7516. DOI: 10.1088/1475-7516/2014/01/011. URL: http://dx.doi.org/10.1088/1475-7516/2014/01/011.

[172] D. Grin, T. L. Smith and M. Kamionkowski. 'Axion constraints in nonstandard thermal histories'. In: *Physical Review D* 77.8 (Apr. 2008). ISSN: 1550-2368. DOI: 10.1103/physrevd.77.085020. URL: http://dx.doi.org/10.1103/PhysRevD.77.085020.

[173] E. Di Valentino et al. 'Robustness of cosmological axion mass limits'. In: *Physical Review D* 91.12 (June 2015). ISSN: 1550-2368. DOI: 10.1103/physrevd.91.123505. URL: http://dx.doi.org/10.1103/PhysRevD.91.123505.

[174] E. Di Valentino et al. 'Cosmological axion and neutrino mass constraints from Planck 2015 temperature and polarization data'. In: *Physics Letters B* 752 (Jan. 2016), pp. 182–185. ISSN: 0370-2693. DOI: 10.1016/j.physletb.2015.11.025. URL: http://dx.doi.org/10.1016/j.physletb.2015.11.025.

[175] M. Archidiacono et al. 'Future cosmological sensitivity for hot dark matter axions'. In: *Journal of Cosmology and Astroparticle Physics* 2015.05 (May 2015), pp. 050–050. ISSN: 1475-7516. DOI: 10.1088/1475-7516/2015/05/050. URL: http://dx.doi.org/10.1088/1475-7516/2015/05/050.

[176] E. Shellard. 'AXIONIC DOMAIN WALLS AND COSMOLOGY'. In: *27th Liege International Astrophysical Colloquium on Origin and Ea Early History of the Universe.* 1986, pp. 173–180.

[177] M. Cicoli, M. D. Goodsell and A. Ringwald. 'The type IIB string axiverse and its low-energy phenomenology'. In: *Journal of High Energy Physics* 2012.10 (Oct. 2012). ISSN: 1029-8479. DOI: 10.1007/jhep10(2012)146. URL: http://dx.doi.org/10.1007/JHEP10(2012)146.

[178] T. Higaki, K. Nakayama and F. Takahashi. 'Moduli-induced axion problem'. In: *Journal of High Energy Physics* 2013.7 (July 2013). ISSN: 1029-8479. DOI: 10.1007/jhep07(2013)005. URL: http://dx.doi.org/10.1007/JHEP07(2013)005.

[179] F. Aharonian et al. 'A low level of extragalactic background light as revealed by γ-rays from blazars'. In: *Nature* 440.7087 (Apr. 2006), pp. 1018–1021. ISSN: 1476-4687. DOI: 10.1038/nature04680. URL: http://dx.doi.org/10.1038/nature04680.

[180] J. Albert et al. 'Very-High-Energy Gamma Rays from a Distant Quasar: How Transparent Is the Universe?' In: *Science* 320.5884 (June 2008), pp. 1752–1754. ISSN: 1095-9203. DOI: `10.1126/science.1157087`. URL: `http://dx.doi.org/10.1126/science.1157087`.

[181] G. Galanti et al. *Hints for an axion-like particle from PKS 1222+216?* 2014. arXiv: `1409.4401 [astro-ph.HE]`.

[182] A. Arvanitaki, M. Baryakhtar and X. Huang. 'Discovering the QCD axion with black holes and gravitational waves'. In: *Physical Review D* 91.8 (Apr. 2015). ISSN: 1550-2368. DOI: `10.1103/physrevd.91.084011`. URL: `http://dx.doi.org/10.1103/PhysRevD.91.084011`.

[183] A. Arvanitaki et al. 'Black hole mergers and the QCD axion at Advanced LIGO'. In: *Physical Review D* 95.4 (Feb. 2017). ISSN: 2470-0029. DOI: `10.1103/physrevd.95.043001`. URL: `http://dx.doi.org/10.1103/PhysRevD.95.043001`.

[184] M. Ajello et al. 'Search for Spectral Irregularities due to Photon–Axionlike-Particle Oscillations with the Fermi Large Area Telescope'. In: *Physical Review Letters* 116.16 (Apr. 2016). ISSN: 1079-7114. DOI: `10.1103/physrevlett.116.161101`. URL: `http://dx.doi.org/10.1103/PhysRevLett.116.161101`.

[185] D. Hooper and P. D. Serpico. 'Detecting Axionlike Particles with Gamma Ray Telescopes'. In: *Physical Review Letters* 99.23 (Dec. 2007). ISSN: 1079-7114. DOI: `10.1103/physrevlett.99.231102`. URL: `http://dx.doi.org/10.1103/PhysRevLett.99.231102`.

[186] K. A. Hochmuth and G. Sigl. 'Effects of axion-photon mixing on gamma-ray spectra from magnetized astrophysical sources'. In: *Physical Review D* 76.12 (Dec. 2007). ISSN: 1550-2368. DOI: `10.1103/physrevd.76.123011`. URL: `http://dx.doi.org/10.1103/PhysRevD.76.123011`.

[187] G. Galanti and M. Roncadelli. 'Extragalactic photon–axion-like particle oscillations up to 1000 TeV'. In: *Journal of High Energy Astrophysics* 20 (Nov. 2018), pp. 1–17. ISSN: 2214-4048. DOI: `10.1016/j.jheap.2018.07.002`. URL: `http://dx.doi.org/10.1016/j.jheap.2018.07.002`.

[188] J. Isern et al. 'Axions and the Cooling of White Dwarf Stars'. In: *The Astrophysical Journal* 682.2 (July 2008), pp. L109–L112. ISSN: 1538-4357. DOI: `10.1086/591042`. URL: `http://dx.doi.org/10.1086/591042`.

[189] S. Knapen et al. 'Searching for Axionlike Particles with Ultraperipheral Heavy-Ion Collisions'. In: *Phys. Rev. Lett.* 118 (17 Apr. 2017), p. 171801. DOI: `10.1103/PhysRevLett.118.171801`. URL: `https://link.aps.org/doi/10.1103/PhysRevLett.118.171801`.

[190] M. Baak et al. 'HistFitter software framework for statistical data analysis'. In: *Eur. Phys. J. C* 75 (2015), p. 153. DOI: `10.1140/epjc/s10052-015-3327-7`. arXiv: `1410.1280 [hep-ex]`.

[191] C. Azevedo, V. P. Gonçalves and B. D. Moreira. 'Exclusive dilepton production in ultraperipheral *PbPb* collisions at the LHC'. In: *Eur. Phys. J. C* 79.5 (2019), p. 432. DOI: `10.1140/epjc/s10052-019-6952-8`. arXiv: `1902.00268 [hep-ph]`.

[192] ATLAS Collaboration. 'Luminosity determination in pp collisions at $\sqrt{s} = 8$ TeV using the ATLAS detector at the LHC'. In: (2016). arXiv: `1608.03953 [hep-ex]`.

[193] M. Bauer, M. Neubert and A. Thamm. 'Collider probes of axion-like particles'. In: *JHEP* 12 (2017), p. 044. DOI: `10.1007/JHEP12(2017)044`. arXiv: `1708.00443 [hep-ph]`.